Department of Chemistry

Metakaolin as a Model System for Understanding Geopolymers

Shani Sperinck

This thesis is presented for the degree of

Doctor of Philosophy

of

Curtin University

October 2012

Declaration

I, Shani Sperinck, declare that to the best of my knowledge and belief this thesis contains no material previously published by any other person except where due acknowledgment has been made.

This thesis contains no material which has been accepted for the award of any other degree or diploma in any university.

Signed: _____

Date: _____

"Do not fear mistakes. You will know failure. Continue to reach out."

Benjamin Franklin

Abstract

Geopolymers are a class of amorphous aluminosilicate materials that exhibit a range of properties depending on synthesis parameters. Determining the molecular interactions responsible for the different characteristics experimentally is hindered by the compositional variation of the source materials. Computational methods are thus used to provide atom level insights, with metakaolin used as a model system to represent the Al/Si geopolymer matrix. The formation of metakaolin through the thermal de-hydroxylation of kaolinite was simulated with molecular dynamics using an interatomic potential model identified through testing of several models from the literature. The simulated metakaolin exhibited a 1:1 Al/Si ordering with a loss in periodicity due to the migration of aluminium ions through the structure. The change in the aluminium coordination as a function of de-hydroxylation results in a final structure composed of primarily 4-fold Al with up to 20% of the Al in a 5-fold coordination.

A complex cavity network was identified and characterised in metakaolin and provided sites for the inclusion of sodium, potassium and calcium interstitial defect ions. The results showed that whilst ionic size controlled the final locations of the defect ions, ionic charge influenced the degree of interaction with the surrounding oxygen atoms and resulted in greater variations in the final defect site characteristics. Introducing hydroxyl groups into the structure caused the interactions of the defects with the aluminium to increase compared to silicon, demonstrating that the degree of source material hydration is as important as the type of metal cations present in the geopolymerisation reaction.

A procedure for the generation of stable, partially hydrated metakaolin surfaces was developed and the resulting surfaces had a high degree of roughness that increased in the presence of water. The Al-terminated surfaces in metakaolin demonstrated the greatest level of interaction with water compared to Si, causing a surface puckering effect that resulted in a widening of the surface layers. The results indicate that water plays an important role, as the presence of water in the reaction mixture combined with high levels of structural disorder in the source materials increase their susceptibility to the caustic attack involved in geopolymerisation.

Acknowledgements

I would first like to thank my supervisors: Kate Wright, Nigel Marks and Paolo Raiteri. Without their guidance and vision none of this would have been possible. The depth and breadth of expertise I had at my disposal was more than any student could ask for.

I would like to acknowledge Curtin University, the Centre for Sustainable Resource Processing and the Nanochemistry Research Group for providing funding through scholarships. The Australian National Computing Infrastructure and iVec are also acknowledged for the provision of the computing resources used in this research. I would also like to thank Julian Gale for provision of and help with the GULP software.

I would like to thank the computational chemistry group at Curtin and all its variations for the immense support provided during my time there. I would particularly like to thank Marc Robinson, Dino Spagnoli, Irene Suarez-Martinez, Phillip English and Patrick Higginbottom - a significant portion of this thesis would not have happened if not for their help and support.

Finally, I would like to thank my friends and family. Their unwavering support, pride and love have always been the driving force in my endeavours, and to them I owe everything.

Contents

List of Figures

List of Tables

Abbreviations

AVAS	**A**tomic **V**isualisation and **A**nalysis **S**oftware
BET	**B**runauer–**E**mmett–**T**eller
BFGS	**B**royden-**F**letcher-**G**oldfarb-**S**hanno
DFT	**D**ensity **F**unctional **T**heory
EDS	**E**nergy **D**ispersive **S**pectroscopy
FTIR	**F**ourier **T**ransform **I**nfra-**R**ed
GDIS	**G**TK **D**isplay **I**nterface for **S**tructures
GULP	**G**eneral **U**tility **L**attice **P**rogram
HRTEM	**H**igh **R**esolution **T**ransmission **E**lectron **M**icroscopy
LAMMPS	**L**arge-scale **A**tomic/**M**olecular **M**assively **P**arallel **S**imulator
LJ	**L**ennard-**J**ones
MC	**M**onte **C**arlo
MD	**M**olecular **D**ynamics
MK	**M**eta**K**aolin
MAS-NMR	**M**agic-**A**ngle **S**pinning-**N**uclear **M**agnetic **R**esonance
MSD	**M**ean **S**quare **D**isplacement
NBO	**N**on **B**onded **O**xygen
NPT	Constant **N**umber of atoms, **P**ressure and **T**emperature
NσT	Constant **N**umber of atoms, Stress (σ) and **T**emperature
NVE	Constant **N**umber of atoms, **V**olume and **E**nergy
NVT	Constant **N**umber of atoms, **V**olume and **T**emperature
OCO	**O**ver **C**oordinated **O**xygen
OPC	**O**rdinary **P**ortland **C**ement
PBC	**P**eriodic **B**oundary **C**ondition
PS	**P**oly**S**ialate
PSS	**P**oly**S**ialate **S**iloxo
PSDS	**P**oly**S**ialate **DiS**iloxo
QM	**Q**uantum **M**echanics
RDF	**R**adial **D**istribution **F**unction
SAED	**S**elected **A**rea **E**lectron **D**iffraction
SPC/Fw	**S**ingle **P**oint **C**harge/**F**lexible **W**ater
SPME	**S**mooth **P**article **M**esh **E**wald
vdW	**v**an **d**er **W**aals
XRD/F	**X**-**R**ay **D**iffraction/**F**luorescence

Chapter 1

Introduction

The increase in industrial operations across the world has brought with it the need to develop sustainable and environmentally conscious approaches to waste management. In recent decades the increase in the production of carbon dioxide gas, CO_2, as a waste by-product of the burning of fossil fuels has led to debate on its effects on the environment and the implications for the global warming phenomenon. Studies by the Department of Climate Change and Energy Efficiency showed that Australia produced approximately 550 mega-tonnes of CO_2 in one year with 5% of this due to industrial processes and waste [1]. This makes Australia one of the biggest green house gas producers per capita, and minimising the production of this potentially toxic by-product is encouraged.

A significant proportion of CO_2 production is from the heating or calcination of minerals for use in the cement and concrete industries. One of the most common cements used in the world is ordinary Portland cement (OPC), which is manufactured by heating the raw minerals to sintering temperatures. This process requires vast amounts of fuels such as coal and natural gas to be burnt in order to reach the temperatures required, with additional chemical CO_2 released as part of the calcination process. The result is that the production of 1 tonne of OPC produces approximately 1 tonne of CO_2 [2], and this does not include the additional CO_2 associated with transportation. With concrete and cementitious materials providing the backbone to much of modern infrastructure, minimising the CO_2 production from this industry is highly beneficial to the environment.

The need to reduce carbon dioxide emissions has lead to the development of greener technologies such as *geopolymers* as an alternative to OPC. Geopolymers

are poorly ordered aluminosilicate materials that do not require calcination of the source materials. They exhibit excellent physical and chemical properties, including high mechanical strength, low alkali-aggregate expansion, freeze-thaw, sulphate and corrosion resistance and minimal response to acid leaching and consequently lead to a diverse range of potential applications [3–5].

Geopolymers can be formed from a range of inorganic waste materials such as fly-ash and residues from mineral processing operations, and this has led to a significant level of interest in these materials [6–8]. The utilisation of waste is attractive from an environmental perspective, and the majority of studies regarding the engineering of geopolymers deal primarily with products based upon fly-ash and slag [4, 9–15]. Fly ash is a waste product from power stations and slag is a by–product from the smelting of ores in the metal extraction process, and the variability in composition of the coal and ores used in these processes result in highly heterogeneous compositions of the waste products.

The large-scale industrial adoption of geopolymer technology has been slowed by the lack of a detailed chemical understanding of the geopolymer formation and structure [15]. To determine the molecular structure of a geopolymer, the interactions of the different components of the network need to be determined, and the use of highly heterogeneous source materials has hindered the development of this fundamental understanding due to the presence of materials that may or may not play a significant role. In these circumstances, more homogenous source materials are required to reduce the variability. Metakaolin is one such material that is commonly used in the investigation of the geopolymer structure and synthesis [16–26] and is composed of a disordered aluminosilicate network that shares some common characteristics with geopolymers. Investigations of metakaolin-based geopolymers provide useful information regarding the physical characteristics and interactions of geopolymers, and the following sections provide a brief overview of the current knowledge of these materials.

1.1 What is a Geopolymer?

In the late 1970's Joseph Davidovits [27] introduced the term *geopolymer* to describe the "mineral polymers resulting from geochemistry" [6, 28, 29] that resulted from mixing naturally occurring aluminosilicate materials with a concentrated aqueous alkali solution. Since the introduction of the term geopolymer, much confusion has developed over its exact definition. In broad terms geopolymers are a class of synthetic aluminosilicate materials. However, this definition is insufficient as it can include many other cementitious materials and manufactured aluminosilicates, which are not geopolymers. Definitions that include the alkali activation or the polymer-like aluminosilicate network characteristic of these materials provide better classification.

The terms *inorganic polymer* or *alkali activated* binder, cement or concrete are often used synonymously with geopolymers. It should also be noted that a significant proportion of the geopolymer literature uses the term to refer to the final products formed by the alkali activation of a aluminosilicate source material mixed with an aggregating medium such as sand. In the production of regular concrete it is the mixture of aggregate and *cement* that produces the final product, and so here, as in the concrete industry, the term geopolymer refers to the material used to 'bind' the aggregate together.

Geopolymers can exhibit a wide variety of properties and characteristics depending on the raw materials and the manufacturing conditions [4, 11, 15, 30–32]. The range of physical properties and the ability to tailor them using different reaction conditions make geopolymers potentially useful in many applications beyond concrete such as fire and acid resistance coatings [33–36], binders or adhesives [37–39] or in toxic waste immobilisation and storage [40–43].

1.2 Geopolymerisation

Geopolymers are classified as mineral or inorganic polymer materials, and contain large chains or networks of repeating molecular units called a monomer. The process by which the monomers react to form a polymer is called polymerisation. In the case of geopolymers, this process is called *geopolymerisation*. Traditional organic polymers are formed from carbon based monomer units with the C–C bond forming the polymer backbone, whilst an inorganic polymer typically has a silicon based backbone. Although demonstrating similar chemistry to carbon, silicon rarely forms Si–Si bonds. Instead silicon based polymers backbones are formed from Si–O–Si chains, and form materials such as polysiloxanes and polysilicates. Other inorganic polymers that do not contain silicon include polygermanes, polystannanes and polyphosphazenes.

Geopolymers belong to the class of inorganic polymers formed with these Si–O–Si backbones, where the Si–O bonds in the chains are strong but flexible and the silicon is tetrahedrally coordinated to four oxygen atoms. The Si^{4+} ion in these chains can be substituted by the Al^{3+} ion in a mainly tetrahedral coordination with the oxygen atoms, although an octahedral coordination is also possible. The substitution of the Si^{4+} ion by the Al^{3+} ion creates a charge imbalance on the network and requires additional cations to be present to balance this. The ratio of aluminium to silicon and the coordination of the aluminium in the network dictate the concentration of other ions in the network and the types of chains that make up the inorganic polymer networks.

There are an abundance of composite aluminosilicate materials in nature that are easily broken up into the individual AlO_n $(n = 4, 6)$ and SiO_4 units by treatment with alkaline solutions. In the geopolymerisation process, the alkaline solution liberates the monomeric AlO_4 and SiO_4 units from the source materials, which then rapidly coalesce or *polymerise* to form chains of linked tetrahedra connected

by oxygen atoms. These chains of AlO_4 and SiO_4 tetrahedra form larger oligomer structures called *polysialates* (PS) and provide the actual unit structures that then further polymerises to form the three-dimensional network of a geopolymer. This results in a poorly ordered array of aluminate and silicate tetrahedra in a network polymer-like structure that is balanced by cations such as Na^+, K^+, Li^+, and Ca^{2+} provided by either the alkaline solution or as impurities in the source materials.

1.2.1 Reaction Mechanisms

The formation of a geopolymer is an exothermic process that first involves the dissolution of a solid aluminosilicate oxide material in a MOH solution (M: alkali metal). The dissolved Al and Si complexes diffuse from the surfaces of the particles into solution and undergo polymerisation to form a gel phase. The gel phase then hardens and any remaining unreacted Al-Si source material becomes incorporated into the structure. The amount of Al-Si material required depends on the particle size, extent of dissolution of Al-Si materials and the concentration of the alkaline solution, and the rapid gelation and hardening prevent the aluminosilicate network becoming a more ordered structure.

Differential scanning calorimetry measurements taken during the geopolymer setting period show multiple heat flow peaks indicating that there are many chemical steps involved [44–48]. Figure 1.1 shows a conceptual model of the complexity of the geopolymerisation process proposed by Provis *et al.* [49]. The model incorporates various stages of the process, such as the requirement of additional silicate species to control the Si/Al ratio, the formation of the gel phase in the reaction and a secondary pathway to incorporate the formation of nano-crystalline zeolitic phases that are shown to be present in some geopolymers [50]. Since it was initially proposed, the Provis [47] model has been extended [17, 48] to allow

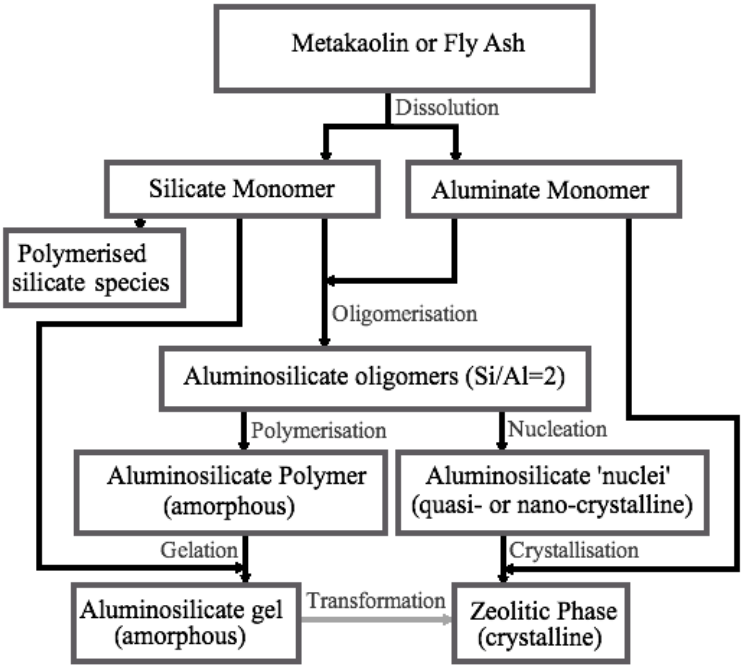

FIGURE 1.1: The conceptual model for geopolymerisation proposed by Provis *et al.* [17, 48, 49] showing the multiple steps involved in the synthesis of a geopolymer.

variability of stoichiometry of all aluminosilicate species, allowing for metastable or pozzolanic minerals to be used as the source materials.

The two main reaction processes involved are dissolution and polymerisation. The dissolution process is the liberation of the aluminate and silicate groups into the geopolymer liquor. This process is relatively well understood as there are many studies on the dissolution of aluminosilicates in alkaline conditions [48]. However, the way that these units coalesce and condense in the polymerisation phase to form the final geopolymer is not well understood. This polymerisation phase is considered to be autocatalytic [51] and occurs when there is a sufficiently large quantity of the polysialate units present. These rapidly react to form longer polymer chains which then precipitate out of solution, increasing the solid/liquid ratio. These large polysialate chains act as sites for further units to condense, causing the chains to become elongated and branched out. This transformation

is visible in the reaction vessel as the initially liquid phase transforms into a gel and the gel in turn solidifies into the final solid geopolymer material.

Reaction kinetic modelling using the Provis [17, 48, 49] concept model has provided a quantitatively accurate description of the measured heat evolution during the early stages of the metakaolin geopolymerisation [17, 48]. However, the model is still an over-simplification of the process, since for instance, it does not take into account the potential for the polymeric silicate and aluminate species to combine. Furthermore, it does not provide information of the chemical reactions that are occurring at each stage of the process. It also does not give a time scale for each of the processes that occur at each stage of the model. This is important for synthesis purposes, as the transformation from the amorphous aluminosilicate gel to the nano-crystalline zeolitic phase takes a substantially longer period of time than any of the other processes involved.

An important factor not included in the model is the nucleation process in geopolymerisation. Nucleation in zeolitic systems occurs via replacement of water in the hydration shells of cations by small aluminate or silicate species [52–54], but in a geopolymerisation system, the degree of supersaturation and number of nucleation triggers are very high. These triggers could include undissolved particles, newly formed crystals or amorphous aluminosilicate particles, or any other solid-liquid interface.

1.3 Engineering a Geopolymer

Much of the geopolymer literature is focused on developing materials suitable for industrial applications. Geopolymer synthesis is undertaken in ambient conditions, and upon setting the geopolymer mixture is cured at low temperatures to drive off any remaining moisture [20, 55]. There are three main reaction components involved that effect the final product: the source materials, the geopolymer

liquor and the filler materials. Each material provides a source for structural components such as the aluminate and silicate groups that form the Al/Si network or the cations required to charge balance the resulting structure. Identifying how these different components interact with each other to form the final structure is important if an atomic level understanding of geopolymers is to be developed.

1.3.1 Source Materials

The source materials can theoretically be any aluminosilicate material, and provide the source aluminate and silicate groups for the reaction. For geopolymerisation to occur, a sufficient quantity of the aluminate and silicate groups needs to be present in solution to form the polysialate oligomers. This affects the choice of source material, as the different rates of aluminate and silicate dissolution that are exhibited by different aluminosilicate materials plays a role in the final composition and properties of the geopolymer. Some of the factors to consider are the chemical composition of the material, purity and crystallinity and porosity.

Table 1.1 shows some of the typical chemical compositions of the various source materials used in geopolymerisation. The metakaolin and kaolinite sources are reasonably homogenous in comparison and exhibit lower levels of impurities such as iron and calcium than the other materials. Whilst the homogeneity in composition is useful for characterisation and fundamental investigations of geopolymers, from a practical perspective the kaolinite and metakaolin geopolymers exhibit a weaker, more brittle structure compared to fly-ash and slag [65, 66]. Figure 1.2 shows the effect of using metakaolin and fly-ash as source materials, with the metakaolin sample exhibiting a chalky structure compared to the smooth and solid fly-ash sample.

TABLE 1.1: The percentage oxide compositions for the main components in various geopolymer source materials from different locations.

	Kaolinite			Metakaolin		
	Australia [56]	China [57]	Egypt [58]	Australia [19]	UK [59]	Egypt [58]
SiO_2	51.3	44.11	44.64	54.2	54.78	52.26
Al_2O_3	32.6	37.21	38.9	42.1	40.72	42.93
Fe_2O_3	1.1	0.55	0.95	1.29	0.76	1.01
CaO	0.1	0.26	0.55	0.13	0.1	0.43
MgO	0.3	0.21	0.25	0.19	0.41	0.26
TiO_2	1.1	0.31	1.64	1.15	-	1.87
Na_2O	0.2	0.1	0.31	0.14	0.07	0.02
K_2O	0.3	0.58	0.01	0.2	2.72	0.19
SO_3/S	-	-	0.22	-	-	0.52
	Slag			Fly-Ash		
	Unknown [59]	Belgium [60]	Colombia [61]	Australia [62]	Greece [63]	USA [64]
SiO_2	34.4	33–38	32.29	47.88–64.79	29.95	50.7
Al_2O_3	14.1	9–13	16.25	23.5–31.2	13.5	19.9
Fe_2O_3	0.11	0.1–15	2.35	3.07–13.00	5.48	14.3
CaO	43	38–43	42.45	1.72–5.82	32.25	5.1
MgO	6.3	7–12	2.87	0.75–2.60	2.62	0.95
TiO_2	-	0.3–0.9	-	1.19–2.10	0.71	0.95
Na_2O	0.3	-	-	0.23–3.92	0.54	1.4
K_2O	0.33	0–0.8	-	0.90–1.21	1.11	2.4
SO_3/S	0.58	0–2.5	-	0.16–0.37	3.18	1.91

The increase in strength of fly-ash and slag based geopolymers is partly attributed to the high calcium content [17, 58, 59, 61] as the presence of Ca^{2+} ions in structure lowers the porosity thus leading to higher mechanical strength. Investigations of calcium aluminosilicate glasses [67] show that the Ca^{2+} actively participates in the oligomeric linkages during the formation of the aluminosilicate network by enhancing silicate and polysialate network formation. Calcium silicate hydrate gels have been found to form simultaneously with geopolymers [59] when high levels of CaO are present in the source materials, and within the geopolymer itself regions of varying calcium concentration have been identified [17, 59, 68]. Despite the evidence that calcium is important in the geopolymer structure, the exact nature of its role is not clear, and further investigation of the interactions of this ion with the aluminosilicate structure is necessary.

FIGURE 1.2: Two geopolymer binders that have been synthesised in identical conditions using sodium silicate activating solutions and different source materials. The larger, darker cylinder is formed using fly-ash and the lighter, smaller cylinder is formed using metakaolin. The insets show cross-sections taken from each cylinder to show the differences in the internal structure.

The degree of crystallinity in the raw materials is important as source materials that have mostly amorphous content display higher reactivity during geopolymerisation compared to more crystalline materials [56]. An x-ray scattering investigations into the formation of fly-ash based geopolymers showed that increasing the level of amorphous content in the source materials leads to an improvement in the development of the geopolymer structure [62]. This is most likely due to the increased liberation of the monomeric silicate and aluminate units from disordered source materials, although there is a lack of conclusive evidence regarding this in terms of geopolymer formation.

Porosity also plays a role in geopolymerisation as it controls the degree with which the source materials interact with the alkali solution. The higher porosity of metakaolin compared to kaolinite [20] results in a higher rate of dissolution as more solution enters the structure through the pores. The increase in the number of monomeric units thus leads to higher degrees of polymerisation and

this leads to the reaction mixture setting too rapidly. Thus additional water is added to slow down the process to allow for complete geopolymerisation. This can result in a product that is too soft for construction applications [4] but ideal for applications as adhesives, coating and hydro-ceramics. The lower porosity may account for the lower reactivity of kaolinite in comparison, which results in a longer time required for the interactions among the source materials to occur for the gel phase to form. A large amount of kaolinite, however, does not take part in the reaction at all, leading to large concentration of unreacted particles held within the geopolymer matrix. This may be due to slow dissolution rates due to both the crystallinity and decreased porosity as compared to metakaolin, which tends to fully react.

1.3.2 Geopolymer Liquor

The formation of the geopolymer binder phase a caustic solution with the ability to leach aluminate and silicate ions into solution. This caustic solution is called the geopolymer liquor or activating solution and is usually made up of either an alkali metal silicate or hydroxide solution which acts as an alkali activator. The reaction conditions need to be set up such that there is rapid dissolution of the aluminosilicate materials that leads to a rapid increase in the concentration of aluminate and silicate units in solution. If the process is undertaken in less caustic conditions, the rate of liberated aluminate and silicate units is slow enough to allow the formation of more ordered zeolitic structures.

Geopolymers formed with hydroxide solutions form more ordered final aluminosilicate networks than those formed with silicate solutions [23]. The hydroxide-activated solutions demonstrate nucleation occurring throughout the solution as the release of aluminate and silicate into solution occurs roughly simultaneously. The rate of nucleation in the hydroxide solutions is consequently dependent on the presence of monomeric silicate species liberated into solution, where as in

silicate solutions a readily available supply of the silicate species is immediately available. The presence of the silicate groups in the solution cause nucleation near the particle surfaces [26] as the silicate monomers reacts with exposed aluminate species. This can lead to large differences in the final structure of the geopolymer, depending on the type of alkali solution used.

Theoretically any Group I metal cation can be used as the alkali element (M) in the geopolymer activating solution, and the choice depends on the type and composition of the source material as well as the intended application of the synthesised geopolymer. The presence of cations in the original material as impurities or added as metal hydroxides is considered to be important due to their potential catalytic role. Optimum polymer properties are obtained when the M^+ concentration is sufficient to provide a charge balancing mechanism for the substitution of tetrahedral Si by Al, but not in excess as this produces unwanted by-products such as sodium carbonate by atmospheric carbonation [58, 69–71].

The metal cation used in the geopolymer liquor is usually sodium or potassium, with both cations producing different effects on the geopolymerisation process and the final structural properties. The smaller sodium cation increases the rate of dissolution, whilst the larger potassium cation increases the condensation rate and speeds up the rate at which the gel hardens [72, 73]. The smaller size of sodium better stabilises the silicate monomers and dimers present in the solution [53, 74], whereas the larger size of potassium favours the formation of larger silicate oligomers with which $Al(OH)_4^-$ prefers to bind. Therefore in potassium solutions more geopolymer precursors exist resulting in better setting and stronger compressive strength [74]. The potassium ion is also seemingly responsible for a higher degree of condensation when compared to sodium under the same conditions. An investigation by Duxson *et al.* [75] on mixed alkali geopolymers showed that potassium is incorporated into the charge balancing sites in the network in preference over sodium and that matrices containing potassium exhibit a lower degree of crystallinity.

Water

The requirement of water in geopolymerisation is important to attenuate the speed of reaction. For instance, if solid alkaline materials are used such as solid KOH pellets instead of KOH solution the reactions occur too rapidly and little geopolymerisation is evident in the final structures [76]. However, it is unknown whether the water is only required to facilitate slower reaction times to allow for greater dissolution and reorganisation in solution, or if the water plays an important role in the reaction. Some studies propose that water is a vehicle for the reaction to take place in [7, 77], whilst others show that non-evaporable water is a structurally necessary component of the geopolymer [57].

Generally the quantity of water added depends on the source materials, since it is used to control the rate of reaction. This is to ensure that the setting time is slow enough to allow for the dissolution of the source materials, but fast enough so that dense networks form with reasonable compressive strength. Geopolymers contain pore, structural and absorbed water [7] and *in situ* neutron diffraction experiments by White *et al.* [23] show that the structure of the water does not change during the reaction. Once the gel has set the water mainly exists in the pore solutions in the geopolymer, usually hydrating a cation within the pore. This indicates that water does not play an important role in the structural properties in the geopolymer, but the loss of non-evaporable water during curing of the geopolymer structure produced a slight decrease in compressive strength [57], and thus the role of water in the geopolymer structure is still not clear.

1.3.3 Filler Materials

The rate of the geopolymerisation and resultant structure of the product is highly dependent on the ratio of silicon to aluminium in the source materials [7, 9, 74]. As the quantity of silicon in the source materials increases compared to aluminium,

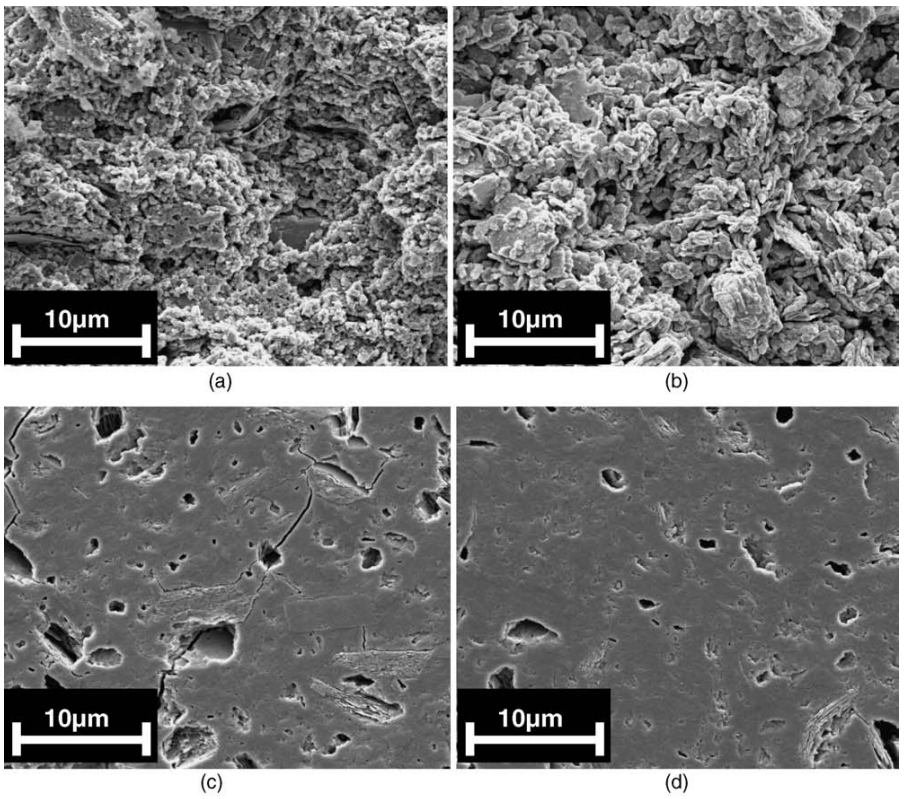

FIGURE 1.3: Scanning electron microscope image showing the change in microstructure of a metakaolin based geopolymer with varying Si/Al ratios of (a) 1.15 (b) 1.40 (c) 1.65 and (d) 1.90. Taken from Duxson *et al.* [9]

the compressive strength of the final product increases [7]. Figure 1.3 shows the variation in the microstructure of a metakaolin (Si/Al = 1) based geopolymer as a function of the Si/Al ratio, where the Al/Si ratio is varied by the addition of an alkaline silicate solution.

Higher quantities of silicon resulted in less brittle, denser structures as the increasing silicon concentration allows for more silicate monomeric units to participate in the polymerisation process and since the increase in proportion of silicate units in the network requires fewer charge balancing cations, a more dense structure can form. Typical ratios used for construction purposes are between $1.40 \leq \text{Si/Al} \leq 2.20$. If the source material does not exhibit the required ratio, filler materials can be added to provide additional sources of the aluminate and silicate ions.

The filler materials are often obtained from readily available aluminosilicates such as kaolinite and metakaolin, but other materials such as silica fume or the use of a sodium silicate solution as the alkaline activating solution are also used. The use of fillers in the reaction can provide an excess of nucleation sites in the solution, and this can lead to a phenomenon called *syneresis*. As the aluminosilicate gel continues to polymerise and form the geopolymer matrix, the excess solution is expelled from within the network into the bulk, and this can cause the gel to break up into discrete regions of varying porosity [9]. This is not always undesirable, as systems with no syneresis often harden whilst the gel is still composed of smaller and poorly condensed cross-linked clusters. This can lead to chemically bound water in the form of silanol or aluminol groups within the binder phase, and lead to poor structural characteristics.

Since the properties of the manufactured geopolymers are dependent on the ratios of the components in the final structures, a set of manufacturing limits have been identified as ideal for the production of geopolymers and are given in Table 1.2 below. In addition to the activating solution, the filler materials can be added in order to tailor these ratios to produce the desired properties. The filler materials are mainly added to provide extra Al^{3+} ions as the rate of aluminium dissolution from some source materials is usually insufficient to produce a gel of the desired composition [17, 26, 78–80].

Table 1.2: Molar ratios identified as ideal for the manufacturing of geopolymers, where M = alkali metal [4, 53, 73, 76]

M_2O/SiO_2	SiO_2/Al_2O_3	H_2O/M_2O	M_2O/Al_2O_2
0.20 – 0.48	3.3 – 4.5	10 – 25	0.80 – 1.60

Filler materials are used in synthesis of geopolymers for industrial applications, and are not generally included in the investigation of the structure and formation of geopolymers. In metakaolin-based geopolymers the ratios are consequently different to those in Table 1.2, with an $Si/Al \simeq 1$ and the other parameters changing according to the property being investigated.

1.4 Physical Characterisation

The geopolymerisation process results in a solid binder material similar to concrete that must be characterised prior to the acceptance of the material as a commercial product. Several characteristics of the geopolymer as a function of its synthesis conditions have been identified that require the atomic structure of the geopolymer to be determined in order to be fully investigated. To determine the molecular composition and structure of a geopolymer, a range of physical characterisation techniques is used, and are outlined below with the structural characteristics identified by each method included in the discussion.

The ratio of aluminium to silicon in the geopolymer as well as the presence and quantities of cations, impurities and by-products of the geopolymerisation reaction is determined by using X-ray fluorescence (XRF) and energy dispersive spectroscopy (EDS) to provide elemental analysis. XRF and EDS results provide a semi-quantitative analysis of the geopolymer [7, 9, 10, 19, 59, 73, 78] and are useful to establish the chemical compositions that may be responsible for the range of physical properties. These methods are also used to provide quantitative compositional analysis of the source materials to determine purity (in metakaolin and kaolinite) and allow characterisation of heterogeneous materials such as fly-ash. It is from these methods that the presence of the cations in the aluminosilicate network are identified, and the variation in elemental composition throughout the structure can be determined.

X-ray diffraction (XRD) patterns for geopolymer materials typically display a broad diffraction hump centred between 27°–29° 2θ [4, 8, 18, 50, 73]. Figure 1.4 shows the XRD patterns associated with metakaolin, kaolinite and a metakaolin-based geopolymer. The XRD patterns show that the geopolymer microstructure is amorphous, however, strong peaks are often noted within this broad peak that are attributed to the un-reacted crystalline particles in the geopolymer matrix.

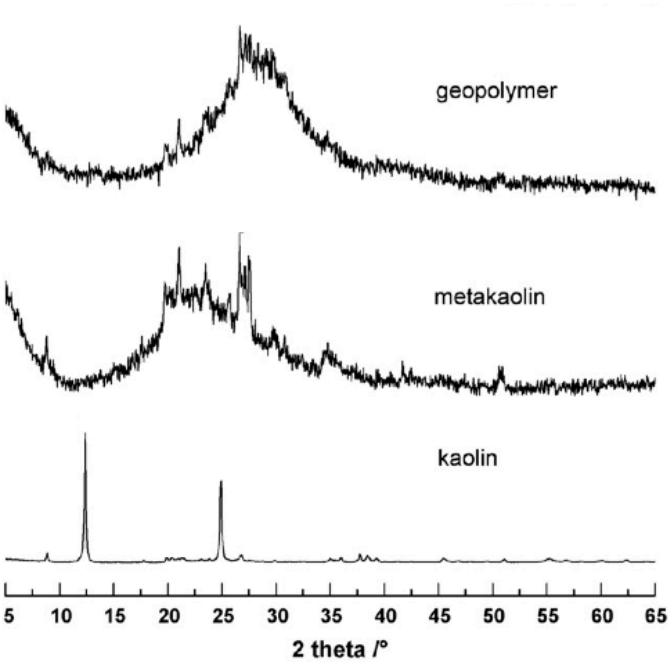

FIGURE 1.4: Characteristic XRD patterns relevant to geopolymerisation, taken from Prud'homme *et al.* [81]. The characteristic geopolymer peak centred around 28° 2θ shows a more amorphous structure than the metakaolin and kaolin samples. The geopolymer in this example is synthesised from metakaolin and a potassium-silicate/hydroxide solution.

The presence of both amorphous and crystalline phases suggests that the rapid setting of the gel in the geopolymerisation process results in a final material that contains a large amount of unreacted source material that is encompassed by the amorphous geopolymer phase [8, 69, 73]. XRD is useful for structural characterisation of crystalline materials, but is limited by this amorphous phase. Initial studies using XRD consequently focus on the identification of the unreacted crystalline particles [9, 59, 78] and in combination with XRF have been successful in determining the composition of the different phases of fly-ash based geopolymers [62].

Another way to understand the nature of the bonding and structure in the geopolymer amorphous phase is though the use of nuclear magnetic resonance

(NMR) spectroscopy. NMR allows the determination of the properties of materials that contain magnetic nuclei and has been used to show the presence of different aluminosilicate species in the geopolymer matrix [4, 69, 74, 76, 78]. An example of some typical magic-angle spinning (MAS) NMR spectra for metakaolin-based geopolymers is shown in Figure 1.5. Geopolymers all show the single broad resonances characteristic of amorphous materials containing a range of slightly different environments [69].

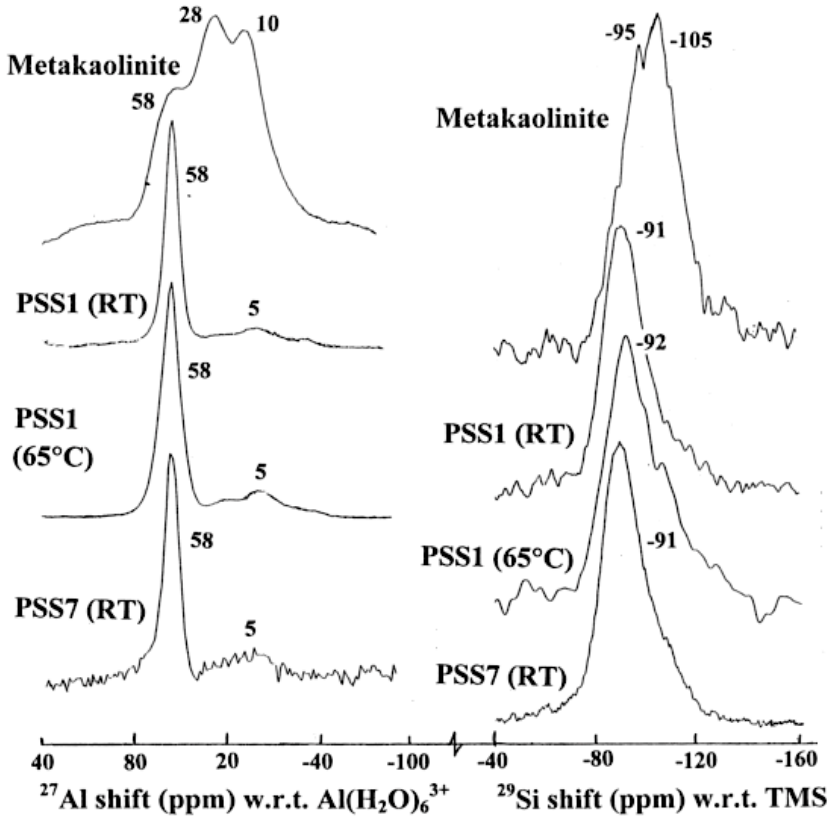

FIGURE 1.5: Examples of solid-state MAS-NMR spectra of metakaolin and metakaolin-based polysialate-siloxo (PSS) geopolymer compositions, taken from the work by Barbosa, MacKenzie and Thaumaturgo [69]. The left panel shows the ^{27}Al spectra with the peaks at 52 ppm, 10 ppm and 28 ppm corresponding to tetrahedral, octahedral and 5-fold aluminium respectively. The right shows the corresponding ^{29}Si spectra with the peak at -104 ppm attributed to tetrahedral silicon.

The technique of ^{27}Al and ^{29}Si MAS-NMR has been used to interpret the microstructure of the geopolymer, with the aluminium spectrum showing the presence of a three-dimensional network of aluminosilicate polymeric units, including the presence of low molecular weight polymeric units such as dimers and trimers. An important result from the MAS-NMR experiments is that both the silicon and aluminium are predominantly tetrahedrally coordinated.

Fourier transform infra-red (FTIR) spectroscopy is used to further characterise the nature of the Al–O or Si–O bonding in the structure [9]. FTIR spectra of geopolymers show a central peak between 1010 cm^{-1} and 1098 cm^{-1} which is attributed to the Si-O-Si or Al-O-Si asymmetric stretching mode [56, 60, 69, 74]. The shift of the bending peak of the Si–O bond (1050cm^{-1}) from metakaolin to a lower frequency (990 cm^{-1}) is also observed in fly-ash based geopolymers [74, 82] and is characteristic of the formation of a geopolymer. The presence of Al in the geopolymer gel structure is also characterised by the absorption bands at 1207 cm^{-1} and 1170 cm^{-1}, and the change in the co-ordination of the aluminium from octahedral to tetrahedral causes peaks to appear at approximately 850 cm^{-1} [83].

The NMR and FTIR techniques provide evidence for the network of sialate (silicon-oxo-aluminate) chains composed of SiO_4 and AlO_4 units connected by shared oxygen atoms. Detailed analysis of the results show that the structure of a geopolymer is in fact composed of various sized rings consisting of six to eight or more tetrahedral aluminate and silicate units [84]. The presence of water in geopolymers is usually determined using differential scanning calorimetry (DSC) techniques, and the various ions through a combination of EDS, XRF and wet chemistry methods.

Transmission electron microscopy (TEM) experiments show that there are regions of varying crystalline behaviour, ranging from highly crystalline, nanocrystalline or poly-crystalline through to completely amorphous, but indexing

of the diffraction patterns is rarely attempted. High-resolution transmission electron microscopy (HRTEM) shows that the geopolymer phase contains distinct regions of short to mid-range order, which are rapidly amorphised by beam damage [3, 5, 50, 78]. In 2011 Xuemin *et al.* [85] published a HRTEM micrograph showing these nano-crystalline regions within the geopolymer amorphous phase, shown in Figure 1.6. The HRTEM results do not agree with XRD results, in which no newly formed crystalline phases were identified, only those related to the un-reacted raw materials. There is also evidence [50] of nano-sized zeolitic phases within the geopolymer that may be a part of the slow process of transformation of the amorphous geopolymer gel to a more ordered structure, as shown in the extended geopolymerisation reaction model in Figure 1.1.

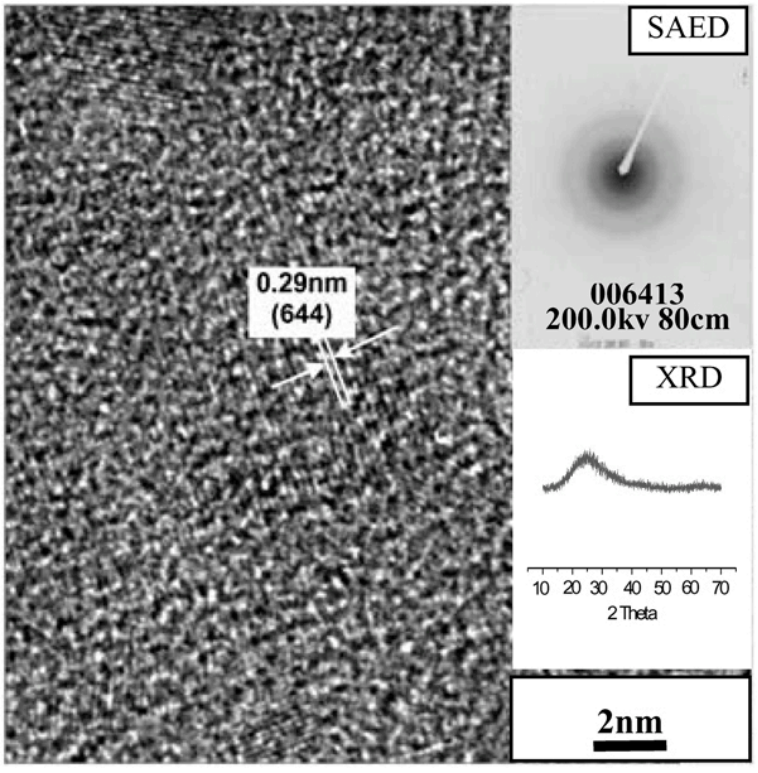

FIGURE 1.6: A HRTEM image of a geopolymer demonstrating regions of nano-crystallinity within the amorphous binder phase. The selected area electron diffraction (SAED) and XRD insets show the characteristic amorphous geopolymer features. Taken from Xuemin *et al.* [85]

The apparent disagreement between then HRTEM and XRD results can be attributed to the fact that the crystallinity observed in the microscopy work is on a length scale below the detection limit of the XRD. Similar results have been found in studies performed on aluminosilicate zeolite precursor gels, as well as in a variety of inorganic systems [50, 56]. In each case, crystallinity on a length scale of about 5 nm was detectable by electron diffraction, but not by XRD. Thus the geopolymeric binder phase is considered to be x-ray amorphous [50, 69] and has been suggested to consist of an agglomeration of zeolitic nano-crystallites, which is plausible from a chemical, thermodynamic and mechanistic standpoint [50]. Since the crystalline state has a lower energy than the amorphous state, the formation of crystalline regions is not unexpected, yet the identification of the chemical nature of these regions is still ongoing [47, 50].

Geopolymers have been shown to have a micro-porous framework, with the characteristic pore size dependent on the nature of the cation(s) used in synthesis [5]. Stereology measurements using electron diffraction images on cross-sections of geopolymers have been used extensively to demonstrate the porosity of geopolymers [14, 22, 86]. Increasingly, porosity measurements have been conducted using gas (usually nitrogen) adsorption measurements. These involve measuring the volume of gas that can be absorbed into a structure without affecting the structural integrity, using the Brunauer-Emmet-Teller (BET) method to determine surface area from physisorption isotherm data [87, 88]. These experiments have shown that geopolymers have a range of porous structures, from pores with diameters up to 5 μm [9, 89] to pores with radii below 1 nm [86]. The pore solutions extracted from low calcium fly-ash geopolymers have been shown [90] to have cation rich environments with a pH$>$ 13, and so the porous nature of the geopolymer may be important for the encapsulation and immobilisation of the cations within the structure.

1.4.1 Microstructure

Physical characterisation of geopolymers has provided a general understanding of the geopolymer microstructure. The polysialate structure is the simplest polymer structure, with a Si/Al = 1. In practice varying the silicon and aluminium ratios in the production of geopolymers results in an additional two different geopolymer types: the polysialate-siloxo (PSS) and polysialate-disiloxo (PSDS) polymers. The PSS structure typically has Si/Al = 2 and the PSDS structure has Si/Al = 3. The name is often preceded by the charge balancing cation present, for instance a sodium polysialate-siloxo geopolymer is called a Na-PSS geopolymer. The information from the various experimental investigations has led to several structural schematics being proposed for the various geopolymer structures, two of which are shown in Figure 1.7.

In the K-PSDS model proposed by Zhang *et al.* [76], no attempt has been made to identify the location neither of the cation, nor for the presence of water within the structure whereas in the Na-PSS geopolymer model proposed by

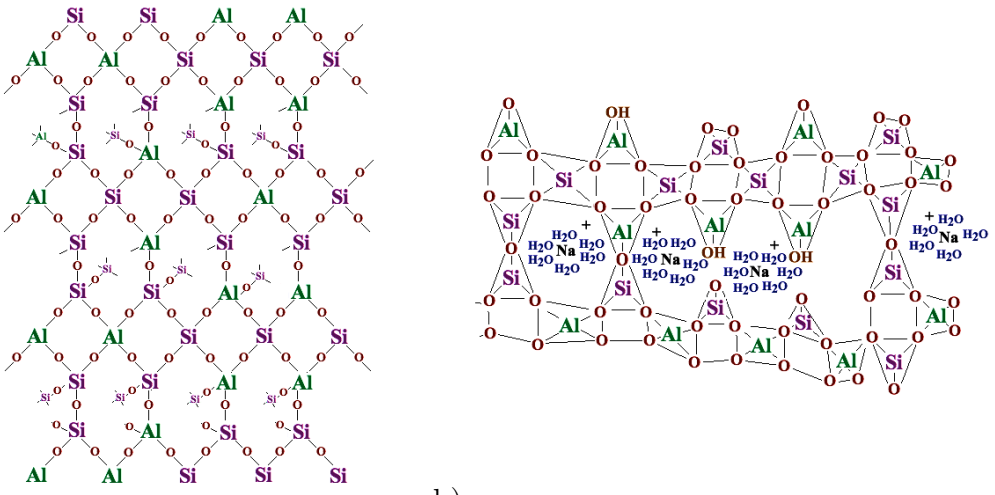

FIGURE 1.7: Various structural models for the different geopolymer types have been proposed over time. Image (a) shows a semi-schematic for the sialate network in a K-PSDS geopolymer [76]. Image (b) shows a Na-PSS geopolymer structure [69].

Barbosa *et al.* [69] accounts for all the ions. This latter model introduced the concept that the cations in the geopolymer matrix exist within hydration shells in the pores of the network. These structures are primitive and do not account for many of the physical characteristics of geopolymers determined from experimental characterisation.

Many geopolymer properties are not easily explained and in some cases experimental data cannot be fully investigated due to the lack of understanding of the structure [47]. The alkalinity, charge and size of the cations, and quantity of water all affect the microstructure of a geopolymer as the measured properties change upon varying these factors [4, 8, 11, 17, 20, 26, 57, 58, 66, 70, 73, 76, 91]. Exactly how the interactions between the aluminosilicate network and the various structural components result in these changes is unknown, and all these factors must be taken into consideration when a molecular model for geopolymers is proposed.

1.5 Computational Studies of Geopolymers and Related Materials

The geopolymer binder phase has been shown [85] to exhibit short-range order, but as it is x-ray amorphous it is difficult to characterise with conventional techniques. Computational investigations of geological and inorganic materials have been successful in determining the atomic structures in cases where traditional experimental methods have not been able. These techniques have been used to simulate materials ranging from ordered materials such as zeolites and clays, to amorphous glasses and other disordered systems. This has led to an increase in interest by the geopolymer community in the investigations of these materials from a computational perspective. However, most computational investigations

of geopolymers are concerned either with the reaction kinetics and thermodynamic modelling of aluminosilicate dissolution [48, 49, 92, 93] or the modelling of the individual aluminosilicate framework components [21, 94–96].

One of the first structural characteristics investigated by computational techniques was the type of linkages that were most likely to occur in the geopolymer structure. The Loewenstein or aluminium avoidance rule states that chains formed by successive tetrahedral aluminate units (i.e. -Al-O-Al- linkages) are not possible, and governs the tetrahedral substitutions of alumina in silica chains [97]. However, quantum mechanics simulations performed by Tossel [98] in 1993 showed that the energy penalty for these paired linkages is modest, and later experimental studies [99] have shown that high temperature and disordered aluminosilicate materials can demonstrate these "forbidden" structures. This must be considered when describing the structure of geopolymers [100] as the synthesis environments typically involve amorphous components that may allow the violation of the Loewenstein rule.

Investigations of the framework components that could exist in a geopolymer are investigated by simulation methods to determine the short-range aluminosilicate structures that would be most favourable in the dissolution environments. In 2000 Xu and van Deventer [94] performed *ab initio* simulations of five-membered aluminosilicate rings in an alkaline environment and showed that the tetrahedral aluminium dissolves more readily than silicon in the local environment. Semi-empirical *ab initio* simulations have investigated the reaction pathways involved in the reorientation process of metakaolin based geopolymerisation [95, 101], however, the conclusions reached from these simulations are the subject of a debate regarding the selection of species simulated as well as the methods used [21, 102]. Kinetic effects were not included, and as such the reaction pathways proposed as a result require further investigation.

Monte Carlo simulations by Rankin *et al.* [103] looked into the gelation mechanism in silica polymerisation, finding that a distribution of polycyclic siloxane chains form during the gelation process. White *et al.* [54] similarly used Monte Carlo methods to investigate the solubility and precipitation of silica in the initial stages of zeolite synthesis, and both silica and alumina in geopolymerisation [26] using a simplified model of metakaolin. Simulations of a sodium silicate activating solution indicated a preference for aluminate monomeric units to be released into the solution over silicate units, in agreement with experimental data [26, 100]. The presence of silicate ions in solution initially increased the probability of a liberated aluminate monomer encountering a silicate monomer near the particle surfaces, and so localised nucleation of the oligomer species near these surfaces occurs. Thus if an alkaline silicate solution is used a higher concentration of silicate in the source material is required during synthesis of geopolymers.

1.5.1 Metakaolin as a Model System

There are still many unknown factors in the formation and the structure of geopolymers. The majority of the simulations reported for geopolymers focus on understanding the components present in the reaction solution, and how these components interact and polymerise to form the final structure. It is proposed by this research that instead of attempting to build the structure from the individual monomers or oligomers, a known disordered aluminosilicate network is simulated and the various interactions such as the influence of the cations within the bulk or the interactions at the solution-surface interface are investigated using it as a simplified model system. Once the role the different components play within the structure is fully understood, this information can then be used to reduce the number of variables when it comes to producing the final geopolymer molecular structure.

Metakaolin is ideal for this purpose as it exhibits structural similarities to geopolymers, with both being composed of a disordered tetrahedral aluminosilicate network. The metakaolin structure could thus be used to determine the interactions within the geopolymer structure such as the influence of the various cations on the local network. It is also used as a precursor material in the synthesis of geopolymers, and so is suitably ideal for surface-solution investigations. The mechanism of the de-hydroxylation process of kaolinite to metakaolin has been the subject of various experimental investigations [104–119] with the general agreement that metakaolin is formed by a gradual loss of structural water through diffusion accompanied by the change in aluminium coordination from six-fold to four-fold.

The final structure of metakaolin however, is not well understood, as characterisation experiments such as scattering methods have met with difficulties due to the amorphous nature of the material. In 2010 White *et al.* [118, 119] simulated the transformation of kaolinite to metakaolin using a combination of first-principle *ab initio* methods with neutron scattering experiments. The simulated transformation through a gradual removal of the hydroxyl content from the structure produced a final metakaolin structure, although complete de-hydroxylation was not simulated. The results provide one of many possible de-hydroxylation paths, and reported evidence of the presence of both 3- and 5-fold aluminium in addition to the known 4-fold configuration. Further empirical modelling of the transformation can improve upon these results by increasing the scale of the simulation, allowing for more de-hydroxylation paths to be sampled and including the effects of temperature. The effects of the degree of de-hydration can also be explored; White *et al.* [118, 119] only simulated up to 88% de-hydroxylation. This will provide structural information for the entire range of concentrations of structural water found in metakaolin.

1.5.2 Simulation Studies of Related Materials

The success in the use of computational atomistic modelling techniques in simulating some aspects of the geopolymerisation process and the structure of metakaolin show that there is a definitive potential in using accurate modelling techniques. However, there is a variety of computational simulation techniques available from electronic structure methods such as quantum mechanics and *ab initio* methods to classical atomistic approaches using empirical potential models in molecular dynamics and Monte Carlo simulations. The choice of method depends on the structure and chemical phenomenon of interest, and each method has limitations such as the size of the atomic system simulated or the level of accuracy obtained from the simulation. The methods chosen for this research are based upon those that have been used to investigate structures that share common structural features with geopolymers: zeolites, clay minerals and silica and alumina glasses.

Zeolites are formed from three dimensional networks of $[TO_4]$ tetrahedra (T = Al, Si), exhibiting highly ordered and often complex structures. The similarities between the synthesis conditions of zeolites and geopolymers have led to the suggestion that geopolymers are in fact amorphous precursors to zeolites [20, 50]. Zeolites have greatly benefited from computational techniques as the advantages of visualising and manipulating the complex zeolite structure have allowed the investigation of many of the properties of interest [120]. Lewis *et al.* [121] and Catlow *et al.* [122] used *ab initio* molecular dynamics methods to investigate the solvation of silica clusters and the properties of solvated silica-template clusters. Monte Carlo simulations performed on lattice systems [54, 123] provide qualitative insights into the formation of the nano-particles that play a role in zeolite synthesis [124–127]. Of particular interest to this research are the molecular dynamics simulations used to investigate zeolite formation and the sol-gel process [128–130] in dynamic environments, as these are similar to the some of the interactions present in geopolymerisation.

Another field of interest is the investigations of clay minerals by computational methods. Clay minerals are aluminosilicate minerals composed of alternating layers of four-fold silicon and four- or six-fold aluminium. Many clay minerals contain water, hydroxyl groups and interstitial cations as part of the atomic structure, characteristics that are similar to the geopolymer structure. The swelling and dehydration properties of clays are of much interest to the clay community and have been extensively studied [131–133]. Empirical atomistic simulations have been predominantly used to investigate structural and surface phenomena in clay hydroxides, oxyhydroxides and many different clay phases [133–141]. The success of the empirical atomistic simulations in describing the structures and interactions of clays in a variety of environments makes these methods suitable for the purposes of this research.

The atomic structures of disordered materials such as geopolymers are not easily determined in a laboratory and thus computational analysis is particularly useful. Investigations into the structure and properties of amorphous materials using computational techniques generally require relatively large simulation cells and methods such as molecular dynamics and MC methods [142]. For example, the computer simulations of silica glasses have aided in structural characterisation as experimental methods are impeded by the disordered structure and insulator properties of these materials. Empirical molecular dynamics techniques have proved useful in producing glassy silica structures that reproduce the experimental radial distribution functions [143–145], and the polymerisation process of silica to form amorphous phases has been investigated using both molecular dynamics [128, 146] and Monte Carlo [54, 147–149] techniques. The simulation of alkali silicates using molecular dynamics has been able to interpret highly accurate neutron diffraction data [150, 151], and the effect of varying the Al coordination in aluminosilicate glasses have been investigated by Zirl and Garofalini [152].

Amorphous alumina is another important material that has benefited from computational investigations. Amorphous alumina is found in the surface layers of oxidised aluminium and is also present in alumina films grown electrochemically or by the atomic layer deposition [153]. Simulations of amorphous alumina by Gutierrez and Johansson [154] showed that it consists of a porous network of AlO_4 tetrahedra, similar to that found in the structure of silica glasses. The alumina surfaces have also been investigated successfully using molecular dynamics [153, 155] and have provided insights into surface behaviour in alkaline environments, such as the preference for the location of edge sharing Al tetrahedra configurations at the surface of alumina than in the bulk. Thus use of empirical atomistic methods using interatomic potential models in dynamics environments where time-scale and temperature play a role in the simulations are determined to be appropriate for the investigation of geopolymers.

1.6 Thesis Aims and Outline

The focus of this research is to understand the structure and behaviour metakaolin as a simplified precursor and analogue for a geopolymer using atomistic simulation approaches. In the following chapters the computational methodology is introduced, providing a description of the techniques that are used and a review of the underlying theory. A summary of the computational simulation packages used in this research is given, along with explanations for the choice and validity of each. The description and development of the interatomic-potential model used for this research is included and potential models from the literature are identified and investigated for suitability. The final set of parameters selected are tested to ensure that the implementation of the interatomic potential model allows for an accurate representation of the all the materials and interactions simulated.

The structure of metakaolin is investigated using atomistic molecular dynamic techniques, with larger atomic systems sampled compared to the *ab initio* simulations [23]. Aspects of the structural development of metakaolin are discussed and the final structure that is developed compares well with experimental observations. A range of the final metakaolin structures from the molecular dynamics simulations, along with the kaolinite structure, are then used for the bulk investigations. The porosity of metakaolin is described in detail for the first time and this information is used to determine the influence of the interstitial ions sodium, potassium and calcium on the structure of metakaolin, which in turn give insights into how these ions interact with the geopolymer structure.

The interactions of kaolinite and metakaolin surfaces in an aqueous environment are investigated, with a discussion on the development and stability of metakaolin surfaces included. The metakaolin surfaces are hydrated and simulated in the presence of water in ambient conditions, demonstrating that water may play an important role in the dissolution of the source materials in geopolymerisation. This thesis concludes with a discussion of the results and recommendations are provided for future research and possibilities for further development of the results reported herein.

Chapter 2

Computational Methodology

Computer simulations are a powerful tool based on theoretical knowledge of molecular and atomic behaviour, and can be used for exploring the structure of materials and provide insights into the properties such as crystal structures, thermodynamics and transport properties. Structural investigations from a computational perspective can be approached from a variety of different methods, and those used in this thesis will be outlined in this chapter.

2.1 Introduction

The investigation of chemical and physical phenomena via computer simulations is now a well-established practise in the fields of science and engineering. With the advancement of software and computing capabilities, the ability to create and study systems at conditions otherwise difficult to study in a laboratory environment becomes invaluable. In the physical sciences computer models are used to investigate various phenomena; from those that occur on the galactic scale to understanding the way the atmosphere changes and interacts with external factors such as pollution. Computational methods have found applications in the biological sciences in areas such as protein modelling or the study of ecological systems such as the modelling of the flocking behaviour of birds. Applications in chemistry and physics can vary from the investigation of aqueous solutions, molten salts, the identification and study of phase changes to understanding how defects in solids occur and propagate.

In its simplest form, a simulation takes a series of parameters and starting conditions and attempts to find a numerical solution dependent on the mathematical models assumed for the system. The mathematical models of a simulation in chemistry are based on theoretical quantum chemistry as well as experimental observations of materials. The initial conditions such as cell parameters and atomic coordinates are generally chosen to be similar to those measured in experiments and the simulation parameters and models are chosen depending on the property or phenomena being investigated.

Computational simulations require resources such as the computer memory and the time taken by the computers to do the required calculations. The size and complexity of a system is primarily dictated by the degree of accuracy required to simulate the structure or phenomenon of interest, but consideration must also be made for the computational resources available. With the increase in processing power of computers and the development of multi-processor computing in the last few decades, the amount of resources required for simulations has decreased considerably. As the computational methods become more efficient, larger and more complex systems can be simulated with higher degrees of accuracy. The choice of method and model is thus always a function of the minimum degree of accuracy required and the time and resources available for that simulation.

The development of a metakaolin structure for the investigation of geopolymers will require a relatively large atomic system simulated at high temperatures to fully investigate the degree of long-range disorder caused by the thermal dehydroxylation of kaolinite. For these purposes classical interatomic potential function methods are used in this research. These methods consider the atoms in a system as individual particles and do not include electrons and other sub-atomic entities, but rather assume an *effective* atom which represents all the particles involved. Simulation of this type are the main method used in the investigations of aluminosilicate materials [156], and so are the most suitable approach to undertake the investigation of the interactions of the components influencing the

geopolymer structure through the simulation of the metakaolin structure. There are other methods available that include the electrons explicitly to improve accuracy, such as quantum mechanics (QM) simulations, however, these are more complex and have a higher associated cost compared to the classical methods.

2.2 The Classical Model Approach

The description of the atoms in a physical system in the classical approach uses a "ball and spring" representation of the atomic interactions. This simplified method of describing an atom or molecule as a discrete *particle* instead of a combination of wave-functions reduces the computation requirements for a simulation considerably compared to QM methods. To give the particle its atomic character a set of descriptors are defined so that it becomes an atom or ion in the simulation.

The interactions between atoms are due to a combination of attractive and repulsive forces experienced as a function of the interatomic distance. Consider that the electron density in any atom is not static, and is subject to instantaneous fluctuations due to the delocalised nature of the electrons. At large interatomic distances, the charge distribution on an atom can be considered to be on average spherically symmetric, and the electrostatic interaction is generally sufficient to describe the behaviour of the atoms in the system. As the atoms are brought closer together, the fluctuation of the charge density in one atom may cause the electrons on the other atom to shift in such a way to produce a small dipole moment. The polarisation of the charge density leads to an electrostatic attraction between the two atoms.

As the distance between the two atoms is further decreased, the electron clouds eventually overlap. The Pauli exclusion principle prevents electrons from occupying the same region of space simultaneously, and so the overlap of the electron clouds results in a repulsive force between the atoms. The distance at which the

overlap occurs is designated as the characteristic Van der Waals radius for each atom. The combination of the repulsive and attractive intermolecular forces are responsible for all of the physical properties of solids, liquids, and gases.

The intermolecular forces can be modelled by interatomic potential functions. These functions have various parameters whose values are derived specifically for individual interactions. The type of functions and parameters needed for a simulation depend on the system of interest, for instance, the Al–O interactions in an aluminium oxide compound such as corundum are different to the Al–O interactions in an aluminium hydroxide compound such as gibbsite. The Al–O interactions for each system have a different set of parameters, and the values of these parameters are derived either empirically by fitting to experimental values, or determined from QM calculations.

The potential functions are designed to correctly describe all the interactions between the components of an atomic system. The potential energy between two atoms is given by U, and is related to the force experience by the atoms, F, as a function of interatomic distance, r, by:

$$F_i = -\nabla_{r_i} U \tag{2.1}$$

However, in a system with N atoms, the relative separation between atoms is no longer the only consideration as the position of other atoms to relative the each other becomes important. In an N-atom system, an individual atom will interact with all the atoms within this system and the total energy is determined by a series of terms consisting of all the N-body components [157]:

$$U_{total} = \sum_{i}^{N} U(i) + \frac{1}{2}\sum_{i,j}^{N} U_{i,j} + \frac{1}{6}\sum_{i,j,k}^{N} U_{i,j,k} + ... \tag{2.2}$$

The first term represents the self-interactions of individual atoms, the second term represents the two body interactions and is the dominant term in close-packed

ionic systems and the third term represents three-body interactions and so forth [158]. Higher order interactions are included depending on their necessity in the atomic system being investigated, but are typically negligible (along with the self-interaction terms if there is no external electric field) compared to the two body interactions.

The second term in Equation (2.2) can be separated into three contributions: the electrostatic energy between charged ions and the long- and short-range interactions. The latter two interations are due to a range of phenomena such as the Pauli repulsion and covalent bonding at shorter distances and induced dipoles at larger distances. The combinations of these interactions are classified bonded or non-bonded forces, and are described through a series of mathematical expressions that describe the potential energy of the different interactions between pairs of atoms as a function of the interatomic distance r_{ij}.

2.2.1 Bonded Interactions

Interatomic potential functions do not include descriptions for the electrons and thus can not include the phenomenon of electron 'sharing' that results in covalent bonding. If the bonded interactions such as bond length and angular vibrations are important in the accurate description of a material, potential functions that describe the characteristics of the bonds are included.

Bond–Stretching

The simplest bonded interaction to consider is the effect of bond stretching between two atoms. The nature of a covalent bond within an atomic system involves the vibration of the bonds around an average equilibrium bond-distance, and the

simplest method to describe it is to use a simple harmonic oscillator as an approximation of the energy as a function of interatomic distance:

$$U_{ij}^{\text{Harmonic}} = \frac{1}{2}k(r_{ij} - r_0)^2 \tag{2.3}$$

where r_0 is the equilibrium bond length, r_{ij} is the atomic separation and k is the force constant. The interaction is relatively simple, and is suitable for systems that do not demonstrate large deviations from r_0.

However, the harmonic oscillator does not accurately represent bond vibrations as it over-estimates the stability of a bond by not allowing for bond disassociation. Thus the harmonic oscillator approach is not suitable for all interactions and in these cases the vibrational structure of a molecule around the equilibrium bond length is better approximated by the Morse potential [159]:

$$U_{ij}^{\text{Morse}} = D_e \left\{ \left[1 - \exp\left(-a\left(r_{ij} - r_0 \right) \right) \right]^2 - 1 \right\} \tag{2.4}$$

where D_e is the well depth which is associated with the bond dissociation energy, r_0 is the equilibrium bond distance and a controls the width of the potential well. Figure 2.1 demonstrates the differences between the Morse potential and the harmonic potential. The increased complexity of this interaction allows for a more realistic interactions as it allows for the effects of 'bond-breaking' as well as the anharmonicity present in real bonded systems.

An example of the necessity of the Morse potential is in the simulation of OH groups. This group is present in many clay minerals and other aluminosilicates, and the inclusion of this group in simulations is important in understanding many mechanisms such as clay dehydration and hydration as well as many bulk and surface properties. The Morse potential is suitable for these purposes as it accurately reproduces the spectroscopic data [160].

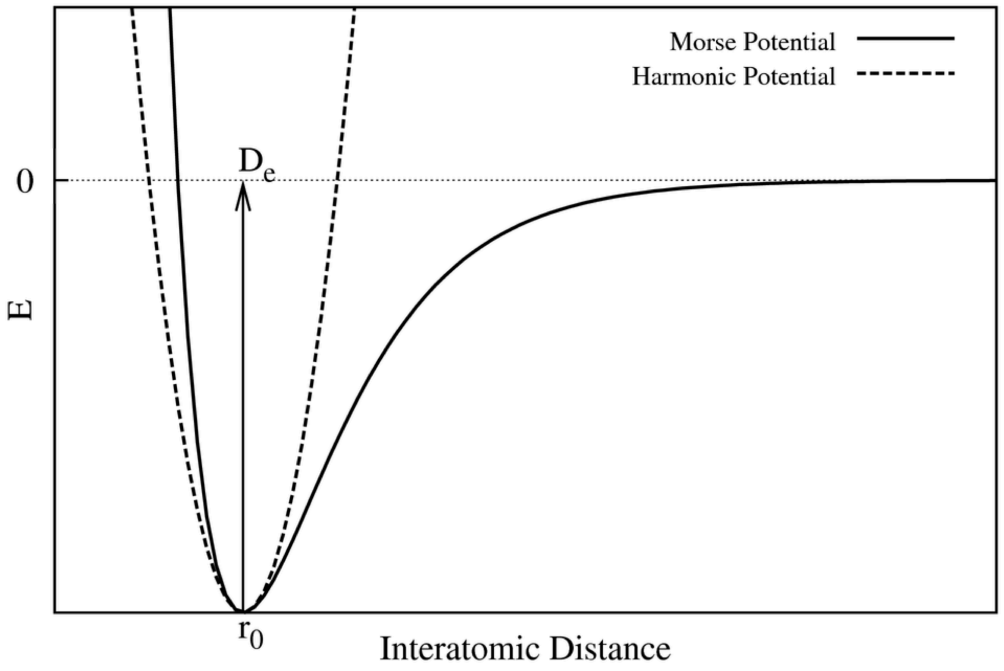

FIGURE 2.1: The typical potential energy curve for a Morse potential given in Equation (2.4), compared to the traditional harmonic model given in Equation (2.3). D_e represents the dissociation energy of a molecule, which consequently allows the effects of bond dissociation in a simulation.

Angle–Bending

The third term in Equation (2.2) is included in the total potential energy function when the accurate description of a bond between two atoms requires three–body effects such as bond-angles. These interactions are most often represented by a simple harmonic angle-bending potential similar to the harmonic description of the bond

$$U_{ijk}^{\text{angle-bend}} = \frac{1}{2}k(\theta_{ijk} - \theta_0)^2 \tag{2.5}$$

where θ_0 is the equilibrium bond-angle and k is a force constant. As in the case of the vibration of a bond, there are different methods available to describe angle-bending, such as the Stillinger-Weber potential [161].

The description of the O-Si-O angle in tetrahedral SiO_4 is an example where three-body terms are necessary. Vitreous silica is not accurately simulated using

only pair potentials, and requires the inclusion of the three-body term to better describe experimental results [128, 145, 162–164]. Similarly the correct description of the bond angle between the H–O–H atoms in water has been shown to be a vital component to the description of liquid water [165].

2.2.2 Non-Bonded Interactions

The non-bonded interactions describe the interatomic forces present in systems with ionic character, as well as noble gasses. The majority of computational simulations are of atomic systems composed of charged ions, and as such the effects of ionicity are always present. The forces involved in ionic materials occur at both short as well as large interatomic distances, and as such as described by of a variety of different interatomic potential functions.

The Van der Waals and Pauli Interactions

The repulsive forces due to the Pauli exclusion principle at short range and the attractive forces experienced at larger interatomic distances due to the development of instantaneous dipoles, also known as dispersion forces, are present in all atomic systems. The long-range force, despite being relatively weak forces when compared to electrostatics and the short-range repulsion, is still significant in the accurate description of an atomic system.

In 1924 Lennard-Jones proposed a potential function to approximate the interatomic interactions between two neutral atoms [166–168]:

$$U_{ij}^{\text{Lennard-Jones}} = 4\varepsilon \left[\left(\frac{\sigma}{r_{ij}} \right)^{12} - \left(\frac{\sigma}{r_{ij}} \right)^{6} \right] \tag{2.6}$$

where ε is the depth of the potential well (see Figure 2.2) and σ represents the distance at which the interatomic potential is zero. The values of σ and ε are

fitted to specific atomic interactions. The repulsive component of the interaction is given by the r^{-12} term, and the attractive component is described by the r^{-6} term. The effect of combining these two interactions is shown in Figure 2.2.

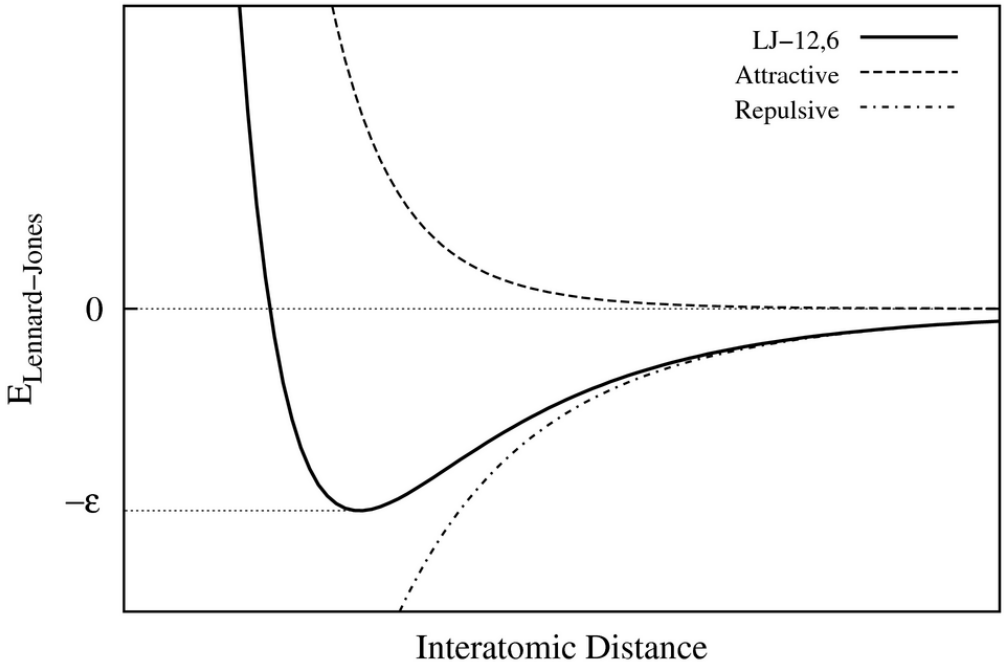

FIGURE 2.2: The typical potential energy curve for a Lennard-Jones 12-6 potential (solid line). The attractive and repulsive components of the potential are shown by the dashed and dotted dashed lines respectively.

An alternative to the Lennard-Jones potential was proposed in 1938 by Buckingham [169]. The Buckingham potential replaces the r^{-12} term in the Lennard-Jones potential with an exponential term:

$$U_{ij}^{\text{Buckingham}} = A \exp\left(-\frac{r_{ij}}{\rho}\right) - \frac{C}{r_{ij}^6} \tag{2.7}$$

where A is the amplitude of the repulsion, ρ defines the range of the effective repulsion and C describes the attractive interaction. If the C term is set to zero (often for interactions where the ions have small polarisabilities) the potential reduces to the Born-Mayer potential [170].

The majority of interatomic potential models in use in computational chemistry include two-bodied potentials based upon these functions. The different parameters such as σ, ε, A, ρ and C are tailored to fit the required potential energy form to correctly represent the interactions in the system being investigated.

Electrostatics

The final contribution to the potential energy function in Equation (2.2) that is important to all ionic and non-ionic systems is the electrostatic energy. In the description of a system, each particle is considered as a point charge, and the most general description of electrostatic energy between two point charges is given by Coulomb's law:

$$U_{ij}^{\text{Coulomb}} = \frac{1}{4\pi\epsilon_0}\frac{q_i q_j}{r_{ij}} \tag{2.8}$$

where q_i and q_j are the atomic charges with an atomic separation distance of r_{ij}. This description for the electrostatic energy becomes complicated when periodic systems composed of multiple point charges are considered. In an infinite bulk material, the evaluation of Equation (2.8) for all point charges becomes difficult as the strength of the interaction decays as $\frac{1}{r}$ but the number of point charges involved increases as r^3. Methods to approximate the resulting infinite summation involve introducing a truncation distance to the interaction sphere, however, this can result in a possible charged sphere around an ion.

To overcome this problem, several summation techniques have been developed to allow for the electrostatic contribution to be determined in an atomic system. The most common methods was proposed by Ewald [171] that separate the sum into two components, one in real space and another in reciprocal space. The Ewald method is not the only method available to determine the electrostatic contribution to the potential energy. There are also the Particle-Mesh Ewald (PME) [172, 173], Smooth Particle-Mesh Ewald (SPME) [174] and Particle-Particle/Particle-Mesh (PPPM) [146, 175, 176] algorithms.

Assigning Charge

The magnitude of the charge on an ion is typically assigned according to empirical values based on valence information. These formal charges are appropriate in ensuring the transferability of the models and parameters used to describe a set of atomic interactions [157]. However, full formal charge models can generate artificially large Coulombic contributions to the potential function and have been shown to strongly influence the interlayer structure and dynamics of clay minerals [133].

Many interatomic potential functions are based upon the assignment of partial (or fractional) charges to the atoms. The charges are typically smaller than the full formal charge but retain the same proportions. For instance in quartz the charge of silicon can be formal $q = +4$ or partial $q = +2.4$, and is then counter-balanced by an oxygen charge of either $q = -2$ for a formal charge model or $q = -1.2$ for the partial charge model [160]. Partial charges can be calculated from *ab initio* or QM calculations, or from experimental data such as dipoles and electronegativities.

The Shell-Model for Ions

The description of the atoms as classical particles does not include any consideration for the electron cloud around an atom when interacting with neighbouring ions. In some cases, ignoring this effect can result in a poor description of the interactions within a material and can lead to misleading or incorrect results. A method to overcome this is by introducing a representation of the electron cloud using a "shell" model. Instead of describing the atoms as point particles with an assigned charge, the atom is described by a core point charge with all the associated mass connected to second massless point charge by a simple harmonic spring to represent the flexibility of the electron cloud [177]. The total charge on

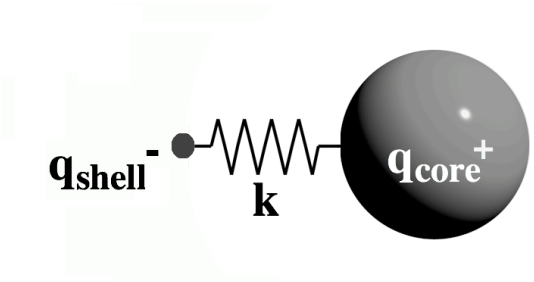

FIGURE 2.3: The representation of the shell-model description of an atom. The sum of q_{core} and q_{shell} equals the total charge on the atom, but allows the polarisability of the electron cloud to be approximated.

an atom is typically divided into a positive charge on the core combined with a negative charge on the shell, as shown in Figure 2.3.

The interaction between the shell and the core is electrostatically screened and described by a harmonic spring with force constant k:

$$U^{\text{core-shell}} = \frac{1}{2}k\left(r_{\text{core}} - r_{\text{shell}}\right)^2 \tag{2.9}$$

where r_{core} is distance of the core from the centre of the shell and r_{shell} is the shell radius. The implementation of the shell model is such that the short-range interactions are generally specified to act only on the shell and the electrostatic potential acts upon both. Whilst it is convenient to view the assignment of the charges according to a simple representations of the physical structure of an atom (electron valence shell is negative, nucleus is positive) it is not always necessary and the opposite case can be used in a simulation if it provides a more accurate description for the system.

The shell model has become a popular tool for low symmetry crystals [178] and oxides, which have particularly benefitted from the shell model implementation [158, 179–182]. This increased accuracy does however involve a higher degree of complexity in the description of the atomic system and carries with it a higher associated cost.

2.2.3 Periodic Boundary Conditions

The simulations of bulk materials are hampered by the size of the atomic systems necessary to represent the bulk. If a bulk material is being investigated, more than 10^{23} atoms are required to accurately simulate any macroscopic property. These numbers are not achievable in simulations; even the largest atomic simulations with millions of atoms still have a surface atom to bulk atom ratio far greater than that in a real material. This leads to a greater influence of surface effects on the simulation compared to what would be observed experimentally, and results in poor accuracy in the simulation results.

The smallest repeatable unit of a material, called unit cell, can be repeated in all directions to give an approximation of the bulk material. By assuming this unit is surrounded by an infinite number of replicas of itself, surface influences are negated. This sampling of a material is thus sufficient to represent the bulk. The conditions applied at the boundaries of the unit cell to implement this are called the *periodic boundary conditions* (PBC). An example is shown in Figure 2.4.

Periodic boundary conditions are usually applied when simulating bulk liquids, solids and gases in dynamics simulations. Simulations of individual molecules and surfaces may employ either none or a variation on the conditions depending on the requirements of the simulation. Surface simulations, for example, will only implement PBC in two directions and cluster simulations where individual molecules and clusters of atoms are of interest do not require a representation of the bulk and so have no boundary conditions applied.

Minimum Image Convention

The application of periodic boundary conditions requires that the interatomic potential functions are truncated to avoid duplicating calculations when an atom

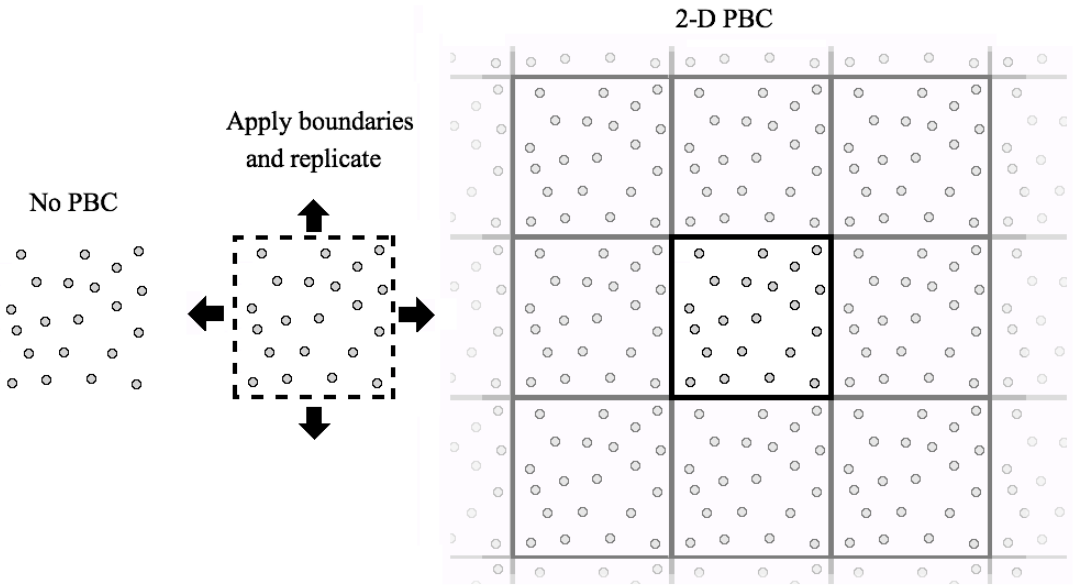

FIGURE 2.4: A cluster of atoms (left), that represent a unit cell are replicated in two dimensions (centre) to produce a two-dimensionally periodic system (right).

interacts with its own periodic image. This is called the *minimum image* convention, and ensures that the system appears to be non-periodic to all the atoms within it (shown in Figure 2.5). Not all simulation packages implement this convention, however, and it is important to be aware of the different methods used as this can have an impact on the size of the atomic system simulated and the interatomic potential functions used.

Truncation of potential functions

The most successful molecular simulation codes place importance on not only accurately calculating the energy but to do so *efficiently*. A method employed to increase the efficiency of a simulation is to truncate a potential energy function by introducing a cut-off distance, r_{cut}, where the energy of the interaction beyond this distance is considered to be zero. This is possible due to the rapid decay of most interatomic potential functions with increasing r_{ij}. The cut-off distances

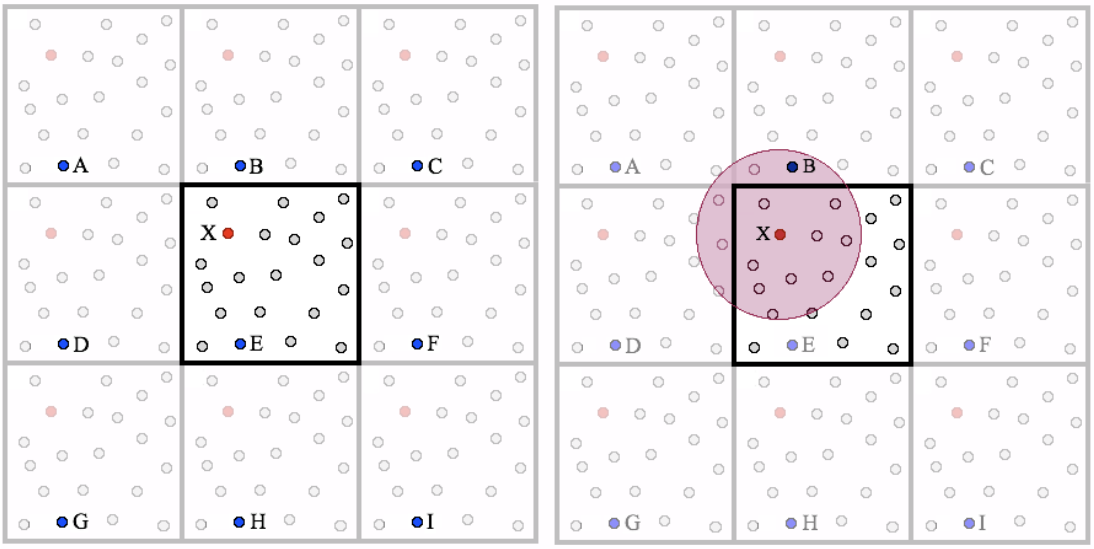

FIGURE 2.5: The image on the left shows a primary cell (centre box) surrounded by 8 periodic images. The interaction of the atom, X has 9 possible interaction distances between atoms A–I. By applying a cut-off to the interaction at $r_{cut} < \frac{1}{2}$ the primary box length (shown in the image on the right by the shaded circle), only the shortest interaction distance, XB, is included in the simulation.

are chosen at distances where the effects of the potential can be considered negligible. In cases where the minimum image convention is used, a small potential cut-off radius allows smaller simulation cells to be simulated which reduces the computational costs.

Truncation often results in a discontinuity in the potential function and this results in poor conservation of energy. This is avoided by shifting the function such that the potential smoothly tends to zero before the cut-off distance or by multiplying the potential by a tapering function that goes to zero. Long-range corrections can also be implemented, where the potential energy beyond the cut-off is approximated by an additional constant contribution.

2.3 Simulation Methods: Energy Minimisation

Simulation approaches using classical methods allow the potential or internal energy of a system to be calculated using the interatomic potential functions for a specific set of atomic coordinates. The total potential energy for an atomic system is the sum of all the contributions for all the atomic interactions and by changing the coordinates and conditions a range of configurations can be sampled. The process of adjusting an atomic system to its most stable configuration is known as energy minimisation (also called structural optimisation). The potential energy of a system can be explored by calculating different possible configurations of the structure of an atomic system, thereby sampling the potential energy surface. The lowest point or minimum on this surface corresponds to the most stable configuration, thus driving the direction in which the minimisation proceeds.

Minimisation algorithms calculate the first and second derivatives of the internal energy of the system for a number of points on the potential energy surface in order to find a minimum. The minimisation is considered complete when the first derivatives of the energy with respect to the structural variables converges to zero [183]. There are several algorithms available depending on the size of the system and the number of variables. One of the more efficient algorithms is the Broyden-Fletcher-Goldfarb-Shanno (BFGS) algorithm [184]; and this is employed for all energy minimisation simulations in this research.

Energy minimisation allows the lowest energy configuration for a material to be calculated, but does not take into account factors such as temperature and the structures determined are usually the equivalent of a material at 0 K. Thus it can not be used to investigate properties that rely on these factors, nor can it be used to determine dynamic properties such as diffusion.

2.4 Simulation Methods: Molecular Dynamics

The simulations in this thesis used large crystalline and amorphous atomic systems in dynamic environments. To access dynamical processes and the effects of temperature and pressure, molecular dynamics (MD) simulations are used. Molecular dynamics has been useful in simulating the temperature induced transformations between the crystalline polymorphs of SiO_2 such as cristobalite, coesite and the amorphous silica phase [185]. High temperature simulations have been successful in providing details of structures and of interactions occurring at the atomic level in conditions that are difficult to achieve in a laboratory [186–189], similarly the behaviour of fluids in various ambient conditions have been successfully studied using MD [190–194].

The introduction of atomic motion involves assigning velocities to the atoms, which thus implies a time-dependence of the particles' motion. The atoms now have both kinetic and potential energy contributions, and in an isolated system, the total energy at any point in time must be a constant of the motion of all the atoms:

$$E_{total} = K\left(\mathbf{p}^N\right) + U\left(\mathbf{r}^N\right) = constant \tag{2.10}$$

The motions of the particles are described using classical Newtonian mechanics. Newton's second law of motion states that the force applied to a classical particle produces an acceleration according to:

$$a_i = \frac{F_i}{m_i} \tag{2.11}$$

where m_i is the mass and a_i is the acceleration of the particle i and $a_i = d^2r_i/dt^2$. As has been stated previously, the force on that particle can be related to the potential energy U of the system by calculating the derivative of the energy with respect to the position according to Equation (2.1). Consequently the atoms'

acceleration can be related to the gradient of the potential energy by Equation (2.12):

$$a_i = -\frac{1}{m_i}\nabla_{r_i} U \tag{2.12}$$

This allows the acceleration of the particles to be directly calculated from the potential energy.

2.4.1 Solving the Equations of Motion

The equations of motion use the Euler formalism [195] for a particle with constant acceleration to describe particle motion:

$$a_i(t) = constant \tag{2.13}$$

$$v_i(t) = v_0 + a_i t \tag{2.14}$$

$$r_i(t) = r_0 + v_0 t + \frac{1}{2} a_i t^2 \tag{2.15}$$

where v_0 and r_0 are the initial velocities and positions respectively at time t and a_i is the acceleration. In MD simulations the solutions to the Equations of motion are determined through numerical integration, and thus require that the Equations are solved for discrete time intervals. This is possible due to the assumption that for a sufficiently small time-step, δt, any given atom experiences an approximately constant force.

The time step is one of the most important parameters in a molecular dynamics simulation. If the time step is too large, the atoms will deviate from the true trajectory. This produces unrealistic results as it assumes that the atomic motion was completely unaffected by interactions with neighbouring atoms during the time period. In extreme cases the atoms final positions may overlap, which would result in a large repulsive force producing velocities in the next time-period that

would be unrealistic. An overly large δt also results in a divergence of total energy as the simulation proceeds, and thus affects the conservation of energy.

Time-steps that are too small, however, require more iterations to simulate the same length of time and can make the simulations excessively expensive. A general rule is that the time step should be one order of magnitude less than the timescale of the shortest motion expected to occur in the simulation [196]. This can be the shortest time between collisions or the shortest time for one complete bond vibration, and is generally in the femtosecond scale depending on the type of simulation.

Integrators

For each time-step, the numerical solutions to the Equations of motion are determined through an integration algorithm. There are several algorithms available that use a combination of the positions, accelerations and velocities of the current and previous time steps to calculate the positions of the atoms for the next step. Ideally the use of *all* possible information provides the most accurate trajectories but, as with many cases in computational chemistry, the increase in cost to achieve higher accuracy can be a limiting factor.

Each atom has a constant acceleration that can be calculated by Equation (2.12), and the positions and velocities of the atoms after a period of time, δt, can be related to the acceleration by truncating the Taylor series expansions after the acceleration terms as follows:

$$r_i(t + \delta t) = r_i(t) + v_i(t)\delta t + \frac{1}{2}a_i(t)\delta t^2 \tag{2.16}$$

$$v_i(t + \delta t) = v_i(t) + a(t)\delta t \tag{2.17}$$

Using the Euler equations alone results in diverging trajectories and an increase in the accumulated error over time, thus several integration methods have been proposed that improve upon the accuracy of the calculated trajectories.

The Verlet algorithm includes the truncated Taylor expansions of the position vector $r_i(t \pm \delta t)$ in different time directions, where $r_i(t - \delta t)$ is given by:

$$r_i(t - \delta t) = r_i(t) - v_i(t)\delta t + \frac{1}{2}a_i(t)\delta t^2 \tag{2.18}$$

and adding this to Equation (2.16) gives:

$$r_i(t + \delta t) = 2r_i(t) + r_i(t - \delta t) + a_i(t)\delta t^2 \tag{2.19}$$

The derivative is approximated as finite differences of the positions, with the velocities given by:

$$v_i(t) = \frac{1}{2\delta t}\left[r_i(t + \delta t) - r_i(t - \delta t)\right] \tag{2.20}$$

This method does not require velocities to calculate the atomic trajectory and is stable with large time-steps. The disadvantage is that it not self-initialising, however, this is rectified by including a Euler step (Equations (2.16) and (2.17)) as the initial iteration.

A variant of the Verlet algorithm is the Velocity-Verlet method that only includes the positions and velocities at the present step to calculate the atomic trajectories:

$$r_i(t + \delta t) = r_i(t) + v_i(t)\delta t + \frac{1}{2}a_i(t)\delta t^2 \tag{2.21}$$

$$v_i(t + \delta t) = v_i(t) + \frac{\delta t}{2}\left[a_i(t) + a_i(t + \delta t)\right] \tag{2.22}$$

The method requires the acceleration for the next time step, and thus to complete the integration the sequence of calculating the velocities is performed is as follows:

$$v_i(t + \frac{1}{2}\delta t) = v_i(t) + \frac{1}{2}a_i(t)\delta t \tag{2.23}$$

$$r_i(t + \delta t) = r_i(t) + v_i\left(t + \frac{1}{2}\delta t\right)\delta t \tag{2.24}$$

$$v_i(t + \delta t) = v_i\left(t + \frac{1}{2}\delta t\right) + \frac{1}{2}a_i(t + \delta t)\delta t \tag{2.25}$$

The velocity Verlet method thus only requires the current information at time t and so is self-initialising. The choice of algorithm depends on the degree of accuracy that needs to be attained and the memory and computational time available to a simulation. There are other integrator algorithms available but are not used in the simulations reported in this research.

Total Simulation Time

The total number of time-steps over which a simulation runs for depends on the size of the system and the purpose of the simulation. Increasing the simulation time increases the number of simulation steps and adds to the computational cost. Properties such as diffusion constants or thermodynamic properties require time scales long enough to collect sufficient statistics, as do simulations of thermal annealing, melting, and the simulation of liquids. Molecular dynamics simulations using interatomic potential functions typically explore timescales up to the nanosecond scale, but the restrictions in the computing costs mean that the time scales required to simulate phenomenon that take any appreciable time in the laboratory (such as seconds, minutes or hours) are not directly accessible to MD simulations.

Phase-Space Trajectories

The objective of a molecular dynamics simulation is to generate the motion for all atoms in the system over a period of time. Since the atoms' movement is described by the classical equations of motion, the atoms trace out trajectories that are represented by time-dependent position vectors, $\mathbf{r}_i(t)$. Interactions with neighbouring atoms affect the momenta of all the atoms, and so a set of time-dependent momentum vectors is introduced. In a system containing N atoms, a $3N$-dimensional configuration space contains the coordinates of the position vectors, $\mathbf{r}_i(t)$, and a $3N$-dimensional momentum space contains the components of the momenta for the coordinates, $\mathbf{p}_i(t)$. The combination of the configuration space and the momentum space is called the *phase-space*.

2.4.2 Ensembles

An ensemble is a collection of microscopic states that have a common set of macroscopic properties such as temperature and pressure. There are several different types of ensembles used in molecular dynamics, each defined by 3 quantities that are kept constant, such as the number of atoms (N), the energy (E), pressure (P), temperature (T), volume (V), chemical potential (μ) and external stress (σ). The different combinations of these quantities are designated different names: the micro-canonical ensemble (NVE), canonical ensemble (NVT), isobaric ensemble (NPE), isothermal-isobaric ensemble (NPT), isotension ensemble (NσE), isotension-isothermal ensemble (NσT) and the grand-canonical ensemble (μVT).

Micro-canonical Ensemble

The NVE ensemble represents an isolated system where there is no change in the number of atoms, energy and volume. Simulations in the micro-canonical ensemble represent adiabatic processes where there is no heat exchange. However,

temperature is a statistical thermodynamic quantity, and the statistical temperature of the system will fluctuate around the average macroscopic value.

The kinetic energy of an atom can be related to the velocity:

$$K_i = \frac{1}{2} m_i v_i(t)^2 \tag{2.26}$$

where the probability of an atom with a specific velocity is described by a Maxwell-Boltzmann distribution. The equipartition theorem predicts that every particle in an ideal gas has an average kinetic energy of $\frac{3}{2}k_BT$ where k_B is Boltzmann's constant and T is the instantaneous temperature of the system, and thus allows the introduction of temperature into MD simulations. At any instant, all the velocities of the atoms can be calculated, and this will give the *instantaneous* temperature of the system.

$$\frac{3}{2} N k_B T = \frac{1}{2} \sum_{i=1}^{N} v_i(t)^2 \tag{2.27}$$

Canonical Ensemble

The canonical (NVT) ensemble exchanges energy with an external system within the ensemble to allow for a constant temperature simulation. Since the instantaneous temperature depends only on the atoms' velocities, the temperature of a system can be controlled by scaling these velocities using thermostat algorithms to control the system temperature. The simplest method to scale the velocities of the atoms is by coupling the system to an external hypothetical heat-bath with a reference temperature $T_{desired}$. The system is coupled to the heat-bath by introducing a coupling or scaling factor, λ, to rescale the atomic velocities at each integration step to reach and maintain the desired temperature [197].

$$\lambda = \sqrt{\frac{T_{desired}}{T(t)}} \tag{2.28}$$

The effect of the thermostat on a MD simulation must maintain the correct sampling of the distribution of the velocities that represent the canonical ensemble. The Berendsen thermostat [198] scales the velocities such that the rate of change in temperature is proportional to the difference between the system and bath temperature:

$$\frac{dT(t)}{dt} = \frac{1}{\tau_T}(T_{bath} - T(t)) \tag{2.29}$$

where τ_T is a coupling parameter called the thermostat relaxation time and determines how tightly the bath is coupled to the system. This results in a scaling factor of :

$$\lambda = \sqrt{1 + \frac{\delta t}{\tau_T}\left[\frac{T_{bath}}{T(t)} - 1\right]} \tag{2.30}$$

The smaller τ_T is the more closely the bath is coupled, and when $\tau_T = \delta t$ this reduces to Equation (2.28).

The Nosé-Hoover thermostat [199, 200] is often used once the system has reached the reference temperature. In this approach the heat bath is made an integral part if the system by adding a degree of freedom (s) for the position of the bath and its fictitious mass Q. The extra degree of freedom represents the interaction of the system with the bath, and it acts as a time-scaling parameter. The Q parameter controls the energy flow between the system and the bath, if Q is large the energy flow is very slow, but if Q is too small, the energy oscillates in such as way as to lead to nearly periodic temperature fluctuations.

The benefit of using an NVT ensemble in molecular dynamics simulations is that the temperature is explicitly included and the kinetic energy can assist the atomic motions to overcome potential energy barriers. This allows MD simulations to overcome some of the limitations associated with static energy minimisation calculations, as this kinetic energy assists in better sampling of the potential energy surface.

Isobaric-Isothermal Ensemble

The NPT ensemble can be considered to represent an experimental set up with controlled temperature and pressure in real everyday life. In these cases in addition to a thermostat a *barostat* is also included. Similar to using a thermostat, a barostat is used to control the pressure in a simulation. The instantaneous pressure of an atomic system can be calculated using the Virial theorem [201]:

$$P(t) = \frac{Nk_BT}{V} + \frac{1}{DV}\left\langle \sum_{i<j} F \cdot r_{ij} \right\rangle \tag{2.31}$$

where V is the volume of the system D is the number of degrees of freedom and F is the force acting between atoms i and j. The pressure consists of configurational and kinetic components. The pressure of a system can be controlled by scaling the volume of the simulation box by a scaling factor μ.

$$\mu = \sqrt{1 + \frac{\delta t}{\tau_P}\left(P(t) - P_0\right)} \tag{2.32}$$

This scaling factor can be applied to the volume as a total ($V = \mu^3 V$) or to the individual lengths of the simulation box ($L = \mu L$). The pressure can thus be kept constant either by scaling isotropically (in all directions) or anisotropically (a scaling factor calculated for each direction). In some cases the shape as well as size of the simulation box may need to change such as simulations that include transformations of crystalline structures as a function of temperature or with applied stress. In these cases isotension-isothermal ensembles may be more useful than the NPT ensemble.

2.4.3 Computational Simulation Packages

There are many computational packages available for the various simulations of materials in chemistry. Most are designed for specific types of simulations, such

as energy minimisation or molecular dynamics and are parallelised to be able to run simulations on multiple processor systems, thereby increasing the speed at which the simulations are completed at in real time.

The General Utility Lattice Program (GULP) is a computational package developed by Gale [202] primarily to provide information on crystalline structures through the use of lattice dynamics rather than molecular dynamics. GULP is capable of simulating solids, clusters, embedded defects, surfaces, interfaces, and polymers through a variety of energy minimisation techniques. It is also useful for calculating the physical properties of a material that are based upon the curvature of the potential energy surface, such as the elastic constants, bulk and shear moduli, phonon frequencies, heat capacity to name a few [157]. Unless otherwise specified, all structural optimisations conducted in this research used the BFGS [184] optimiser routine in GULP, with larger systems employing a limited memory BFGS algorithm to reduce simulation time.

The DL_POLY 2 computational package developed at the Daresbury Laboratory by Smith and Forester [203, 204], is a molecular dynamics simulation package for macromolecules, polymers, ionic systems, solutions and other molecular systems. It has some structural optimisation functionality, but this is best suited for use in bringing atomic systems to a suitable starting point for a MD simulation and it is not recommended for use as general structure optimiser [205]. The Large-scale Atomic/Molecular Massively Parallel Simulator or LAMMPS code is also a molecular dynamics simulation package that can simulate atomic, polymeric, biological, metallic, granular, and coarse-grained systems using a variety of interatomic potential functions and boundary conditions [206, 207].

The simulations in this research use the Berendsen [198] and Nosé-Hoover [199, 200] algorithms for temperature and pressure control where the application of the barostat can be either as a scalar pressure (NPT ensemble) or as components of a symmetric stress tensor (NσT ensemble). DL_POLY uses a reversible

velocity-Verlet integrator based upon the work of Martyna *et al* [201]. All simulations implement the SPME method to calculate the electrostatic contributions with a precision set to 10^{-6}. LAMMPS uses time-reversible measure-preserving Verlet and multiple time-scale integrators derived by Tuckerman, Berne and Martyna [208] with Equations of motion based upon those of Shinoda, DeVane and Klein [209]. The electrostatic contribution is calculated by the particle-particle/particle-mesh methods [175] with a precision of 10^{-4}. Whilst similar in capabilities to DL_POLY, the LAMMPS code runs more efficiently in larger atomic systems than DL_POLY and so is used in later simulations on systems of greater than $10,000$ atoms.

Both MD codes output the trajectory files for the simulations that include information such as the energy for each time step, temperature, pressure, cell lengths and so forth. Analysis of the trajectories to determine the properties of interest are usually conducted with methods developed depending on the required information. Several visualisation packages are available to view the trajectory files and final structures and whilst the choice of these programs does not influence the final results from the simulations, some packages have additional capabilities. For example, the porosity measurements in Chapter 5 are completed using the Atomic Visualisation and Analysis Software (AVAS) [210], which allows for the identification and analysis of the nano-porosities of periodic simulated structures.

2.5 Calculating Properties

To simulate a material satisfactorily, the results of a simulation must be able to confirm or reproduce observations and measurements made in the laboratory. There is a large quantity of experimental structural characterisation research available that has provided the bulk properties for many materials such as the

elastic constants and phonon dispersion curves, and so a comparison of the calculated values with experimental values provides a good indication of the quality of the simulation parameters. This is particularly important when verifying the accuracy and transferability of interatomic potential models.

The energy minimisation approach produces an optimised structure, and the curvature of the energy surface around the minimum can be analysed to calculate a wide range of physical properties. One such set of properties are the elastic constants, which represent the second derivatives of the energy density with respect to strain:

$$C_{ij} = \frac{1}{V}\left(\frac{d^2U}{d\epsilon_i d\epsilon_j}\right) \tag{2.33}$$

The elastic constants are represented by a 6×6 symmetric tensor matrix which incorporates the 6 possible strains, with the number of unique elements of C dependent on the symmetry [211]. Experimental restrictions on sample size and shape have resulted in the full tensor being unavailable for many structures, and so the ability to calculate this information from a simulation is very useful. Related to the elastic constants are the bulk (K) and shear (G) moduli. These moduli contain information about the hardness of a material with respect to various types of deformation. The bulk and shear moduli are useful as they are easier to obtain in a laboratory than the full elastic constant tensor, and thus are good sources for comparison. All the elastic constants as well as the bulk and shear moduli can be calculated by GULP once structural optimisation is complete.

One of the simplest and most useful properties that can be calculated from a dynamic computational simulation is the Radial Distribution Function (RDF), given by:

$$g(r) = \frac{1}{N4\pi r^2 \rho dr}\left\langle \sum_i \sum_{i \neq j} \delta(r - r_{ij}) \right\rangle \tag{2.34}$$

where N is the number of atoms in the system, dr is the sampling width at a distance r and ρ is the density of the system [212]. This is an ensemble average taken

over all the atomic pairs in the system, and thus describes the density of atoms as a function of the interatomic distances, compared to a completely random distribution of the same density. Deviations from unity are due to correlations in the atomic interactions, with crystalline materials demonstrating well-defined peaks characteristic of the atomic structure. Figure 2.6 shows an example of a RDF from a simulations conducted in this research of kaolinite at 1000 K.

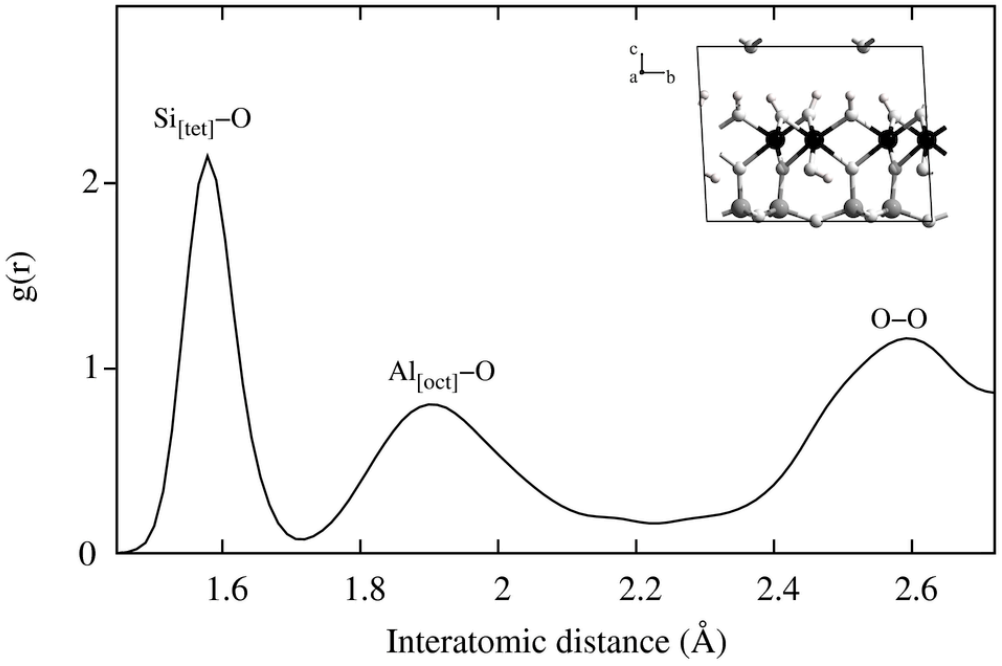

FIGURE 2.6: Example of the RDF from a kaolinite structure at 1000 K, with the unit cell inset (large black atoms = Al, large grey atoms = Si, medium grey atoms = O and small grey atoms = H). The different peaks are due to the characteristic distances between atomic pairs, and the area under the peaks gives coordination information.

The RDF is readily comparable to experimental diffraction data, as the Fourier transformation of the diffraction data gives a radially averaged measure of deviations from the average density. Integration of the area below the peaks in the RDF gives information regarding the coordination of the atoms, which is important in identifying the local order within the structure. It is particularly important in the study of amorphous materials such as glasses. Although the experimental

methods do not always provide exact atomic positions, the RDF can be used for comparison to simulation and is the most common method in validating a simulation of an amorphous material, along with calculating macroscopic properties such as density.

The diffusion coefficient for a molecule in a liquid is an important dynamic property that can be calculated from a molecular dynamics simulation. The method for finding the diffusion of an atom is by calculating the Mean Square Displacement (MSD) of an atom or molecule during the period of simulation, which is the measure of the average distance an atom travels as it follows the random path of motion.

$$\mathrm{MSD}(t) = \frac{1}{N}\sum_{i=1}^{N} |r_i(t) - r_i(0)|^2 \tag{2.35}$$

The MSD is useful as a plot of the displacement against time shows a linearly increasing relationship if a system is in a liquid state. Figures 2.7 show the typical behaviour expected to be present in such a plot for atoms in a liquid.

Alternatively Figure 2.8 shows how atoms in a solid material behave. The molecular dynamics simulation of metakaolin at 1000 K produces no diffusion of the atoms within the structure, confirming it is a solid. Assuming random brownian motion, Einstein [213] related the MSD to diffusion. The slope of the MSD when plotted against time is thus related to the self-diffusion coefficient:

$$\mathrm{MSD}(t) = 6D \cdot t + b \tag{2.36}$$

where D is the self diffusion coefficient and b is a constant. When simulating liquids such as water, calculations of the self-diffusion can then be compared with experiment for validation, along with the diffusion of ions in aqueous phases.

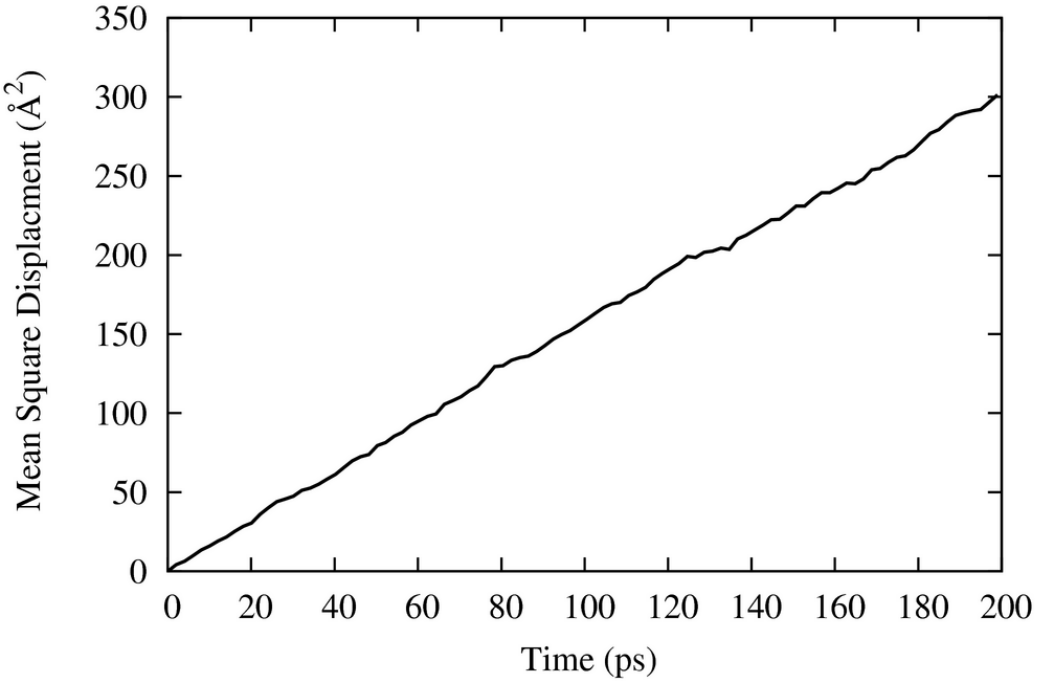

FIGURE 2.7: The mean-square displacement of an atom as a function of time for a molecular dynamics simulation of a liquid. The gradient can be related to the diffusion coefficient D with units of distance^2 time^{-1}.

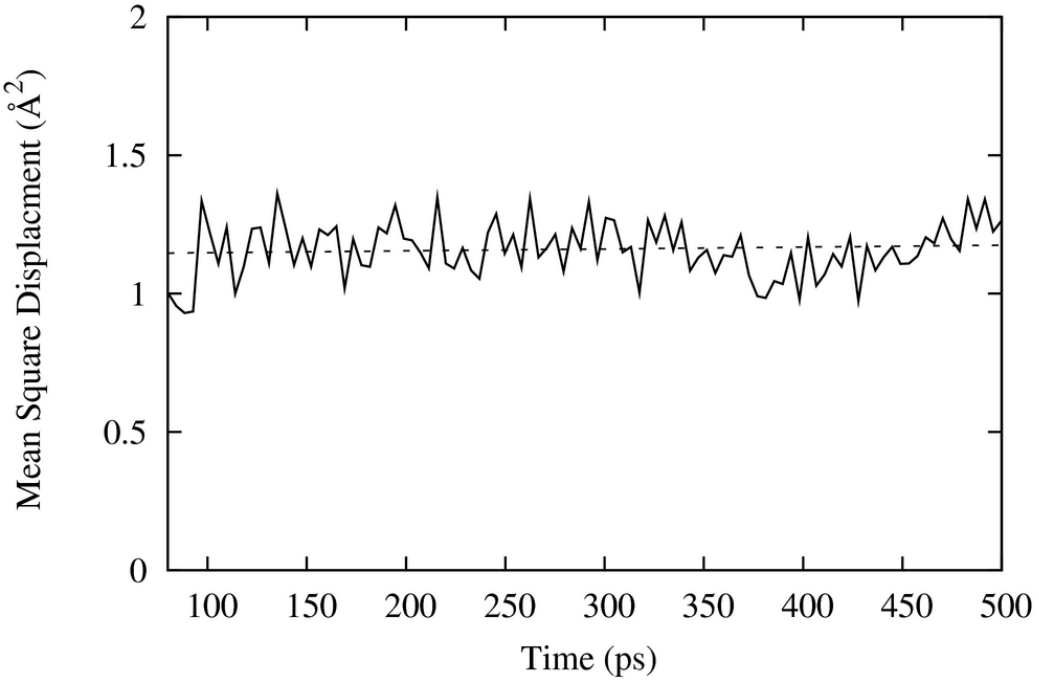

FIGURE 2.8: The mean square displacement as a function of simulation time of an atom in a solid at 1000 K. The high temperature causes some thermal vibration, but no net diffusion through the system.

Chapter 3

The Interatomic Potential Model

The structure of a geopolymer is composed of an amorphous aluminosilicate network charge balanced by cations, as well as molecules such as OH and H_2O. How these components interact to influence the final structure and properties is poorly understood, and the investigation of metakaolin as a model system will aid in addressing this. The structure of metakaolin will be investigated in this research through simulation methods, and this requires that an interatomic potential model be identified that will accurately and efficiently describe the variety of atomic interactions.

3.1 Introduction

A diverse range of interatomic potential function models are available in the literature that deal with the interactions of the ions in aluminosilicate materials in a variety of structural conformations and environments. Aluminosilicate materials in general are composed of Al and Si in 4–fold coordination with oxygen, although the presence of 5– and 6–fold aluminium must also be accounted for. The many different aluminosilicate materials found naturally and commercially incorporate many additional ions and molecules but since not all are necessary to this research, the focus here will be upon the inclusion of Na^+, K^+ and Ca^{2+} as well as OH^- and H_2O. The interatomic potential function must also be able to represent both amorphous and crystalline behaviour. Finally, the interactions of aluminosilicates in aqueous environments should also be considered as the solid–liquid interactions are investigated in Chapter 6.

To summarise all the interactions of interest, a list of criteria that the model must address has been constructed:

1. Model an aluminosilicate material:
    - Include all M–O interactions, where M= Si, Al, Na, Ca and K.
    - Allow for 4–, 5– and 6–fold Al–O coordinations.
    - Correctly account for the strength and rigidity of the SiO_4 tetrahedral unit.
    - Include the hydroxyl group and all associated interactions.
2. Model an aluminosilicate material in contact with water:
    - Structure and properties of water.
    - Aluminosilicate surfaces.
    - Liquid water in contact with an aluminosilicate surface.
    - Structural water within an aluminosilicate material.

The choice of interatomic potential model is also dependent on the properties of interest, and related to this the types of simulation method being used. Bulk properties such as elastic constants, crystal properties and vibration spectra are generally simulated using static energy minimisation techniques. These simulation techniques require accurate descriptions of the interatomic interactions, and often use models with higher complexities such as the inclusion of three– and four–body terms in the potential energy function, or the use of shell models to describe the polariseability. Properties such as diffusion constants or radial distribution patterns can be calculated by methods such as molecular dynamics. The interatomic potential functions for these simulations must as a consequence be suitably robust to describe interactions in the different ensembles.

This chapter investigates three interatomic potential sets of relevance to this research from the literature. Calculation of both bulk and dynamic properties and thus both energy minimisation and molecular dynamics simulations are required to evaluate the interactions and structures investigated. As such the interatomic potential model must be accurate in the description of the bulk properties, whilst able to simulate large systems using molecular dynamics.

3.2 Empirical Potential Functions

Computational simulations have been used to investigate minerals for over two decades. The increase in computational resources during this time has led to an increase in the complexity of the interactions and size of atomic systems that could be described for these purposes. Original simple two-bodied interactions were extended to include the influence of polariseability (shell models) [214–216] and directionality (three-body terms) [163, 217]. The parameterisation of interatomic potential models is generally undertaken by two types of fitting procedures; using experimentally observed properties to fit the variables in the potential function; and fitting the parameters to *ab initio* results. The two methods have been used with varying success and a large variety of interatomic potential models exist in the literature.

Empirical potential methods that derive variable potential parameters by fitting experimental data require several properties for the structures of interest in order for a potential to be robust. These properties include atomic coordinates, elastic properties and in some cases spectroscopic data. The parameters are usually varied until the sum–of–squares is minimised, a measure that allows you to determine how 'good' the fit is. The fitting to second derivative information, such

as the elastic constants, is also important to improve the accuracy of the potential model, as without this added level of accuracy many models would lose their applicability [157].

The discussion presented here will focus on three interatomic potential models for aluminosilicate materials. These models have been developed separately using different fitting procedures and have been used extensively in the simulation of these materials. Each of these potential models will be tested by simulating a variety of structures that have well-characterised properties. The simulated materials will be compared to the known experimental values, and the interatomic potential parameters that are the most accurate will be used to simulate metakaolin and any other structures simulated in this research.

3.2.1 Models from the Literature

Empirical interatomic potential models were initially developed to describe the cohesive energy in simple ionic solids [179] such as metal halides and oxides. These models were based upon the assumption of full ionicity [182], used full formal charges on the ions, described interactions using two–body potentials. The original potential parameters were based upon interatomic potentials derived by Catlow and co-workers (see review by Catlow and Price, 1990 [218]) that were fitted to experimental parameters. These simple two-bodied potentials employed the shell model for the description of the ion polariseability proposed by Dick and Overhauser [177] and were successful in modelling a range of ionic materials [179, 219].

The lack of accuracy in the simulation of the SiO_2 polymorphs using the simple two-bodied ionic interactions [218] led to the extension of the original parameters for oxides by Sanders *et al.* [216] to simulate quartz [220] as well as more complex silicates such as forsterite [221, 222], feldspars [223] and the zeolite minerals [224,

225]. The extended parameters included three-body terms that led to a much better description of the covalency associated with the SiO_4 tetrahedra, and as a result the THB potential model (THB = THree Body) has been extensively used in simulating the properties of major earth forming minerals. Variations of the THB potential have been used to investigate the phase stability, defects and diffusion behaviour for a variety of minerals such as forsterite and other Mg_2SiO_4 polymorphs [226, 227], feldspars such as albite [228] and garnets [229].

The investigations into the active sites in zeolite minerals led to the necessity of the inclusion of the OH group into the structures of nominally anhydrous materials. This was accomplished by Schröder *et al.* [160] and Kramer *et al.* [230], the latter simulating a pseudo–lattice oxygen atom for the hydroxyl group, and the former modelling the atoms explicitly. The Schröder parameters incorporated a Morse potential description of the OH molecule derived from QM calculations by Saul *et al.* [231] of sodium hydroxide, and were developed to describe bridging hydroxyl groups in zeolites. The resulting models were successfully used in the simulations of many hydrated phases such as clay minerals [133, 232, 233] and other inorganic solids [234, 235].

The introduction of the OH group necessitated the development of a scheme to systematically incorporate the description of the OH-O and OH-cation interactions as described by Schröder *et al.* [160]. The addition of this group to the Catlow potentials [182] has been used successfully to simulate the hydroxyls interactions in a range of materials [236] such as hydrated magnesium silicates [237–239], spinels [240] and olivines [241]. These potentials have thus shown themselves to be extremely robust at describing a range of atomic environments, and as such are included as possible parameters for modelling metakaolin.

The potential model developed by Kramer *et al.* [230] to simulate silicas, aluminophosphates and zeolites was determined by fitting to *ab initio* energy surfaces. There were no higher order body terms such as bond bending involved and

as such this model represented a decrease in complexity than that proposed by the empirically fitted parameters of Catlow and co-workers [182]. The model included the interactions of the hydroxyl group by fitting the parameters for H_4TO_4 molecular clusters (T=Al, Si, P), however, subsequent simulations have shown that the parameters give a poor description of the vibrational spectra for some zeolites [242]. Nevertheless, the parameters developed by Kramer *et al.* have been used to simulate the structural properties of several silica polymorphs [243, 244] and zeolites [245, 246], and will consequently be included for consideration.

The interatomic potential model proposed by Teter [247] was derived by simultaneously fitting parameters to a large number of oxide phases involving +1, +2 and +3 metal cations, using a combination of information from experimental data and DFT calculations. The advantage of using this approach is that it allows for a great deal of flexibility in the environment and is thus more likely to be transferrable across a range of structures. The concept of transferability is important in potential model parameters. The fitting of potential parameters to a single or small set of structures may result in highly accurate descriptions for those specific interactions, but any deviation beyond the sampled configurations may result in very inaccurate results. Several studies in the simulation of clay minerals have commented on the unsuitability of the existing tetrahedral aluminium parameters in early potential models [133, 248] in describing the octahedral configuration of Al in many systems.

The disadvantage of the simultaneous fitting approach is that no single phase is perfectly simulated, resulting in a potential loss of accuracy in some simulations. The model has however, been successfully used to investigate alkali silica glasses [249–251] at temperatures up to 6000 K as well as crystalline and amorphous zircon [252]. This combined with the large set of parameters available has resulted in this model being included for the purposes of this research.

Metakaolin is formed from the clay mineral kaolinite. The simulation of clay minerals initially used rigid-framework molecular models that did not allow for the flexibility of bonds, angles and dihedrals in the simulations [131, 139]. These simulations could simulate structural and thermodynamic phenomenon such as interlayer swelling [253] reasonably accurately, however, the lack of flexibility in the lattice led to an inability to accurately describe effects such as hydrogen bonding between layers, hydroxylated surfaces and adsorption processes. To investigate these phenomenon, several flexible potential model parameters were developed [248, 254], with a recent model by Cygan *et al.* [133] gaining popularity due to it's increased accuracy and functionality.

The model proposed by Cygan *et al.* [133] is parameterised for all the interactions of interest in this research including specific parameters for both tetrahedral and octahedral aluminium. This requires the locations of the 4- and 6-fold Al to be well defined within the simulated atomic system. Determining the coordination of each aluminium ion within a disordered structure such as metakaolin is challenging however, and as such the clay parameters are not used in this research.

3.3 Testing of the Potential Models

The three sets of parameters have been identified as potentially suitable for this research. The first, model 1, is composed of the parameters from Catlow and colleagues *et al.* [182, 216, 224, 255–257] with the inclusion of the hydroxyl group from Schröder *et al.* [160]. The second model, model 2, is composed of the *ab initio* parameters from Kramer *et al.* [230] and finally model 3 includes the partial charge rigid-ion parameters derived by Teter [247]. These three models will be investigated for suitability in accurately simulating the various structural criteria listed in the beginning of this chapter.

3.3.1 Testing Procedure

General testing of potential models require that the parameters be simulated in structures outside of those used in the fitting procedures. The structures chosen should have well defined physical properties that the calculated values can be compared with, and must include a range of different structural characteristics. The polymorphs of SiO_2, quartz, coesite and cristobalite, were chosen to test the simulation of the SiO_4 tetrahedra in different configurations. Stishovite, the high-pressure phase, includes 6-fold silicon in the structure and whilst this was not expected to be present in the structures simulated in this research, it was included to test the ability of the Si-O parameters to simulate a variety of conformations. The unit cells of these structures, taken from experimental crystallographic data, are shown in Figure 3.1. To test the aluminium interactions gibbsite and corundum were chosen, as the former included a considerable dependence on the Al–OH interaction and the latter the Al–O interaction. Both gibbsite and corundum demonstrate a 6-fold coordination environment of Al. The unit cells for these structures, taken from experimental values, are given in Figure 3.2.

The Al_2SiO_5 polymorphs were included as they involved the different coordinations of All as well as the interactions of the aluminate and silicate groups in various configurations. This group of structures was the most important, as it demonstrates the ability of the model to simulate 4-, 5- and 6-fold aluminium. Finally, the presence of the interstitial cations was tested (in the models that have the necessary parameters) in three aluminosilicate structures incorporating cations such as sodium and calcium. The structures chosen were sodalite, albite and anorthite, and the unit cells for each are given in Figure 3.4. This final set of tests was important as in later simulations the interaction of metakaolin with interstitial calcium and sodium ions is investigated, and the potential model must be able to simulate the incorporation of these ions into the structure accurately.

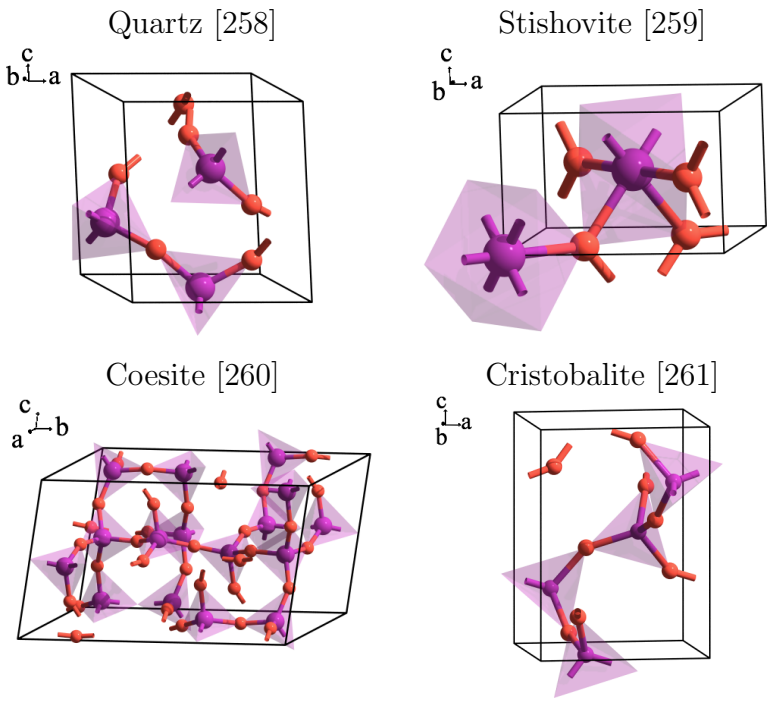

FIGURE 3.1: The unit cells for each SiO_2 structure simulated for the potential model investigation. The coordination of silicon is shown for each structure, with the shaded regions showing the orientation of the polyhedra. Si = purple, O = red. The references give the sources of the crystallographic information.

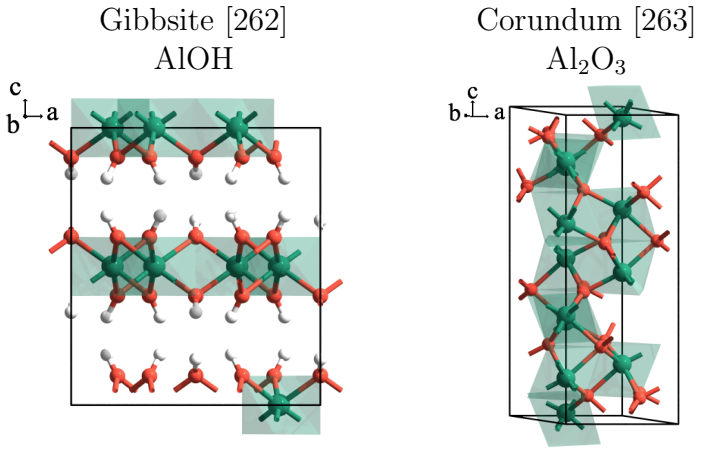

FIGURE 3.2: The unit cells for the AlOH and Al_2O_3 structures simulated for the potential model investigation, with the polyhedra shown by the shaded regions. O = red, Al = green, H = white.

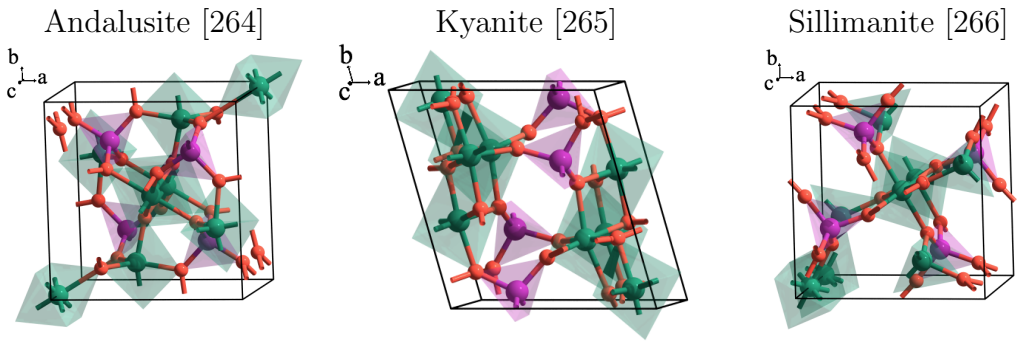

FIGURE 3.3: The unit cells for each Al_2SiO_5 structure simulated for the potential model investigation. Si = purple, O = red, Al = green.

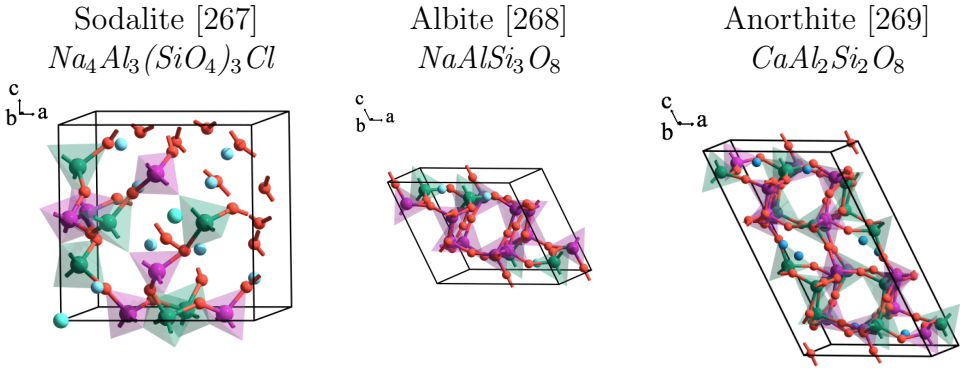

FIGURE 3.4: The unit cells for the aluminosilicate structures that include interstitial ions simulated for the potential model investigation. Si = purple, O = red, Al = green, H = white, Ca = small blue, Na = large blue.

Each crystal structure was optimised using GULP [157] with the potential parameters from each of the three potential models identified to describe the different interactions. The smaller the deviations between the experimental and calculated values, the better the performance of the potential model. To further test the parameters, the bulk elastic properties were calculated for each structure and compared to values from experiment. If the method by which the experimental elastic constants had been calculated was available (Ruess, Voight or Hill), the GULP value corresponding to that method is compared. If the method was not available, the values calculated by the Hill method are reported.

As stated in Chapter 2, elastic properties calculated in experimental environments often involve large uncertainties, so calculated values that deviate by up

to 20% from the experimental values do not necessarily indicate a poor set of parameters. There is emphasis however, that at least the bulk modulus should be reasonably accurately calculated, as this value represents the ability of the potential parameters to describe the ability of the structures to respond to strain. This is important as the simulation of the formation of metakaolin introduces many defects into the structure, and this will have considerable effect on the strain within the material.

3.3.2 Results: Model 1

The contributions to the potential energy in model 1 was described by electrostatics, a core–shell interaction for the oxygen atoms and a two–body Buckingham potential for all M-O (M = Al, Si, Na) interactions, with the relevant parameters given in Table A.1. The model used full formal charges and a rigid ion description for all species except the oxygen atoms, which were modelled as shell ions. Parameters for the OH group were included from Schröder *et al.* [160]. Parameters for the calcium and chlorine were not available, thus anorthite and sodalite were not simulated. The variations in the atomic structures were shown by determining the crystal properties of the structure from energy minimisation and comparing with experimental values as given in Table 3.1. The cell parameters a, b and c are given, however, the values for α, β, and γ were not as greatly affected by the simulations, and instead the total volume is provided to show the affect of the potential model parameters on the entire structure. Experimental values not available from the original sources for the crystallographic information are taken from Ahrens [270].

The interatomic potential model was reasonably accurate in reproducing the experimental structures for the SiO_2 and Al_2SiO_5 polymorphs and corundum, with all structures bar the high pressure and temperature phases of sillimanite and coesite demonstrating differences in volume below 5%. The relative accuracy in

TABLE 3.1: Comparison of some of the structural properties for optimised systems simulated using Model 1.

Structure	Exp.	Calc.	Exp.	Calc.	Exp.	Calc.	Exp.	Calc	%Diff
	a (Å)		b (Å)		c (Å)		Volume (Å^3)		
Quartz	4.913	4.847	4.913	4.847	5.405	5.334	113.01	108.52	-4.0
Stishovite	4.181	4.113	4.181	4.113	2.666	2.687	46.61	45.45	-2.5
Coesite	7.140	7.026	12.371	12.290	7.175	7.115	546.96	518.23	-5.3
Cristobalite	4.972	4.944	4.972	4.944	6.922	6.706	171.01	164.90	-3.6
Gibbsite	8.742	9.022	5.112	5.295	9.801	8.696	463.64	413.19	-10.9
Corundum	4.757	4.779	4.757	4.779	12.987	12.564	254.53	248.53	-2.4
Kyanite	7.117	6.901	7.860	7.880	5.575	5.664	293.70	289.39	-1.5
Andalusite	7.793	7.720	7.897	7.723	5.556	5.651	341.93	336.89	-1.5
Sillimanite	7.473	7.051	7.652	7.468	5.763	5.982	329.56	314.98	-4.4
Albite	8.115	8.479	12.762	12.899	7.158	7.191	659.83	694.05	4.9

the simulation of andalusite, which contains 5-fold aluminium, was noted and is potentially important in the simulation of metakaolin.

The average Al–O bond distances in the calculated values were always lower than the experimental values by approximately is 2.1%. For example, the experimental Al–O average distance of 1.92 Å in sillimanite was greater than the calculated average distance of 1.88 Å, which caused the simulation cell to decrease in the *a*- and *b*-directions. The Si–O distances were also slightly under-estimated by the potential model by approximately 0.8%, thus resulting in the general decreases in volumes calculated for the SiO_2 polymorphs.

The largest difference calculated was the 10.9% decrease in the volume of gibbsite, which was due to a 11.3% compression of the gibbsite cell in the *c*–direction. Gibbsite is a layered material, and the compression was due to a reduction of the interlayer spacing. The results suggested that the simulated repulsion between the layers was unsatisfactory, and may be due to the structural oxygen–hydroxyl oxygen parameters underestimating the net repulsion.

The calculated elastic properties are given in Table 3.2, and compared to experimental values where available.

TABLE 3.2: Comparison of elastic properties for structures simulated using Model 1

Structure	Bulk Modulus (GPa)			Shear Modulus (GPa)		
	Exp.	Calc.	%Diff	Exp.	Calc.	%Diff
Quartz	36.40	47.84	23.9	31.14	51.28	39.4
Stishovite	316.00	345.19	8.5	220.0	180.64	-17.9
Coesite	113.70	105.67	-7.1	61.60	46.49	-24.5
Cristobalite	16.40	12.57	-23.4	39.10	38.94	0.4
Gibbsite	85.00	48.60	-42.8	NA	32.83	NA
Corundum	253.30	347.05	27.0	163.20	163.06	-0.1
Kyanite	233	216.64	-7.0	NA	118.22	NA
Andalusite	162.00	204.63	20.8	99.10	97.76	-1.4
Sillimanite	170.80	175.24	2.5	91.50	89.14	-2.6
Albite	64	62.30	-2.66	41	40.17	-2.02

The elastic properties calculated using the parameters produced deviations greater than 5% for either the shear or bulk moduli for most structures, with differences of greater than 20% calculated in 39% of the elastic properties calculated. Gibbsite had the largest difference of -42.8% in the bulk modulus, and this is due to the incorrect description of the interlayer interactions. The large differences calculated are not necessarily indications of poor accuracy in the potential model, but must be considered as the structure of metakaolin, as a disordered material, will most likely include a higher level of strain

3.3.3 Results: Model 2

The potential model developed by Kramer *et al.* [230] was composed of a rigid–ion model with a mix of partial charges on the framework ions (Al, Si, O) and formal charges on the interstitial ions (Na and Cl), and consists of two–body interactions described by the Buckingham potential coupled with electrostatics. The parameters are given in Table A.2. This model included the hydroxyl group implicitly through the description of the oxygen atom, and does not include parameters for the hydrogen interactions explicitly. For the simulation of gibbsite this description was not adequate and as a result it was not included. This model

also did not include parameters for calcium and so anorthite was not simulated. The results for the structural characteristics of the simulated structures are given in Table 3.3.

TABLE 3.3: Comparison of some of the structural properties for optimised systems simulated using Model 2

Structure	Exp.	Calc.	Exp.	Calc.	Exp.	Calc.	Exp.	Calc	%Diff
	a (Å)		b (Å)		c (Å)		Volume (Å^3)		
Quartz	4.913	4.922	4.913	4.922	5.405	5.434	113.01	114.02	0.9
Stishovite	4.181	4.145	4.181	4.145	2.666	2.660	46.61	45.70	-2.0
Coesite	7.140	7.104	12.371	12.485	7.175	7.268	546.96	554.84	1.4
Cristobalite	4.972	4.898	4.972	4.898	6.922	6.550	171.01	157.12	-8.1
Corundum	4.757	4.479	4.757	4.479	12.987	12.438	254.52	216.04	-15.1
Kyanite	7.117	6.875	7.860	7.598	5.575	5.304	293.70	260.98	-11.1
Andalusite	7.793	7.384	7.897	7.628	5.556	5.371	341.93	302.56	-11.5
Sillimanite	7.473	7.159	7.652	7.209	5.982	5.661	329.56	292.19	-11.3
Albite	8.115	7.408	12.762	12.325	7.158	6.832	659. 83	555.60	-15.8
Sodalite	8.836	8.215	8.887	8.215	8.887	8.215	701.87	554.48	-21.0

The simulations showed that the model reproduced the structures of the SiO_2 phases better than the previously tested model, with a 20% increase in accuracy in the calculated volumes. However, a 70% decrease in accuracy in the calculated volumes for the aluminium containing phases was noted, with all showing a decrease in volume of 11% or greater upon optimisation. Investigation of this effect showed that the experimental structures had average Al–O bond lengths of 1.83 ± 0.07 Å, whilst the calculated values had bond lengths of 1.77 ± 0.06 Å, which resulted in a decrease of 3.3% overall. This decrease applied to all the Al-O interactions in the structures caused the cell parameters to decrease, resulting in a total decrease in the volumes in the optimised structures.

The largest variations occurred in the structures that included interstitial cations, namely sodalite and albite. Upon inspection of the changes in the atomic pair-distances, the variations were due to the tendency of the potential model to over-estimate the strength of the Na–O interactions, resulting in a decrease in the average Na–O distances of up to 32% in albite and 22% in sodalite. The

interaction of sodium and the aluminosilicate network in metakaolin is important in developing an understanding of geopolymers, and this deviation must be considered if this potential model is to be used.

To further investigate the suitability of this potential model, the elastic properties were calculated as before and compared to experimental values, shown in Table 3.4. The calculated elastic properties were consistently higher than the experimental values, with only the calculated shear modulus in coesite in the calculated structure lower than the experimental value. In this model, 50% of the calculated elastic properties deviated from the experimental values by 20% or greater, and the poor accuracy in the simulation of the aluminosilicate structures was also an important factor to consider.

Table 3.4: Comparison of elastic properties for structures simulated using Model 2

Structure	Bulk Modulus (GPa)			Shear Modulus (GPa)		
	Exp.	Calc.	%Diff	Exp.	Calc.	%Diff
Quartz	36.40	41.31	11.9	31.14	38.87	19.9
Stishovite	316.00	418.04	24.4	220.00	255.68	14.0
Coesite	113.70	122.73	7.4	61.60	52.89	-14.2
Cristobalite	16.40	22.83	28.2	39.10	39.92	2.1
Corundum	253.30	433.62	41.6	163.20	232.51	29.8
Kyanite	233	304.28	23.4	NA	160.95	NA
Andalusite	162.00	230.95	29.9	99.10	107.74	8.0
Sillimanite	170.80	237.17	28.0	91.50	114.28	19.9
Albite	64	94.01	31.9	41	41.47	1.1
Sodalite	52.80	123.12	57.1	NA	36.45	NA

3.3.4 Results: Model 3

The final model included in the interatomic potential tests was the model derived by Teter [247] using simultaneous fitting procedures. There were two model types available, one set of parameters using a rigid-ion approach and a second set of

parameters with the oxygen described with a shell charge model. The rigid–ion set of parameters was chosen as this would allow for greater system sizes to be simulated. This choice does, however, come with a potential sacrifice in the quality of the simulations in particular environments.

A Morse potential for the hydroxyl pairs was included based upon those of Schröder *et al.* [160]. The potential energy function consisted of a Buckingham potential coupled with electrostatics and partial charges on the ions. The parameters are given in Table A.3. The results for the structural properties before and after optimisation are given in Table 3.5.

Table 3.5: Comparison of some of the structural properties for optimised systems simulated using Model 3

Structure	Exp.	Calc.	Exp.	Calc.	Exp.	Calc.	Exp.	Calc	%Diff
	a (Å)		b (Å)		c (Å)		Volume (Å^3)		
Quartz	4.913	4.935	4.913	4.935	5.405	5.445	113.01	114.86	1.6
Stishovite	4.181	4.172	4.181	4.172	2.666	2.665	46.61	46.39	-0.5
Coesite	7.140	7.084	12.371	12.410	7.175	7.220	546.96	547.51	0.1
Cristobalite	4.972	4.944	4.972	4.944	6.922	6.706	171.01	163.90	-4.2
Gibbsite	8.684	8.941	5.078	5.109	9.736	9.949	436.62	454.45	3.9
Corundum	4.757	4.768	4.757	4.768	12.988	13.165	254.52	259.20	1.8
Kyanite	7.117	7.152	7.860	7.889	5.575	5.579	293.70	296.54	1.0
Andalusite	7.793	7.784	7.897	7.9954	5.556	5.562	341.93	344.35	0.7
Sillimanite	7.372	7.469	7.524	7.544	5.724	5.859	329.56	330.15	0.2
Anorthite	8.194	8.037	12.897	13.029	14.190	14.181	1346.52	1331.29	-1.1
Albite	8.115	7.728	12.762	12.854	7.158	7.136	659.83	637.24	-3.4
Sodalite	8.836	8.858	8.887	8.858	8.887	8.858	701.87	695.12	-1.0

This potential model performed better than the previous two models in the simulations of the structures reported here, with an increase in accuracy in the volumes for all structures calculated. No deviations of greater than 5% were noted, although the potential model did overestimate the Si–O interactions, with calculated average Si–O bond lengths of 1.59 ± 0.03 Å shorter than the experimental values of 1.62 ± 0.02 Å. To investigate the overall affects of Si–O bond length discrepancies the final energies for the SiO_2 polymorphs were compared to determine relative stabilities, with the results show in Table A.6. The energies calculated

by model 1 and 2 were also included, as well as for the Al_2SiO_5 polymorphs for comparison. The parameters for models 1 and 3 accurately predicted quartz as the most stable SiO_2 phase, and only model 3 accurately predicted andalusite as the stable Al_2SiO_5 phase. The accuracy of model 3 in predicting structural stability for both the silicon and aluminium phases consequently showed that the deviations in the bond lengths were not a major concern.

Further comparison of the three models is given in Table 3.6. In each case, the third model produced the most accurate structures, whilst the second model performed the most poorly. However, structural characteristics alone were not the only properties to be considered in the choice of potential model. The elastic properties were calculated for the final model and compared to those calculated from the previous two potential models tested.

TABLE 3.6: Averages of the absolute value for the % differences for the calculated structural properties. The total values are split into the different structural types to show the effects on the different interactions each model has.

Model	Average% Diff	Model	Average% Diff	Model	Average% Diff
Total		SiO_2		AlOH	
1	4.1 ± 2.6	1	3.9 ± 1.0	1	10.9
2	9.8 ± 6.4	2	3.1 ± 2.9	2	NA
3	1.6 ± 1.4	3	1.6 ± 1.6	3	3.9
Al_2O_3		Al_2SiO_5		Different Ions	
1	2.4	1	2.5 ± 1.2	1	4.9
2	15.1	2	11.3 ± 0.2	2	18.4 ± 2.6
3	1.8	3	0.6 ± 0.3	3	1.8 ± 1.1

Table 3.7 shows the calculated elastic properties for the simulated structures. The elastic properties were considerably more accurate using the third model, with only 9.5% of the calculated values demonstrating differences greater than 20% from the experimental values, compared to 39% and 50% for models 1 and 2 respectively. This is further confirmation that the third model is the most suitable for this research and consequently the rigid–ion interatomic potential model developed by Teter [247] is used in this research.

TABLE 3.7: Comparison of elastic properties for structures simulated using Model 3

Structure	Bulk Modulus (GPa)			Shear Modulus (GPa)		
	Exp.	Calc.	%Diff	Exp.	Calc.	%Diff
Quartz	37.80	35.16	6.98	44.30	44.81	1.14
Stishovite	316.00	345.41	8.52	220.0	210.56	4.29
Coesite	113.70	129.01	11.86	61.60	55.80	9.42
Cristobalite	16.40	12.57	23.36	39.10	38.94	0.41
Gibbsite	85.00	58.21	31.52	NA	29.01	NA
Corundum	253.50	268.61	5.63	163.20	135.84	16.76
Kyanite	233	202.22	8.60	NA	113.66	NA
Andalusite	162.00	158.68	2.05	99.10	91.83	7.33
Sillimanite	170.80	181.45	5.87	91.50	92.33	0.90
Anorthite	84.20	86.91	3.12	39.90	35.86	10.11
Albite	56.90	54.75	3.19	28.60	31.84	10.18
Sodalite	52.80	45.88	13.13	NA	24.05	NA

3.4 Atomistic Simulation of Water

The interactions between the atomic components of the aluminosilicate network and the cations of interest, Na^+, Ca^{2+} and K^+ are included in the Teter [247] interatomic potential model. The interactions between the hydroxyl groups and Al, Si and O are provided from the Schröder *et al.* [160] parameters. However, as stated in the criteria listed on page 63 the interactions of the aluminosilicate material with water must also be considered. Since none of the potential models identified include parameters for water, these interactions must be identified from the literature, as well as the water–aluminosilicate interactions.

Water molecules can form up to four hydrogen bonds with adjacent water molecules that are constantly being broken and reformed above the melting point of water [271], yet are still predominant enough to produce a short–range structure of water molecules within the liquid state. The effect of these interactions produces a network of constantly changing three–dimensional structure within the liquid of H_2O molecules tetrahedrally coordinated with each other. The existence of these hydrogen bonds results in many unusual properties of water [272–274].

For instance, one of the most well known anomalies is that the density of water increases upon freezing, resulting in ice floating on the surface of water instead of sinking. The hydrogen bonded network results in a higher density of liquid water than expected, and is also responsible for the melting and boiling points of water being higher than expected compared to the other group 6 hydrides [275].

The atypical behaviour of water has made it challenging to simulate, with a review in 2002 listing 46 distinct water models [276], with many additional models and changes to the existing models proposed since then. The majority of models are derived empirically and consist of a classical electrostatic interaction combined with a repulsive electronic contribution typically described by a Lennard–Jones two body interaction. The electrostatic charge distribution for a water molecule is generally described by point charges at each of the atomic nuclei, although some models include fictional charged sites both located within and outside of the plane of the molecule.

The different models can be broken up into groups depending on how they describe the water molecule structure, with the molecules described as rigid, flexible or polarisable. Rigid molecules have fixed O–H bond lengths and H–O–H angles, with no consideration for the vibrational aspects of the molecule. Flexible models allow the O–H bond and H–O–H angle to vibrate similarly to classical harmonic springs. Polarisable models attempt to account for the non–equivalency of water molecules in a liquid, since both rigid and flexible models have fixed charges. The polarisable models include a charged fictional particle, called a *drude* particle, or additional point charges that are assigned to account for the lone–electron pairs on the oxygen atom.

Figure 3.5 shows some of the more successful [276] water model configurations. Figures A, B and C are all planar, whilst model D has a tetrahedral configuration. Figure 3.5.A shows one of the simplest configurations and typically only involves the electrostatic contributions of the hydrogen and the oxygen atoms, coupled

with a Lennard–Jones interaction. It is used by the Single Point Charge (SPC) models, including the flexible water (SPC/Fw) [277], extended (SPC/E) [278] and heavy water (SPC/HW) [279] variations, as well as the Transferable Intermolecular Potential for 3 Points (TIP3P) [280] and its flexible variation (TIP3P/F) [277].

Figure 3.5.B includes a drude particle between the two hydrogen atoms and within the plane of the molecule, and is a typical representation of the Transferable Intermolecular Potential for 4 Points (TIP4P) [282] models including the Ewald technique (TIP4P/Ew) [283], fluctuating charge (TIP4P/FQ) [284] and ice (TIP4P/Ice) [285] variations. It is also used in several other types of polarisable models, such as the Charge on Spring (COS) [286, 287] models and the Gaussian Charged Polarisable model (GCPM) [288].

Figure 3.5 model C includes an off-site charged massless point charge opposite to the two hydrogen atoms but still within the plane of the molecule, and is typical for the Polarisable Point Charge (PPC) [289] model of water. Finally, Figure

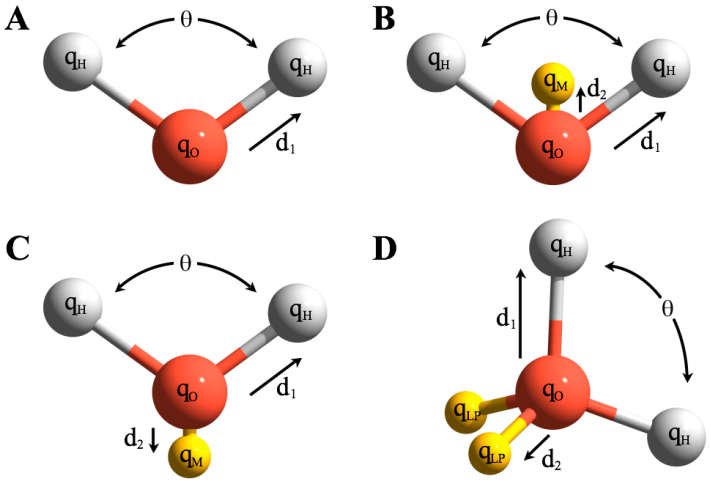

FIGURE 3.5: Different representations of a water molecule, based upon images from reference [281]. A is a typical SPC water model, B is for the TIP3P and TIP4P model, C shows the PPC model and D is the TIP5P model. The charges for the hydrogens and oxygen are given by q_H and q_O respectively, θ designates the H–O–H bond angle and is typically between 102.7° – 113.24°.
Red = oxygen, white = hydrogen and yellow = additional particles.

3.5.D is a tetrahedral representation of the water molecules and in this model the point charges represent the two lone–pair electron contributions and is typical for the Transferable Intermolecular Potential for 5 Points (TIP5P) [290] models as well as the Stillinger (ST2) [190] model.

Replicating the physical properties of a material is the key to the success of any interatomic potential model. The experimental properties of water used to determine the accuracy of a water potential model are the dipole moment, dielectric constant, self diffusion constant, average configurational energy, density maximum and the expansion coefficient. The existence of over 40 of models for water proposed in the literature [276, 291, 292] shows the difficulty in achieving this, with many models only finding success in modelling one or two of the physical properties important in simulating the structure of liquid water.

The ability to replicate the experimental O–O radial distribution function is one of the main properties that is considered important to accurately simulate, and the SPC/E, TIP4P and PPC models are reported to do this poorly [289, 293] whilst the SPC and TIP3P models show improvements. The TIP4P model underestimates the tetrahedral shape of the water molecule environment but does reproduce the correct dielectric constant [289]. An example of some of the values calculated in the literature is given in Table 3.8.

Many studies have been conducted on the accuracy and transferability of these potential models [272, 276, 298], and the validity of the predictions made by many water models have been questioned [272] so caution must be taken when applying a model in a simulation. The three–site planar models, shown by Figure 3.5 A, B and C are the simplest water models, yet despite this they reproduce the bulk properties of water relatively well (as shown by the first five models shown in Table 3.8). These models thus represent the best compromise between accuracy and computational efficiency, and as such only these models were considered.

TABLE 3.8: Comparison of experimental and calculated properties for some water models

Water Model	Diffusion Constant ($\times 10^{-5}$cm^{2}s^{-1})	Dielectric Constant	Dipole Moment	Configurational Energy (kJ mol^{-1})
Experimental [294]*	2.3	78.4	2.95	–41.5
SPC/Fw [277]	2.5	80	2.39	NA
SPC [290, 295, 296]	3.9	65	2.27	–41.0
SPC/E [289, 290]	2.5	71	2.35	–41.5
TIP3P [280, 289]	5.2	82	2.35	–41.1
TIP3P/F [277]	3.5	193	2.57	NA
TIP4P [282, 289, 290]	3.3	53	2.18	–41.8
TIP4P/Ew [283]	2.4	63	2.32	–46.5
TIP4P/FQ [284]	1.9	79	2.64	–41.4
COS/D [287]	2.5	70	2.43	–41.8
GCPM [288]	2.3	84	2.72	–44.8
PPC [289]	2.6	77	2.52	–43.2
TIP5P [290, 297]	2.6	82	2.29	–41.3

* *References indicate sources for the property values*

3.4.1 The SPC/Fw Model

The water model chosen for this research was the flexible single point charge (SPC/Fw) water model, as it gives the closest agreement with experimental data for bulk water for all non–polarisable models [296]. The parameters are given in Table A.4. The model was tested to ensure that the calculated properties in the literature [277] can be reproduced using the simulations method employed here. This was completed by simulating a three–dimensionally periodic (24.872 Å)^3 cubic box of water containing 520 water molecules. This system was equilibrated using molecular dynamics with the DL_POLY [204] package. The simulation was run under ambient conditions using the isothermal–isobaric ensemble (NPT) at 298 K and 1 atm for a period of 200 ps and a time step of 1 fs. The statistics were collected and compared to the published values for water [277].

The first stage was to ensure that the simulation methods used here reproduced the water properties from the literature for this water model. The calculated radial distribution function of the SPC/Fw water is shown in Figure 3.6 (a) and (b), with the mean square displacement function of the SPC/Fw water shown in Figure 3.6 (c). The calculated results show good agreement with the literature values. The locations of the peaks in the OW–OW RDF at $r_1 = 2.73$ Å and $r_2 = 4.45$ Å and at $r_1 = 1.73$ Å and $r_2 = 3.27$ Å in the OW–HW RDF are similar to those calculated by Wu *et al.* [277]. The self–diffusion constant, D, calculated from the gradient of the line of best fit is 2.50×10^{-5} cm^{2}s^{-1}, which is in good agreement with the value of 2.49×10^{-5} cm^{2}s^{-1} calculated using these parameters [277] and the experimental value of 2.30×10^{-5} cm^{2}s^{-1}. The calculated average density is 1.02 g cm^{-3}, which is also in good agreement with published values.

3.4.2 Hydrated Aluminosilicates

The incorporation and interaction of water with silicates and aluminosilicate materials is important in the understanding of many materials; from the swelling of clays and clay minerals, to the development of zeolitic filters and sieves. Initial studies on water–aluminosilicate interactions dealt with hydrated aluminosilicates such as clays where the water molecules were located within the bulk of the structure. Initially the structures were kept rigid and the Matsuoka, Clementi and Yoshimine (MCY) water model [299] (developed using *ab initio* QM methods) was used in Monte Carlo simulations of the water-clay interface [300, 301]. However, a consistent description of water interactions in the bulk and at the surfaces required the clay models to be flexible. This led to a movement towards atomistic MD methods for the simulation of hydrated clays and the TIP3P and SPC type models were employed for these simulations.

Several potential models to describe the clay interactions prior to hydration were proposed that allowed for flexible clay structures [232, 248, 254, 302–305] with

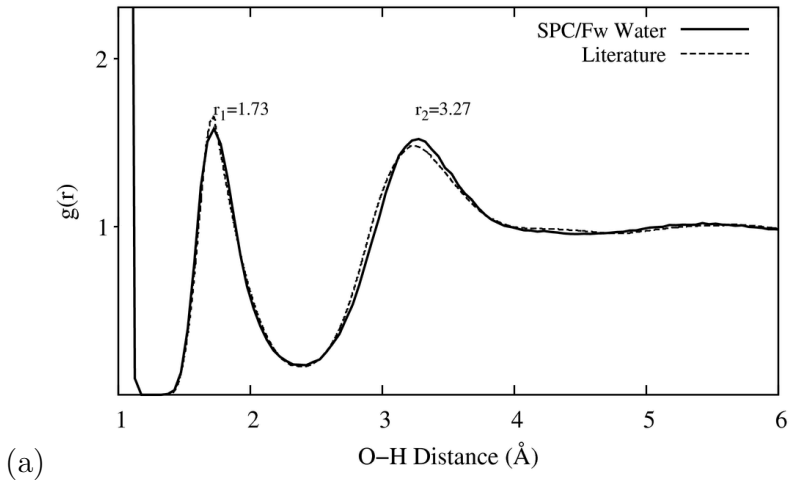

(a)

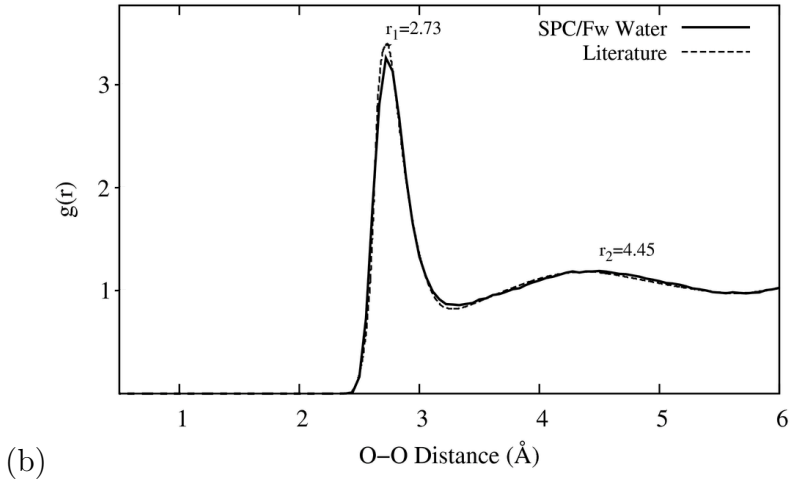

(b)

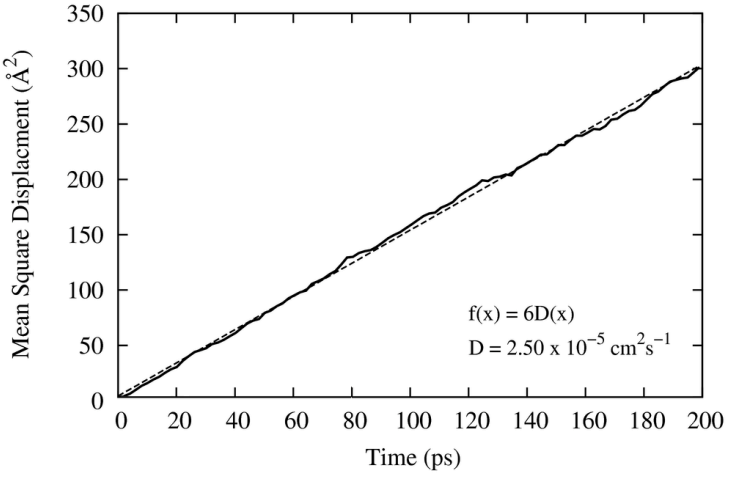

(c)

FIGURE 3.6: Statistics for the SPC/Fw model compared to experiment[277] (a) The RDF of all interactions and the (b) RDF of only OW–OW interactions with the peak of the first and second hydration shells given by r_1 and r_2. (c) The MSD for the OW–OW interactions (solid line), the dashed line is the line of best fit and is used to calculate the self–diffusion constant, D.

energy contributions included for two and three body terms. Simulations with bigger atomic systems and longer simulation periods moved towards more generalised models [133, 306] that did not include the three–body or higher terms. The introduction of the water models to the clay parameters required that the description of the water be relative simple, and so the 3–point planar water models such as the SPC and TIP3P models and their variations were most appropriate. In particular, the SPC and SPC/E models have been used to investigate the dynamics at many clay–water interfaces [16, 134, 135, 307] and the interatomic potential model developed by Cygan *et al.* [133] specifically for clay minerals also uses the single point charge model.

The interatomic potential model developed by Teter [247] was determined to be the most accurate to describe the interactions in the aluminosilicate materials in this research. The rigid-ion parameters did not, however, include parameters for the aluminosilicate-water interactions, and consequently needed to be determined. This was achieved by identifying a set of parameters for the Al,Si,O – H_2O interactions from the literature and fitting the parameters to the new partial charges.

Water–Aluminosilicate Parameters

The simulations of disordered aluminosilicate surfaces in the presence of water in Chapter 6 required the inclusion of robust cation-water interactions, similar to those involved in confined geometries such as in hydrated zeolite phases [308, 309] and the swelling and de–hydration of clay minerals [310]. The behaviour of water in these environments has been the topic of much discussion. Since the publication of the Cygan *et al.* [139] interatomic potential model it is difficult to find atomistic simulations of clay minerals that do not use the proposed model. However, there are two types of aluminium – water parameters defined in this model for the difference coordinations of Al, whilst the Teter [247] parameters only have a

single Al atom type. The final potential model chosen will thus need to have the Al,Si–H_2O interactions fitted from sources other than those by Cygan *et al.* [133].

A review on the simulation of water in nanoporous aluminosilicates [311] outlined the success of the SPC/E and SPC/Fw models [311] using clay parameters from Smith [312] that were modifications of those used by Skipper *et al.* [301, 313] to simulate montmorillonite. The SPC/E model has also recently been successful used by Chanajaree *et al.* [314] with clay parameters from Demontis *et al.* [315] to simulate the water dynamics in the pores of the zeolite chabazite. The parameters used by Chanajaree *et al.* [314] and Smith [312] both have partial charges on the aluminosilicate species, but these charges differ from those used by the Teter [247] model. Similar to the parameters by Cygan *et al.* [133], the parameters used by Smith [312] require the aluminium to be labeled as either tetrahedral or octahedral, and so the Chanajaree *et al.* [314] parameters are used in the scaling and fitting procedure instead.

The two–body potentials used by Chanajaree *et al.* [314] (see Table A.5) for the water–cation interactions are described by a Lennard–Jones potential with the initial charges for the Al, Si and the structural O set to +1.75, +2.05 and −1.20 respectively. The charge on the structural oxygen of −1.20 is the same in the Teter potential model, and thus does not require adjusting, however, the Teter model describes the Al as +1.80 and the Si as +2.40, and thus the interactions must be adjusted to the new charges. This is achieved by fitting the total energy function used by Chanajaree *et al.* to a composite function, given in equation (3.1), using the Teter partial charges and by adjusting the A, ρ and new σ parameters to produce the best fit.

$$U_{ij}^{\text{Total}} = A \exp\left(-\frac{r_{ij}}{\rho}\right) + \left(\frac{\sigma}{r_{ij}}\right)^{12} + \frac{1}{4\pi\varepsilon_0}\frac{q_i q_j}{r_{ij}} \tag{3.1}$$

The final Al–OW and Si–OW parameters before and after fitting are given in

Table 3.9, and an example of the results from the fitting procedure for the Si–OW interaction is shown in Figure 3.7.

TABLE 3.9: The original and fitted Al,Si–OW parameters for the water interactions with the aluminosilicate structures.

Atomic Pair		q_i	q_{j1}	q_{j2}	ε_i (eV)	σ_i (Å)	A (eV)	ρ (Å)	σ (Å)
OW	Al	–0.82	1.75	1.8	0.5315×10^{-2}	1.6926	0.5883	2.7561	1.225
OW	Si	–0.82	2.05	2.4	0.8066×10^{-2}	1.6213	4.7788	2.5235	1.223

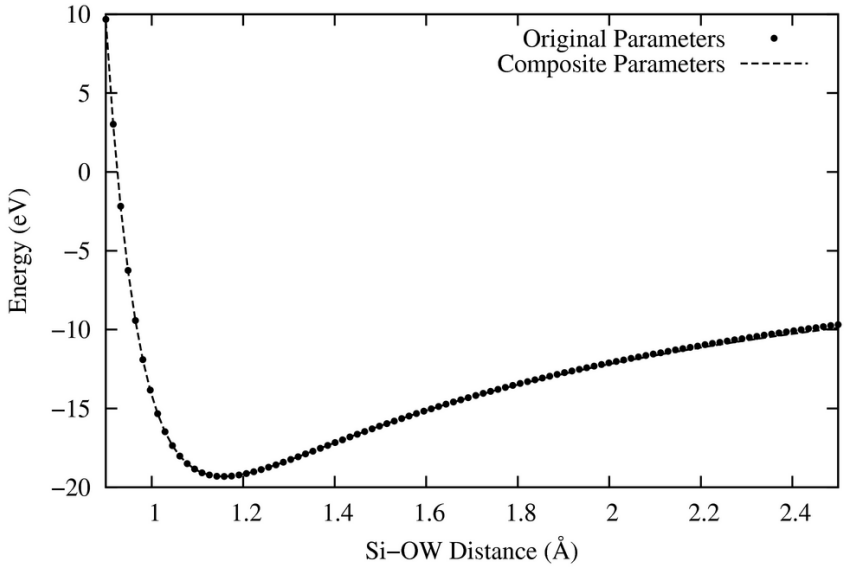

FIGURE 3.7: The total potential energy calculated using the Si–OW parameters and charges from Chanajaree *et al.* model [314] and the new fitted composite potential parameters with the Teter [247] partial charges. The fitted parameters agree well with the existing ones, with an asymptotic standard error of 0.11%.

The new parameters require further verification to ensure the interactions of structural water in an aluminosilicate material are described accurately. To test the new parameters a similar approach was undertaken as previously, where well characterised crystalline material are optimised using the parameters, and the results are compared to the experimental values. Natrolite ($Na_2Al_2Si_3O_{10}.2H_2O$) and lawsonite ($CaAl_2Si_2O_7(OH)_2.H_2O$) are chosen as suitable hydrated structures. These structures include calcium and sodium ions into the structure, and thus

TABLE 3.10: The original and fitted Ca,Na–OW parameters

Atom 1	Atom 2	q_1	q_{2i}	q_{2f}	A_i (eV)	A_f (eV)
Ca	OW	1.20	-1.20	-0.82	7385.3075	7095.4563
Na	OW	0.60	-1.20	-0.82	2755.0323	2616.2137

for this verification step the water–ion parameters are also fitted by adjusting the A parameter in the Buckingham potentials in the Teter model. The results are given in Table 3.10. The interactions for the hydroxyl oxygen are assumed to be the same as the structural oxygen–water oxygen interaction.

Using the new parameters the structures were optimised using GULP with the final structure compared to experiment [270, 316, 317]. The results for both the structural and elastic properties are given in Table 3.11. The new parameters accurately reproduce both the natrolite and lawsonite structures, with all calculated values for the cell parameters within 2% and the bulk modulus for both structures

TABLE 3.11: The structure of natrolite and lawsonite with the corresponding calculated properties compared with experimental data from references [270, 316, 317]. BM = Bulk modulus, SM = Shear modulus.

Structure	Parameter	Exp.	Calc.	% Diff.
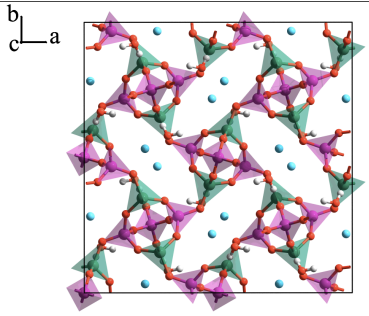	Natrolite			
	a (Å)	18.326	18.312	-0.8
	b (Å)	18.652	18.397	-1.4
	c (Å)	6.601	6.615	0.22
	Volume (Å^3)	2256.33	2228.74	-1.2
	BM (GPa)	48.9	46.4	-5.1
	SM (GPa)	27.4	21.6	-21.2
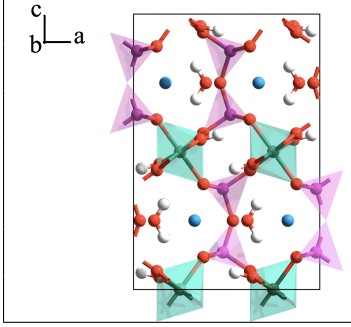	Lawsonite			
	a (Å)	8.795	8.987	2.0
	b (Å)	5.847	5.784	-1.1
	c (Å)	13.142	12.929	-1.6
	Volume (Å^3)	675.82	671.82	-0.6
	BM (GPa)	125	117.8	-5.76
	SM (GPa)	52	67.6	23.1

within 6% of the experimental parameters. Thus it is concluded that the combination of the fitted cation–SPC/Fw potential parameters for the Al,Si,O–H_2O interactions are suitable for the purposes of this research.

3.5 Final Interatomic Potential Parameters

The investigation of a suitable set of potential model parameters to simulate all the interactions listed on page 63 has been conducted successfully with the resulting interatomic potential parameters taken from the following sources:

- M–O (M=Al, Si, Na, Ca, K) parameters from Teter [247]
- OH and M–OH (M=Al, Si) parameters from Schröder *et al.* [160]
- H_2O parameters using the SPC/Fw model [277]
- H_2O–Al,Si,O parameters fitted from Chanajare *et al.* [314]

The combination of these parameters results in a total interatomic potential model that can describe the range of interactions required for this research. The different structural components with all necessary parameters for each ion type and interaction that have been investigated are given in Table 3.12 and is referred to as the Teter–SPC/Fw model for the purposes of this research.

The investigations of the different interactions showed good agreement with experimental values across all structures and properties tested, however, the Si–O interatomic distances in the aluminosilicate structures were under-estimated by up to 1.9%, the electrostatic repulsion between the water and the partially charged calcium ion was under-estimated by up to 1.1%, and the sodium water interaction was over-estimated by up to 10.1%. It was not anticipated that these discrepancies would produce significant effects in the simulations undertaken in this research, and it was with confidence that this interatomic potential model was proposed for use in the simulation of metakaolin and the interactions with water and the cations sodium, potassium and calcium.

TABLE 3.12: The final potential parameters used in this research.

Atom and Label	Charge	Atom and Label	Charge
Aluminium (Al)	1.80	Calcium (Ca)	1.20
Silicon (Si)	2.40	Sodium (Na)	0.60
Structural Oxygen (O1)	–1.20	Potassium (K)	0.60
Hydroxyl Oxygen (O2)	–0.856	Water Oxygen (O3)	–0.82
Hydroxyl Hydrogen (H2)	0.256	Water Hydrogen (H3)	0.41
2–Body Buckingham potential parameters			
Atomic Pair	A (eV)	ρ (Å)	C (eV Å^6)
Al – O1	12201.417	0.195628	31.997
Al – O2	9701.4170	0.195628	31.997
Si – O1	13702.905	0.193817	54.681
Si – O2	12433.827	0.193817	54.681
Na – O1	2755.0323	0.258583	33.831
Na – O2	2629.3649	0.258583	33.831
Na – O3	2616.2137	0.258583	33.831
Ca – O1	7385.3075	0.255185	100.26
Ca – O2	7122.9160	0.255185	100.26
Ca – O3	7095.4563	0.255185	100.26
K – O1	20510.758	0.233726	51.490
K – O2	20333.1961	0.233726	51.490
K – O3	20315.2109	0.233726	51.490
O1 – O1,2	1844.7548	0.343645	192.58
O1,2 – H2,3	100.0	0.250	0.0
Morse potential parameters			
Atomic Pair	D_e (eV)	α (Å^{-1})	r_0 (Å)
O2 – H2	7.0525	1.800	0.94850
Bond–Stretching potential parameters			
Atomic Pair		k_2 (eV/ Å^2)	r_0 (Å)
O3 – H3		45.93	1.012
2–Body Lennard–Jones potential parameters			
Atomic Pair		ε (eV)	σ (Å)
O1,2 – O3		0.24309×10^{-1}	2.4952
O3 – O3		0.67348×10^{-2}	3.1690
Angle–Bending potential parameters			
Dihedral group		A (eV/rad^2)	θ_o (°)
H3 – O3 – H3		3.29136	113.24
2–Body Composite potential parameters			
Atomic Pair	A (eV)	ρ (Å)	σ (Å)
Al – O3	0.5883	2.7561	1.225
Si – O3	4.7788	2.5235	1.223

3.6 Summary

An investigation into some of the available interatomic potential models from the literature was presented, with three main interatomic potential models identified as suitable to simulate the structural components expected to be required. The models were tested by simulating a variety of different structures demonstrating different characteristics. The influence of different coordination environments, the presence of hydroxyls, cations and water molecules were tested using the potential model parameters and the results compared with experimental data, with the rigid–ion model proposed by Teter [247] producing the most accurate results. The model was then further parameterised to include interactions with water to simulate an aqueous environment. The SPC/Fw model was chosen for this purpose and molecular dynamics simulations using this model reproduced the properties of liquid water within reasonable agreement with the literature. The inclusion of additional Al,Si,O–H_2O parameters were investigated and the resulting parameters performed well when tested in the simulation of the hydrated minerals, natrolite and lawsonite. The resulting potential model is thus used for all simulations reported in this research.

Note

Parts of this chapter are discussed in the paper "Dehydroxylation of kaolinite to metakaolin – A Molecular Dynamics Study", by S. Sperinck, P. Raiteri, N. Marks and K. Wright, published in *Journal of Materials Chemistry* 2011, 21(7), pages 2188 – 2125.

Chapter 4

Modelling Metakaolin

Metakaolin is a semi-amorphous aluminosilicate material widely used in the food-processing industry, oil shale processing, in ceramics and as a pozzolanic material. It is also the focus of research into the fundamental structure and properties of geopolymers. The atomic structure of metakaolin, like geopolymers, is not well understood and this chapter investigates the structure of metakaolin through the thermal de-hydroxylation of kaolinite through the use of classical molecular dynamics simulation techniques in combination with the interatomic potential model from Chapter 3.

4.1 Introduction

Metakaolin is formed through the calcination process of the clay mineral kaolinite, which is the most important of the kaolin group of minerals. These layered aluminosilicates belong to the clay group of materials called phyllosilicates and are composed of a sheet of vertex sharing SiO_4 tetrahedra forming six-membered silicate rings that are linked by common oxygen atoms parallel to the c-axis to a sheet of edge-sharing AlO_6 octahedra forming four-membered aluminate rings. The silicate and aluminate layers are connected by weak hydrogen bonds, with the inter-layer space a characteristic feature of clay minerals. Figure 4.1 shows an idealised structure of kaolinite, although disorder is common in the kaolin minerals.

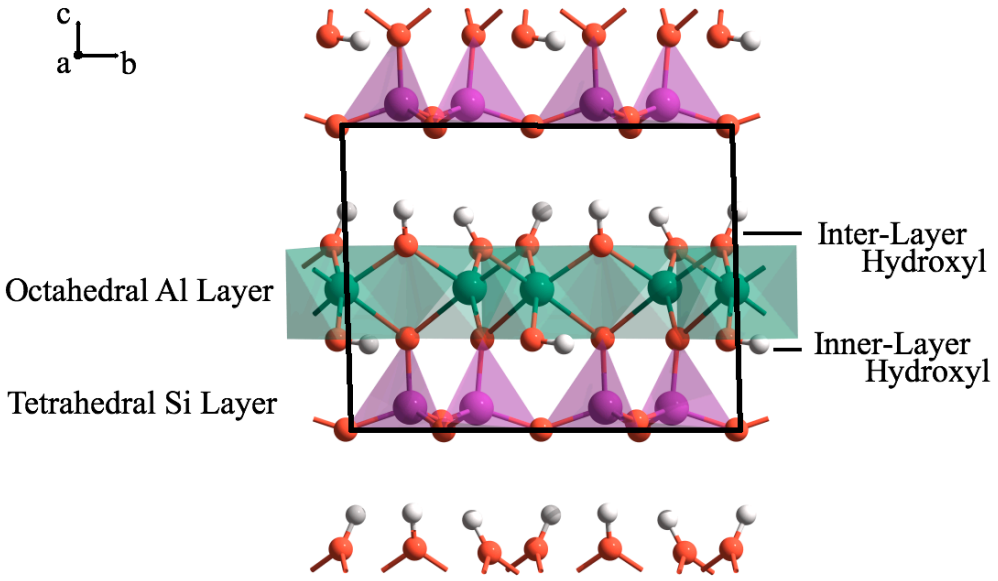

FIGURE 4.1: Ideal layered structure of kaolinite, showing the kaolinite unit cell: aluminium (green), silicon (purple), oxygen (red) and hydrogen (white). The locations of the inter- and inner-layer hydroxyls are shown for clarity.

The thermally induced structural transformations of kaolinite are completely governed by the de-hydroxylation of the structure. The calcination of kaolinite has three main thermally induced stages; the first is the endothermic de-hydroxylation to the metastable metakaolin phase that occurs in the temperature range of 450 °C to 700 °C according to the following reaction:

$$Al_4[Si_4O_10](OH)_8 \overset{\Delta T}{\rightarrow} 2Al_2Si_2O_7 + 4H_2O \tag{4.1}$$

Cubic spinel and amorphous silica are produced in the range of 700 °C to 950 °C and the thermodynamically stable mullite phase forms in an exothermic reaction over 1100 °C with crystallisation of cristobalite from the amorphous silica phase proceeding beyond that [318]. Whilst the high temperature phases have been the focus of much interest [104, 105, 319–321], the metastate is often overlooked due to its non-crystalline nature, and conclusive structural information is limited.

In 1959 Brindley and Nakahira [106] suggested a set of criteria that any proposed metakaolin structure should adhere to. The criteria state that:

- Metakaolin should demonstrate lattice parameters that are similar to kaolinite, but that c-axis periodicity must disappear.
- The octahedral Al-O(OH) layer accommodates the majority of the structural reorganisation compared to the silicon layer.
- The inter-layer spacing decreases from 3.8 Å to 3.3 Å.

The distances measured were between the oxygen atoms in adjacent layers, as the experimental method of x-ray diffraction did not allow for the calculation of the hydrogen positions at the time.

In 2010 the simulation of the structure of metakaolin was reported using DFT computational simulation techniques by White *et al.* [118, 119]. The proposed metakaolin structure was obtained by the gradual removal of hydroxyls from a kaolinite system, performing geometry optimisations after each removal. The kaolinite unit cell was constructed using structural information from simulations of kaolinite [322] based upon experimental values from Bish [323]. A $2 \times 2 \times 2$ supercell (272 atoms) was used and the rate of water molecules removed was varied to simulate the experimental increase in rate of de-hydroxylation. A total of 13 de-hydroxylation steps were simulated, to a final structure with a total loss of 87.5% of hydroxyl groups.

The resulting structure is illustrated in Figure 4.2 and shows that the octahedral layer undergoes large structural changes through the loss of the water and that this contributes to a loss in the crystalline structure. The conclusions from the simulations provide a quantitative analysis of the change in the coordination of the aluminium within the structure. The aluminium in 6-fold coordination gradually decreases from 100% to 0%, with the development of 4-fold aluminium starting

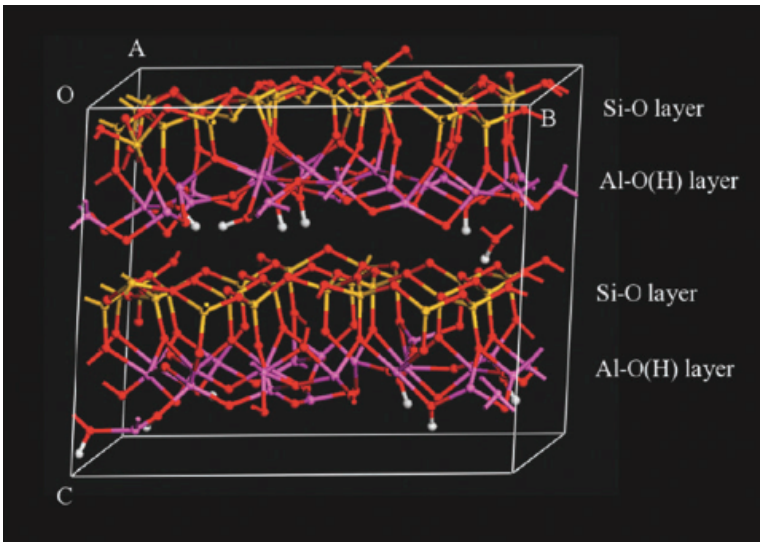

FIGURE 4.2: The final metakaolin structure viewed along the *a*-axis, taken from the DFT simulation by White *et al.* [118]. The break down in periodicity is noted as due to the buckling of the layers.

in the second step and continuing to a maximum of 80% and then dropping to a final value of 65%. A considerable proportion of 5-fold aluminium is shown to occur in the latter stages of the process, culminating in a final structure with 30% 5-fold coordinated aluminium. The authors also report the presence of a small percentage (approximately 2%) of 3-fold aluminium in the structure.

The simulations of White *et al.* [118] provide important clues to the development of metakaolin, although is limited in terms of the size of the simulation cell. This chapter aims to provide complimentary insights into the formation of metakaolin on a larger scale and in a dynamic environment, allowing for the effects of temperature and pressure over a period of time to be included in the simulation. The main focus is to determine the structure of metakaolin and to investigate the atomic mechanisms underpinning the loss of crystallinity and the transformation. By studying the thermal transformation of kaolinite to metakaolin, the mechanisms underpinning the collapse of the inter-layer space and subsequent structural changes can be investigated. The ultimate purpose of this is to provide a suitable structure of metakaolin for further investigations into geopolymers.

4.2 Simulation of Kaolinite

Prior to simulation of the de-hydroxylation of kaolinite to metakaolin, the starting structure for the kaolinite needs to be determined. The atomic coordinates for the periodic structure of kaolinite were generated on the basis of crystal structure refinement data determined from diffraction studies performed at 1.5 K with well-characterised hydrogen position information [323]. This structure was then optimised in GULP using the potential model parameters determined in Chapter 3 for aluminosilicates with hydroxyl groups. This produced the unit cell shown in Figure 4.1, which has the *C1* symmetry as expected. A comparison of the calculated structural properties is shown in Table 4.1, with experimental values for the cell parameters taken from reference [270] and elastic properties from reference [324].

Table 4.1: Comparison of the bulk properties of kaolinite.

Parameter	Experimental	Calculated	% Difference
a (Å)	5.1535	5.2108	1.07
b (Å)	8.9419	9.0496	1.27
c (Å)	7.3906	7.2961	-1.26
α (°)	91.926	93.096	1.27
β (°)	105.056	105.410	0.35
γ (°)	89.797	89.797	0.00
Volume (Å^3)	328.71	331.31	0.79
Shear Modulus (GPa)	31.8	30.7	-3.5
Bulk Modulus (GPa)	55.5	75.2	26.2

The structural properties are accurate, with all variations in the simulated parameters below 1.5%. The calculated bond lengths and angles of the optimised structure corresponded to the experimental ones in all cases. Whilst the shear modulus is accurate, the bulk modulus is over-estimated in the simulation by 26.2%, however, as stated in Mondol *et al.* [325] the elastic properties of minerals such as kaolinite are difficult to determine experimentally due the presence of inter-layer water and other impurities present within the structures, and so this

large deviation from the experimental value is not a cause for concern. The final structure also agrees well with the simulated kaolinite structure used by White *et al.* [322], and thus the structure of kaolinite simulated using the Teter [247] potential parameters combined with the hydroxyl parameters from Schröder *et al.* [160] is suitable for use in the investigation of the structure of metakaolin.

4.3 Computational De-hydroxylation Process

A periodic $7 \times 4 \times 5$ supercell (4670 atoms) was constructed from the optimised kaolinite unit-cell parameters to allow for an approximately cubic structure with dimensions ($36.47 \times 36.20 \times 36.48$) Å. The size of the cell was necessary to due to the implementation of the minimum image convention used in the DL_POLY simulation package for a potential model cut-off of 15 Å. This resulted in a structure that was 16 times larger than that used in the previous DFT simulations [119], thus allowing for the long-range changes to be modelled.

The loss of water in the calcination of kaolinite occurs through a range of temperatures, however, the exact rates of water loss per temperature step are unknown. For the purposes of this research it was determined that the introduction of additional variables into the simulation would be undesirable. As a consequence, the removal of hydroxyl groups from the structure was completed manually at a constant rate of a certain percentage of hydroxyl groups per 1000 ps at a constant temperature of 1000 K (≈ 700 °C).

To simulate the de-hydroxylation process, the kaolinite supercell was simulated at 1000 K and run at temperature over the necessary time period to equilibrate the structure. At the end of the high temperature run the system was checked for complete equilibration by assessing whether the change in the average energy over a period of 150 ps varied appreciably or not. An example of the typical potential energy vs. time plot for a simulation used in this research is shown in Figure 4.3.

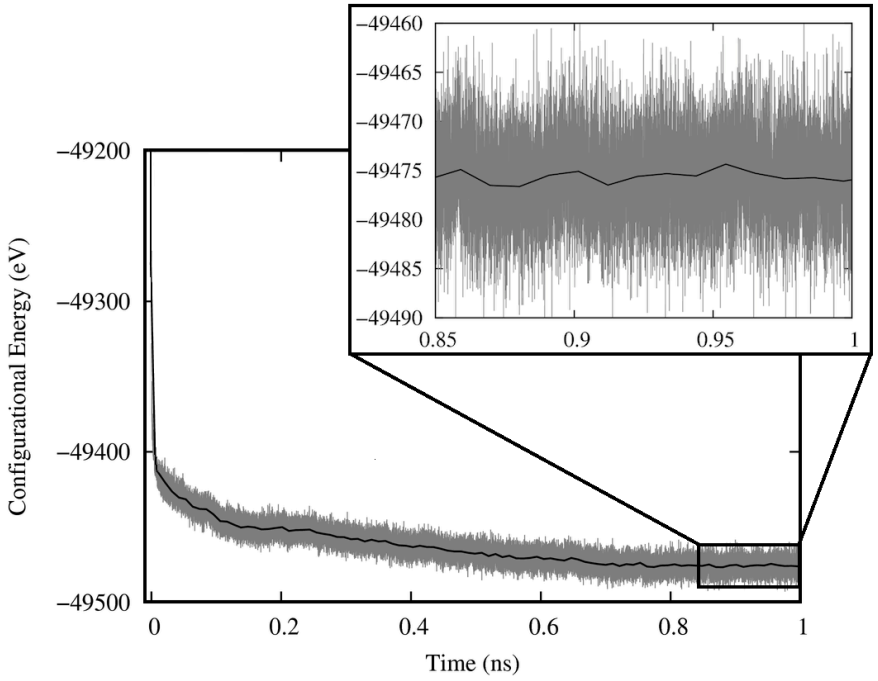

FIGURE 4.3: A typical energy vs. time plot for a partially de-hydroxylated structure. The darker line shows the average potential energy (calculated over 10 ps periods). The inset shows the energy stabilising in the final 150 ps of the simulation, with variations of less than 2 eV observed in the fluctuations of the average energy.

This process was repeated a total of 10 times to produce 10 kaolinite structures at 1000 K. The increase in the number of configurations sampled was necessary to provide statistical relevance to the data and conclusions reported herein.

The interatomic potential model did not allow for chemical reactions involving bond dissociation and formation, thus the liberation of a H_2O molecule was simulated manually. According to the model, the structural oxygen atoms are designated as O1, the hydroxyl oxygen atoms as O2 and the hydrogen atoms as H. The removal of an H_2O unit was achieved by deleting a complete hydroxyl group (O2-H), plus a H from a second hydroxyl group. The remaining O from the second group was then labeled O1 to maintain charge neutrality. This is summarised by the following equation:

$$(\text{O2–H}) + (\text{O2–H}) \xrightarrow{-2H-O2} \text{O2} \rightarrow \text{O1} \tag{4.2}$$

Although an actual H_2O molecule was not involved in these simulations, this study refers to the removed atoms collectively as H_2O. Ignoring the water molecule in the simulations is justified by kinetic studies by Bellotto *et al.* [114] on the kaolinite-mullite reaction sequence showing that the de-hydroxylation reaction of kaolinite is not controlled by the physical diffusion of water vapour.

The required amount of H_2O was removed to simulate the de-hydroxylation of the structure, and the structures were then re-equilibrated at 1000 K to allow for the structural reorganisation facilitated by the loss of the hydroxyl groups. There were two main concerns that needed to be investigated in the de-hydroxylation process. The first was the relative locations of the pairs of hydroxyl groups removed to simulate the liberation of water, as no information was available on whether or not this influenced the structural formation.

Verification: Choice of Hydroxyl Groups Removed

The choice of hydroxyl locations to be removed was varied to ensure that it did not impact the final structure obtained. The full 4670 atom system was not required for these simulations, so smaller $2 \times 2 \times 2$ kaolinite supercells were constructed (272 atoms) to reduce computational cost. In these tests a single H_2O molecule was removed by choosing hydroxyl pairs that represented the three different configurations of hydroxyl that may occur during the process: adjacent inter-layer, separated, and intra-layer. This structure was then optimised in GULP and the final energy of the structure compared to that of the original cell prior to optimisation. This change in energy is a measure of structural relaxation on creation of these defects and is shown in the Table in Figure 4.4.

The differences between the energy show that less energy was required relax the structure on removal of H_2O groups from nearest neighbour hydroxyl pairs than

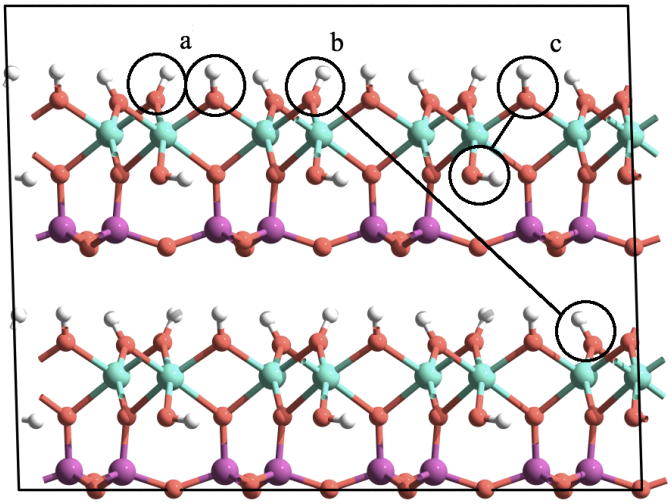

Situation	Separation Distance (Å)	ΔE (eV)
a	2.83	4.524
b	11.36	5.373
c	2.89	4.522

FIGURE 4.4: The three main hydroxyl pairs that can be removed to simulate the liberation of one H_2O molecules are shown: a) two neighbouring inter-layer groups, b) two inter-layer groups located far apart and c) an inner-layer and a neighbouring inter-layer group. The interatomic distances between the oxygen atoms for each pair are shown.

from pairs that were far apart. The calculations show almost no (0.002 eV) difference in energy between configurations (a) and (c). However, the difference between nearest pairs and pairs with greater separation was higher by up to 0.85 eV in comparison, and so some preference for the nearest-neighbour pairs must be made in the simulations. The average distances between nearest neighbour pairs in kaolinite (including both the inter- and inner-layer hydroxyls) is 3.09 ± 0.32Å, so a cut-off distance of 3.50 Å was designated to ensure only nearest neighbours were considered during first few steps of the de-hydroxylation process. Once the de-hydroxylation process progressed beyond 70%, this cut-off was removed as the occurrence of neighbouring hydroxyl groups within the cut-off distance set became negligible and pairs located further apart needed consideration.

Verification of Computational Approach I: De-hydroxylation Rate

The second factor in the de-hydroxylation approach that needed to be investigated was the influence of de-hydroxylation rate on the final structure. There is no evidence, either from experiment or from simulation, that the formation of metakaolin is dependent on the *gradual* loss of water from the structure. Although the calcination of kaolinite to form the high temperature phases is generally described as a function of increasing temperature [106, 326–328], the rate of temperature increase on the structure has not been investigated experimentally. It was decided to test for any such dependence by removing all the hydroxyl groups from kaolinite in a single step and then to allow the structure to equilibrate.

The 10 kaolinite simulation cells (4760 atoms each) equilibrated at 1000 K contained 1120 hydroxyl groups, or 560 potential H_2O groups. The single-step approach removed all 560 H_2O groups from the structure and then allowed the structure to equilibrate at 1000 K. The time to equilibrate was approximately 1500 ps. The final structures were then rapidly cooled to 300 K to remove thermal noise and statistics were collected. The de-hydroxylation process was continued beyond the experimental threshold of 12% residual water, to a 100% de-hydroxylated structure.

The single-step approach was then compared to a gradual de-hydroxylation process. To remove each possible H_2O group individually would have resulted in the total resources required for these simulations to become excessively high. As a consequence a rate of the gradual approach was set to 10% of the hydroxyl groups (or 56 H_2O molecules) removed from the structure per de-hydroxylation step. The groups were selected randomly from the heated kaolinite structure based upon the cut-off distances set by the hydroxyl group location tests performed previously. The structures were then allowed to equilibrate at 1000 K. At each step a further 10% of the hydroxyl groups were removed randomly, and the system again allowed to equilibrate at 1000 K, with each removal step requiring

approximately 800 ps to 1200 ps to equilibrate. Once all the water had been removed, the structures were then also cooled to 300 K and statistics collected for comparison. The averages of the results for the structures simulated with the complete and gradual hydroxyl loss are shown in Table 4.2.

TABLE 4.2: Comparison of the cell parameters for the final structure from the single-step and gradual de-hydroxylation approaches with the initial kaolinite supercell. All statistics gathered from structures at 300 K.

Parameter	Initial	Single	% Diff	Gradual	% Diff
a (Å)	36.5	32.6 ± 0.3	-10.7	32.6 ± 0.3	-10.7
b (Å)	36.2	33.5 ± 0.1	-7.5	32.0 ± 0.3	-11.6
c (Å)	36.5	35.6 ± 0.3	-2.5	38.0 ± 0.4	3.9
α (°)	93.1	93.7 ± 1.6	0.6	88.5 ± 1.4	-4.9
β (°)	105.4	107.5 ± 2.0	2.0	109.8 ± 1.1	4.0
γ (°)	89.8	88.4 ± 1.1	-1.6	90.0 ± 0.9	0.2
Volume Å^3	46411	36559 ± 261	-21.2	37333 ± 244	-19.6

Both approaches produce similar results, however, there is a more pronounced shift in the cell parameters from the gradual approach as compared to the initial kaolinite structure. The volume decrease in the gradual procedure of 19.6% is less than the single-step approach with 21.2%, with both approaches producing slight shifts in the cell parameters. The *a*-, *b*- and β parameters all show similar trends of either increasing or decreasing values compared to the initial structure regardless of the removal process. One notable difference is the *c*-parameter, which increases by 3.9% in the gradual approach compared to a decrease of 2.5% in the single-step simulations.

The similarities between the two final structures confirms that the rate of de-hydroxylation is not an important factor in the development of the metakaolin structure. However, whilst the single-step approach uses less computational resources to produce the final structure, the process of structural reorganisation is also of interest and thus the gradual de-hydroxylation procedure is chosen for the purposes of this investigation.

4.4 Thermal De-hydroxylation of Kaolinite

The results from the gradual de-hydroxylation calculations are discussed here in greater detail. The molecular dynamics simulation of kaolinite to metakaolin was conducted in DL_POLY using the gradual step-wise approach, at a temperature of 1000 K and 1 atm, using the NσT ensemble with a Berendsen thermostat employed with 0.1 ps and 1.0 ps as the thermostat and barostat relaxation times respectively. The process was repeated for all 10 kaolinite structures equilibrated at 1000 K with a random number generator employed to ensure the choice of hydroxyl groups used to make up the H_2O removed was completely random. Whilst the final atomic positions in each of the structures simulated differed, the same trends and observations were made in all 10 simulations. The results reported here give the averages for all the de-hydroxylation simulations, unless otherwise specified.

Depending on the locations of the hydroxyl groups removed, the length of time for the system to equilibrate varied, although there was no observed correlation between de-hydroxylation step and time taken to equilibrate. Once 100% de-hydroxylation was achieved, the final configuration in each step was rapidly cooled to 300 K over a period of 50 ps to remove the effects of thermal vibration from the statistics. The NσT ensemble used in the simulations allowed for flexible simulation cell parameters, and the average cell parameters for each structure through the de-hydroxylation process are shown in Figure 4.5.

The changes in the cell parameters show that the removal of hydroxyls from the structure had little effect on the lattice up to 40% de-hydroxylation. As more hydroxyl groups were removed, the simulation cell decreased in size, as both the a and c parameters decreased by up to 12.3%. The β parameter decreased by up to 5°, whilst the α and γ parameters remained approximately constant. The c parameter in kaolinite at 300 K is 36.5 Å, whilst at 1000 K it increases

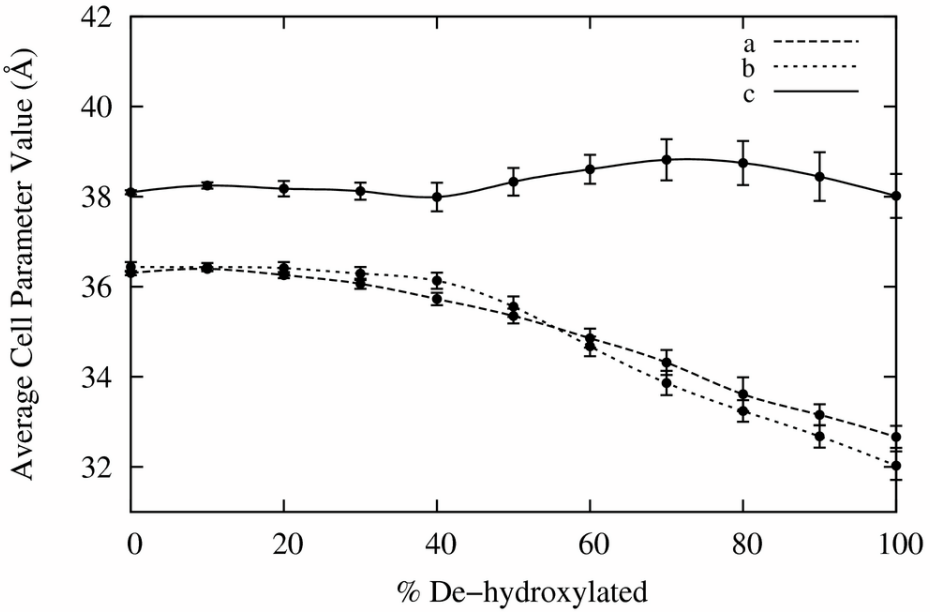

(a)

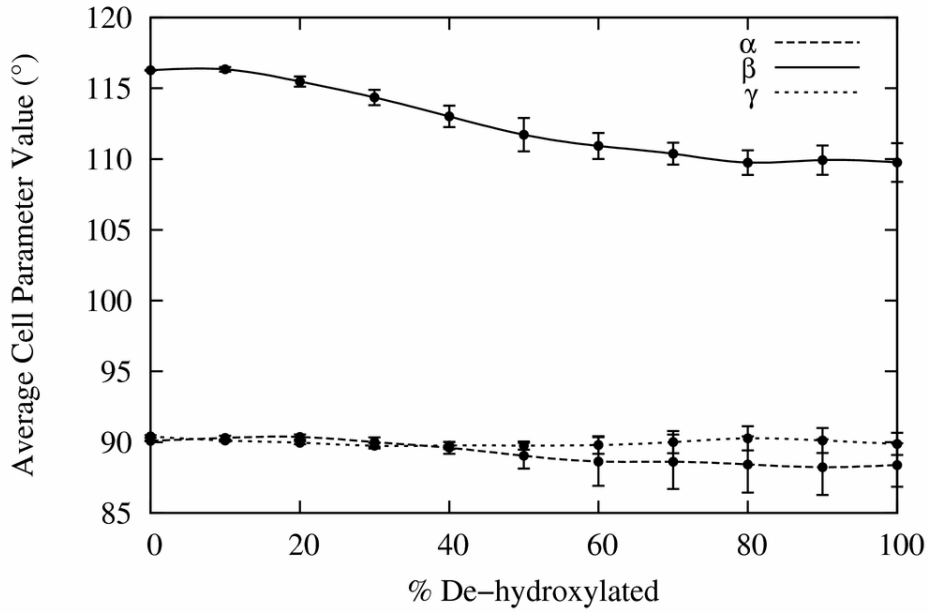

(b)

FIGURE 4.5: The changes in the cell parameters of the structure through the de-hydroxylation process, with the standard deviations shown as error bars.

to 38.0 Å, and during the simulation it briefly increases and then returns to approximately the same value initial value of 38.0 Å. This would suggest that heating the kaolinite is an important factor in the formation of metakaolin, and is thus necessary to accurately simulate the process.

The final structures generated from one of the de-hydroxylation simulations are shown in Figure 4.6. It is evident that as the simulation proceeds the inter-layer spaces partially collapse, although the 1:1 Al:Si layering is preserved. In the initial stages of the de-hydroxylation, the vacancies produced by the loss of hydroxyls from the structure create large distortions in the layers. These distortions are the result of the localised migration of the silicon and aluminium ions into the inter-layer spaces, creating bridges between the layers. These bridges anchor the layers, thus constraining the inter-layer space and halting any major changes that may have occurred otherwise.

Compared to the aluminium layers, all silicon bridging is facilitated by smaller distortions in the local environment and is much less pronounced, with no migration further than the initial move into the inter-layer space evident. A bridge caused by the migration of an aluminium ion produced the most prominent effect and is caused by neighbouring pairs of inter-layer hydroxyl groups being removed i.e. two sets of adjacent hydroxyl groups reacting to form two waters and two residual oxygen atoms. The removal of inner-layer hydroxyl groups compared to inter-layer groups also has a large effect on the structure, increasing the disorder within the layers and ultimately resulting in the slight widening of the layers where this occurred and thus diminishing the inter-layer spacing. Thus the migration of the aluminium ions through the structure clearly has a pronounced effect, and thus is further investigated.

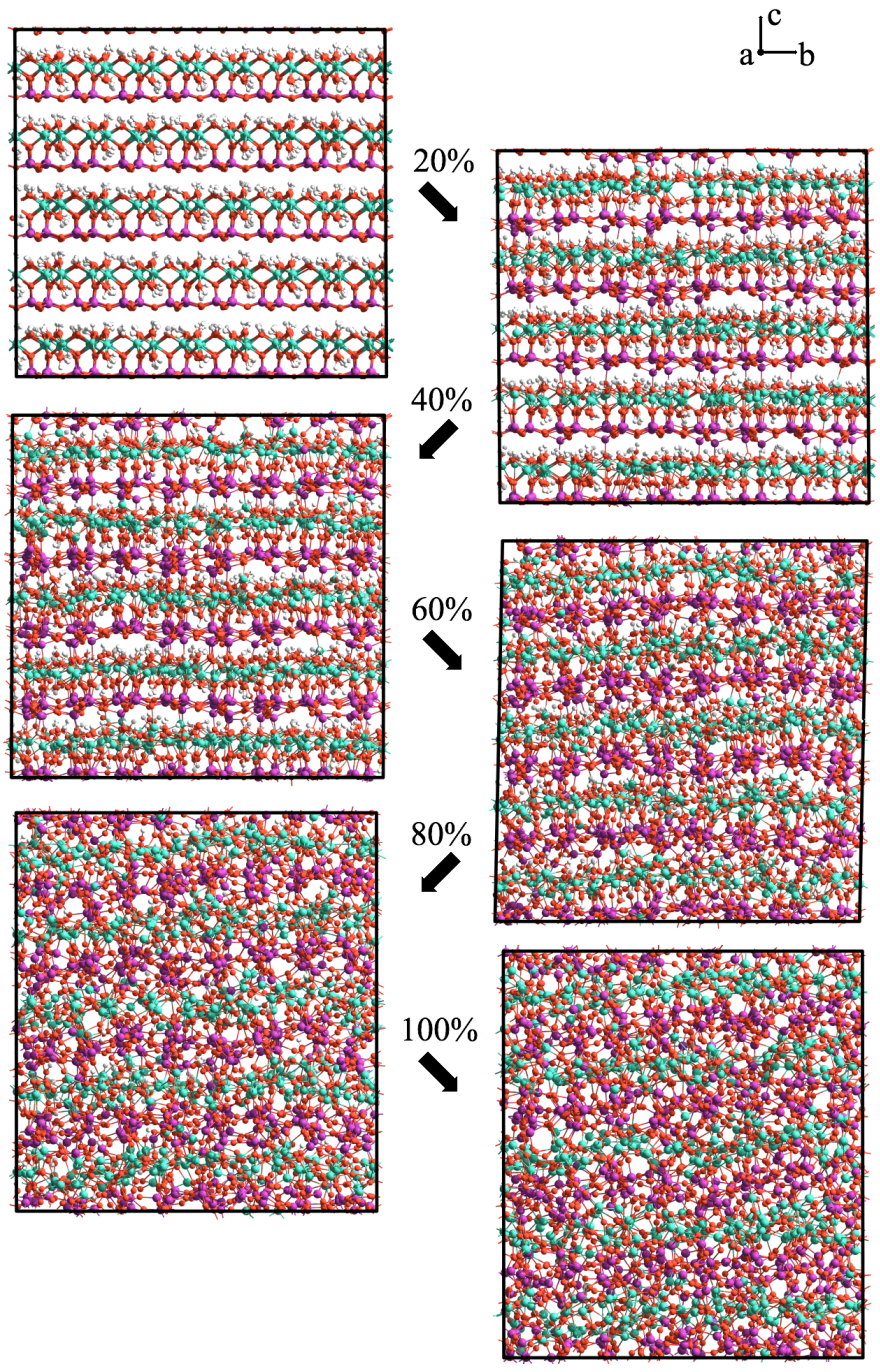

FIGURE 4.6: Snapshots of one of the de-hydroxylation simulations viewed along the *a*-axis. Starting from the kaolinite structure at 300 K (top left), each image shows the quenched 300 K structure after a 20% de-hydroxylation step. These images show the rapid collapse of the inter-layer spacing and the buckling of the layers.

4.4.1 Structural Reorganisation: Al Migration

The observed migration of aluminium ions in clay minerals has been reported in density functional studies of the de-hydroxylation of 2:1 dioctahedral aluminous clay minerals [329]. These authors find that in kaolinite, the migration of the Al ions created large distortions within the local structure of the layers. The combination of the bridging of the inter-layer spacing and the distortions of the layers caused the localised buckling of the layer. If a defect was introduced in the local vicinity of migrated Al ions, this caused the ions to further migrate within the layers. This buckling phenomena has also been reported by White *et al.* [118, 119]. The migration of the Al in this study similarly resulted in distortion within the structure, as shown in Figure 4.7.

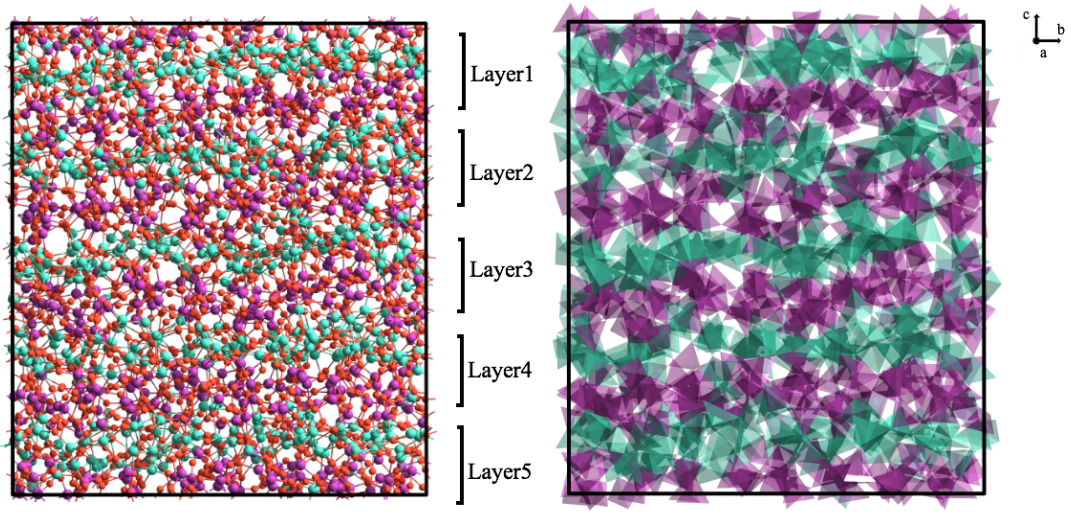

FIGURE 4.7: The fully de-hydroxylated structure showing the 1:1 layering is still present. The image on the right shows the Si-O and Al-O polyhedra.

Cross-sections of the final structure, Figure 4.8, show that the aluminium layers have a large degree of disorder within them, with the majority of the aluminium existing in a 4-fold coordination. The silicon layers, however, appear relatively unchanged with little disorder present. The migration of the aluminium is not confined to within the individual layers. Further investigation of the movements

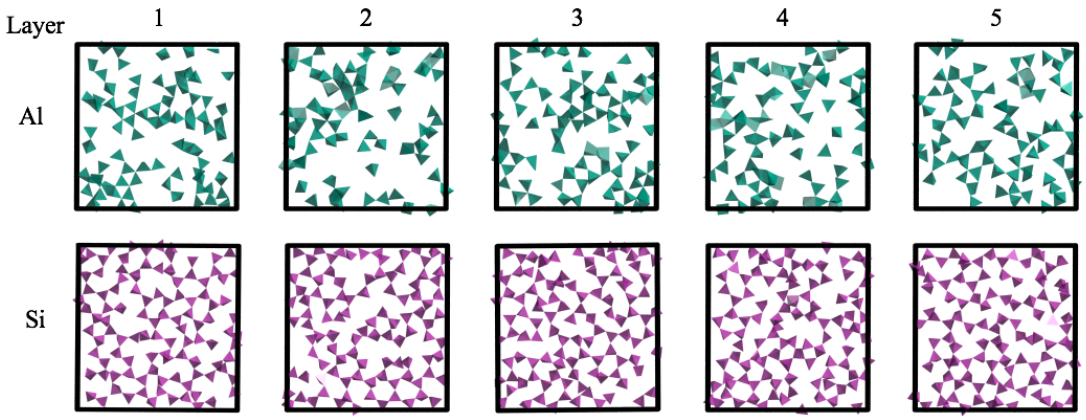

FIGURE 4.8: Cross-sectional slices of the individual layers as a progression down the c-axis. The majority of the aluminium exists in clusters of tetrahedral configurations. By comparison, the silicon layers are relatively unchanged and evenly dispersed. The labels are in reference to Figure 4.7

of the cations during de-hydroxylation showed migration of the aluminium cations occurred between the layers themselves, as shown in Figure 4.9. Some relocation of the silicon atoms was noted, but occurrences were rare and there was never more than a single Si relocation present in any structure.

The majority of the migration occurred between the aluminium layers leading to the formation of whole cation bridges between the layers. So while the 1:1 ordering of the cations was preserved in general, isolated instances of a loss of this periodicity in the c-direction also occurred. The degree of migration varied, but typically no more than one or two cation relocations were evident per layer, and only between adjacent layers. The relocation of one cation to another layer does not necessarily instigate a further relocation to maintain a constant number of cations present in each layer. This resulted in the number of cations in each layer changing through the process of de-hydroxylation, with the final structures demonstrating local variations in the aluminium distribution throughout the structure.

The results from the simulations present conclusive evidence that the mechanism of structural deformation is governed by the migration of the aluminium through the structure. This migration causes a distortion in the local structure, and

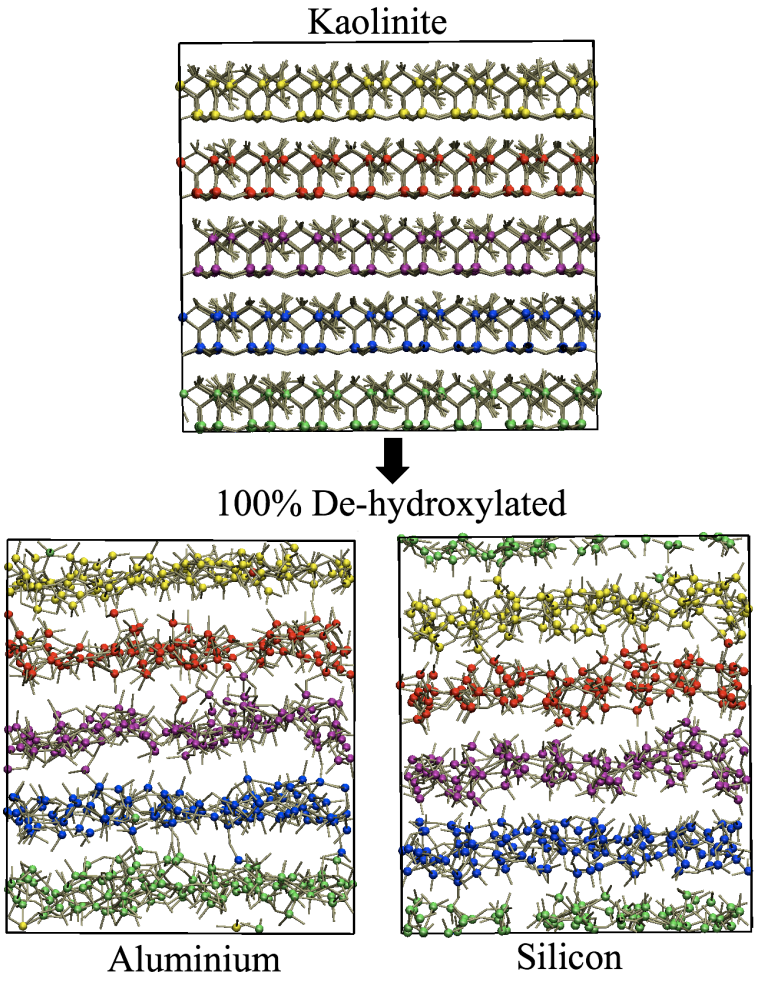

FIGURE 4.9: The kaolinite structure (top) and the final 100% de-hydroxylated structure deconstructed to show the Al-O (left) and Si-O (right) bonds respectively. The cations are shown as coloured spheres, where the colours indicate the layer from which each Al/Si atom originated. Note the considerable interlinking of the aluminium layers compared to the silicon layers which remain relatively uniform and separate.

results in the buckling of the layers. The degree of buckling is considerable and high-resolution surface imaging of metakaolin crystals [330] show an increase in surface roughness, which may be a product of the buckling effect.

4.4.2 Structural Reorganisation: Al Coordination

With the process identified, the question of how this migration of the aluminium affected the overall coordination needs investigation. The nature of the structural changes during the de-hydroxylation process can be determined quantitatively by calculating the radial distribution function for each of the simulated structures. The normalised individual functions for each simulation are given in Appendix B, with the averages of all the normalised runs shown in Figure 4.10.

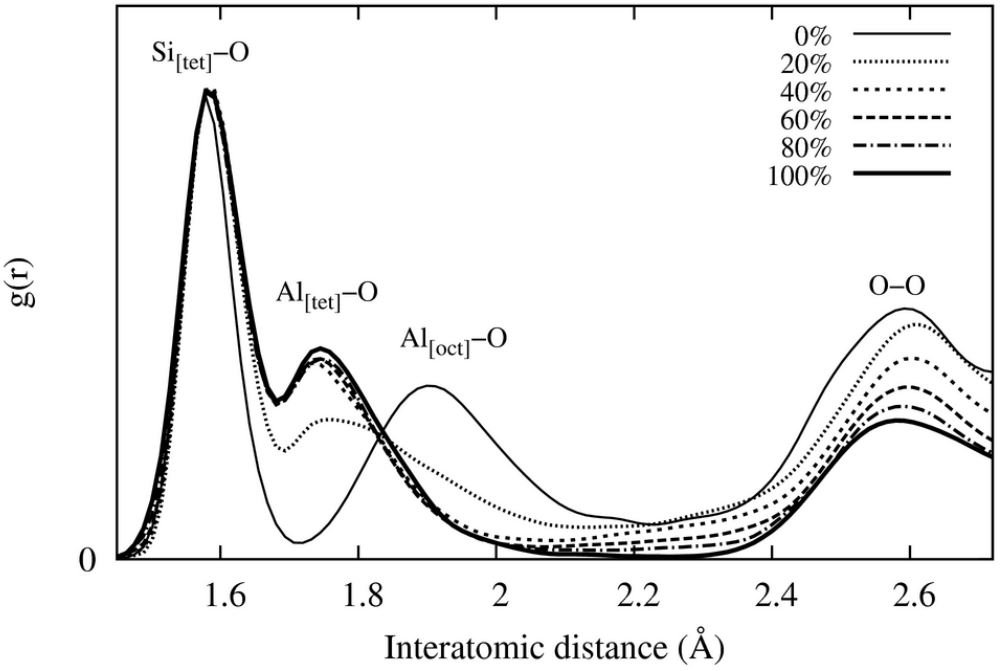

FIGURE 4.10: Normalised calculated total radial distribution function showing the three main interactions for the de-hydroxylation process. Calculated from the averages of the all equilibrated structures at the end of each de-hydroxylation step.

The silicon and oxygen peaks remain in the same positions, with the decrease in the oxygen-oxygen peak intensity due to the decreasing oxygen concentration in the cell. The silicon-oxygen peak remains the same in both location and intensity, indicating that although there is considerable structural reorganisation occurring, this does not cause enough disruption to break the strong SiO_4 tetrahedral unit.

The feature of interest is the shift of the Al-O peak from 1.93 Å to 1.75 Å, which corresponds to the change in coordination from octahedral to tetrahedral. A slight shoulder on the right of the peak that develops through the latter stages of the de-hydroxylation is indicative of the formation of 5-fold Al. Experimentally, 5-fold Al gives a peak at around 1.8 Å [331], and so further analysis of the coordination of the aluminium was conducted to quantitatively determine the amount of the 5-fold Al in the structure.

The loss of hydroxyl groups produced aluminium ions with coordination numbers of less than 6, and the decrease in the number of oxygen atoms in the system meant that the return to a six-fold coordination was not possible. To determine the effects on the coordination quantitatively, the coordination of each Al atom was determined by summing the number of oxygen atoms falling within a chosen cut-off distance of 2.3 Å of the ions. This cut-off value was chosen as the value at which the minimum following the first peak in the calculated partial RDF for the Al-O interactions occurred. The change in the Al coordination through the de-hydroxylation is shown in Figure 4.11.

The analysis shows that along with the change from 6-fold to 4-fold, there is also a considerable contribution of 5-fold Al present throughout the de-hydroxylation process. This corresponds with NMR studies [112, 332–334] that show an appreciable amount of 5-fold Al in samples of kaolinite calcined at temperatures ranging from 600 °C to 1000 °C. An unexpected feature from the coordination analysis is the non-linear relationship between the level of de-hydroxylation and the Al coordination. The majority of the structural reorganisation occurs in the removal of the first 4 steps of the de-hydroxylation, with almost half of the octahedral aluminium transformed to 4- and 5-fold configurations equally in the first step. This is followed by the second step which has more of the 6-fold Al converted to 4-fold. This trend continues until the 6th removal step where the 6-fold coordination reaches a minimum of $\approx 1\%$) and the 4-fold coordination reaches a maximum of 88%. This corresponds to the development of a structure that has

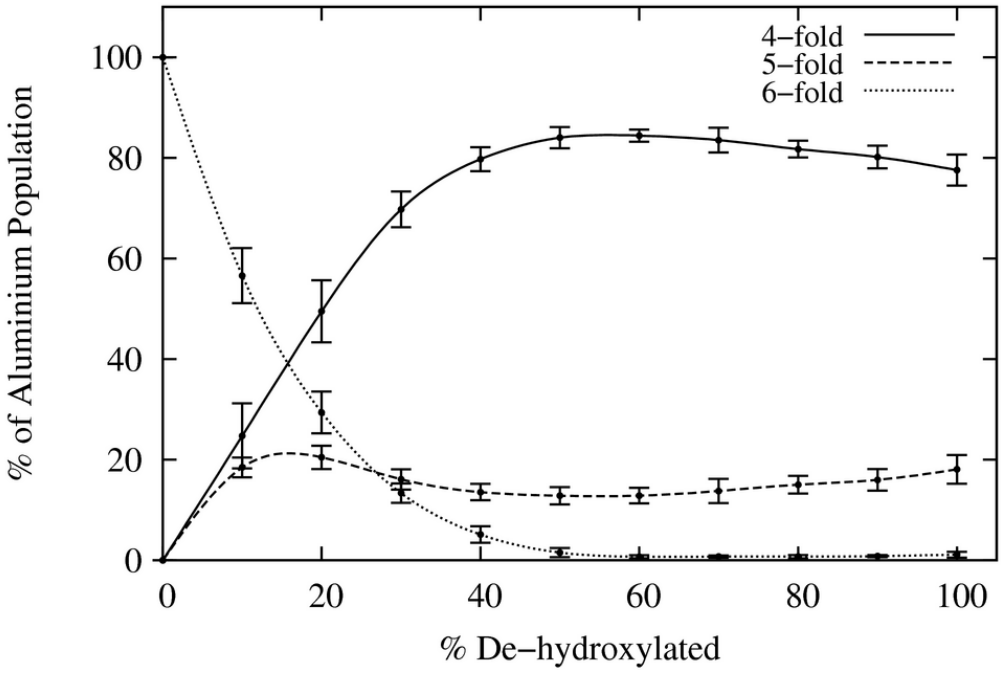

FIGURE 4.11: Changes in aluminium coordination through the de-hydroxylation process: from 6-fold to a combination of 4- and 5- fold.

been distorted to such a degree that migration of the Al is inhibited by the ions becoming locked into the structure.

At this stage the hydroxyls in the structure can all be considered as inner-layer OH groups. In the 7th and 8th removal steps, the further de-hydroxylation causes a loss of some 4-fold coordinated Al to the 5-fold configuration. This is unexpected, as one would expect the loss of further oxygen atoms from the system to encourage the formation of the 4-fold coordinated Al over the 5-fold. However, at this stage an important aspect of the structural change must be considered. Since the hydroxyl removals are not uniform, neither is the Al migration. In the latter stages the majority of the Al migration has already occurred, and as such the resulting aluminium layers consist of "clusters" of 4-fold with some 5-fold aluminium included. This clustering effect has not been previously reported, and could explain the experimentally observed lack of crystallinity in the c-direction of the metakaolin structure.

There is little change in the coordination beyond 80% de-hydroxylation as there is not enough space left for reorganisation within the structure, and the final system consists of 74% of the aluminium population in 4-fold coordination, with 21% in 5-fold and 3% in 6-fold coordination (the remaining $< 2\%$ consists of residual Al in 3-fold coordination). White *et al.* [119] similarly reported a 20% contribution of 5-fold aluminium a 2% contribution of the 3-fold aluminium, as well as the final drop in this value in the final stages of de-hydroxylation.
The stability of the structure through the final stages of de-hydroxylation (80% - 100%) confirms that the metakaolin structure is established prior to complete hydroxyl removal. This corresponds with experimental findings [109, 119, 334] that suggest that the metakaolin structure is established at this stage, with little structural change beyond the 12% water content structure.

The effect of de-hydroxylation rate on the final structure was also investigated, using the 100% de-hydroxylated structures from the gradual de-hydroxylation simulations as well as the single-step de-hydroxylation simulations reported previously, shown in Table 4.3. The final coordination concentrations of the aluminium in the

Table 4.3: Comparison of the results for the final structure from the single-step and gradual de-hydroxylation approaches as a function of the percentage of the Al population in a specific coordination.

Coordination	Initial	Single	Gradual
3-fold	0	6.8 ± 1.5	1.7 ± 0.6
4-fold	0	70.7 ± 1.3	74.1 ± 3.4
5-fold	0	19.6 ± 2.5	21.3 ± 3.2
6-fold	100	1.4 ± 0.5	2.9 ± 0.7

structures show that a greater concentration of four-fold Al is present in the gradual approach compared to the single-step approach, and suggests that the slow removal of water from the structure allows for a greater conversion of the six-fold Al to a four-fold coordination. The high concentration of three-fold coordinated Al in the single-step approach is also of concern, as this suggests that there has

not been sufficient structural reorganisation involved to reduce this strained configuration. These results further validate the chosen de-hydroxylation approach of allowing the gradual reorganisation of the structure during the de-hydroxylation process to occur.

4.5 The Structure of Metakaolin

The molecular dynamics simulations show kaolinite decomposes to a structure that in all aspects discussed thus far represents metakaolin, but further analysis is required before any conclusions on the structure of metakaolin can be made. This study has shown that the migration of the Al ion through the structure is the major driving force in the structural transformation to metakaolin, which corresponds to the criteria proposed by Brindley and Nakahira [106] that state that the octahedral layer should also exhibit the majority of the structural reorganisation. The collapse of the kaolinite layers is also addressed, with the inter-layer spacing almost completely collapsed. The fully de-hydroxylated structures generated in this study had cell dimensions that decreased by an average of 5.9% from the initial kaolinite structure, which is a larger change than expected according to the criteria.

The main deviation from the expected results is in the measurement of the inter-layer spacing. In the simulated metakaolin structures, the inter-layer spacing is observed to completely collapse. The value for the final inter-layer spacing proposed by Brindley and Nakahira [106] of 3.3 Å is thus not observed, however, the criteria do not account for the buckling effect, nor for the variations in aluminium distribution though the structure, and as such the overall decrease observed for the density of metakaolin is maintained. Lee *et al.* [82] however report a metakaolin periodicity of 6.9 Å in the *c*-direction, which is within reasonable agreement with the average width of the Al-Si layers reported here of 7.2 Å.

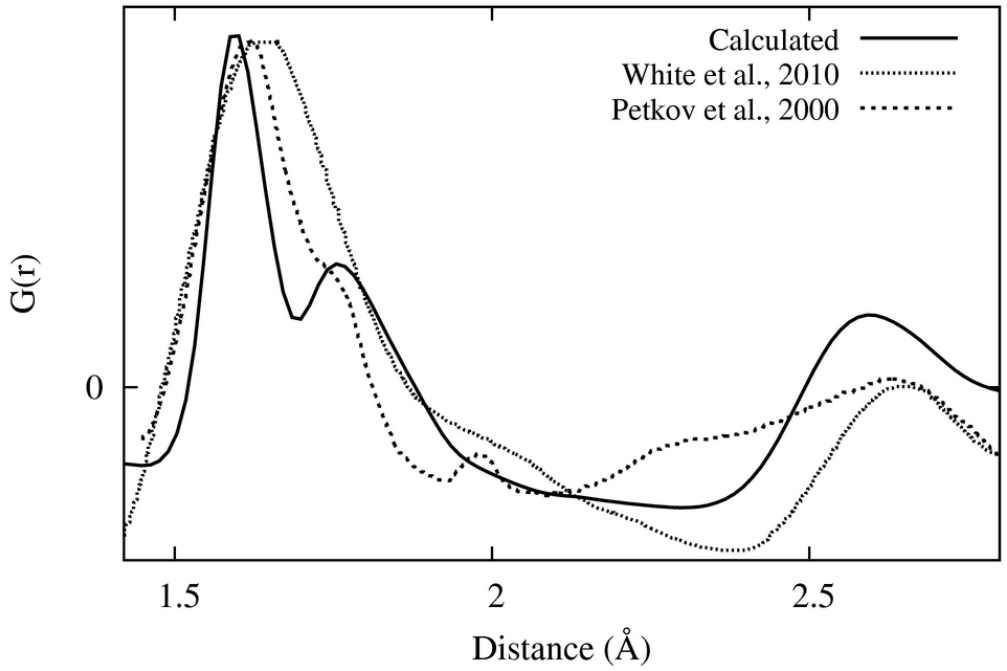

FIGURE 4.12: Comparison of the reduced RDF, $G(r) = 4\pi r\rho_o[g(r) - 1]$, for the fully de-hydroxylated structure compared to experimental data from White *et al.* [119] and Petkov *et al.* [67].

A comparison of the simulated reduced radial distribution function for the fully de-hydroxylated structure compared with experimental x-ray diffraction data [119] is shown in Figure 4.12. The simulated metakaolin produced a Si-O interaction peak at 1.68 Å (compared to the experimental value of 1.71 Å), an Al-O peak at 1.75 Å (compared to 1.76 Å) and an O-O peak at 2.58 Å (compared with 2.6 Å). There is a shoulder on the experimental Si-O peak at approximately 1.95 Å that is not shown in the simulated data. This could be due to octahedral Al-O in the sample, which could indicate either that the original sample was not fully de-hydroxylated or that there were impurities that are producing this interaction. The 4-fold Al-O interaction is clearly visible in the simulated data, but is obscured in the experimental data by the Si-O peak.

Figure 4.13 shows simulated x-ray diffraction plots from the fully de-hydroxylated structure at several stages through the de-hydroxylation process. The sharp kaolinite peaks in the initial stages rapidly degrade into a low intensity broadened

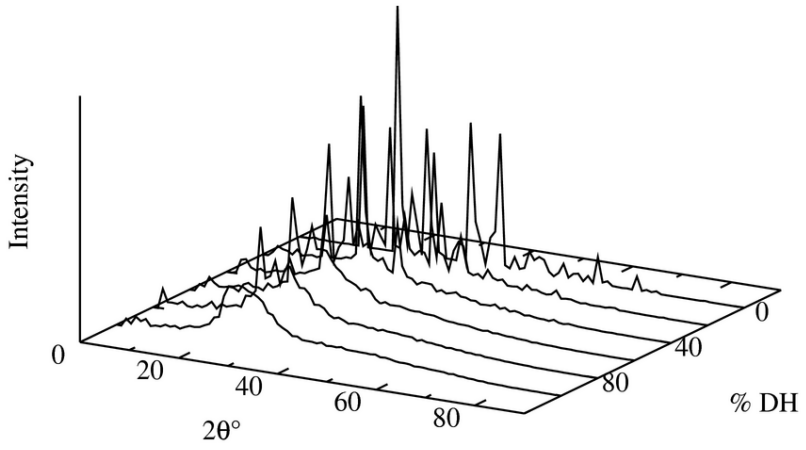

(a)

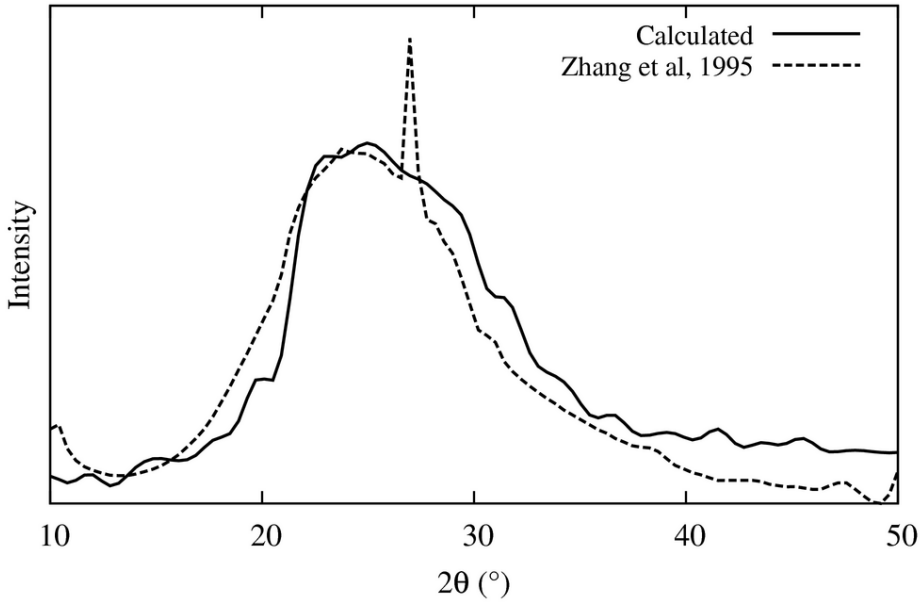

(b)

FIGURE 4.13: (a) X-ray diffraction data calculated using the GTK Display Interface for Structures (GDIS) [335] at various stages during the dehydroxylation process using simulated CuKα x-ray radiation. (b) The XRD data for the final simulated structure (simulated with a Gaussian broadening function at each point with a width of $2\theta = 3°$) is displayed and compared to a typical metakaolin pattern [336].

spectrum between $2\theta = 20°$ to $40°$, with the kaolinite structure completely lost at 80% de-hydroxylation. The broadening is demonstrated in experimental studies on metakaolin [80, 104, 105, 108, 112, 114, 115, 118, 119, 336, 337], and confirms the loss of long-range order within the structure. Experimental diffraction patterns of metakaolin often exhibit various peaks that are attributed to impurities in the samples studies; however, the typical feature present is a broadening of the pattern, which is reproduced in the simulated pattern. The rapid loss of crystallinity is also observed in x-ray diffraction analysis by Alexandre *et al.* [328] of the thermal transformation of kaolinite between 300 and 1200 °C.

Finally, the elastic constants for the metakaolin structures were calculated, with a bulk modulus of 83.5 ± 1.3 GPa and shear modulus of 36.2 ± 0.8 GPa compared to 75.2 GPa and 30.7 GPa in kaolinite respectively. The increase in elastic moduli in metakaolin is expected with the collapse of the inter-layer spacing resulting in a structure more resistant to external stresses. Whilst there were no experimental elastic moduli for metakaolin available, comparisons with values for amorphous silica and alumina were possible. Simulated amorphous silica with a density of 2.4 gcm^{-1} had a bulk modulus of 87.3 GPa [338], and *ab initio* simulations of amorphous Al_2O_3 with a density of 3.37 gcm^{-1} calculated a bulk modulus of 193.41 GPa [339]. The density for amorphous silica is closer to the 2.77 ± 0.02 gcm^{-1} value for metakaolin, and consequently the relative similarities in the calculated bulk moduli show that the simulated metakaolin structure is reasonably accurate.

The metakaolin structures simulated from the molecular dynamics simulations agree with experimental results and observations. The preservation of the 1:1 layering is observed, and the loss of periodicity is determined to occur through the collapse of the inter-layer spacing caused by the buckling of the layers. The results from the simulations confirm the presence of as much as 20% of the aluminium population in 5-fold coordination. This is less than the 30% reported by the DFT simulations, however, as the migration of the Al through the system showed,

the calculated percentages can depend on the size of the volume sampled by the simulation. The results demonstrate that more than one general configuration can be present within the relatively small sampled volume of the atomic system with some regions exhibiting higher concentrations of the different coordination types when compared to others.

The local environment in metakaolin also varies from aluminium rich to aluminium deficient, depending on the sampled volume investigated. This will produce very different environments when metakaolin is used in chemical reactions and the varying aluminium concentrations will create areas of higher or lower reactivity. In some cases the Al could even migrate in such a way that it creates small areas demonstrating higher crystallinity, which would offer an alternative explanation to the consistent observations of crystalline peaks in the measured diffraction patterns of metakaolin, which typically are explained as crystalline impurities.

4.6 Summary

This chapter has successfully used molecular dynamics simulations to aid in the understanding of the atomic mechanisms underpinning the loss of crystallinity during the de-hydroxylation of kaolinite to metakaolin. Through a gradual step-like removal of the hydroxyls of a simulated kaolinite model, the de-hydroxylation to metakaolin has been simulated with the final structure agreeing well with experimental observations. This study shows that metakaolin is constructed of layers of vertex sharing SiO_4 tetrahedra forming six-membered silicate rings sandwiched between layers of AlO_n polyhedra units (where n=4,5 and 6) arranged in a non-regular manner such that considerable buckling is evident in the layers when viewed along the a- and b-directions. The concentration of silicon remains

constant throughout the structure, and the aluminium concentration varies depending on the degree of local disorder with the structural transformations caused by the migration of the Al ions through the structure due to the loss of hydroxyl groups. The structures produced from the molecular dynamics simulations of the de-hydroxylation of kaolinite compare well with experimental values, and are thus good representations of metakaolin.

Note

Parts of this chapter are based upon the paper "Dehydroxylation of kaolinite to metakaolin – A Molecular Dynamics Study", by S. Sperinck, P. Raiteri, N. Marks and K. Wright, published in *Journal of Materials Chemistry* 2011, 21(7), pages 2188 – 2125.

Chapter 5

Interactions of Interstitial Cations in Bulk Metakaolin

The structure and final properties of a geopolymer depend on the choice of alkali metal cation in the geopolymer liquor. The effects of these cations on the different physical properties have been quantified experimentally, but the atomic interactions that are responsible for the changing properties are unknown. The exact locations of the different cations in the geopolymer structure are difficult to determine in experiments, however, cations such as sodium and potassium typically exist within the geopolymer aluminosilicate network and ions such as calcium are also known to be incorporated. This chapter investigates the effects of sodium, calcium and potassium as interstitial defects in the aluminosilicate networks of kaolinite and metakaolin. The influence of these cations on the atomic environments provide insights into the possible structural influences of the cations on the geopolymer structure. In order to identify sites for the interstitial cation inclusions into the structures, the nano-porosities of both materials are characterised.

5.1 Introduction

Gas adsorption measurements of geopolymers [86] give porosity values of approximately 40% by volume, with 10% of the pore volume located in large globular pores of on average 105 Å in size [340]. Extraction of the solutions held within these macroscopic pores show that the metal cations provided by the geopolymer activating solutions are predominantly located within the pores [90] and do not

form part of the geopolymer network. All the experimental investigations completed thus far show that the properties of the geopolymer materials are influenced by the presence of these cations, although the mechanisms for the incorporation of the cations into the network are unknown.

The presence of the sodium, potassium and calcium ions in the raw materials or added as alkali hydroxides produce different effects in geopolymer formation, leading to different properties in the final structures [4, 341, 342]. Sodium produces smaller silicate oligomers, which results in the monomeric units forming weaker aluminosilicate networks with higher degrees of order present [343]. Potassium in contrast encourages higher rates of dissolution and condensation than sodium in the same conditions [73] and potassium based geopolymers exhibit denser aluminosilicate networks and more disordered structures [344]. Calcium has been shown to drastically increase the rate of solidification [17], and interferes with the formation of crystalline regions in the geopolymer matrix [68, 345].

The influence of the interstitial cation defects on the metakaolin aluminosilicate structure may provide insights into the types of interactions that are responsible for the different characteristics of the geopolymer structure, as the disordered aluminosilicate network of predominantly SiO_4 and AlO_4 tetrahedral units is similar to the polysialate networks in geopolymers. The porous structure of metakaolin [328, 346] provides locations for the placement of the defect ions, however, the exact nature of the pore structure is not known and thus is investigated in this chapter. The interactions of the cations in the cavities identified in the metakaolin structures are then studied, and it is the resulting influence of these ions on the network that provide evidence for some of the structural characteristics shown experimentally.

5.1.1 Defining Porosity

Porosity is an important property of a material that is difficult to define precisely. In a perfect porous solid, the pores are regularly shaped and thus simple to define, for example, zeolites have channels of well defined widths and lengths are thus defined by the these parameters. In practice very few structures have easily described porous structures, with typically highly irregular and variable pore shapes and sizes. Consequently the calculation of the porosity of a material is dependent on the definition of pore size and shape and the methods used to determine these properties.

The International Union of Pure and Applied Chemistry (IUPAC) proposed a set of guidelines to aid in the definition and discussion of the porosity of materials [347]. The most important point made is that *no experimental methods provides the absolute parameters such as porosity, surface area, pore size, surface roughness: each gives a characteristic value which depends on the principles involved and the nature of the probe used* [347]. The measurement of porosity always involves simplifications and assumptions, and thus any stated measurement of the porosity of a material must make clear the methods and assumptions used to achieve the stated value.

The description of a porous solid must be clear in the *types* of pores expected to be measured. For instance, many investigations are only interested in the pores that are accessible to an external fluid or gas. These pores must be exposed to the environment, and are consequently classed as open pores. Some of the different pore types are shown in Figure 5.1. A through pore (marked as A in Figure 5.1) is open at both ends, whilst a blind or dead-end pore has only one end exposed to the surface. A closed pore may have impact on the density, mechanical strength and thermal conductivity of a material, but not on processes such as fluid flow or diffusion. Similarly, an ink bottle shaped pore has implications for fluid flow and diffusion. Very rough surfaces can lead to some confusion on whether pores

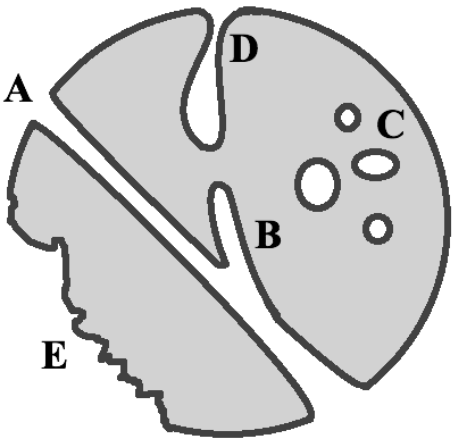

FIGURE 5.1: A cross section of a hypothetical porous solid. **A** represents a *through* pore, **B** and **D** are considered *blind* or *dead-end* pores, **C** represents a *closed* pore and **D** represents an *ink bottle* shaped pore. A rough surface (**E**) can lead to some confusion on whether pores are evident or not. Image based upon that from Rouguerol *et al.* [347].

are evident or not. Generally, a rough surface is considered porous if the depth of the pores are greater than the width.

For quantitative measurements, the porosity, ε, is defined as the fraction of the apparent volume of the materials that is attributed to the pores detected by the specific method used:

$$\varepsilon = \frac{V_P}{V} \tag{5.1}$$

where V_P is the total pore volume and the apparent volume V is the total volume of the material that does not include inter-particle voids. Some methods only have access to open pores, and so results must be defined as open porosity measurements. If total porosity is required, the methods must be able to measure all types of pores in the structure. Related to the porosity is the specific surface area, s, which is defined as the accessible or detectable area of the solid per unit mass of the material. This is also dependent on the method used to measure this value and in particular the size of the probe is important. The validity of the results are thus subject to the accuracy of the model used to interpret the experimental information.

5.1.2 Porosity in Atomistic Simulations

The calculation of porosity in computational simulations is generally focussed on porous carbon materials [348–350] and use a variety of methods based upon whether the pores are open, closed, have channels and whether a probe molecule, such as hydrogen, is of interest [351]. The pores determined in simulations generally have at least one dimension in the nanoscale, and thus it is the nano-porosity that is measured.

In classical atomistic simulations, the structures are composed of atoms with specific atomic coordinates. Generating porosity information requires the molecular surface of the material to be defined, giving any pores their apparent shape and size. The molecular surface is generated by rolling a representative probe molecule (usually spherical with a given radius) over the van der Waals surface, created by the outward facing surfaces of the van der Waals spheres of the atoms represented as point particles in the simulation [197]. This is shown in Figure 5.2.

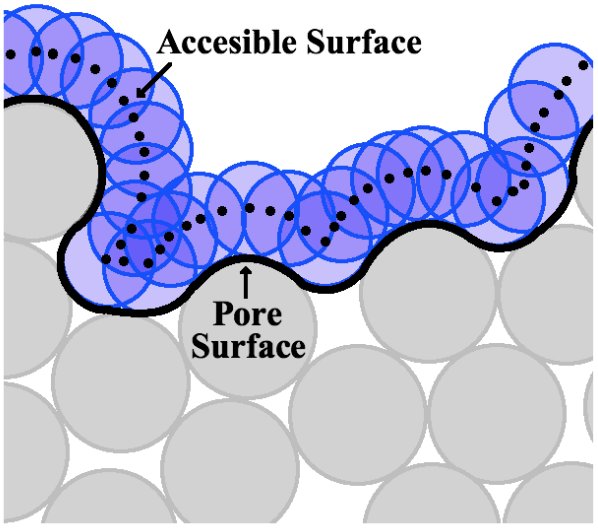

FIGURE 5.2: The two possible surfaces produced by rolling a spherical probe (shown in blue) over atoms around a pore space. The solid line represents the surface of the pore, whilst the dotted line is the surface formed by the centre of the probe sphere, and is the surface accessible to the probe.

The surface generated in this manner also provides the *accessible* surface, which is is traced by the centre of the probe molecule as it rolls over the van der Waals surface [352]. This is often the more useful definition, as a molecule can be placed anywhere on this surface and not penetrate the van der Waals volume of the structure.

5.2 Calculating Porosity

The nanoporosity of metakaolin is investigated to find cavities within the metakaolin structure to accommodate the interstitial cations of interest: calcium, potassium and sodium. The porosity for the purposes of this research is the ratio of the volume of the cavities identified and the total volume of the structure. At the time of writing the freely available Atomic Visualisation and Analysis Software (AVAS) package [210] was identified as appropriate for this purpose due the ability to identify empty space within a simulated structure. However, the capabilities of the software in this regard had not been fully tested and as such a further investigation into the suitability of this method was required.

5.2.1 Atomic Visualisation and Analysis Software Package

The AVAS software is capable of identifying empty space within an atomic structure through the implementation of a grid search algorithm. A three-dimensional grid is overlaid on the simulation cell, with the spacing between individual grid points defined by R_g. The atoms are defined by a sphere with the characteristic van der Waals radius overlaid on the atomic coordinate, and grid points that do not overlap with the atoms of the structure are identified as empty or void space. Groups of points that are connected result in *regions* of void space being identified, with the volume bounded by regions representing the cavity volume.

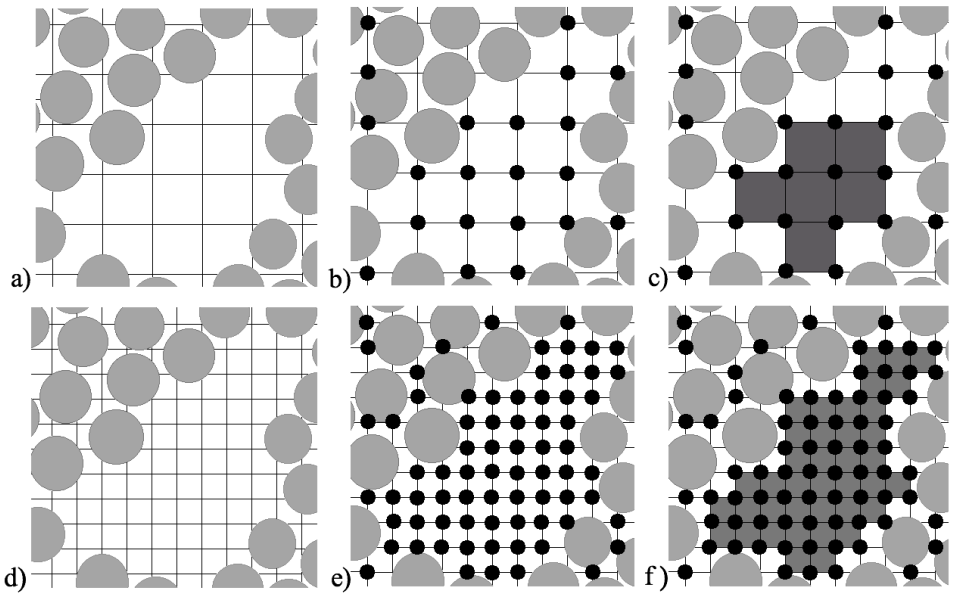

FIGURE 5.3: Two-dimensional view of a hypothetical cavity, bounded by atoms of a single type (shown as pale grey spheres) with radii set to the vdW radius. Empty grid points (shown as black dots) are identified on the mesh in between the atoms and the resultant volume bounded by these points is shaded in dark grey. Figures a–c demonstrate that a large grid does not adequately calculate the cavity shape or size. Figures d–f show that a smaller grid provides a more accurate approximation.

The size of the mesh is the main factor that influences the shape of the cavities identified. Better approximations of the cavity shape are achieved by using smaller grid widths, however, as is demonstrated in Figure 5.3 (e), the smaller widths also identify the interatomic spaces between the atoms as empty space. If these points were included, the porosity would be over-estimated and thus not an accurate representation of the material. To avoid this over-estimation AVAS includes a cut off for the minimum number of adjacent grid points, N_p, that must be present before the identified empty grid points are considered a cavity. Figure 5.4 shows the effects of changing N_p. If a minimum of four grid points is specified, Figure 5.4 (b) is produced, with three separated cavities identified instead of the single elongated cavity. Figure 5.4 (c) shows a more accurate approximation to the pore shape, thus demonstrating that adjusting both the R_g and N_p values produces more accurate results for the porosity.

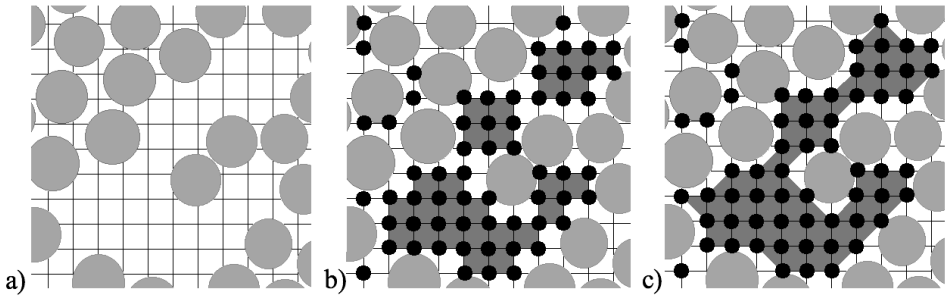

FIGURE 5.4: Two dimensional view of a hypothetical cavity, with a more elongated shape. Figure b shows the cavity volumes identified if a minimum of four grid points is required to bound the volume. If this is reduced to three, the resultant cavity volume is shown in figure c.

The final aspect to consider is the presence of the probe molecule used in adsorption measurements. Accounting for the probe produced a value for the porosity that was easier to compare to experimental results, and reduced the overestimation of the porosity. In AVAS a minimum distance from each atomic centre was specified that allowed an approximation of a hypothetical 'probe' particle to be included, with a radius given by R_p. Empty grid points that were unable to accommodate the search probe, were not identified as empty regions for the porosity measurements. This further increased the accuracy of the calculated porosity and also allowed for a more accurate approximation of the accessible surface of the cavities (as shown in Figure 5.2).

5.2.2 Optimisation of AVAS Parameters

The AVAS parameters depend on the nature of the cavity structure within the material investigated and the size of the simulation cell. For the determination of the cavities in metakaolin the optimum parameters were investigated using a 100% de-hydroxylated metakaolin structure from Chapter 4. Figure 5.5 shows the effects of adjusting the parameters on the resulting cavity structure identified by AVAS. Figures 5.5 A–E show that by gradually decreasing the grid width more cavities are identified, however, for values below $R_g = 0.4$ Å no new cavities

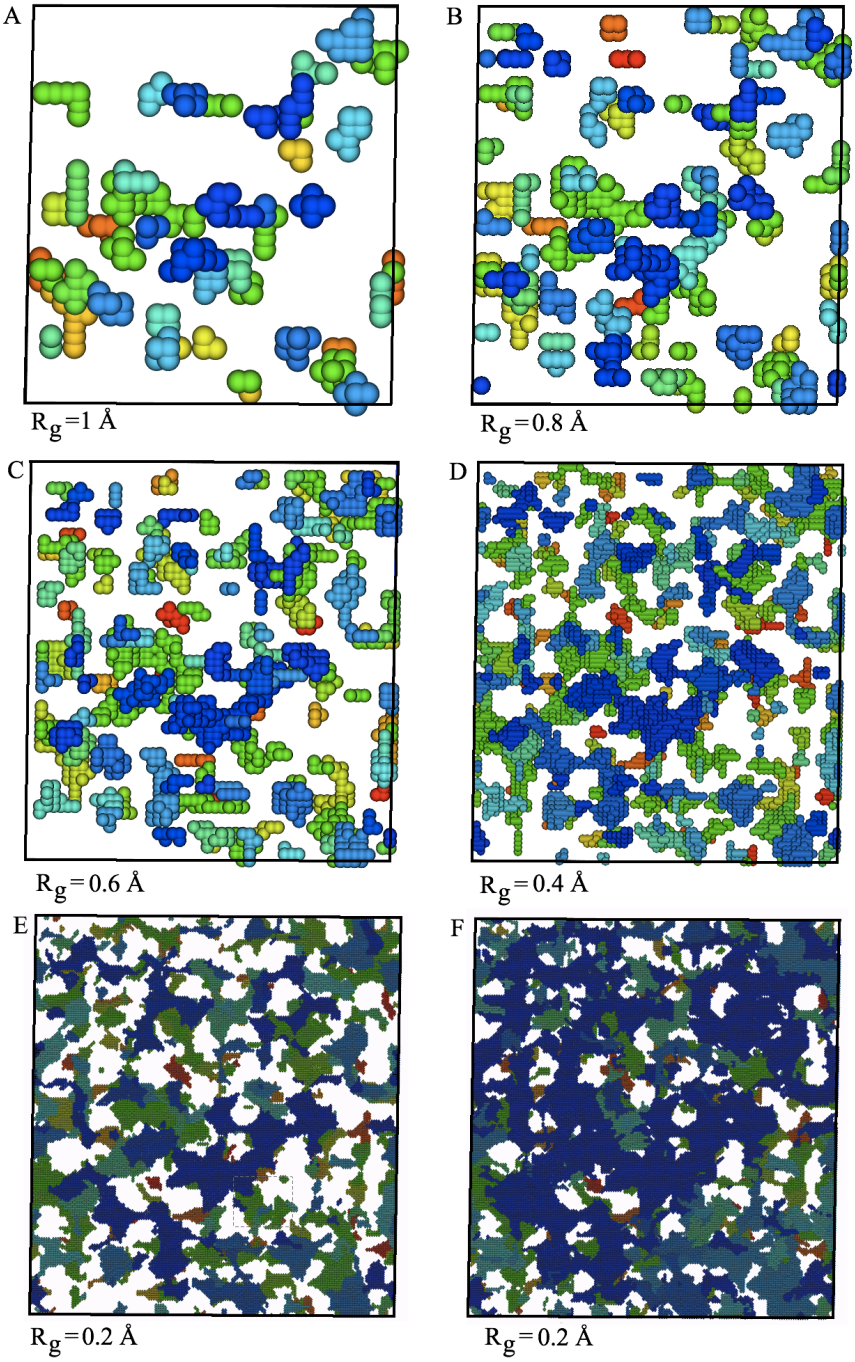

FIGURE 5.5: The cavities identified in the 100% de-hydroxylated metakaolin structure viewed along the a-axis. Only the empty grid points are shown. Points grouped together in the same region and as a function of location along the a-axis are shown in the same colour. A – F use $N_p = 4$ and $R_p = 0.7$ Å with R_g varying as shown. F: $R_p = 0.6$ Å.

are identified and only the complexity in the cavity shapes identified increase. Figure 5.5 F shows the effect of decreasing the probe radius, R_p, also resulting in a greater level of detail in the description of the cavity structure. However, with larger atomic cells the decrease in the grid width leads to an increase in the computational cost. The metakaolin structures simulated are approximately (34 Å)^3 in size and the increased complexity in the cavity shape is not required to produce an accurate representation of the porosity.

The cavity volumes were calculated for increasingly smaller R_g values, keeping the other parameters constant with the results shown in Figure 5.6. The results show the volumes converge at $R_g = 0.3$ Å. The values of N_p and R_p were also tested to determine the optimum values to produce the most accurate information on the cavity structures, with $N_p = 4$ and $R_p = 0.7$ Å identified as the most appropriate. The resulting cavity structure is shown in Figure 5.7.

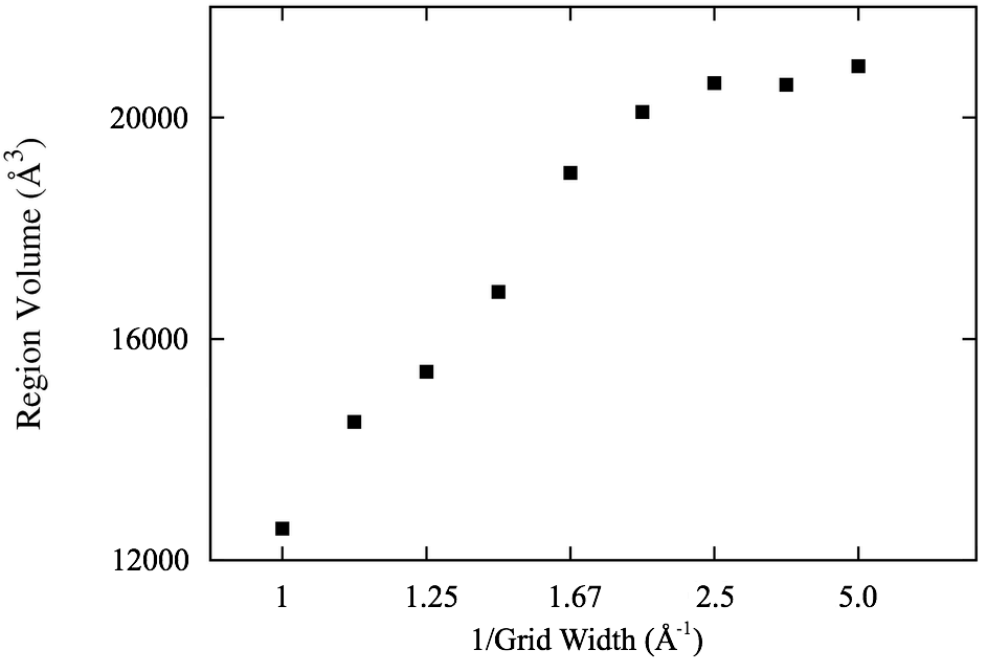

FIGURE 5.6: The effect of changing R_g on the calculated cavity volumes. The cavity volumes converge at approximately $R_g = 0.3$ Å. Results shown for $N_p = 4$ and $R_p = 0.7$ Å.

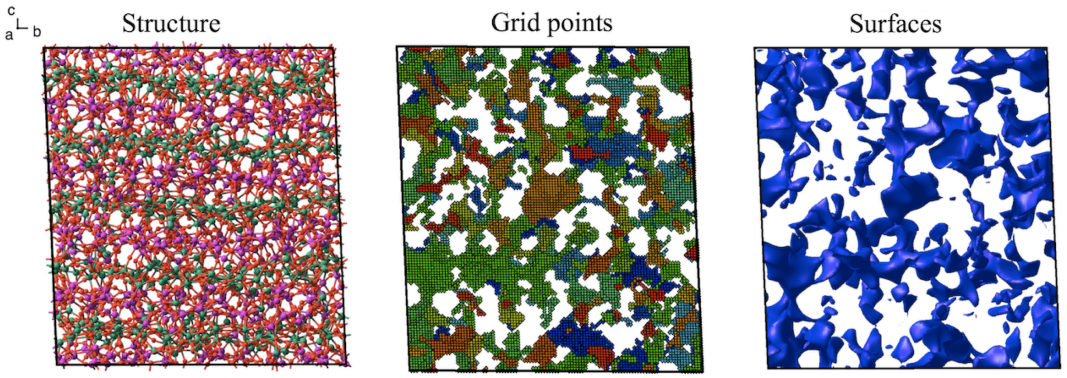

FIGURE 5.7: Cavity regions in the 100% de-hydroxylated metakaolin structure calculated using the optimised porosity parameters, $R_g = 0.3$ Å and $N_p = 4$. The figure on the left shows the atomic structure, the centre shows the cavity structure and the image on the right shows the smoothed accessible surfaces using a probe molecule with radius $R_p = 0.7$ Å.

5.3 The Porosity of Kaolinite and Metakaolin

Experimental measurements of the porosity of kaolinite using dry and brine-saturated samples under increasing vertical effective stress [325], give a value of $\varepsilon = 0.59$. The simulated kaolinite and metakaolin structures from Chapter 4 were investigated using AVAS with the optimised parameters (unless otherwise specified). The porosities were calculated for each structure by using the ratio between the apparent volumes of the structures and the region volumes using equation (5.1).

The cavity structure determined from AVAS is shown in Figure 5.8, with a slightly larger R_g value used to make the locations of the cavities in kaolinite clearer, although the optimised value of $R_g = 0.3$ Å is used in the calculations. The porosity of kaolinite is calculated to be $\varepsilon = 0.51$, which is slightly lower than the experimental value of $\varepsilon = 0.59$ [325], but within reasonably agreement considering the errors associated with the experimental water absorption techniques used [353]. The calculated porosity for the ten 100% de-hydroxylated metakaolin structures from Chapter 4 is given in Table B.1, with an average value of $\varepsilon = 0.52$ and an average deviation from the mean of 0.03.

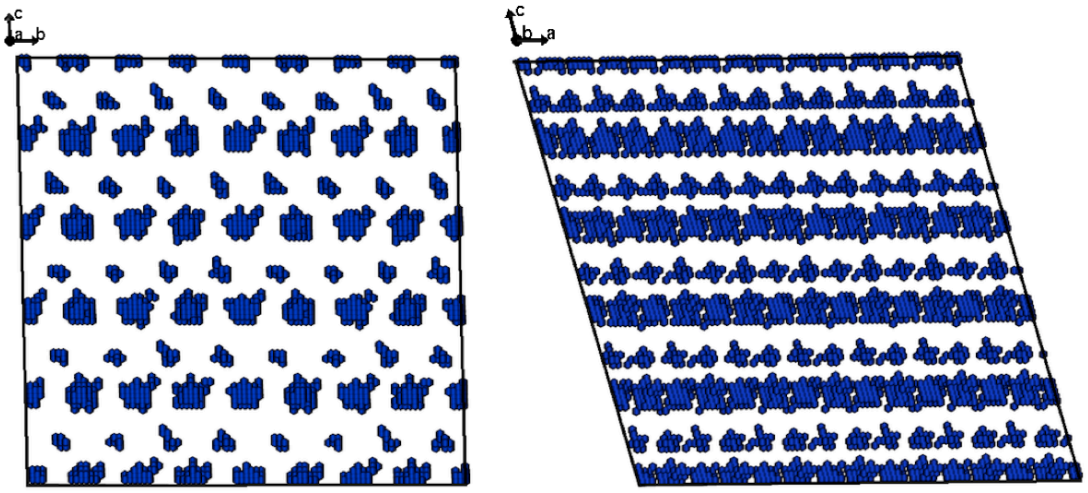

FIGURE 5.8: The cavity structure of kaolinite calculated using $R_g = 0.5$ Å, $N_p = 4$ and $R_p = 0.7$ Å. The image on the left shows the empty grid points making up the larger cavities in the structure, and the image on the right is the structure rotated to show that the cavities are connected in channels that continue through the inter-layer spacing.

5.3.1 Porosity as a Function of De-hydroxylation

Alexandre *et al.* [328] investigated the porosity of kaolinite as a function of thermal treatment using photo-acoustic thermal characterisation and water absorption methods similar to those used by Mondol [325] for kaolinite. Although the exact temperatures and rates of de-hydroxylation are unknown, the experimental and calculated porosities of the structure of metakaolin as a function of de-hydroxylation were compared. The porosity at each stage of the structural transformation was calculated, with the development of the cavities within the structure shown in Figure 5.9 Although kaolinite has one of the higher calculated porosity of $\varepsilon = 0.51$ in this series, the cavities that are present are only small compared to those present in fully de-hydroxylated metakaolin.

The initial loss of hydroxyl groups from the kaolinite structure results in the collapse of the inter-layer spacing, whilst the structural ordering within the layers remains relatively intact. This is due to the loss of hydroxyl groups located within the inter-layer spacings in the first few de-hydroxylation steps (see Figure 4.1 on

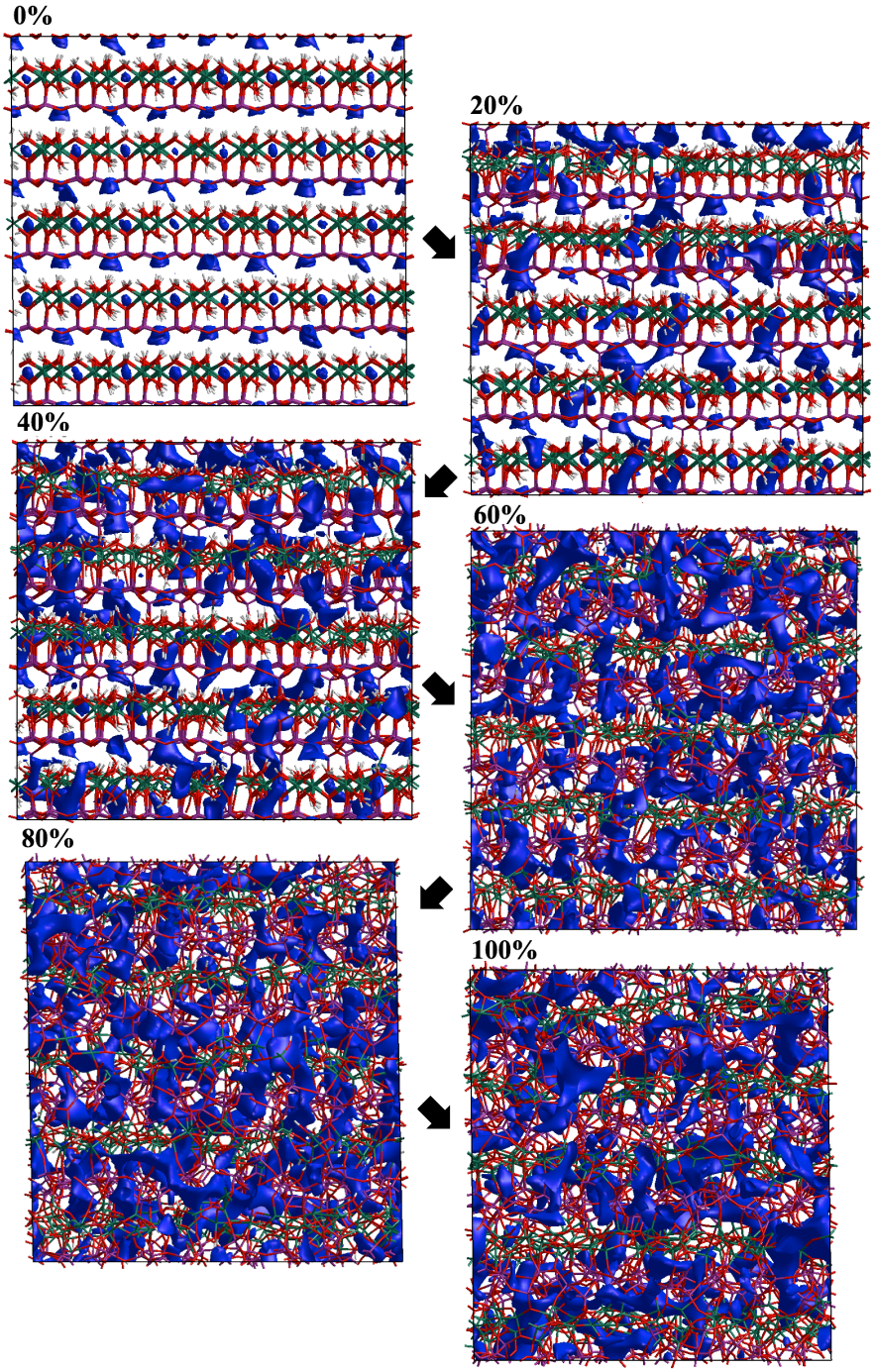

FIGURE 5.9: The smoothed surfaces of the cavities at each stage of the dehydroxylation process are shown in blue. A larger probe with $R_p = 1.0$ Å was used to generate these images to provide a clearer view of the development of the cavity network, with $R_p = 0.7$ Å used in the calculations. The atomic structure is shown around the cavities, with Al = green, Si = purple, O = red and H = white.

page 94 and Figure 4.4 on page 101 for clarification). As more hydroxyl groups are removed, the structure reorganises to account for the introduction of these defects, which results in the development of large interconnected cavities within the structure.

Figure 5.10 shows the calculated average porosity measured from the final room temperature structures of the ten simulations reported in Chapter 4, with the literature values shown in Figure 5.11 for comparison. The volumes that the porosities were calculated from are listed in Table B.1, and are calculated by summing the volumes of the bound by the individual grid-points. The results show similar trends in both the literature and calculated values, with an initial drop in porosity followed by a peak of approximately $\varepsilon = 0.74$ ($\varepsilon_{\text{calc}} = 0.73$ compared to $\varepsilon_{\text{exp}} = 0.74$) then dropping off as the transformation proceeded to the more crystalline high temperature polymorphs (not simulated). The maximum porosity from both the literature and the calculated values are in good agreement. The final calculated value for 100% de-hydroxylated metakaolin of $\varepsilon = 0.52$ is lower than the experimental value at 850 °C of $\varepsilon = 0.60$, with the value at 90% de-hydroxylation providing a closer approximation of $\varepsilon = 0.60$.

The water retention methods measure can only measure open porosities, whilst the simulated cavities are representations of closed pores. The methods are measuring two different properties and are not directly comparable, however, the changes in porosity as a function of de-hydroxylation shown in both the experimental studies and the simulated structures indicate that the simulated structures are accurate representations of the changes in the pore structure. The collapse of the inter-layer spacing in the thermal transformation of kaolinite to metakaolin not only facilitates the loss of the periodicity in the *c*-direction, it also produces a porous structure comparable to kaolinite in the magnitude of the porosity. However, as is evident in Figure 5.9, the shapes and distribution of the cavities in metakaolin are less regular than in kaolinite, and required characterisation to determine the locations of suitable sites for cation inclusion within the structure.

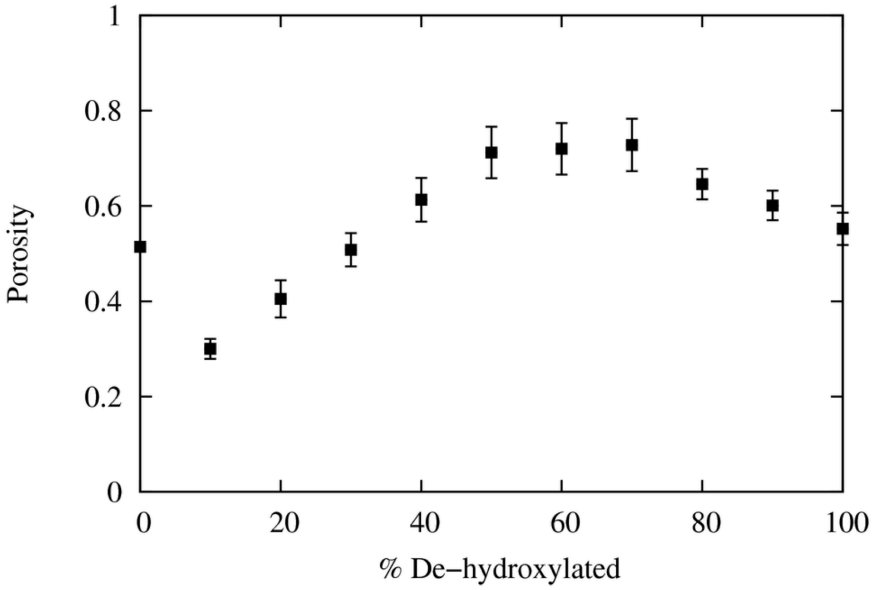

FIGURE 5.10: The calculated porosities for the de-hydroxylation of kaolinite to metakaolin. Compared to the literature values shown in Figure 5.11 below, the trend to initially see a decrease in porosity followed by an increase to approximately $\varepsilon = 0.74$ and then a drop to a similar porosity to kaolinite is observed in both sets of results.

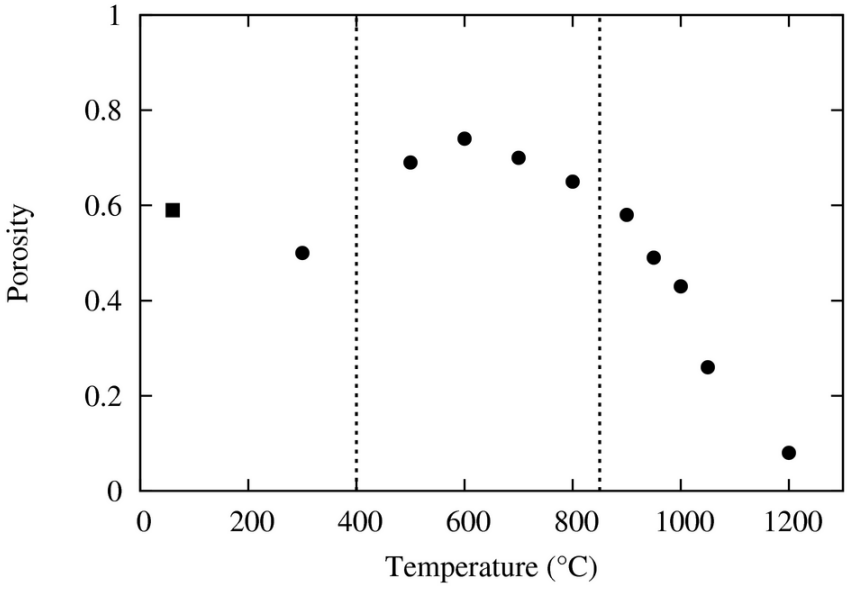

FIGURE 5.11: Literature porosity values at different temperatures for the thermal treatment of kaolinite (circles from Alexandre *et al.* [328] and squares from Mondol *et al.* [325]). The region between the dotted lines shows the temperatures over which the transformation of kaolinite to metakaolin typically occurs.

5.3.2 Pore Characterisation

The characterisation of the cavities in metakaolin required further investigation of the internal cavity structure. For this investigation three of the 100% dehydroxylated metakaolin structures were used for cavity characterisation. The cavity shapes were investigated by visualising the grid points identified in individual regions, with some of the larger cavities shown in Figure 5.12. As is expected for a highly disordered material, there are no regular or repeating shapes within the cavity structure of metakaolin. Instead, the porosity is characterised by long elongated *channels* connecting larger pockets of empty space together.

The scale of the channels connecting the larger areas within metakaolin is investigated by determining the largest possible non-linear lengths that could be traversed within a cavity by a hypothetical probe molecule. This measurement

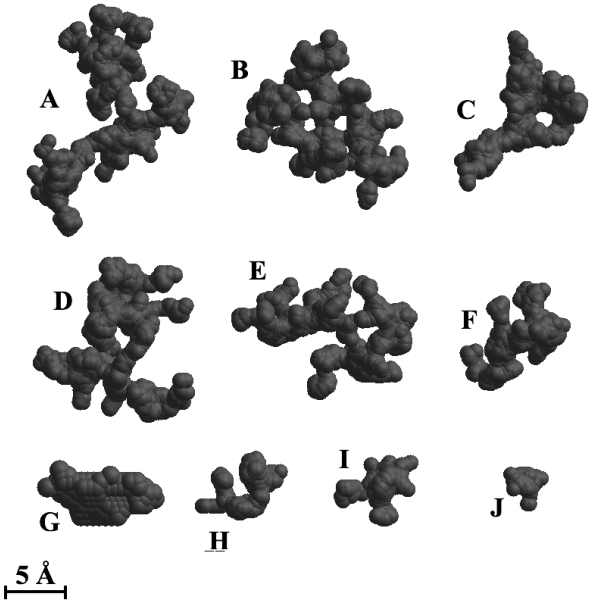

FIGURE 5.12: Several of the larger cavities present in metakaolin are shown, constructed using the grid points from AVAS with the hypothetical probe particle overlaid onto each grid point show the cavity shape. Pores A – F show pockets of space connected by smaller channels. The cavity shapes are convoluted, with most branching into several arms, whilst cavities G – J are smaller and more regular in size.

TABLE 5.1: Three longest non-linear channel lengths calculated in the cavities shown in Figure 5.12.

Pore	Length (Å)		
A	47.8	24.9	16.9
B	46.6	13.9	11.6
C	39.9	15.6	12.9
D	43.1	18.1	17.9
E	38.4	21.7	12.4
F	24.5	9.3	8.6
G	22.7	18.4	8.7
H	16.8	8.3	7.1
I	15.6	9.3	7.3
J	5.7	4.7	4.6

allows characterisation of the channels within the structure, and the calculated distances for the channels in Figure 5.12 are shown in Table 5.1. The calculated distances for the inter-connecting channels show that there is a complex cavity network within metakaolin, with non-linear channels up to 48 Å in length connecting up the smaller pockets of void space within the structure with the widths of the channels varying up to 4.4 Å.

The aim of the cavity structure investigation of metakaolin is to determine possible sites for the inclusion of the interstitial cations. The large number of convoluted regions within metakaolin provides these sites, however, the exact locations for the placement of the cations within these regions requires further refinement. The most appropriate sites are located within the larger pockets of space connected by the channels, and the centres of these pockets are located by identifying the largest possible spherical particle, called a *search probe*, that can fit into the regions of space. Only a single site corresponding to the largest search probe is determined within each cavity region, thereby possibly excluding secondary sites that may be present. However, more than 200 interstitial sites were identified per structure investigated, and as such the identification of only primary interstitial sites is considered adequate to provide for statistically significant results.

The cavities for three metakaolin structures were investigated to find the largest interstitial sites for cation inclusion, with the resulting size distribution corresponding to the radii of the search probes shown in Figure 5.13. The distribution shows that the majority of the regions fit search probes with radii of approximately 0.87 Å and 0.95 Å. There are however, a few regions that can accommodate significantly larger probes, with radii up to 2.18 Å. The radii of the search probes are then compared to the volume of the regions (calculated from the volumes bounded by the grid points), and this is shown in Figure 5.14. It is evident that the larger the total region volume, the more likely it is to find larger pockets of space suitable for a large search probe. There is little homogeneity in the cavity shapes, is shown in the spread of region volume for the different probe radii. The inset in Figure 5.14 shows that the locations of the sites are distributed throughout the structure.

The final aspect of the cavities that is investigated is the surrounding environment of the cavity. The centre for each of the largest spherical probes is identified, a reference particle is placed in this location and the partial RDF is calculated to determine the closest atomic neighbours. The results given in Figure C.2 show that the most likely nearest-neighbour atom to the site location is an oxygen atom, which accounts for 96.8% of the sites. Aluminium makes up the remaining 3.2%, with silicon ions rarely present as the nearest-neighbour atoms. The cavities that did not have oxygen as the nearest-neighbour usually have smaller radii, generally below 1.0 Å. The results from Chapter 4 showed that less than 2% of the aluminium in the network was in 3-fold coordination with oxygen, and inspection of the sites showed that the small proportion of cavities found with an aluminium atom as a nearest-neighbour are all within the vicinity of these under-coordinated Al ions.

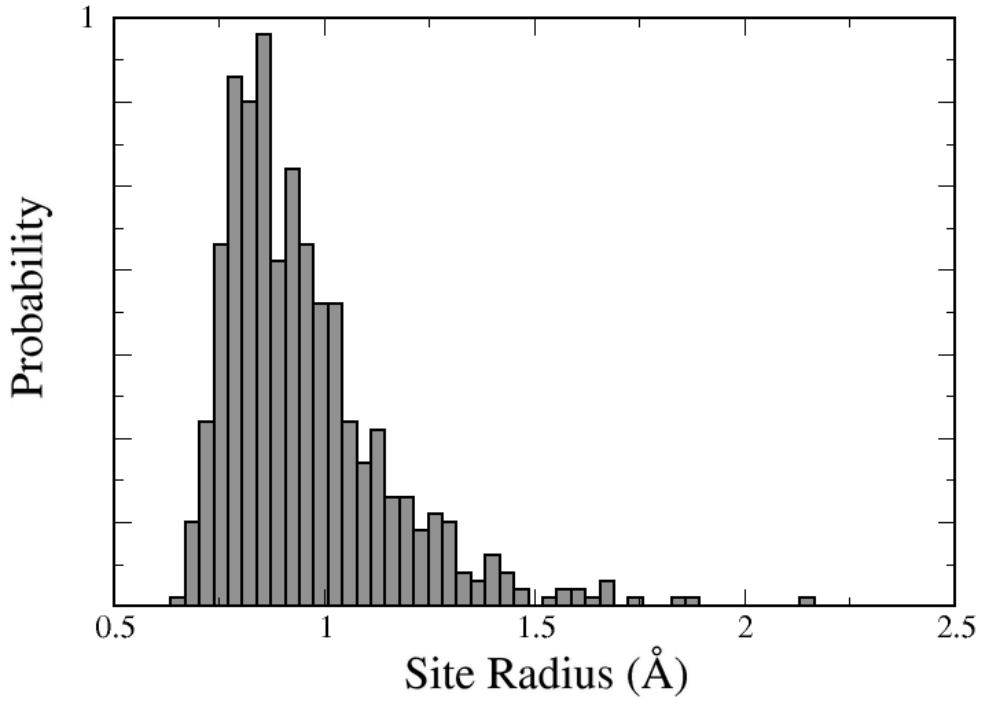

FIGURE 5.13: Size distribution of the radii of the search probes identified in three 100% de-hydroxylated metakaolin structures, with a total of 623 interstitial sites located across all three structures. Bin width = 0.025 Å.

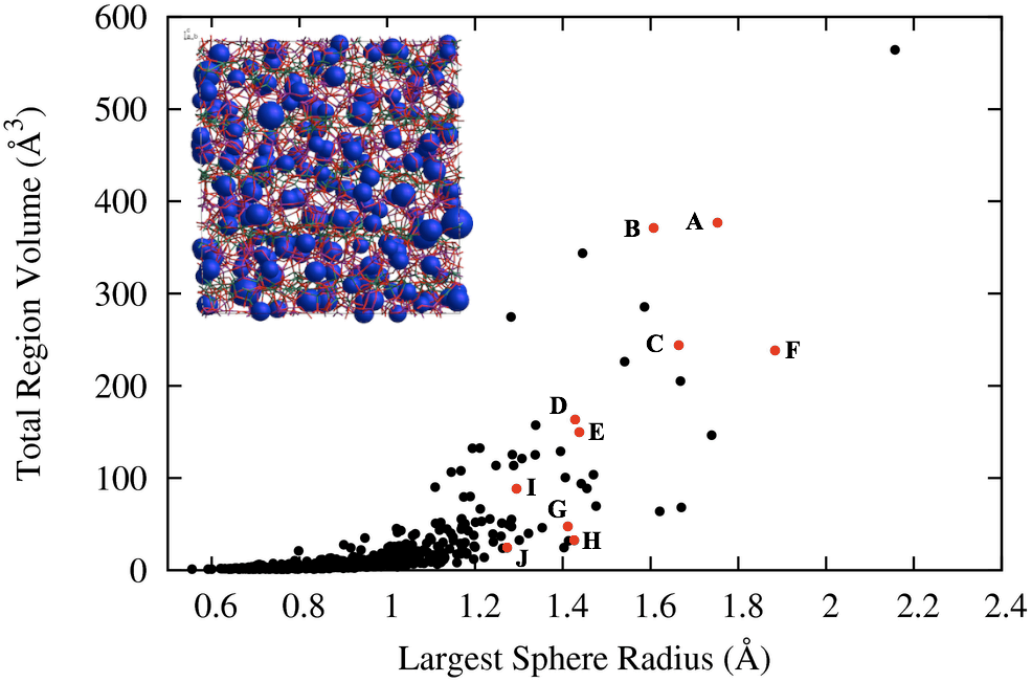

FIGURE 5.14: The radii of the search probes are plotted against the related region volumes, with the red points referring to the regions shown in Figure 5.12. The inset shows the probes (blue spheres) within one of the investigated metakaolin structures.

5.4 Investigation of the Effects of Ion Inclusion

The previous sections investigated the nano-porosities of both metakaolin and kaolinite. Both materials exhibit a porous internal structure containing many potential sites for the interstitial cations. The effects of these cations on three different aluminosilicate systems are studied: (i) the crystalline kaolinite structure, (ii) the disordered 100% de-hydroxylated metakaolin structure and (iii) the 80% de-hydroxylated structure that is close to the residual concentration of OH within the metakaolin used in experimental studies.

The cations investigated are sodium, potassium and calcium. Since ionic interactions are expected to be involved, the ionic radii given in Table 5.2 are used for reference.

Table 5.2: Ionic radii from the literature for calcium, potassium and sodium for different coordination environments.

Ion	Coordination	Ionic Radius (Å) [354]
Na^+	IV	0.99
	V	1.00
	VI	1.02
	VII	1.12
	VIII	1.18
K^+	IV	1.37
	V	1.38
	VI	1.46
Ca^{2+}	VI	1.00
	VII	1.06
	VIII	1.12

The primary differences between the three cations are charge, with sodium and potassium having smaller positive charges than calcium and size, with sodium and calcium being smaller ions than potassium. Although not all cavities identified by AVAS are large enough for the ion, all sites regardless of size are included to improve the statistical sampling and to provide insights into all possible structural

changes. The charges on the ions in the simulations are the scaled partial charges from the potential model: sodium = +0.6, potassium = +0.6 and calcium = +1.2. These charges correspond to the scaled structural charges on the aluminium, silicon and oxygen of +1.8, +2.4 and −1.2 respectively.

The cavities in the kaolinite and 80% and 100% de-hydroxylated metakaolin structures were located using AVAS, with the interstitial cation sites located for each region using the search probe method. Each ion was then systematically placed within each identified interstitial site in the structure, and the system optimised using GULP. Since the addition of the cation into the structure produces a positive charge on the simulation cell, a neutralising background charge [355] is applied, and this process was repeated for each site and for each ion of interest.

5.4.1 Cation Inclusion in Kaolinite

Kaolinite supercells of increasing size were optimised with a single sodium defect placed within the structure to determine the minimum simulation cell required to reduce periodic image effects. The results are given in Figure C.1, and show that a kaolinite $2 \times 2 \times 2$ supercell (V = 2650.5 Å^3) is suitable. This is smaller than the structures of metakaolin investigated ($V_{Metakaolin}$ = 20601.8 Å^3) but allows for reduced computational costs. A comparison to a supercell of equivalent size to the metakaolin structure ($7 \times 4 \times 5$ supercell) in preliminary tests confirmed that no periodic effects were present. The final structure is simulated at 300 K and 1 atm in the NσT ensemble for 200 ps prior to optimisation.

The cavities in kaolinite are located at four interstitial sites as shown in Figure 5.15. The simulations at 300 K result in some variability in the hydroxyl group orientations, and this is responsible for the variations in the radii of the four sites reported. Sites 1 and 2 are located in the inter-layer spacing above the aluminium layer, with site 1 above the Al atoms and site 2 in the spaces created

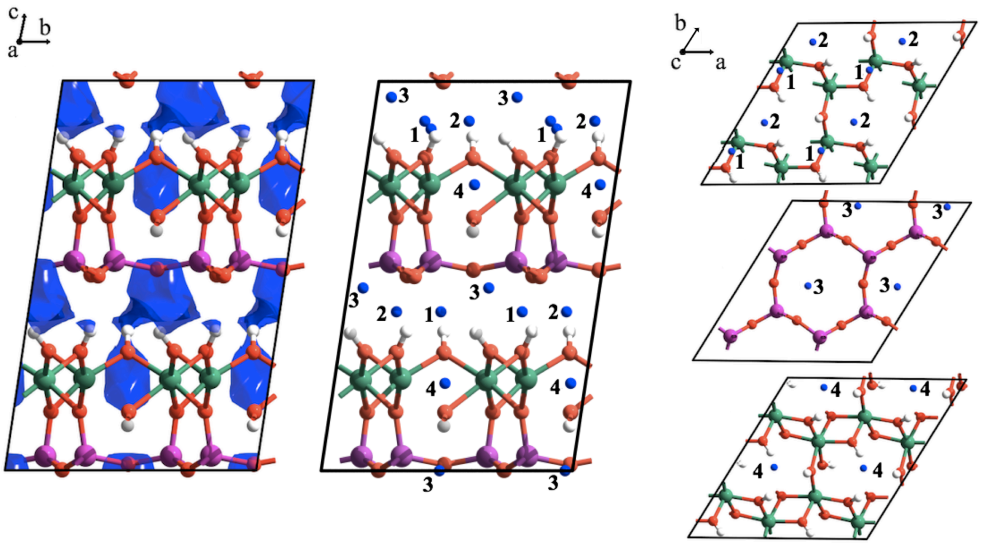

FIGURE 5.15: The cavities within kaolinite are shown on the left, with the centres represented by the blue points. The three snapshots on the right show the locations of the cavity centres viewed down the *c*-axis, showing that sites 1 and 2 are in the interlayer space and associated with the aluminium layer, whereas sites 3 and 4 are located within the holes in the cation rings.

by the hydroxyl groups. Sites 3 and 4 are both located within holes created by the silicon and aluminium hexagonal rings, with site 3 in the hole in the Si layer and site 4 in the Al layer. In the $2 \times 2 \times 2$ supercell a total of 36 sites were identified.

Figure 5.16 shows some examples of the results of the optimised structures after the cations are placed into the kaolinite interstitial sites. The cations in sites 1 and 2 relocate from the initial sites to the holes in the silicon layer (similar to the initial position of site 3). This is due the attraction to the oxygen atoms on the silicon surface combined with this site being the largest possible pre-existing cavity overcoming the attraction of the cations to the hydroxyl groups on the aluminium surface. The presence of the defects within these sites results in the re-orientation of the hydroxyl groups around the cation and varies depending on the cation size. In the sites where the cations are within the aluminium layer (site 4), no change in site location occurs. This is due to the attraction of the cations to the hydroxyl groups within this layer.

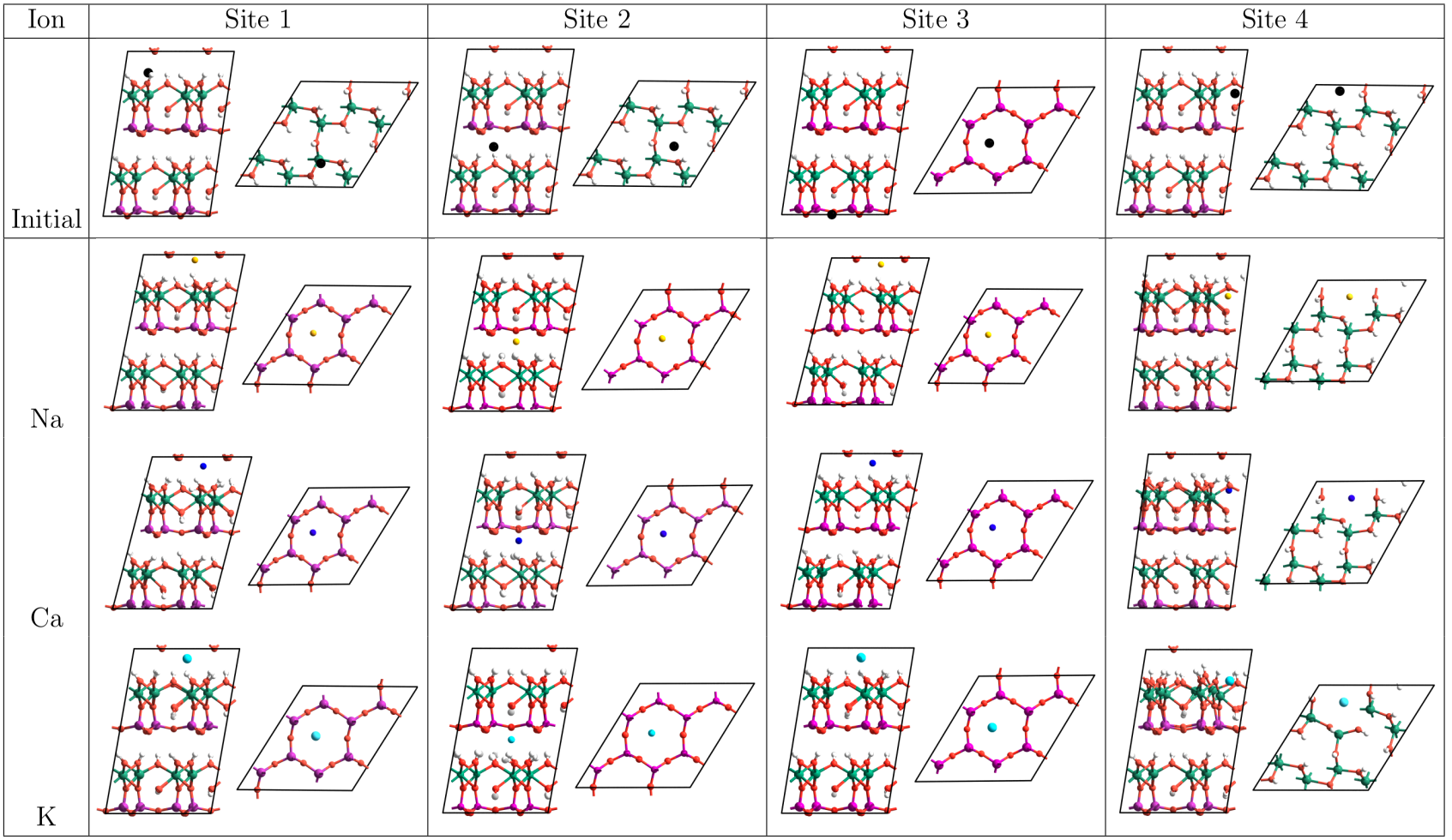

FIGURE 5.16: Some examples of the effects of the cations on the kaolinite structure. A site that represents each of those shown in Figure 5.15 is shown before (initial) and after optimisation, down the *a*- and *c*-axis respectively. All the cations in sites 1 and 2 relocate to site 3 after optimisation, whereas the cations in sites 3 and 4 remain in the same location. Black = initial site, yellow = sodium, dark blue = calcium and light blue = potassium.

The initial cavity size was determined by calculating the distance from the centre of the site (identified by the spherical probe in AVAS) and the nearest neighbouring atom, correcting for the probe size. The distance between the defect ion and the nearest atom is similarly calculated after optimisation to determine the final site radius (although this no longer represents the final cavity size). The final average site radii for each cation is given in Table 5.3, with the standard deviations on the mean calculated to determine the spread of the final radii.

TABLE 5.3: The initial and final site radii for the interstitial sites in kaolinite.

Ion	r_1 (Å)	r_2 (Å)	r_3 (Å)	r_4 (Å)
No Ion	0.68 ± 0.02	0.78 ± 0.01	0.91 ± 0.03	1.02 ± 0.02
Sodium	1.12 ± 0.02	1.18 ± 0.05	1.16 ± 0.01	1.18 ± 0.04
Calcium	1.28 ± 0.12	1.29 ± 0.01	1.30 ± 0.02	1.34 ± 0.06
Potassium	1.24 ± 0.06	1.22 ± 0.08	1.23 ± 0.07	1.31 ± 0.08

The general trend is that the interstitial defect sites increase in size after relaxation. This is consistent with the observations of the relocation of the cations from sites 1 and 2 to site 3, but the final radii are larger than the initial size for site 3 and vary according to cation, with the average final radii increasing according to sodium<potassium<calcium. This trend is also evident in the final radii for site 4, where the hydroxyls that are oriented towards the negatively charged octahedral hole are shifted further down by the presence of the cation. This indicates that cation size is important with potassium being larger than sodium, however the calcium ion has a larger final site radius despite being the same size as sodium. This shows that charge also plays a role, as calcium has twice the charge of both sodium and potassium.

The effect of the different charges on the interstitial site environment is investigated by calculating the electrostatic potential at the sites before and after optimisation (without the neutralising background charge applied) which is given in Figure 5.17. The results show that sodium produces a slightly greater effect than potassium, with the final site potentials slightly lower in all cases, and may

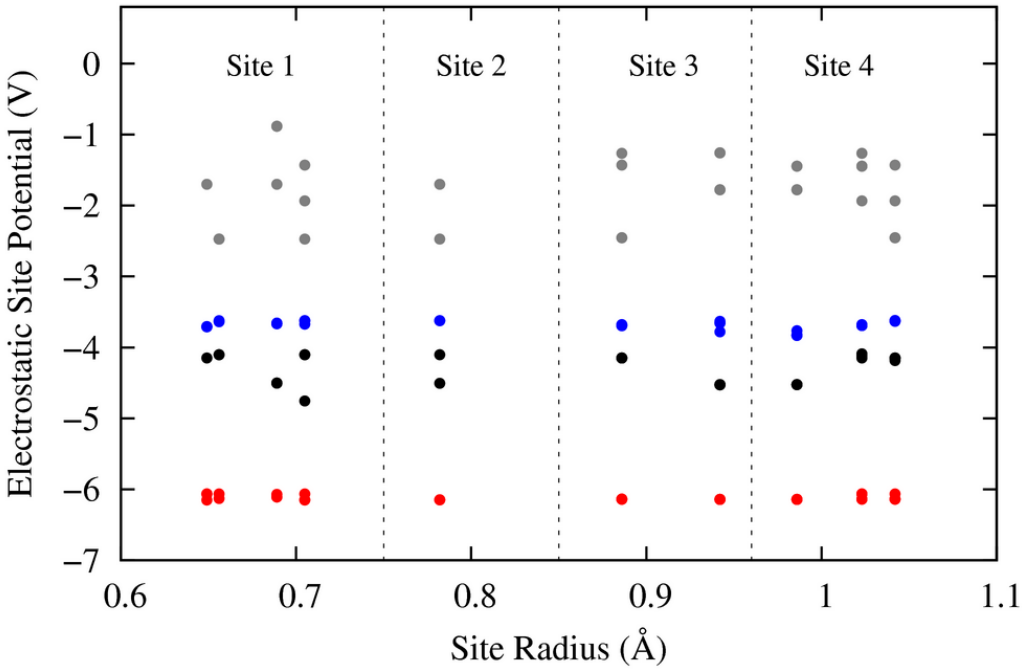

FIGURE 5.17: Electrostatic site potential at the centre of each cavity calculated after optimisation for each interstitial cation site in the kaolinite structure, as a function of initial site radius. The blue points are for potassium, red is calcium, black is sodium and grey shows the initial site potential values.

be attributed to the smaller final site radii for sodium when compared to potassium (see Table 5.3). However, the influence of the calcium defects on the sites produce electrostatic site potentials much more negative than both potassium and sodium, and thus the change in site potential is mainly due to ionic charge.

5.4.2 Cation Inclusion in Metakaolin

A total of 623 potential interstitial cation sites were identified in the metakaolin structures investigated in Section 5.3. Since the metakaolin simulation cells are 17.5 times larger than kaolinite, the influence of periodic images is considered negligible. There are no recurring site environments or locations within the structure such as those identified in kaolinite, and thus there is no differentiation between the interstitial sites, with the radii of the cavities ranging from 0.58 Å to 2.18 Å.

Prior to cation inclusion, the electrostatic potential at the centres of the interstitial sites was calculated to allow the charge environment of each site to be measured to give an indication of which sites are more amenable to the inclusion of the positive interstitial ions. The results, given in Figure 5.18, show that the majority of the cavities demonstrate a negative site potential, indicating a preference for a cation over an anion.

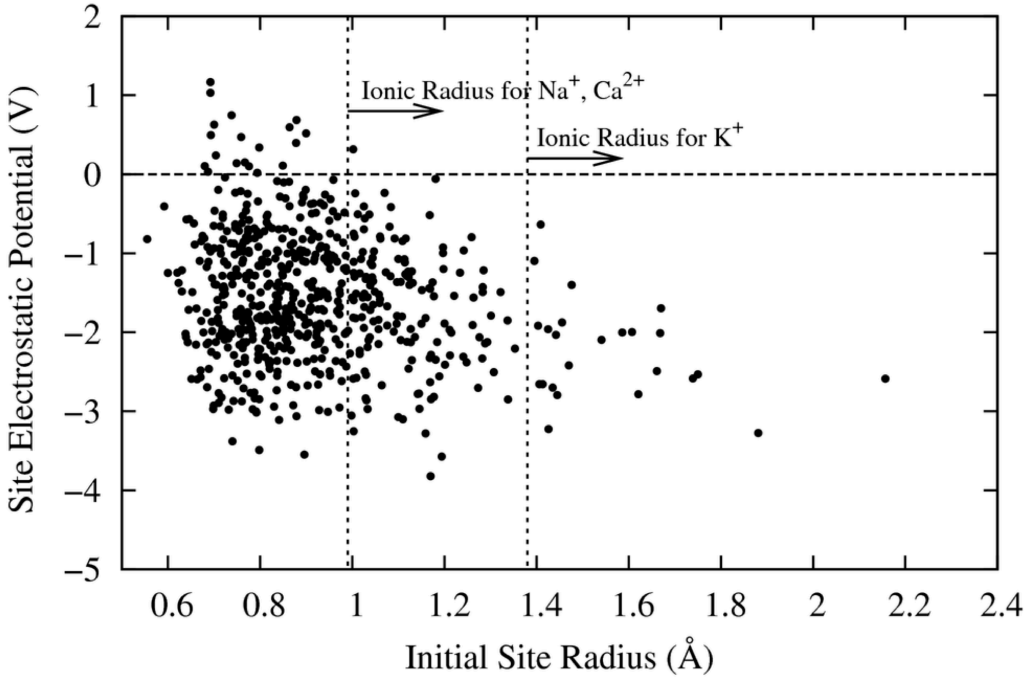

FIGURE 5.18: The electrostatic potential at the centre of each cavity is calculated and shown compared to the initial cavity size. The dotted lines show the sizes of the ionic radii of the cations of interest.

This is due to the sites being predominantly bound by oxygen atoms. There is little correlation between the site potential and the size of the interstitial site, although the larger sites have more negative electrostatic potentials. The smaller sites tend to have aluminium as a nearest-neighbour and all have positive site potentials. As previously stated in the characterisation of the cavities, the sites with Al as the nearest neighbour tended to include three-fold aluminium and the preference for a negative ion reflects this under-coordinated environment.

The majority of the identified sites are smaller in size than the ionic radii of the interstitial cations, with only 29% of the interstitial sites with initial radii large enough to accommodate sodium and calcium, and only 4% are large enough for the potassium ion. In kaolinite the cations relocate to more favourable sites and this is similarly noted in the metakaolin structures, with some of the final sites located up to 5.8 Å away from the initial site locations.

The individual changes in site location for each ion as a function of initial site radius are given in Figure 5.19. In the smaller initial sites ($r < 1$ Å), large changes in site location are present for all cations, with 18% of the potassium ions and 10% of the sodium and calcium ions moving more than 2 Å. Between the ionic radii values of 1.0 Å and 1.38 Å there are no movements greater than 2 Å. The change in distance between the initial and final site locations beyond 1.8 Å increases almost linearly, with calcium demonstrating the largest differences compared to potassium and sodium.

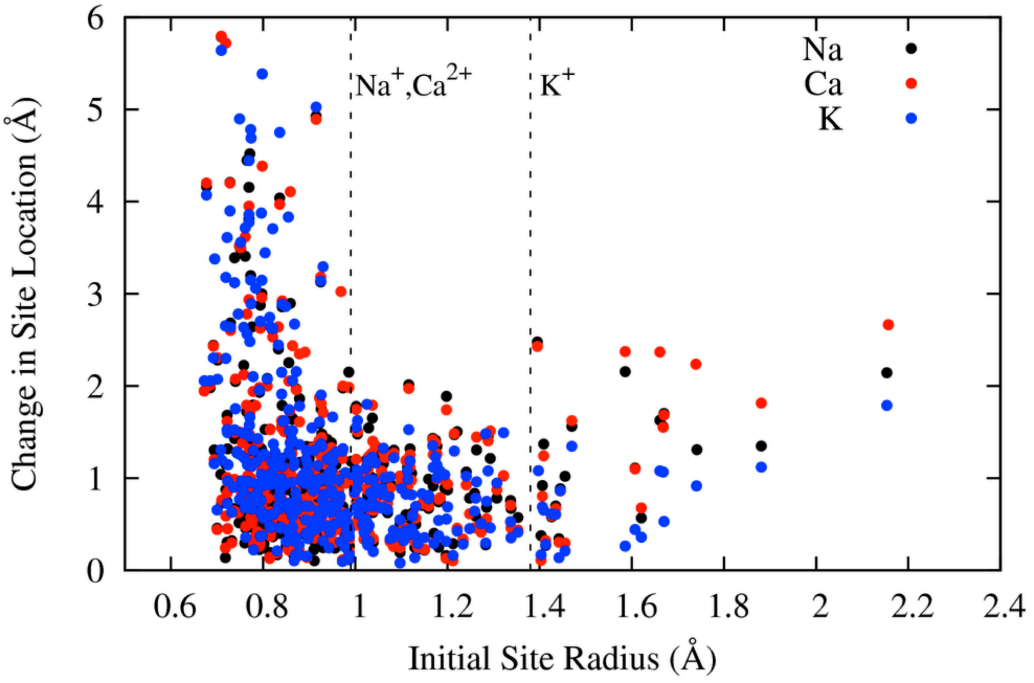

FIGURE 5.19: The distance between the initial site and final site for each cation in the metakaolin structure. The ionic radii are shown by the dashed lines at 1.0 Å and 1.38 Å .

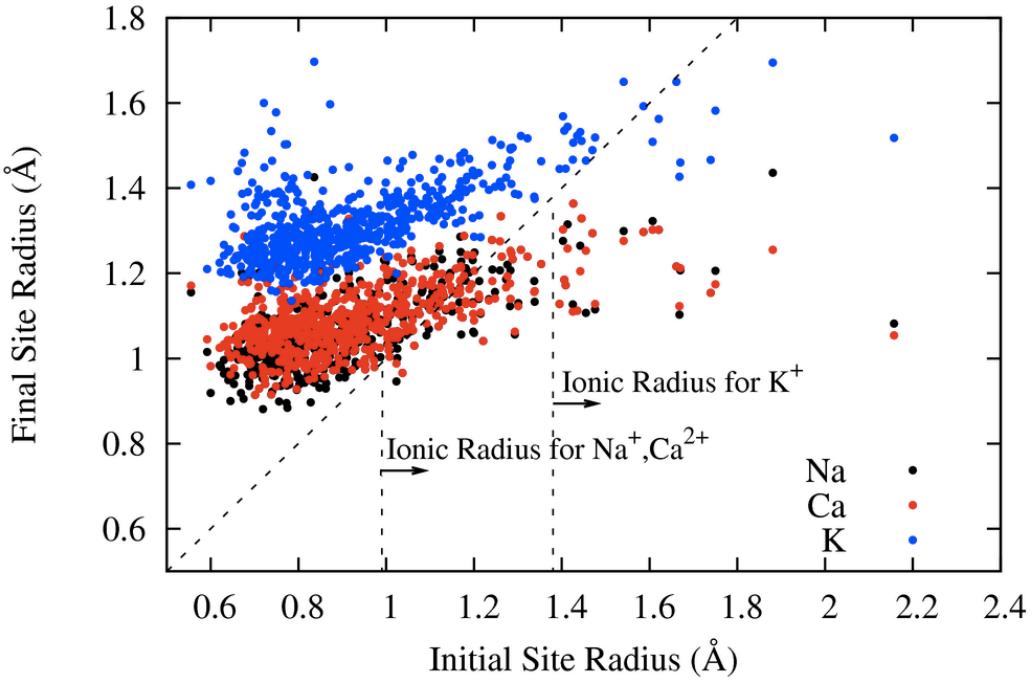

FIGURE 5.20: The relationship between the initial and final interstitial site radii. Similar to kaolinite, the smallest sites undergo the largest change in size, however, unlike in kaolinite several sites showed reduced final site radii after optimisation (located on the right of the $r_{initial} = r_{final}$ line).

The final site radii are calculated to investigate the defect environments for the interstitial cations after optimisation. The relationship between the initial and final site radii shown in Figure 5.20. Similar to the kaolinite structure, the smaller interstitial sites produce the largest changes in site radius after optimisation, however, some of the final sites also demonstrate a decrease in the site radius after optimisation, which is not observed in kaolinite. The radii at which the decreases occur are > 1.0 Å for sodium and calcium and > 1.6 Å for potassium, which are similar to the values for the respective ionic radii. In all cases where the sites decrease in size, the initial site radius is larger than the ionic radii for the ions, given in Table 5.2.

The distribution of final site radii is given in Figure 5.21. Each cation causes the distribution of site radii to decrease in spread and centred around the approximate ionic radius for each cation. Sodium redistributes the site radii around $1.07 \pm$

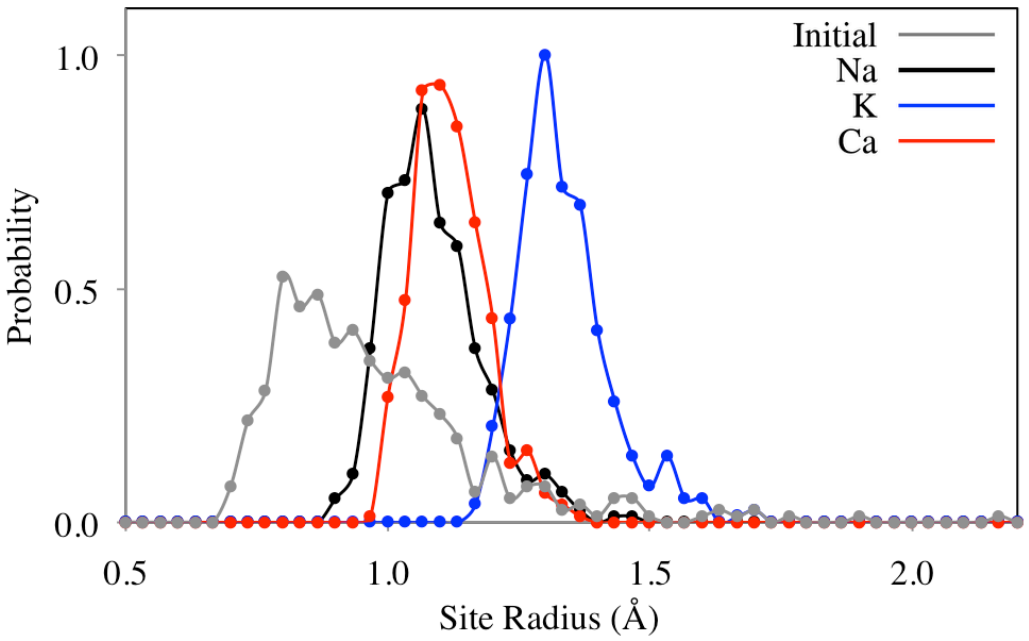

FIGURE 5.21: The normalised probability distribution of the site radii for the three interstitial cations before (initial) and after optimisation.

0.09 Å, calcium to 1.10 ± 0.07 Å and potassium to 1.32 ± 0.09 Å. All three ions increase the average cavity size, with defect sites with radii larger than the ionic values decreasing in size, and the smaller sites increasing in size. Of the three cations, calcium has the greatest effect with only 4% of the sites demonstrating final radii below the ionic value after optimisation. In comparison sodium has 21% of the final interstitial sites with radii below the ionic value, and potassium has 77%.

The investigation of the size of the defect sites prior to and after optimisation in metakaolin thus far demonstrates that the defect ions generally relocate to positions where the nearest structural atom is approximately located at the ionic radius for the interstitial ion. Comparing the site potentials in the final sites after removing the defect ions (Figure 5.22) show that the electrostatic potentials also differs dependent on the type of interstitial ions tested. The sodium and potassium ions demonstrate that while the increase in ionic size produces an increase in final site radius, the final site potential is approximately the same.

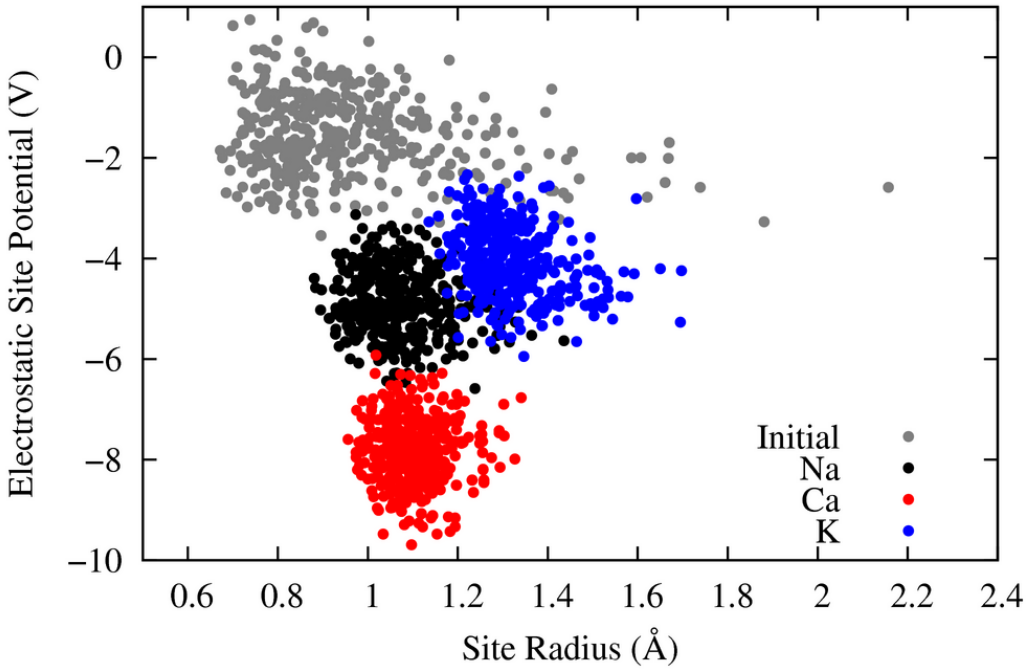

FIGURE 5.22: The final site potential after optimisation compared to the final site radii for each cation tested in the metakaolin structure is shown. The grey points are the initial site radii with corresponding initial site potentials.

The slightly less negative charge at the site occupied by potassium ions may be due to the surrounding ions in the structure being located further away as the size of potassium is greater than sodium and thus resulting in a larger cavity. However, although calcium and sodium produce similar final site radii, sites that had the calcium ion as a defect have a more negative final site potential.

The effect of the ions on the surrounding structure of the interstitial site was investigated by determining the local environment around the ion after optimisation. The partial radial distribution function for each cation interaction was calculated and averaged over all sites tested (see Figure 5.23 to 5.25), with the area under the first peak for each interaction used to determine the coordination environments. The oxygen peak is the strongest interaction for all three cations, and the resultant coordination of the ions with the oxygen atoms is calculated using a cut off of 3.0 Å. Calcium has a larger average coordination with oxygen of 6.6 compared to 5.6 for sodium and 5.8 for potassium. Since both the sodium

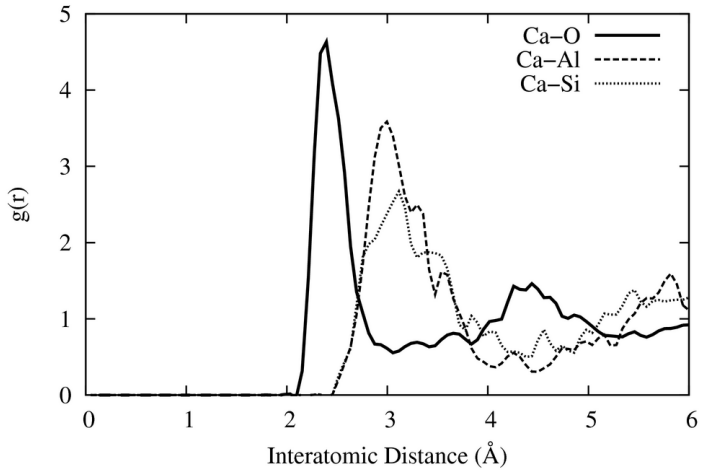

FIGURE 5.23: The partial RDF calculated for the Ca–Al,Si,O interactions.

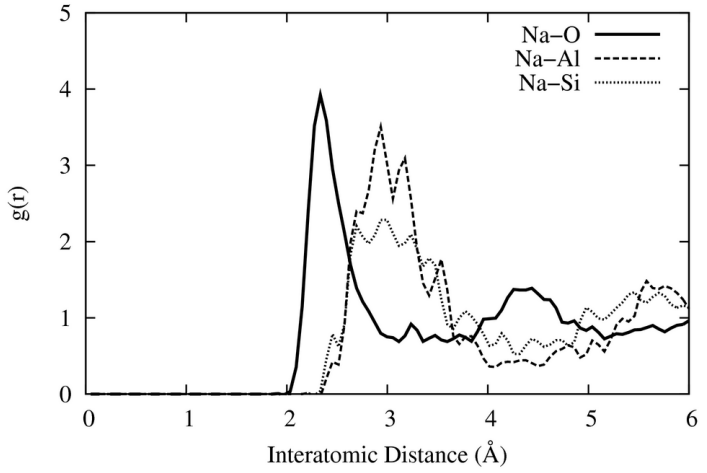

FIGURE 5.24: The partial RDF calculated for the Na–Al,Si,O interactions.

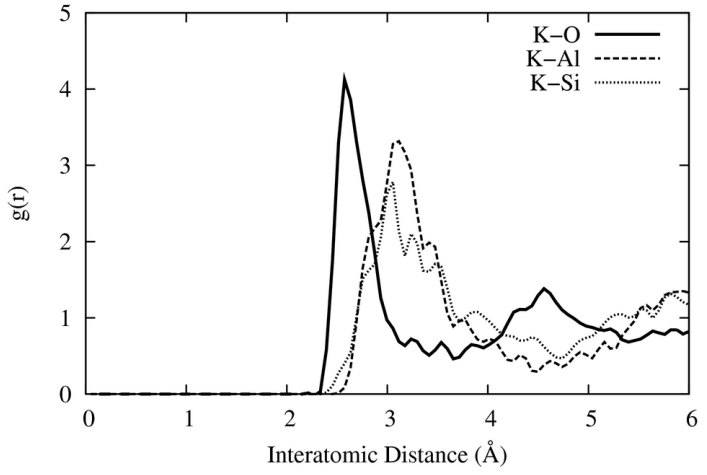

FIGURE 5.25: The partial RDF calculated for the K–Al,Si,O interactions.

and calcium ions have similar final site radii, the local environment for calcium thus includes additional oxygen atoms to increase the coordination. The overall increase in attraction between the calcium and oxygen ions due to the increased positive charge on the calcium compared to the potassium and sodium ion results in greater changes the local structure around the interstitial site as more oxygen ions are included.

The effect of the interstitial ions on the Al-O and Si-O interactions that make up the surrounding cavity is investigated by calculating the number of Al, Si and O ions that are present in the aluminosilicate network within a cut off of 4.5 Å (Al and Si) and 3.5 Å (O) of the interstitial site for each defect ion. The average concentration of Al and Si atoms before and after optimisation are given in Table 5.4, and show that whilst the number of aluminium ions decreases, the number of silicon ions increases consistently across all three interstitial ions. Sodium and potassium have similar effects on the local structure with calcium demonstrating the largest changes in concentration the interstitial cation.

TABLE 5.4: The average number of Al, Si and O atoms located near the interstitial cation site, calculated before and after relaxation.

Ion	n(Al)	Δn	n(Si)	Δn	n(O)	Δn
Initial	8.3 ± 1.6	-	7.0 ± 1.3	-	7.2 ± 1.9	-
Na	7.5 ± 1.5	-0.8	7.5 ± 1.4	$+0.5$	7.2 ± 1.3	0
K	7.5 ± 1.5	-0.8	7.5 ± 1.4	$+0.5$	7.6 ± 1.7	$+0.4$
Ca	7.3 ± 1.5	-1.1	7.8 ± 1.4	$+0.8$	8.1 ± 1.5	$+0.9$

The cations are initially located in sites with higher concentrations of aluminium present, and this is due to the disordered nature of the Al layers providing the largest cavities for the interstitial defects. However, after optimisation the defect ions tend to relocate to sites with higher concentrations of silicon, similar to the cations in kaolinite. The calcium ion shows the greatest attraction to these site, with the increased attraction to the oxygen atoms in these locations resulting in some structural modification of the network to include more oxygen atoms in the cavity environment that in the cases of sodium and potassium.

Cation Inclusion in 80% De-hydroxylated Metakaolin

The effects of the ions in geopolymerisation are linked to different rates of dissolution [4, 7, 73, 80], regardless of source material. In the case of metakaolin, different concentrations of hydroxyl content are often present in the source materials and as such the investigation of a partially de-hydroxylated metakaolin structure is conducted to verify the effects of the cations with hydroxyl groups present in the structure. The 80% de-hydroxylated structure is chosen since metakaolin structures with water contents of approximately 20% are used in geopolymerisation. The same procedure as in the 100% de-hydroxylated metakaolin structures is conducted on an 80% de-hydroxylated structure, with 206 interstitial sites investigated.

The distribution of the initial site radii, given in Figure 5.26, show that the 80% de-hydroxylated structure has a more even distribution of site radii with initial values ranging from 0.68 Å to 1.65 Å. This is a smaller range than the 100% de-hydroxylated structures, which had site radii from 0.65 to 2.18 Å. The calculated porosity for the 80% structure of $\varepsilon = 0.65$ is higher than the 100% structure with a porosity of $\varepsilon = 0.52$, showing that the complete de-hydroxylation of the kaolinite leads to fewer, but on average larger cavities being developed within the metakaolin structure.

After optimisation the interstitial cations generally produce the same effects as in the 100% de-hydroxylated structures, with the corresponding results given in Figures C.7 to C.9. However, the analysis of the concentrations of the ions around the final defect sites showed some differences from the 100% de-hydroxylated results. The change in aluminium and silicon coordination within the vicinity of the interstitial sites after optimisation is given in Table 5.5.

There is still a preference for the cations to be located in cavities with higher silicon concentrations, however, there is now also an increase in the concentration

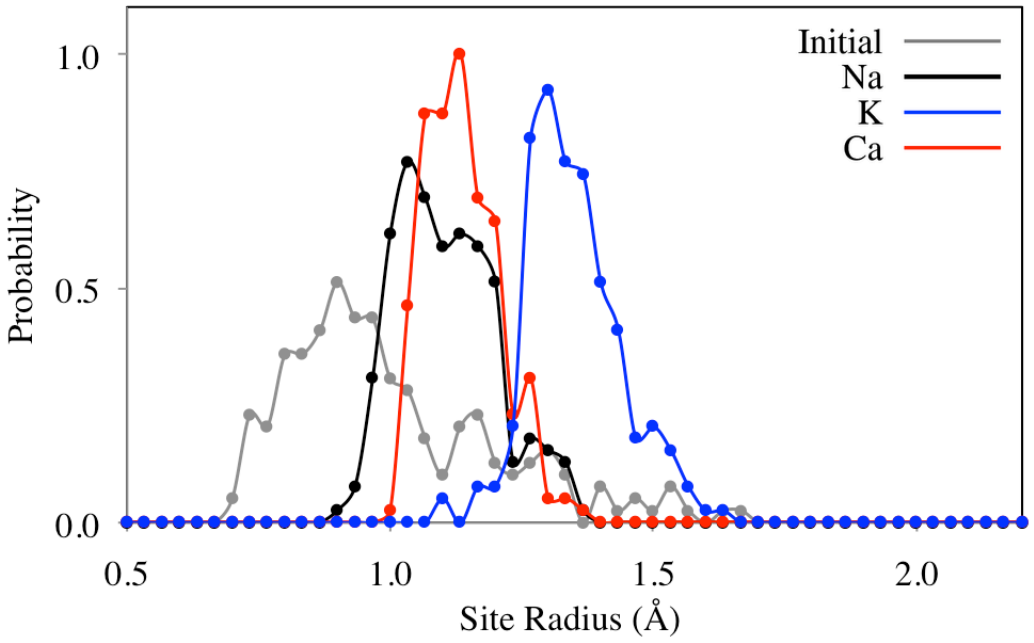

FIGURE 5.26: The normalised probability distribution of the site radii for the three interstitial cations before and after optimisation for 80% de-hydroxylated metakaolin.

of aluminium in the immediate vicinity of the cation. This indicates that the presence of the hydroxyl groups in the structures results in the cations being attracted to sites bound by both Al and Si polyhedra. The hydroxyl groups are bonded to the aluminium ions, and thus are responsible for the increase attraction of the interstitial cations to the aluminium polyhedra. The interactions between the hydroxyl groups and the cations are similar to those in site 4 in the kaolinite structures. Calcium once again produces the strongest attractions, however, the

TABLE 5.5: The average number of Al, Si and O atoms located within 4.5 Å (Al and Si) and 3.2 Å (O) of the interstitial cation site in the 80% de-hydroxylated metakaolin structure.

Ion	n(Al)	Δn	n(Si)	Δn	n(O)	Δn
Initial	7.5 ± 1.5	-	6.5 ± 1.1	-	6.9 ± 1.2	-
Na	8.9 ± 1.7	+1.4	8.5 ± 1.6	+2.1	7.3 ± 1.1	+0.4
K	7.7 ± 1.3	+0.2	6.5 ± 1.0	+0.1	7.6 ± 1.5	+0.7
Ca	9.0 ± 1.7	+1.5	8.6 ± 1.9	+2.2	7.9 ± 1.1	+1.0

changes due to sodium are now more in line with the calcium ion than with potassium. This is different to the 100% de-hydroxylated structures and indicates that the presence of hydroxyl groups changes the nature of the interactions of the defects in the aluminosilicate network by increasing the influence of ionic size over ionic charge.

5.5 Summary

The nano-porous structure of metakaolin was identified and characterised and the cavities used as sites for the inclusion of interstitial sodium, potassium and calcium defect ions. Ionic charge was shown to influence the locations of the defect sites after optimisation, with the larger potassium ion preferring larger sites compared to sodium and calcium. Ionic charge however was also shown to be a significant factor in the interaction of the defects with the structure. The cavities within the structures were primarily bound by oxygen comparisons of the final site locations of sodium and calcium show that although the site radii were similar, calcium interstitial defects prefer sites with higher concentrations of oxygen atoms in the surrounding environment, as well as increased concentrations of Al and Si. This greater interaction of calcium with the aluminosilicate structure compared to sodium and potassium has implications for the development of the aluminosilicate network in the formation of a geopolymer.

The inclusion of hydroxyl groups in the structure affected the cation influence with the cations interacting with greater concentrations of structural aluminium than silicon than in structures where no hydroxyls were present. Consequently, both the choice of alkali cation in the geopolymer activating solution as well as the level of hydration of the source materials are important contributors to the variations in the observed properties of geopolymers formed in different synthesis conditions.

Chapter 6

Surface Interactions of Kaolinite and Metakaolin with Water

Geopolymerisation is initiated by the dissolution of the aluminosilicate source materials such as metakaolin and kaolinite in alkaline activating solutions. Variations in the compositions of the materials and solution alkalinity are known to influence the dissolution rates and consequently the properties of the geopolymers [17, 31], however, the atomic scale interactions responsible for these differences are unknown. In order to fully understand the dissolution process in geopolymerisation, the influence of an aqueous environment on the source materials must first be investigated. In this chapter an atomic-scale investigation of the kaolinite and metakaolin surfaces is presented, and the resulting surface-water interactions provide evidence for the structural reorganisations on the surfaces of these materials that may lead to the various dissolution phenomenon observed experimentally.

6.1 Introduction

The extent of dissolution of kaolin minerals and metakaolin in the geopolymerisation process has been the topic of several investigations [9, 19, 25, 28]. A complication that is inherent in all the experimental studies is that the size, shape and composition of raw kaolin minerals [20, 73] and the degree of calcination undergone to produce metakaolin [356, 357] result in large variations in the precursor

characteristics. These variations lead to considerable spread in the reported results for seemingly similar materials; Granizo *et al.* [44] produced two different geopolymer materials through the dissolution of metakaolin with NaOH, despite using two similar kaolinite precursors to form the metakaolin.

The dissolution of metakaolin in geopolymerisation releases silica and alumina monomeric species into solution that undergo re-polymerisation to form the Al/Si network that is characteristic of geopolymer gels [7, 48]. Obtaining a pure kaolinite or completely de-hydroxylated metakaolin sample is difficult and can make undertaking the experimental investigations into the mechanisms involved in the dissolution process challenging. Neutron diffraction experiments [23] show that the geopolymerisation reaction with metakaolin and hydroxide activating solutions initially exhibit rapid rates of aluminium dissolution, followed by a stoichiometric release of silicon and aluminium. Understanding the atomic level surface–solution processes that lead to the liberation of the different species is important in developing an understanding of the geopolymer formation process. Computational chemistry in these circumstances is valuable, as the fundamental interactions can be investigated without the need to account for impurities or technique dependent limitations.

Computational investigations of the dissolution process in geopolymerisation generally focus on the interactions of the activating solution with partially hydrated metakaolin structures. Recent coarse grained Monte Carlo simulations of metakaolin in NaOH [26] showed that the presence of soluble silicate species inhibited the overall dissolution of metakaolin, with higher rates of aluminium liberation causing precipitation of the aluminosilicate gel on the surfaces. The interactions that are fundamental to the release of these units into solution were not explored, nor was the presence of water investigated. Metakaolin is hygroscopic [358] and readily hydroxylates in the presence of water [112, 359]. Thus the dissolution of metakaolin in geopolymerisation may be influenced by the surface

hydration prior to synthesis and the influence of the water molecules present in the activating solution.

Preliminary investigations into the (001) kaolinite and pseudo-(001) metakaolin surfaces, depicted in Figure 6.1, show that the metakaolin surfaces have more complex topographies compared to kaolinite, with valleys and crests resulting from the buckling of the layers. The differences in both surface composition, hydration and topography could result in considerable differences in the dissolution behaviour of these materials in the geopolymerisation reaction, and thus the atomic interactions of kaolinite and metakaolin in an aqueous solution must be explored before the effects of the caustic ions and solution alkalinity can be investigated. The details for the choice and generation of these surfaces are given in greater detail in Sections 6.3 and 6.4.

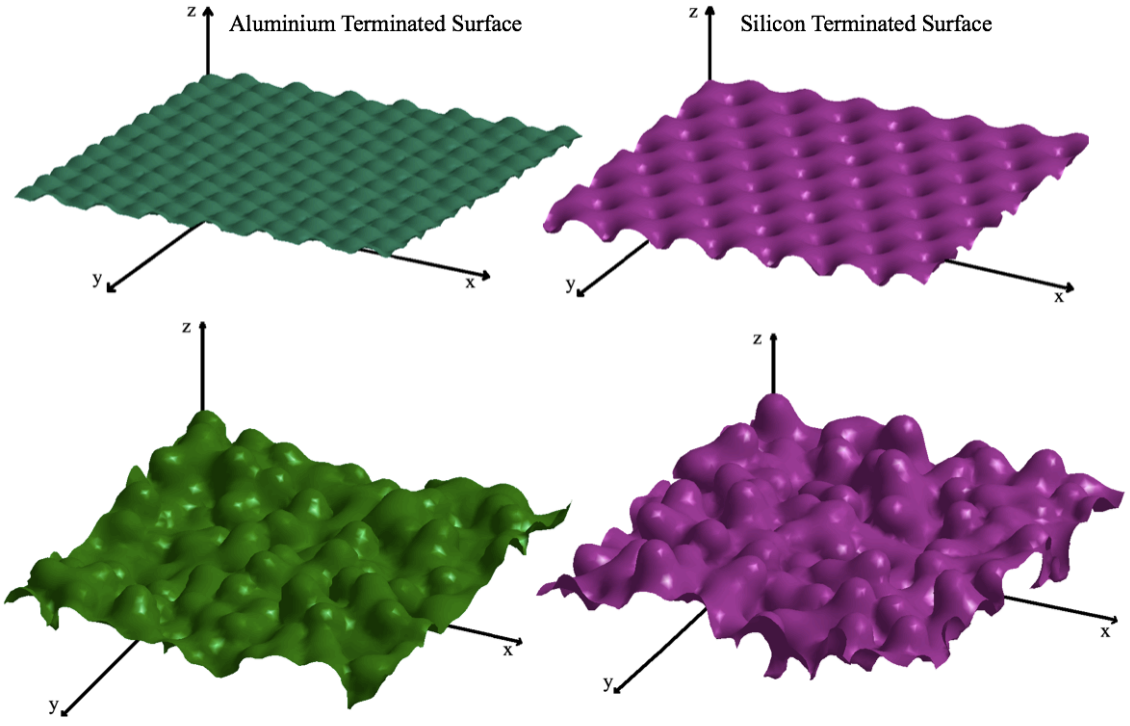

FIGURE 6.1: The surface topography for the two possible kaolinite (001) surfaces (top) and an approximation of the two metakaolin (001) surfaces (bottom) are shown. The surfaces are simulated by rolling a spherical probe of radius 0.5 Å over the atomic surface provded by the Van der Waals radii of the atoms.

6.2 Simulation of Surfaces

Computational simulations of surfaces have been used to investigate a variety of phenomena such as surface stability, morphology, wetting, adsorption and the interactions of different ions with mineral surfaces [131, 140, 227, 307, 360–363]. Approximations to real surfaces are used as in reality very few surfaces are completely clean and free of defects and impurities. This does not detract from the usefulness of the methodology, and computational methods have aided in understanding the interactions and properties at the interfaces of layered materials that would otherwise be difficult to measure in a laboratory environment [139]. Examples include simulations of the inter-layer swelling in clay minerals, which is now well understood [364–367], and the interactions of clays with organic molecules such as in surfactant–modified montmorillonites [368, 369].

Calculations of bulk properties from a single unit cell are possible because the three–dimensional periodicity effectively simulates the bulk of a material. Surfaces are by definition two–dimensionally periodic but in simulations some consideration for the bulk must be made in order to accurately represent surface phenomena. The interactions between the surface and the bulk can be included by using the two–region method, where region 1 simulates the effective surface and is relaxed while region 2 is kept fixed at relaxed bulk positions. The depth of both regions is determined by varying the depth and finding the convergence in the surface energy, which is defined as the energy required to cleave the crystal to produce the desired surface [197]. The advantage of this approach is that the effect of the bulk on the surface can be correctly described, however, surface dipoles must be compensated for or the electrostatic energy may not converge [197].

Another method to simulate a surface involves creating a three–dimensionally periodic slab structure that has two surfaces with vacuum separating the periodic images of the slab. The bulk is approximated by simulating a sufficient number

of repetitions of the structure to provide a large slab thickness such that the two surfaces do not interact with each other through the slab itself. The vacuum gap must also be large enough such that the slab does not interact with its periodic image through the vacuum gap. In such a slab calculation, the surface energy is divided by two to account for the two surfaces present. The advantage of this method is that any surface dipole moments present are easily compensated for by the dipole on the opposing surface. However, the size of the bulk is drastically reduced compared to the two-region method, consequently increasing the effect of the bulk on the surface.

Surfaces created from simulated bulk structures are achieved by cleaving the atomic system along one of the crystallographic directions. Depending on the location of the cleave, three types of surfaces can be generated [197, 370]:

1. Surfaces that consist of neutral planes.
2. Surfaces that consist of charged planes but no net dipole moment is present.
3. Surfaces that consist of charged planes that also have a net dipole moment present.

Type 1 surfaces are generally preferred in simulations, as the effects of dipole moments and surface charges can produce unrealistic results. Both can be reduced through altering the composition of the surface, however, this is more challenging if charged surfaces and dipoles are present and as such cleaves that produce type 3 surfaces are generally avoided.

6.3 Kaolinite Surfaces

In crystalline materials, the location of the surface cut results in surfaces with different relative stabilities, where stability is a measure of the thermodynamic opposition to the fracturing process in nature. Measuring the stability of the different surfaces of a material allows the morphology of a crystal to be predicted [197]. If the morphology of a material is known, the most likely surfaces involved in surface phenomenon can be predicted. Experimental crystallographic measurements also provide information on the morphologies and thus surface stabilities of crystalline materials. Electron microscope images of kaolinite [371–373] show that, like many layered minerals, the crystals are platelet-like in shape with the dominant face belonging to the (001) surface (shown in Figure 6.2).

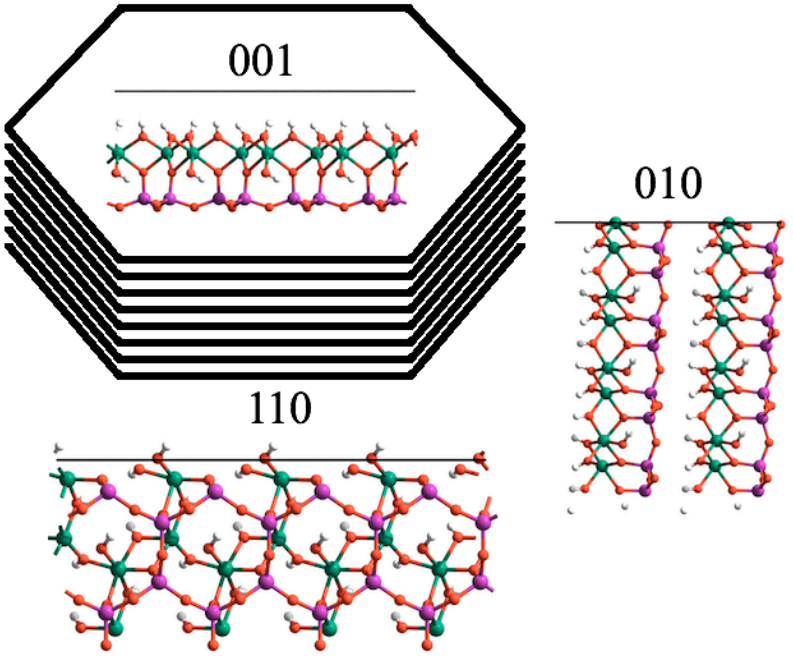

FIGURE 6.2: Kaolinite is composed of thin hexagonal platelet like crystals bound by the (001), (010) and (110) surfaces. The surface termination for each surface is shown (unrelaxed), with the solid lines representing the surface.

The crystal morphology suggests that there is a significant difference in the stability of the (001) surface compared to the (010) and (110) surfaces. This is due to the layered nature of the material, as the hydrogen bonds between the layers are cleaved more easily than the covalent bonds within the layers. In an aqueous environment the influence of the water on the dominant surfaces present are of interest due to the greater interaction area available. The kaolinite (001) surface–water interactions have been explored in several theoretical simulations using DFT [362, 363, 374], molecular dynamics [375] and Monte Carlo [140] techniques. The molecular dynamics simulations of a kaolinite slab composed of several Al-Si layers using interatomic potentials has not been previously reported and the literature results provide a source for comparison to ensure that the methods used to investigate the kaolinite and metakaolin surfaces are accurate.

6.3.1 Investigation of Slab Parameters

The slab thickness and vacuum gap size require optimisation to find the minimum values for each to accurately simulate the kaolinite and metakaolin surfaces. The image on the left of Figure 6.3 shows a surface created from the optimised kaolinite unit cell from Chapter 4, with the (001) surface exposed. Cleaving through the inter-layer space results exposure of either the Al–OH or Si–O terminated surfaces. A slab generated with both surfaces exposed on opposite ends is shown in Figure 6.3).

The kaolinite slab was produced by replicating the kaolinite unit cell along the *c*-direction to a total of 7 Al-Si layers. The resultant structure was relaxed using GULP with several different vacuum gap heights under constant volume conditions. A comparison of the calculated slab energies and vacuum gap heights is shown in Figure 6.4, showing that a minimum vacuum gap of 30 Å is required to minimise the effects of the slab interaction with its periodic image.

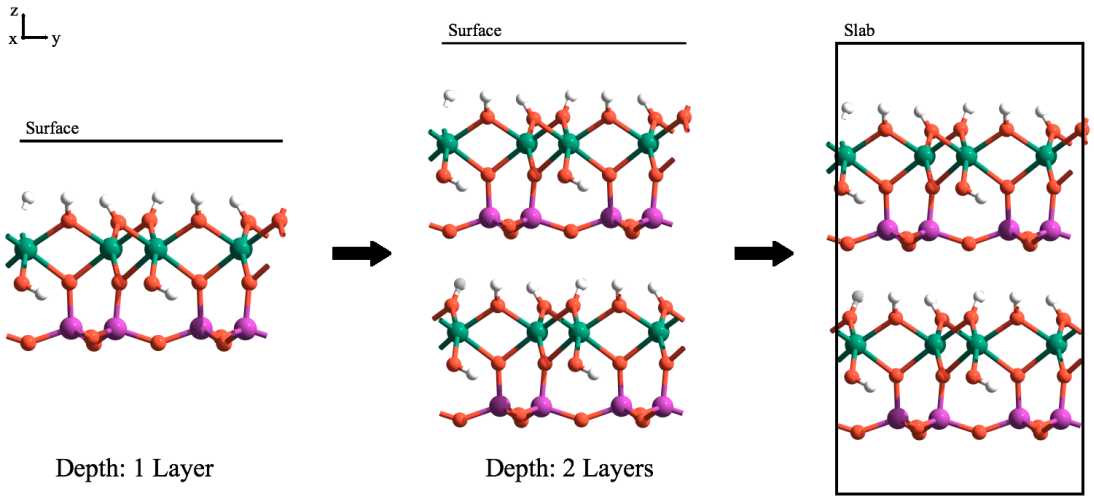

FIGURE 6.3: The figure on the left shows the kaolinite (001) surface and is two-dimensionally periodic. The addition of a second layer (centre) expands the depth of the surface and the imposition of a third dimension (depth) creates a kaolinite slab with a depth of 2 layers (right).

The 30 Å vacuum gap was then used in the optimisation of the slab thickness. The kaolinite unit cell was replicated one layer at a time with the vacuum gap and relaxed in GULP. The slab energy per unit was calculated and the results, given in Figure 6.5, show that this energy converges at approximately ten Al–Si layers.

The final kaolinite slabs generated for the investigation of the surface–water interactions include both a Si–O and Al–OH dominated surface, with a total slab thickness of 36.22 Å and a vacuum gap of 30 Å. To provide surface areas equivalent to those used in the metakaolin simulations, the slabs were replicated in both surface directions, with the final surfaces having dimensions of $a = 36.46$ Å and $b = 67.95$ Å. The increased interaction area for the water molecules increases the statistical significance of the results reported.

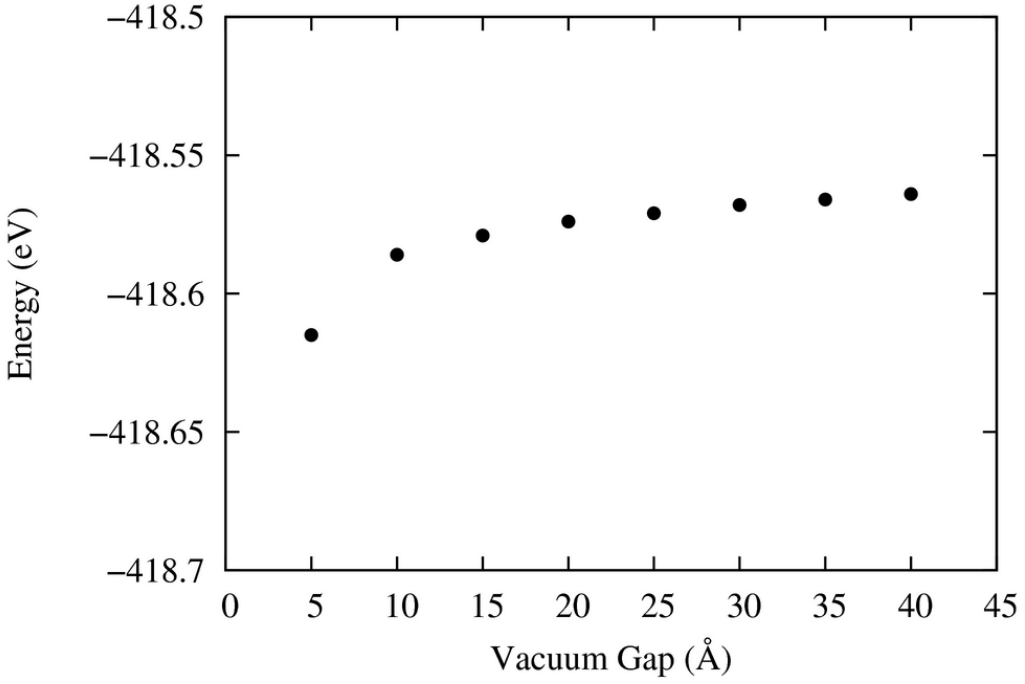

FIGURE 6.4: The slab energies calculated for the kaolinite structure shown as a function of increasing vacuum gap distance between the periodic slab images. The energy converges at approximately 30 Å.

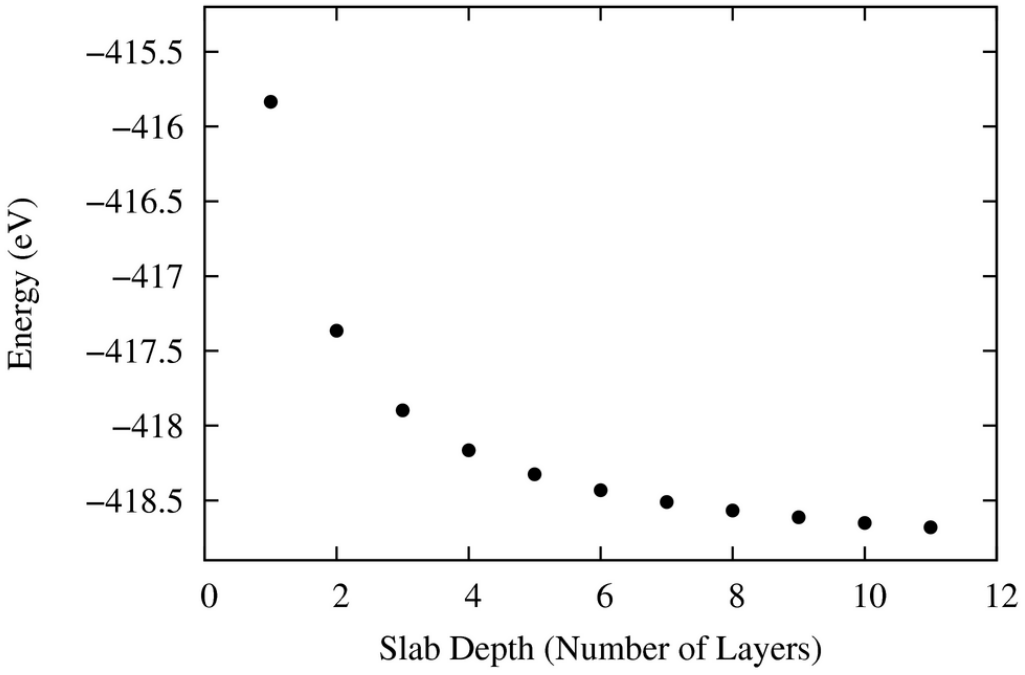

FIGURE 6.5: The slab energy as a function of slab thickness is shown, where the slab thickness is a measure of the number of Al–Si layers of kaolinite present. At approximately 10 Al–Si layers the surface energy converges.

6.4 Metakaolin Surfaces

Electron microscope images of metakaolin [82, 373] show that although the particles do not have as smooth and uniform a shape as kaolinite, the same approximate morphology is maintained. The similarities with kaolinite result in the assumption that an approximation of the (001) surface in metakaolin is the most likely stable configuration, and thus it is chosen as the surface investigated. Cleaving the metakaolin bulk structure to reveal this pseudo-surface results in highly disordered and heterogeneous surfaces, and determining the most stable surface terminations likely to be present in metakaolin requires further investigation.

Bulk metakaolin structures produced in Chapter 4 are composed of 5 Al-Si layers. Doubling these in the c-direction provides the 10 Al-Si layers determined suitable for the kaolinite tests. This depth is considered sufficient as the susceptibility of the structure to surface-bulk effects compared to kaolinite is expected to be diminished due to the collapse of the inter-layer spacings. Two metakaolin slabs were created from two of the 100% de-hydroxylated metakaolin structures from Chapter 4, and the initial dimensions of these slabs were ($a = 31.73$, $b = 32.41$, $c = 71.88$) Å and ($a = 32.48$, $b = 32.62$, $c = 70.67$) Å.

The disordered nature of metakaolin results in surface compositions that are highly dependent on the location of the surface cut. This is due to both the buckling of the Al/Si layers and the migration of the cations (particularly the aluminium atoms) through the structure during the de-hydroxylation process. Consequently, the two metakaolin slabs generated by using cleaving at a specific z-coordinate produced surfaces composed of a mixture of Al and Si atoms, with the majority of these atoms in under-coordinated states. This configuration is neither energetically favourable, nor is it supported by the microscopy information from the literature that shows rough and slightly buckled sheets present in metakaolin particles [373].

The most likely location for the cleave to create a realistic representation of a metakaolin surface is between an aluminium and silicon layer. Since the aluminium and silicon layers share oxygens, this does not entirely negate the presence of under-coordinated surface cations, and as such additional oxygen atoms are added to the structure to ensure that each cation involved in the surface cleave maintains its bulk coordination. This process is summarised as follows:

1. The bulk metakaolin structure is doubled in the c-direction and the supercell is cleaved along a randomly chosen z-coordinate (Figure 6.6 A and B);
2. Cations located at the cleave are relocated as necessary to create an Al and Si surface (Figure 6.6 C);
3. Oxygen atoms are added to any under-coordinated surface cations to maintain bulk coordination. (Figure 6.6 D).

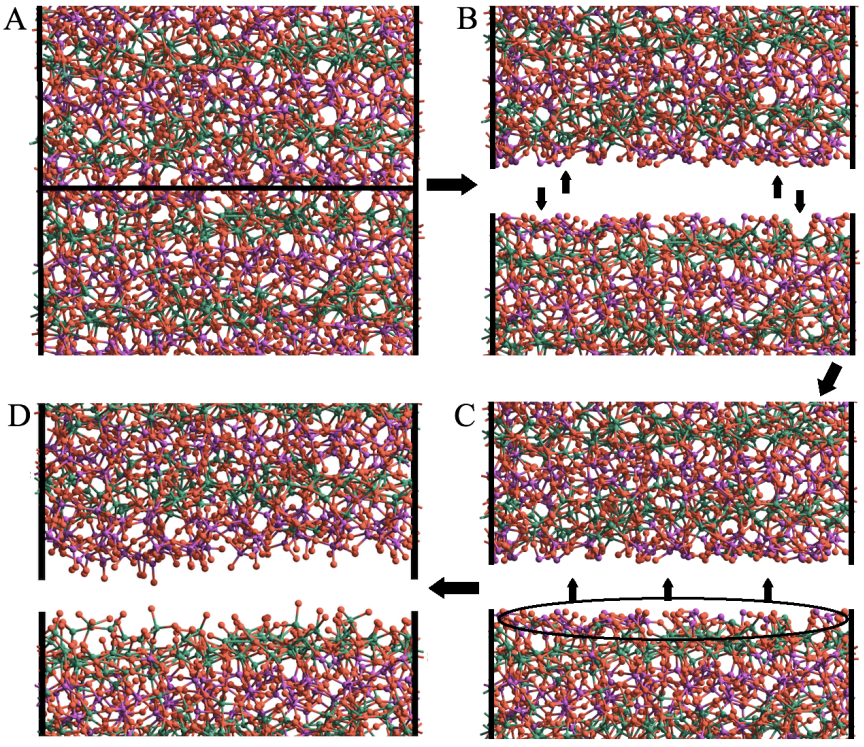

FIGURE 6.6: A close up of the generation of a metakaolin slab. The bulk structure in A is cleaved through a silicon layer, giving B. The silicon atoms (and associated oxygen atoms) are relocated to the opposite surface in C and in D the under-coordinated Al surface atoms have oxygen atoms added to maintain the coordination present prior to the cleave.

6.4.1 Hydration of the Metakaolin Surfaces

The decision to maintain the bulk coordination's of the surface atoms results in negatively charged metakaolin slabs due to the additional oxygen atoms. The negative charge on the slabs produce unrealistic results and thus needs to be compensated for prior to the simulations with water. Hydration of the metakaolin surfaces provides a realistic solution to reducing the surface charge. The hydration of a surface requires one oxygen atom and two hydrogen atoms to be added to the surface, effectively adding a dissociated water molecule.

The non-reactive Teter potential model does not allow for the dissociation of a water molecule to be simulated, and thus the hydration of the metakaolin surfaces was completed manually. This involved the addition of a hydroxyl oxygen–hydrogen pair to the surface, and converting an existing surface oxygen atom to a hydroxyl group with the addition of another hydrogen atom. Continuing the process on page 166, the following following steps are now included:

4. Locating an oxygen atom added to under-coordinated surface Al/Si atoms in the slab generation process;
5. Hydrogenating the identified oxygen atom to form a hydroxyl group;
6. Hydrogenation of an existing oxygen atom to form a second hydroxyl group;
7. Repeating steps 4-6 until the total slab charge is zero.

If there are initially N additional oxygen atoms added to the under-coordinated surface, then a total of $2N$ hydroxyl groups are required to balance the charge of the slabs. The process of adding a hydrogen atom to an oxygen atom to form a hydroxyl group is referred to as a 'hydroxylation'.

Identification of the most likely hydroxylation sites on the surfaces was determined according to the conclusions from Du and Cormack [376] and Adiga *et al.* [153]. In these investigations of silica and amorphous alumina surfaces, several sites that were more amenable to hydroxylation were identified. These were, in order

of preference, the non-bridging oxygen (NBO) atoms, over-coordinated oxygen (OCO) atoms and strained cation rings. The NBO atoms are only bonded to one silicon ion, the OCO atoms are coordinated with two cations, also called bridging oxygen atoms, and strained silicon rings consist of closed $-(\text{–Si–O–Si–O–})_n-$ rings where the number of Si atoms defines the size of the ring and is strained if N(Si) $\neq$ 6 atoms.

It is assumed that Al- and Si-terminated surfaces on the metakaolin slabs behave similarly to the top few Å of the surfaces of the amorphous equivalents, and thus the NBO and OCO atoms on both surfaces are classified as sites with higher hydroxylation probabilities than the remaining surface atoms. The surfaces for the slab in Figure 6.6 D are shown in Figure 6.7, with the NBO atoms in blue. This slab had $N = 80$ added oxygen atoms, and thus a total of 160 hydroxylation sites were required to neutralise the charge on the slab. The two surfaces provided a total of 125 NBO sites for hydroxylation, all of which were hydroxylated and

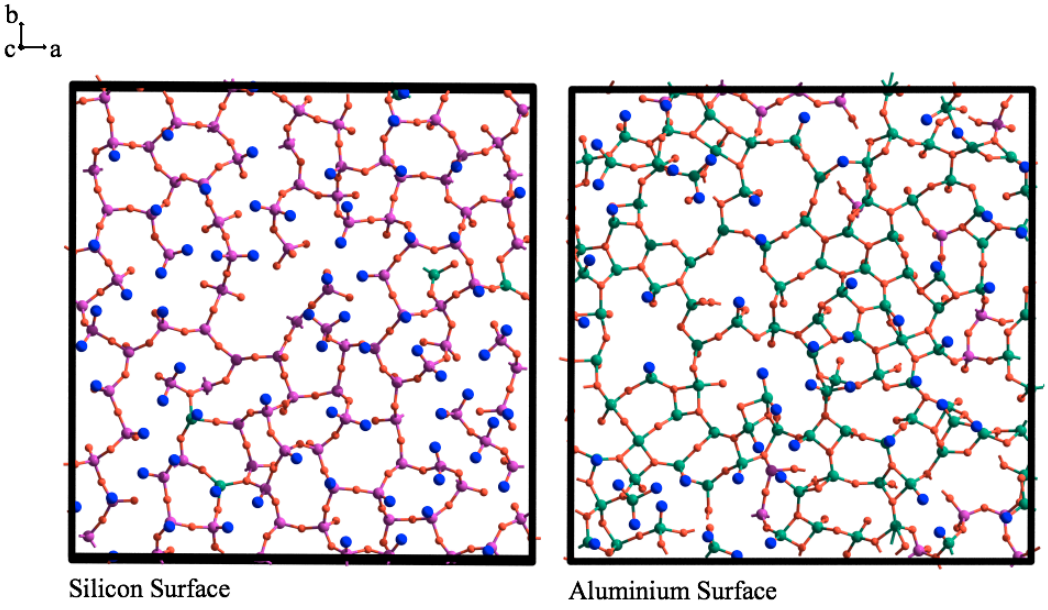

FIGURE 6.7: The aluminium- and silicon-terminated surfaces from the same metakaolin slab. The surfaces shown are the first 8 Å of each side of the slab, and the non-bridging oxygen atoms are shown in blue.

the resultant slab simulated at 300 K for 500 ps using a 1 fs time step in the NVT ensemble to allow the surfaces to adjust to the additional atoms.

The slab still required 35 hydroxylation sites to neutralise the charge, and these sites were sourced from the over-coordinated oxygen atoms. The silicon surface provided none of these sites, whilst the aluminium surface provided a possible 57 OCO sites, 22 more than required. The identified OCO sites are shown in red in Figure 6.8.

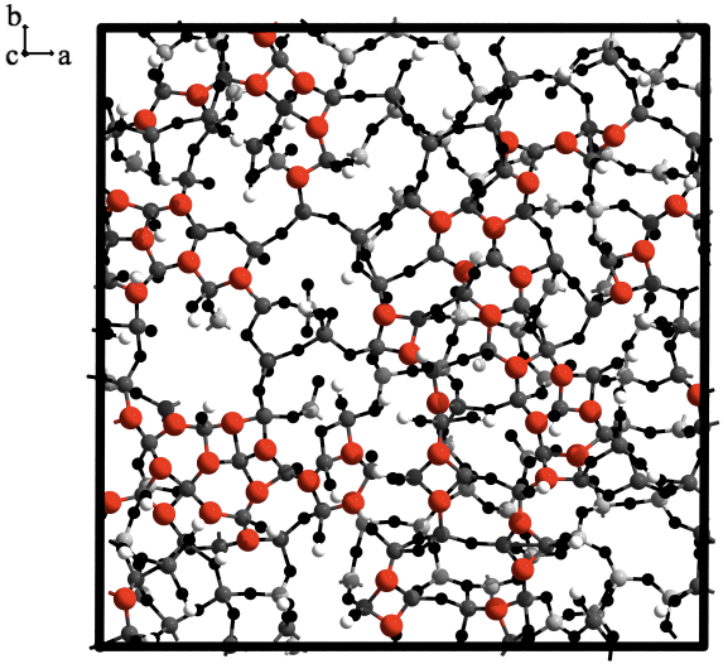

FIGURE 6.8: The aluminium surface showing the possible OCO sites as large red spheres. The small black spheres represent oxygen, dark grey is aluminium and white is hydrogen.

Since there was an excess of sites available, an evaluation of the Al surface was necessary to determine the most suitable OCO sites. Initially, every site was hydroxylated individually and the structures were relaxed using the zero minimisation routine in DL_POLY.[1] Each site was simulated in this manner, and once

[1]The zero minimisation routine in DL_POLY is not the most vigorous algorithm to find the minima, however, it is a suitable method to dissipate the strain energy and provides a good starting point for the molecular dynamics simulations.

all 57 sites were tested, the final energies compared to find the 35 sites providing the most stable slab configurations, which were therefore the most likely to be hydroxylated in solution.

The difference in slab energy between the least and most favourable sites was 7.2 eV, showing that within the surface area sampled there are considerable differences in suitability for the location of the hydroxyl groups. The most favourable sites are located primarily around high concentrations of under-coordinated aluminium atoms, and are grouped together rather than randomly distributed across the surface. This indicates that the aluminium surfaces of metakaolin are composed of regions that may be more susceptible to hydroxylation than others.

The initial hydroxylation process was completed under the assumption that the surfaces were flooded with water and the hydroxylation occurred initially at the NBO sites and then at the OCO sites. However, the hydroxylation of the most favourable site on a surface may change the surrounding environment to provide another suitable site for hydroxylation that was not previously available. This introduces a dependency on the location of the previously hydroxylated site on future hydroxylation events. To investigate whether this 'step-wise' approach makes a considerably difference to the final surfaces, a second hydroxylation of the surfaces was conducted. The initial site was chosen as the most favourable site from the previous investigation of the surface, and after each conversion of a surface oxygen to a hydroxyl group the resulting surface was tested to determine the next most favourable site. Figure 6.9 shows an example of two surfaces produced in this approach.

In each subsequent hydroxylation of the surface in this step-wise approach, the surrounding structure is altered slightly to produce new possible sites for hydroxylation. Testing of the new surfaces for favourable sites after each step also shows that the process causes the local structure of the surface immediately around the site to become more favourable for hydroxylation than sites located further

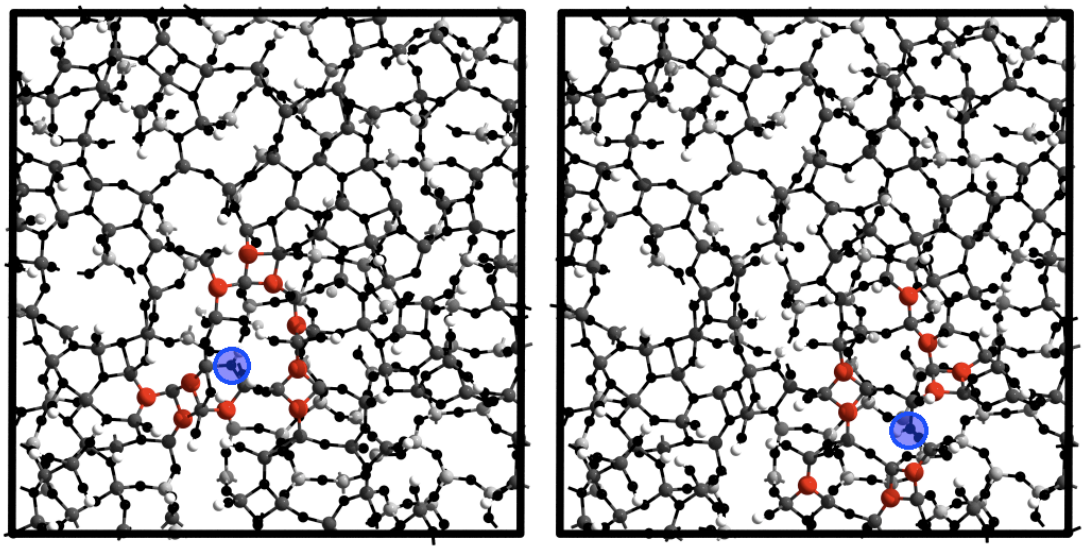

FIGURE 6.9: Two example surfaces produced during the step-by-step hydroxylation of the aluminium surface. The surfaces show the localisation of the ten most favourable sites (red) determined after a single OCO is hydroxylated (circled in blue).

away from the initial site. This provides further evidence that the hydroxylation of the metakaolin surfaces is likely to occur in localised regions and that the hydroxylation of a single site leads to an increased probability that subsequent hydroxylation sites will occur within the vicinity of the initial site.

The step-wise hydroxylation approach was compared to the equivalent surface (10 OCO sites hydroxylated in one step) for the single-step approach. The difference between the calculated energies for the two slabs was 10.1 eV, with the step-wise process producing the more stable surface. The differences in energy suggest that it would be more favourable to allow the surface to hydroxylate in a gradual process in order to produce the most stable system for the simulation. However, it is intuitive that the process in the real material will involve both random sampling of favourable surface sites as well as the hydroxylation of sites produced by previous interactions. Since the step-wise process requires more computational resources compared to the single step approach, the latter method for hydroxylation is used for the slabs generated in this chapter.

Hydroxylated Surface Statistics

The final concentration of hydroxyl groups on the silicon surface is calculated as 6.53 molecules per nm^2, which is similar to the value of 6.96 molecules per nm^2 reported by Garofalini [377] for hydroxylated vitreous silica surfaces, although both values are larger than the amorphous silica surfaces simulated by Du and Cormack [376] with a value of 4.6 molecules per nm^2. The discrepancy in the results is due to the more ordered surface configurations of the silica polyhedra rings on the surfaces simulated by this study and Garofalini [377] compared to those of Du and Cormack [376]. The more ordered structure of the silica surfaces results in a larger concentration of NBO sites than on the amorphous silica structures, leading to the increase in the concentration of hydroxyl groups on the hydrated silicon surface for metakaolin.

The final concentration of hydroxyl groups on the aluminium surface is 8.18 molecules per nm^2. This is larger than on the silicon surface (6.53 molecules per nm^2), and is due to the higher degree of disorder present within the aluminium layers consequently providing more possible sites for hydroxylation. Amorphous alumina exhibits hydroxyl concentrations between 2 and 15 molecules per nm^2 [378], so the degree of surface hydroxylation is within range of experimental values.

The process of cleaving the disordered metakaolin structure creates surfaces with different final characteristics. A second slab, created the procedure from pages 166 and 167 from another metakaolin structure had $N = 91$ additional oxygen atoms, thus requiring a total of 182 hydroxylations. The structure provided 151 NBO atoms and needed another 31 (of a total of 38 possible) OCO atoms to be hydroxylated. However, regardless of the location of the surface cut, only NBO atoms are ever present on the resultant silicon surfaces.

6.5 Surface–Water Interactions

The kaolinite slab produced in Section 6.3 was relaxed in vacuum using GULP. The final surfaces were structurally similar to the bulk with all interatomic distances within approximately 0.1 Å of the bulk values. The main difference in the surfaces after relaxation is a change in the orientation of some of the hydroxyl groups on the Al surface such that the hydroxyl groups are lying almost parallel to the surface. This is consistent with the results from DFT simulations on the stability of kaolinite surfaces by Hu and Michaelides [363].

The two metakaolin slabs constructed in Section 6.4 were relaxed using the minimisation algorithm in DL_POLY, followed by an optimisation in GULP. All slabs were relaxed under constant volume conditions to maintain the 30 Å vacuum gap. The resulting three structures have silicon- and aluminium-terminated surfaces, with both metakaolin surfaces exhibiting hydroxyl groups whilst the kaolinite surface has only the Al surface hydroxylated. Slab statistics are given in Table 6.1.

Table 6.1: Slab statistics for the kaolinite and two metakaolin (MK) slabs.

Characteristic	MK Slab 1	MK Slab 2	Kaolinite
[OH] on Al Surface (nm^{-2})	8.64	9.60	12.72
[OH] on Si Surface (nm^{-2})	6.89	7.70	0
Slab thickness: c (Å)	71.88	70.67	67.95
Surface dimensions: $a \times b$ (Å)	31.73×32.48	32.41×32.62	36.46×36.22

The next stage in the simulation is to introduce water into the vacuum gap. In Chapter 3 the flexible single point charge water model was simulated with an initial 24.86 Å cubic box containing 520 water molecules. This equilibrated box is smaller than the vacuum gaps present in the slabs simulated, and as such is increased in size, with the width of the vacuum gap increased to 49.74 Å for simplicity purposes. The density of bulk water is 0.33 molecules per $Å^3$, and is used to calculate the number of molecules required to fill the vacuum.

A simulation box with the necessary cell-parameters for each vacuum gap for each slab was created and filled with the desired number of H_2O molecules. The resultant simulation cells were equilibrated at 300 K using the NPT ensemble for 200 ps. All the final water statistics are given in Table 6.2, with the calculated diffusion constants of the water in the equilibrated water simulation cells in agreement with the values reported in Chapter 3.

TABLE 6.2: Water statistics for the water simulation cells in preparation for the vacuum gaps for the metakaolin (box 1 and 2) and kaolinite (box 3) slabs.

Characteristic	Water Box 1	Water Box 2	Water Box 3
Volume of Vacuum (Å^3)	51259.04	52594.89	65692.40
Number of H_2O molecules	1732	1778	2220
Diffusion Constant (cm^{2}s^{-1})	2.46	2.48	2.45
Density of H_2O (g cm^3)	1.02	1.02	1.02

6.5.1 Kaolinite–Water Interactions

Molecular dynamics simulations from this point forward were performed using the LAMMPS [206] computational package due to increased efficiencies allowing longer periods to be sampled using fewer resources. The equilibrated box of water (box 3) was placed within the vacuum gap in the kaolinite slab. This system was equilibrated for 500 ps using the NVT ensemble at 300 K followed by a further 3 ns in ambient conditions (300 K, 1 atm) using the NPT ensemble.

The diffusion constant of the water calculated during the final 2 ns of simulation was 2.01×10^{-5} cm^{2}s^{-1}, which is much lower than the bulk value for the SPC/Fw potential model of 2.50×10^{-5} cm^{2}s^{-1}, calculated in Chapter 3. The diffusion of the water is slower due to the interactions of the water molecules with the surfaces. To investigate this further the average density of the atoms is calculated through the simulation cell and is given in Figure 6.10.

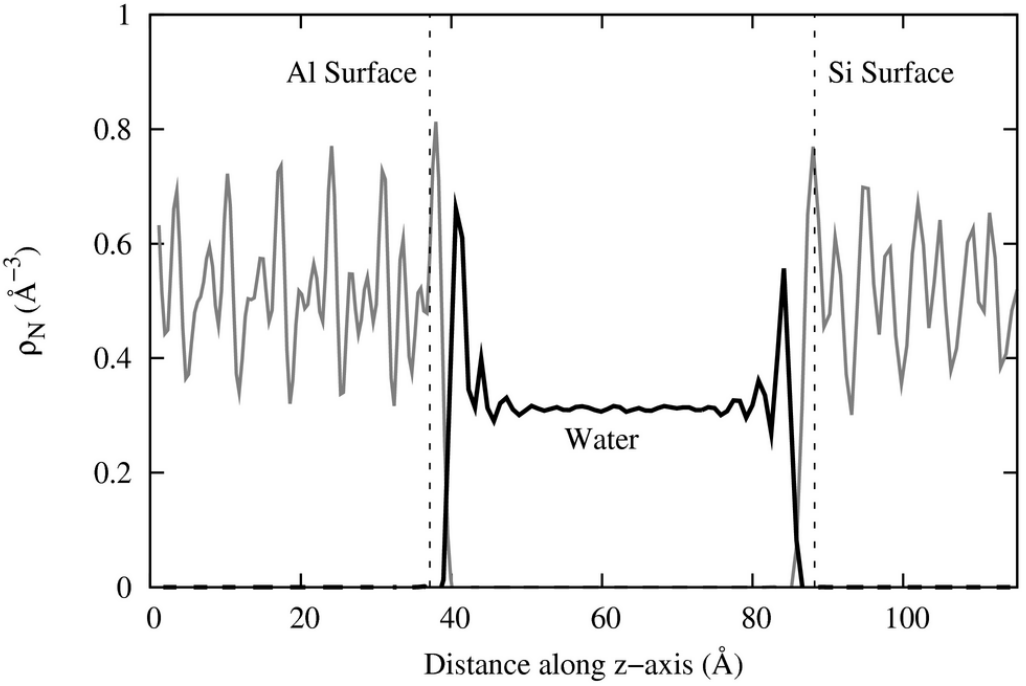

FIGURE 6.10: The atomic density profile of the simulation cell (calculated with a bin width of 0.1 Å) is shown, with the kaolinite structure shown in grey and water in black. The aluminium-terminated surface occurs at approximately $z = 38$ Å and the silicon surface at $z = 87$ Å.

There are two hydration layers present at both surfaces, with the average density of water molecules in the first hydration layer on the aluminium surface greater than that near the silicon surface. Figure 6.11 and Figure 6.12 show close-up images of the surface-interfaces for the Al- and Si-terminated surfaces respectively. The average position of the cation layer below the surface layer is taken as $z = 0$ Å in each case, with the positive z-direction chosen as away from the slab towards the water.

The location of the first hydration layer for each surface occurs at 3.5 Å from the surface Al or Si position, however, since both surfaces terminate with different species the interactions of the water with the surfaces are not the same. The location for the water oxygen atoms in the first hydration layer on the aluminium surface is 2.3 Å away from the average positions of the surface hydrogen atoms, which is in agreement with the *ab initio* molecular dynamics value of 2.2 Å [362,

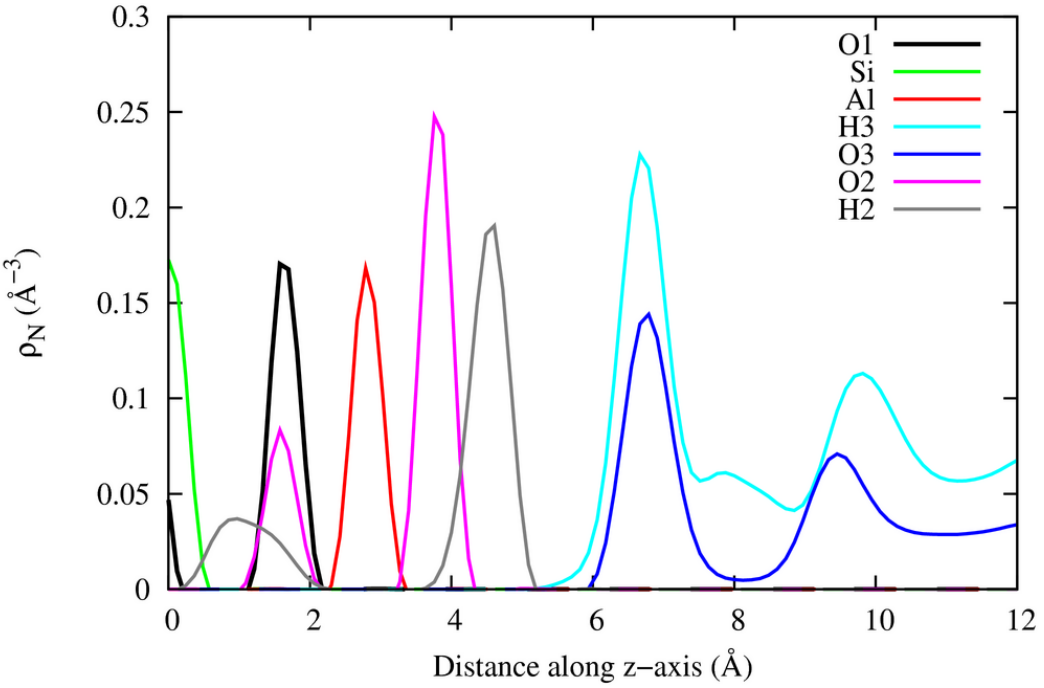

FIGURE 6.11: The average density profile at the Al–water interface during the final 3 ns simulation of water and kaolinite, where $z = 0$ is set to the average location of the Si layer below the surface. Two hydration layers are present on the surface (see Table 3.12 on page 91 for clarification on the atomic labels).

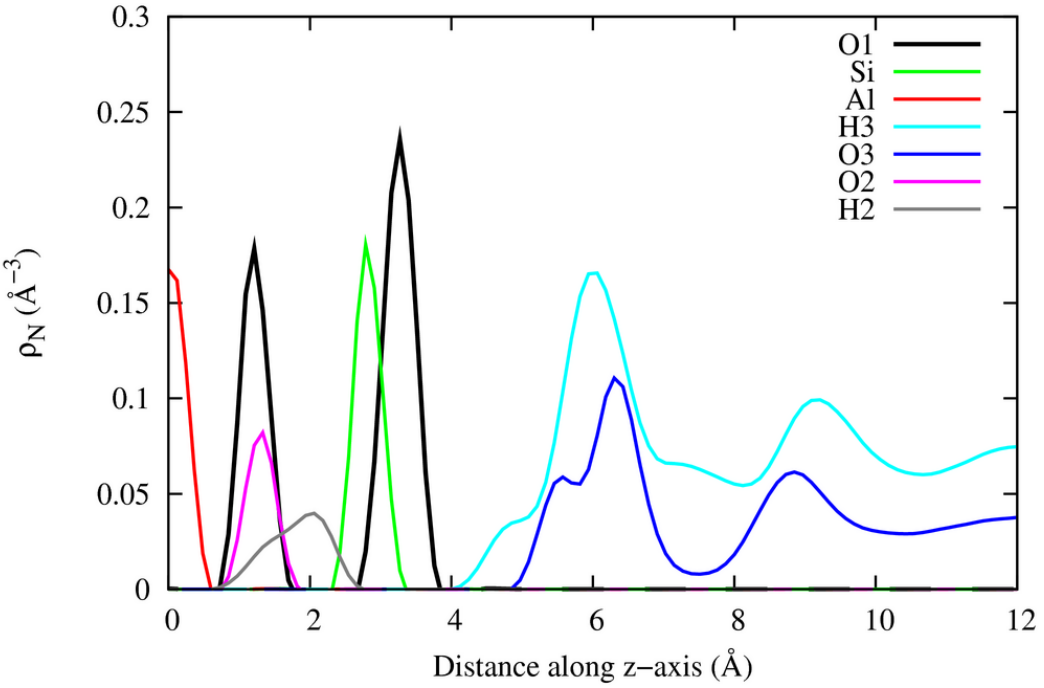

FIGURE 6.12: The average density profile at the Si–water interface during the final 3 ns simulation of water and kaolinite, where $z = 0$ is set to the average location of the Al layer below the surface. Two hydration layers are present on the surface.

374]. The water hydrogen peak is located at a similar location for the first layer, which indicates that the majority water molecules are positioned parallel to the surface. The shoulder at 3.3 Å, however, indicates that a small proportion of the water molecules are positioned such that the oxygen atom is pointed towards the surface with the hydrogen atoms pointed away. The water oxygen peak for the second hydration layer is located at 4.9 Å away from this position, with the hydrogen peak at 5.3 Å.

The majority of the water molecules on the surface in the first hydration layer are located 3.0 Å from the surface oxygen positions, with a shoulder on this peak at 2.3 Å indicating that some of the water molecules are potentially bound to the siloxane rings on the surface. The water hydrogen peaks in the first layer are at 1.6 Å and 2.7 Å, suggesting an average water molecule position where the hydrogen atoms are closest to the surface and the oxygen atoms are pointing away. The second hydration layer is located 5.5 Å away from the surface and is similar to that on the aluminium layer, with the water oxygen atoms located closer to the surface than the hydrogen atoms.

The hydrogen peak from the first hydration layer on the aluminium surface seems to overlap with the hydrogen peak from the surface hydroxyl groups, and thus the orientation for the water molecules located in the first hydration layer on both surfaces is further investigated, and shown in Figure 6.13. The number of water molecules present in the first hydration layer on each surface is 13 molecules per nm^2 and 11 molecules per nm^2 for the Al and Si surfaces respectively, which is slightly more dense than the 10 molecules per nm^2 for a two-dimensional dense water layer [379]. The densities of the water oxygen atoms are calculated 3.5 Å away the two surfaces and averaged over the simulation period. The two-dimensional density information is overlaid onto the surface atomic layer in Figure 6.14. Regions of blue indicate a low probability of locating a water molecules at that location at any stage of the simulation, whereas red areas indicate regions with higher probabilities.

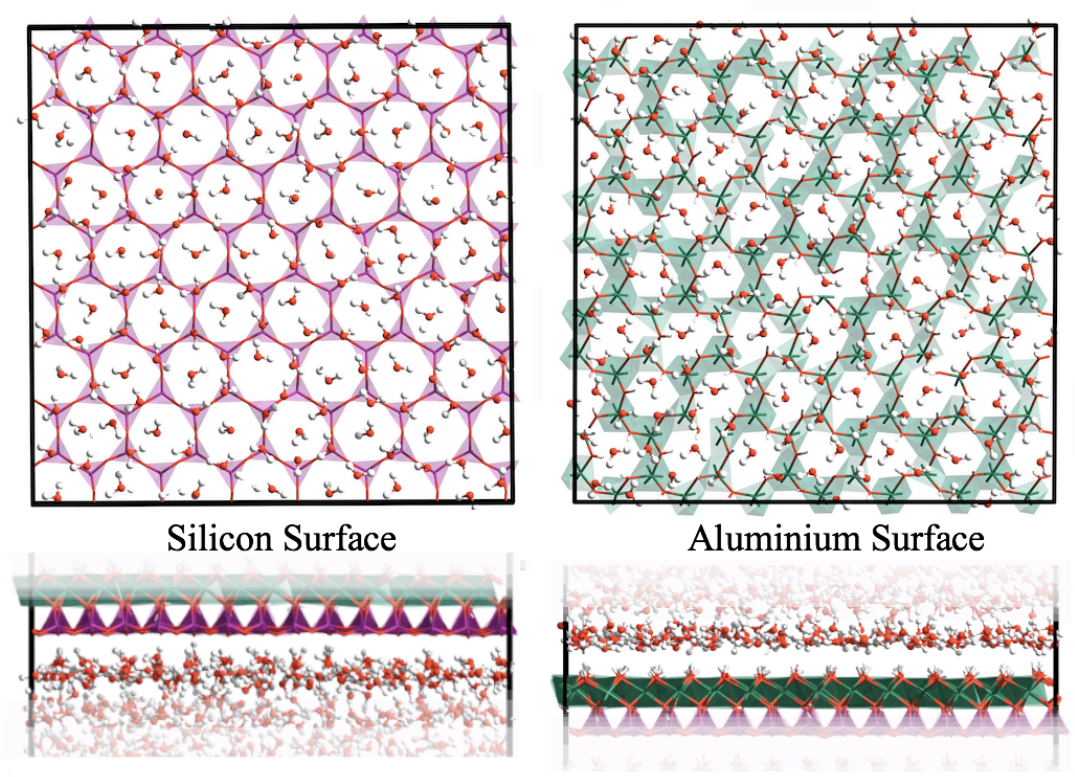

FIGURE 6.13: The orientation of the water molecules near the two kaolinite–water interfaces are shown. The water is generally located within the holes in the cation rings on both surfaces.

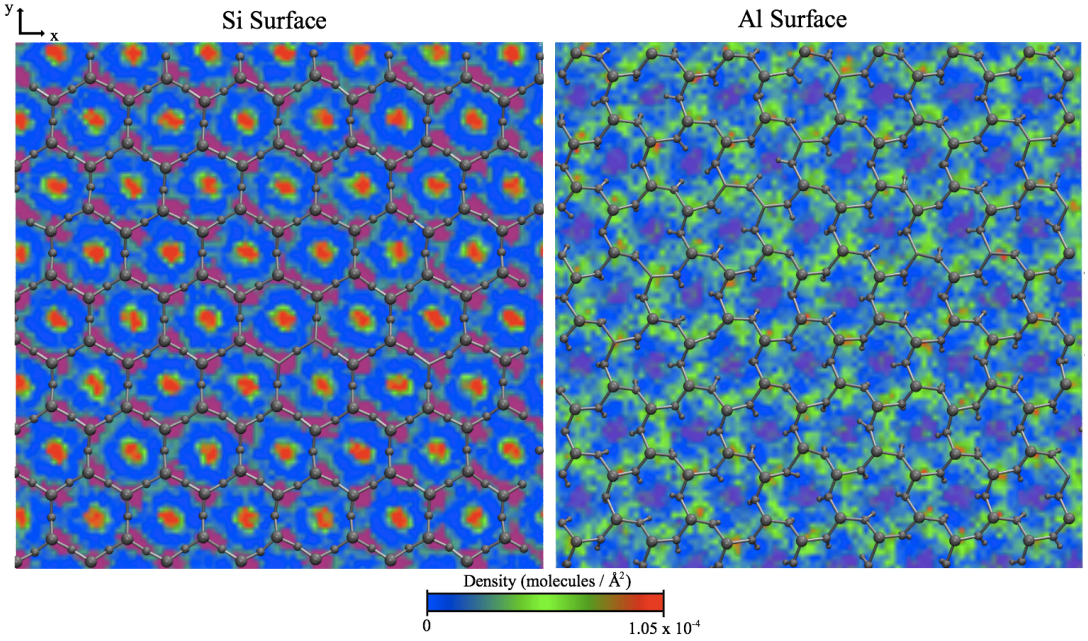

FIGURE 6.14: The average density of water molecules located in the first hydration layer at each surface of the kaolinite–water interfaces. The more water molecules present at any location on the surface over the simulation time, the more the density tends towards the red end of the colour spectrum.

The silicon surface has water molecules mainly located within the holes in the silicon rings, with 66% of the molecules lying parallel to the surface. The remaining water molecules are either located in the holes and positioned such that one hydrogen is pointing towards the surface or located above the silicon atoms with the oxygen atom directed towards the surface. The deep red colour in the two-dimensional density images at the centre of the silicon rings shows a preference for the water molecules to be located in this region compared to other locations on this surface. The results also show a higher density of water present above the silicon rings, caused by the formation of hydrogen bonds between the water hydrogen atoms and the structural oxygen atoms.

The water on the aluminium surface is located in both the holes in the aluminium rings and above the rings, with the majority positioned parallel to the surface. The molecules in the holes tend to have a hydrogen pointed towards the surface, causing the overlap of hydrogen peaks in Figure 6.11. The densities spread out over the surface, with some smaller regions of red/orange located above the Al atoms, indicating that the water molecules are attracted to these locations. The main interactions on the Al surface surface occur between the hydroxyl hydrogen atoms and the water molecules, also indicating that some degree of hydrogen bonding is present at the Al surfaces.

The theoretical studies of Tunega *et al.* [362, 374] found that the octahedral aluminium layer is slightly hydrophilic and the tetrahedral silicon surface slightly hydrophobic. The results reported here support those conclusions as the hydration layer is located closer to the Al surface (at 2.3 Å compared to 3.1 Å) and the average number of hydrogen bonds formed per unit surface area is also higher, with 4.0 molecules per nm^2 compared to 1.9 molecules per nm^2 on the Si surface. The simulation results are also in agreement with the studies of water adsorption on kaolinite surfaces by Hu and Michaelides [363] and Smirnov and Bougeard [380] regarding the orientation of the water molecules in the hydration layers above the surfaces.

Comparisons of kaolinite with silicate minerals shows the possible effects of layering on the water structure at the surface interfaces. Muscovite, a 2:1 phyllosilicate, cleaves to produce a (001) surface similar to the silicon surface in kaolinite, and experimental studies of the effects of water on this surface [381] show that two distinct hydration layers are present 2.5 Å and 4.6 Å above the tetrahedral surface. Orthoclase is a three-dimensional feldspar mineral with no inter-layer space present. Experimental investigations of the hydration of the (001) surfaces by Fenter *et al.* [382] show the presence of two hydration layers at 2.8 Å and 5.4 Å, which is similar to the locations for the hydration layers on the silicon surfaces of kaolinite than in muscovite. The results are consistent with observations that the structural ordering of surface water in muscovite is greater than other mineral surfaces [379]. The decreased distance for the second hydration layer in orthoclase compared to kaolinite shows the effects of the decreased long-range influence of the surfaces on the water structure as a result of the inter-layer space present in kaolinite.

6.5.2 Metakaolin–Water Interactions

The placement of the equilibrated water in the vacuum gap above kaolinite required little further adjustments, as the relatively flat atomic surfaces allow the water molecules to be placed without any residual vacuum. Figure 6.1 shows the difference in surface roughness for the kaolinite and the de-hydrated metakaolin surfaces. Hydrating the metakaolin surfaces further increased the surface roughness, with the final slabs exhibiting a 5.2 Å distance between the highest and lowest points on the surface. This results in small pockets of vacuum within the surface and as the water attempts to re-equilibrate into these spaces the pressure of the water above the slab changes and the final density of water decreases from the bulk value. Thus the simulation cell with both the slab and the water

molecules included is varied in the z-direction to allow for the water between the surfaces to equilibrate to represent bulk water.

The LAMMPS simulation package allows the pressure of the simulation cell to vary anisotropically, and applying this in the z-direction results in the water equilibrating above the metakaolin slab without a change in density in the centre of the water. Anisotropic simulations in LAMMPS are more efficient for cubic simulation cells, and the slabs were adjusted such that $\alpha = \beta = \gamma = 90\ ^\circ$. Since the adjustments are of the order of less than one degree in each case, the resulting metakaolin structures were equilibrated within a few tens of picoseconds at 300 K and 1 atm with no significant structural reorganisation occurring.

The resultant slabs were simulated in the same conditions as the kaolinite slab for a total of 3.5 ns each. All results reported are for metakaolin slab 1, with the water density information for slab 2 given in Appendix D. In all reported phenomena both slabs exhibited the same trends and behaviour. The diffusion of water calculated in the final 2 ns of simulation for each slab was $1.99 \times 10^{-5}\text{cm}^2\text{s}^{-1}$ and $1.98 \times 10^{-5}\text{cm}^2\text{s}^{-1}$. This is lower than in kaolinite, and suggests that there is a greater degree of interaction between the water and the metakaolin surfaces than with the crystalline structure.

The calculated density profiles at the water–metakaolin interfaces are given in Figure 6.15 and Figure 6.16. Unlike in kaolinite, there is considerable overlap of the water with the metakaolin slabs. The water molecules moved into both surfaces of the metakaolin slab as a result of the surface roughness, with water molecules identified in the top 4.7 Å of the surface silicon layer and in the top 6.8 Å of the aluminium layer. There is evidence of a hydration layer present at both surfaces at approximately the same location and with the same general shape, with the diffuse nature of the layer due to the surface disorder making characterisation of the interactions difficult. Approximate measurements from the highest water oxygen peak to the highest hydroxyl oxygen peak gives distances

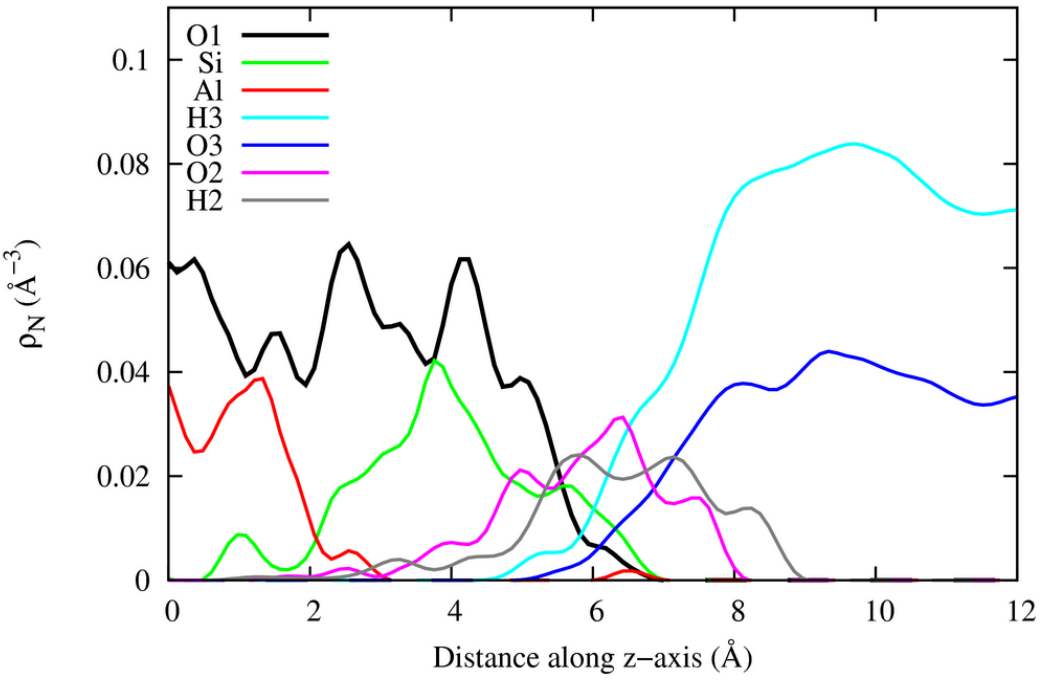

FIGURE 6.15: The atomic density profile at the water–Si interface, where $z = 0$ is set to the average location of the Al layer below the surface.

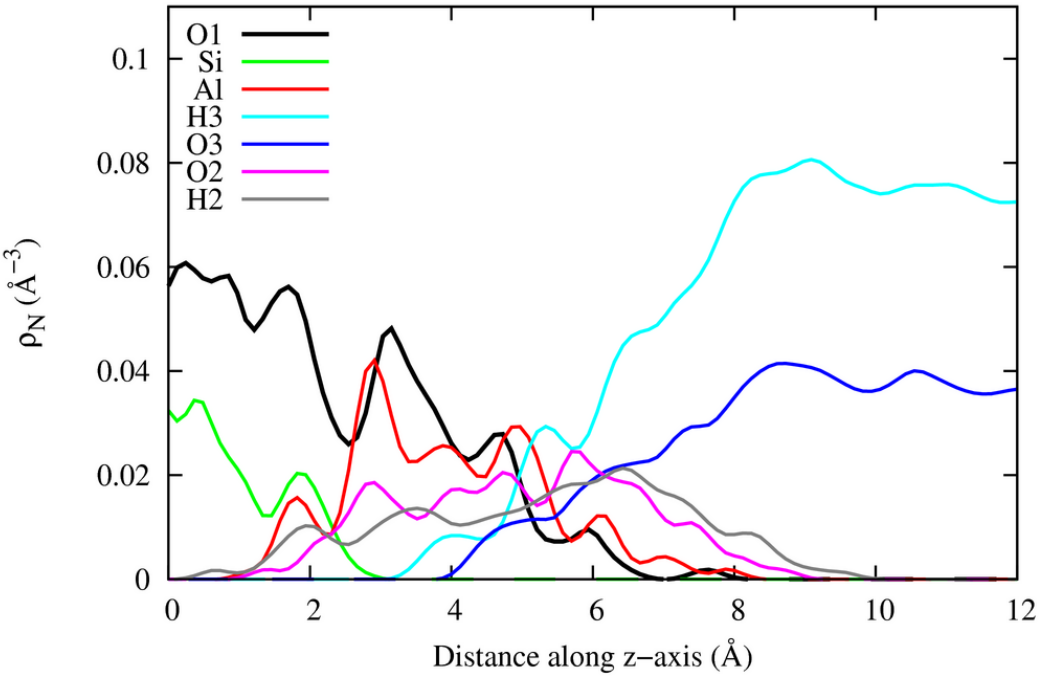

FIGURE 6.16: The atomic density profile at the water–Al interface, where $z = 0$ is set to the average location of the Si layer below the surface.

of 2.9 Å and 3.0 Å for the location of the hydration layer above the Si and Al surfaces respectively. The peaks for the hydration layers at the Al surface occur before the absolute edge of the surface (signified by the end of the H2 density), which shows that more water molecules are present within the surface than on the silicon surface.

Interactions of the slab with the water result in an increase in the surface roughness of the slab, with the distances between lowest and highest points on the silicon and aluminium surfaces increasing from 4.5 Å to 5.0 Å and from 5.2 Å to 8.2 Å respectively. To determine what produces this effect, the two-dimensional density of water molecules is calculated at several distances from the slab surfaces. Figure 6.17 shows the locations of the water density cross-sections for each surface.

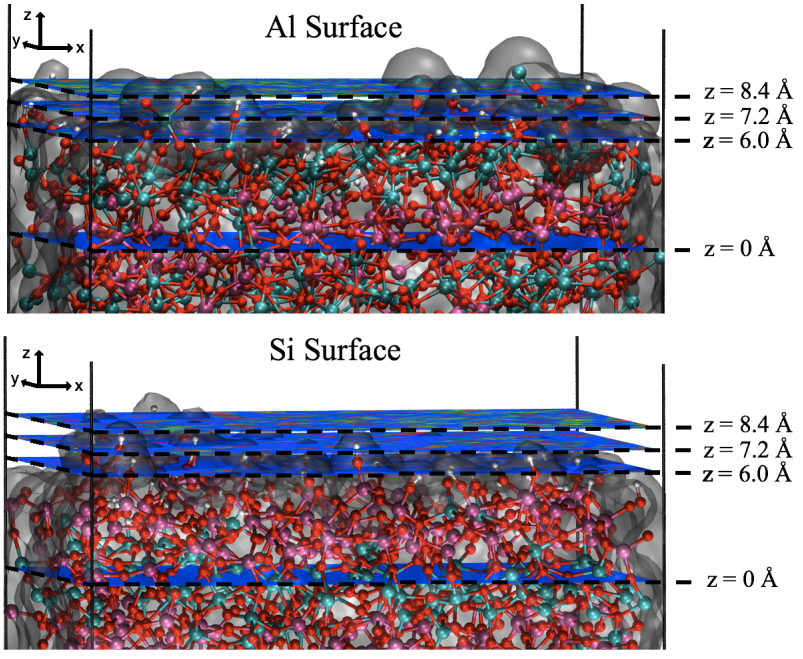

FIGURE 6.17: Metakaolin Al and Si surfaces, generated with a probe of radius 1.2 Å, are shown in translucent grey and overlaid on the atomic structure. The average position of the first Si layer located away from the aluminium surface (top) is set as $z = 0$ Å, whilst the silicon surface (bottom) has $z = 0$ Å set at the location of the Al layer. The average molecular density of water is then calculated at different distances from the surfaces (blue cross-sections) and shown in greater detail in Figure 6.18.

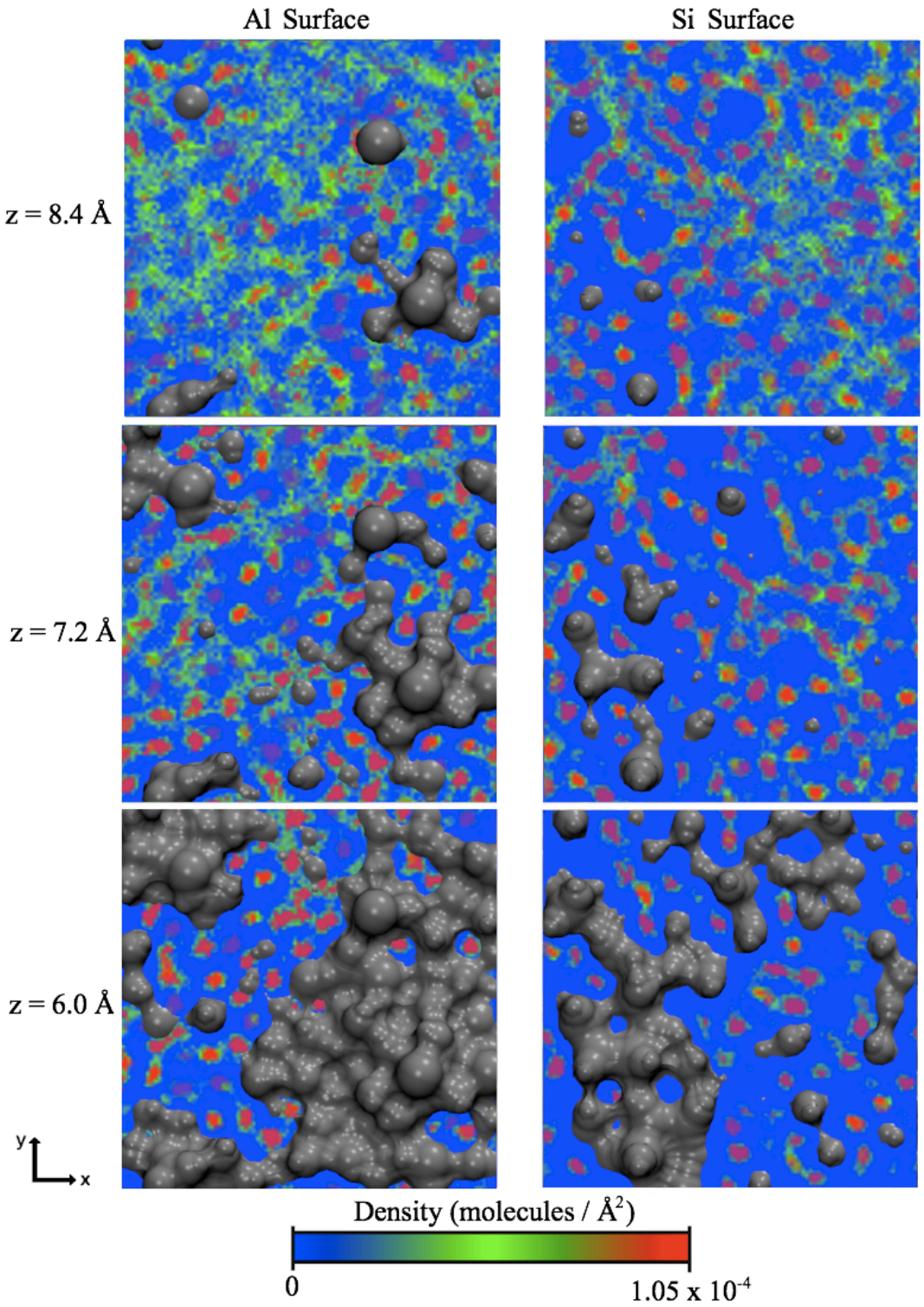

FIGURE 6.18: Surfaces of the metakaolin slabs are shown in grey with cross-sections of the average water oxygen density at different distances from the surface overlaid (see Figure 6.17 for clarification). Increasing red zones show regions of greater probability of finding a water oxygen present during the course of the simulation.

Figure 6.18 shows that although the water molecules are present in the crevices of both surfaces, a greater concentration of water molecules are present (shown by the red areas) deeper within the aluminium-terminated surface layer compared to the silicon surface. This trend continues as the distance away from the surface increases, and at 8.4 Å there are still large areas of dark blue present on the silicon surface compared to the aluminium surface.

The majority of the interactions with the water on the Al surface are due to the under-coordinated aluminium atoms that remain after surface hydroxylation. These atoms become coordinated with the water oxygen atoms, resulting in a 'puckering' effect on the surfaces, with an example shown in Figure 6.19. The increased attraction of the aluminium polyhedra with the water molecules on the metakaolin surfaces are responsible for the increase in the depth of the surface layers, thus allowing water molecules to move deeper within the surface. As the simulation proceeds further, some of the puckered sites that originally involved

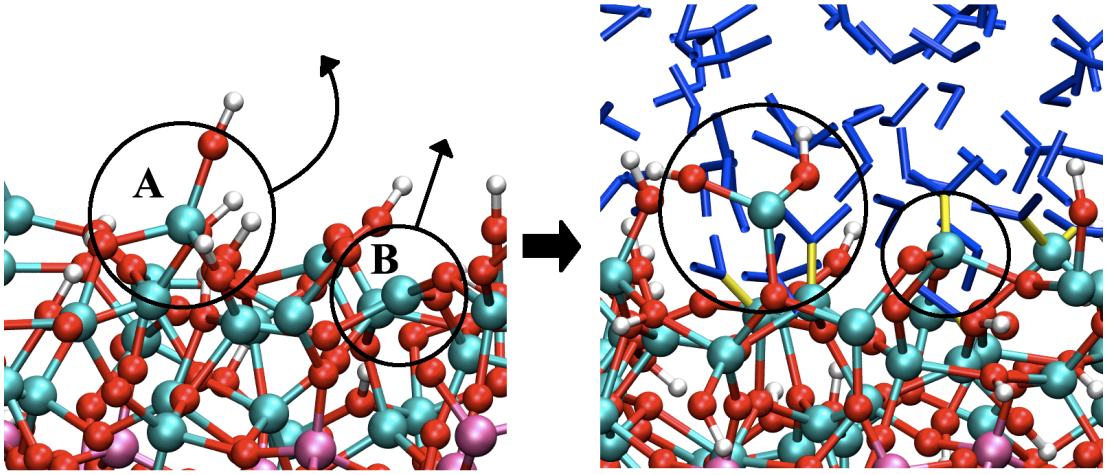

FIGURE 6.19: A portion of the hydroxylated Al surface on one of the metakaolin slabs is shown on the left, with the puckering effect on the aluminium–water interface shown on the right. The shift of the aluminium labelled 'A' is due to interactions of the hydroxyl groups with the water, whereas 'B' shows the effect of the interaction of the Al ion and the water molecules. The water oxygen atoms coordinated to surface Al atoms are shown with a yellow connection. Water = blue, Al = green, Si = purple, O = red, H = white.

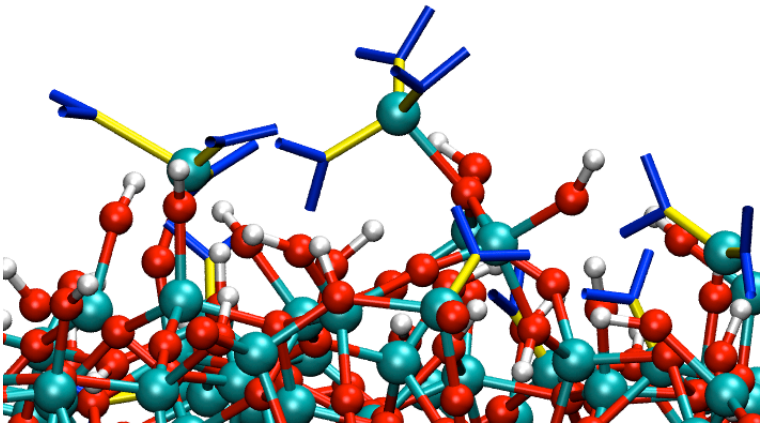

FIGURE 6.20: A portion of the hydroxylated Al surface on one of the metakaolin slabs is shown with evidence of the surface aluminium atoms becoming coordinated with multiple water molecules. See Figure 6.19 for clarification of colours. Water molecules not coordinated to surface atoms are omitted for clarity.

multiple under-coordinated aluminium atoms become coordinated with several water oxygen atoms over the course of the simulation, with Figure 6.20 showing surface aluminium atoms tetrahedrally coordinated with three water molecules.

The presence of the puckering within the relatively short time scales sampled (compared to the time required for dissolution) shows the susceptibility of the hydrated aluminium surfaces of metakaolin to the effects of water. Hydrogen bonding between the water molecules and the surface hydroxyl groups is also present in the kaolinite slabs, however, the additional interactions of the water oxygen atoms with the under-coordinated Al along with the instability of the surface results in the final Al surface layer widening by 1.2 Å (measured as the distance between the lowest and highest Al atoms in the layer). In comparison, the silicon surfaces have no significant structural re-organisation in the time scales sampled.

The surfaces of metakaolin have a higher degree of interaction with the water than kaolinite. Part of this is due to the hydroxyl groups present on the metakaolin

silicon surface that are not present on the kaolinite silicon surface. Both kaolinite and metakaolin aluminium surfaces terminate in Al-OH groups, however, in kaolinite the Al has an octahedral coordination whereas in metakaolin the coordination is much more varied. The number of hydrogen bonds formed as a function of surface hydroxyl concentration were calculated and shows that there is an increased level of hydrogen bonding on both metakaolin surfaces compared to the Al-OH surface on kaolinite. On average 0.46 hydrogen bonds per hydroxide unit are present on the aluminium surface compared to 0.38 on the silicon surface. This is an increase in the kaolinite value for the Al–OH surface of 0.32, and shows that the aluminium metakaolin surfaces are more hydrophilic than those in kaolinite, despite the higher concentrations of hydroxyl groups present on the latter (see Table 6.1).

It is the conclusion of this investigation that it is not just the hydroxyl surface concentration that affects the water interaction, and the disorder in aluminium surface structure is an important factor in the interactions of metakaolin with water. The puckering of the aluminium surface due to the coordination of the under-saturated surface Al ions with the water molecules plays a major role in increasing the hydrophilic nature of the metakaolin.

6.6 Summary

Surface-water interactions of metakaolin and kaolinite have been investigated in this chapter. A systematic method for creating metakaolin surfaces is proposed, with the (001) surfaces for both kaolinite and metakaolin simulated. The hydration of metakaolin surfaces is investigated as a measure to provide realistic and stable surfaces for the interactions with water, and minimum slab and vacuum depths are calculated to be 10 Al–Si layers and 30 Å respectively. The surfaces were generated, hydrated and relaxed and the vacuum gaps were filled

with equilibrated SPC/Fw water and simulated for 3-3.5 ns in ambient conditions to investigate the interactions at the mineral–water interfaces.

The interactions with kaolinite surfaces agreed well with the literature and provided a measure of the accuracy of the methods employed. The interactions with metakaolin showed that the silicon-terminated surfaces are less hydrophobic than those in kaolinite, with hydrogen bonding between the surface hydroxyl groups and the water molecules the predominant interaction. In comparison, whilst the hydroxyls groups on the aluminium surface also interact with the water molecules, the disorder in the aluminium surface result in the water molecules becoming coordinated to the under-coordinated aluminium atoms, causing a puckering of the surface and resulting in a widening of the surface layer. The aluminium surfaces in metakaolin are also more hydrophilic than those in kaolinite, with the overall behaviour of metakaolin showing an increase in the level of interaction with the water molecules. Thus the hydrophilic behaviour of metakaolin combined with the disordered surfaces leads to greater changes in the surfaces in the presence of water and may result in the higher susceptibility of the surfaces to caustic attack in geopolymerisation.

Chapter 7

Conclusions and Future Work

The fundamental investigations of geopolymers are inherently hindered by the compositional variations produced by the raw materials and synthesis conditions. Metakaolin is a source material used in geopolymerisation that has a similar structural composition to the geopolymer Al/Si matrix; with both being composed of a disordered aluminosilicate network of primarily SiO_4 and AlO_4 tetrahedra. Thus metakaolin is used as a model system for the aluminosilicate network in geopolymers to investigate the role of cation inclusion and hydroxyl content on the atomic structure and the role of water in the dissolution process in geopolymerisation.

Classical atomistic modelling of large systems in dynamic environments was used to investigate atomic mechanisms that are not easily discernible from experimental studies. This method required an accurate and robust interatomic potential model to describe the interactions for all the interacting species. The Teter rigid ion, partial charge model combined with the flexible single point charge model for water was identified as suitable from a range of models available from the literature. Testing showed that although this model had not been previously used in the simulation of disordered aluminosilicates, it simulated a variety of aluminosilicate materials with differing aluminium coordination's accurately. Thus it is a useful alternative to the potential models that are popular in the simulation of aluminosilicate materials.

Structure of Metakaolin

The structure of metakaolin was simulated through the gradual thermal dehydroxylation of kaolinite using molecular dynamics techniques. This produced a structure that demonstrated the loss of periodicity in the *c*-direction and maintained the 1:1 Al/Si ordering that is present in experimental data. The migration of aluminium through the structure was identified as the main contributing factor in the loss of periodicity. The final structure is composed primarily of 4-fold Al (up to 74%) with 21% of the Al in 5-fold coordination and has significant buckling present in the layers. The disorder and variability in the aluminium concentration has implications for the reactivity of metakaolin, and is an important structural characteristic to be taken into account when describing the structure.

Defect Interstitial Cations: Na, K and Ca

Ionic size is the primary cited cause for the differences in properties for geopolymers produced with different metal cations. A complex nanoporous structure was identified in metakaolin, and the cavities facilitated the investigation of the effects of sodium, potassium and calcium interstitial defect ions on the disordered aluminosilicate network. Different ionic sizes affected the final sites where the cations were located, with sodium and calcium located in similar sites whereas potassium demonstrated a greater range of final site radii. The results showed that ionic charge plays a more significant role, with calcium interacting to a greater extent with the aluminosilicate structure than both sodium and potassium. The increased interaction of calcium may be responsible for the increased densities of geopolymers observed. Efforts to tailor the synthesis of geopolymers must as a consequence take into account both the size and ionic charge of the cations used in the activating solutions and the impurities in the source materials.

Hydroxyl Concentration

The loss of hydroxyls in the transformation of kaolinite to metakaolin causes the migration of the cations that results in the coordination of aluminium to change from 6-fold to predominantly 4- and 5-fold. The trends in the coordination changes mirrored those in the porosity measurements as a function of de-hydroxylation. This is consistent with experimental measurements of the thermal behaviour of kaolinite and demonstrates that the final structural properties of metakaolin are highly dependent on the hydroxyl concentration. The presence of hydroxyl groups in the structure also led to an increase in the interactions of the defect interstitial cations with the aluminium compared to the silicon in the aluminosilicate network. The conclusion of this research is that the hydroxyl concentration of the source materials is a significant factor in the behaviour of the source materials in geopolymerisation, and must be included for consideration when determining the synthesis parameters used to form a geopolymer.

Mineral-Water Interactions

The role of water in the geopolymerisation reaction was investigated by studying the mineral-water interactions of kaolinite and metakaolin. The disorder in metakaolin results in a structure that is not well suited to traditional surface generation methods. This research presents a procedure for producing partially hydrated metakaolin surfaces that are considerably rougher than the equivalent surfaces on kaolinite. This disorder leads to an increase in the level of interaction with the water molecules and results in a puckering of the aluminium surfaces that in turn increases the surface disorder. The results confirm that water is an important factor in geopolymerisation and this has implications for the dissolution of metakaolin source materials, with the higher rate of aluminium released in the initial stages of geopolymerisation facilitated by the strong interactions between the disordered aluminium surfaces and the aqueous solution.

Future Work

The importance of computational simulations in the development of geopolymer materials is becoming increasingly evident, with the results presented in this thesis providing a significant contribution to the understanding of the atomic-level interactions present in these materials. Application of some of the techniques used in this thesis will be beneficial to investigate aspects of geopolymerisation that are still poorly understood. Metakaolin is an ideal model system to investigate individual atomic interactions, and the structures developed here are easily reproduced by application of the same simulation processes employed in this research.

The interactions of defect interstitial cations with the disordered aluminosilicate network could be further expanded to include a greater range of cations to reinforce the trends reported. In addition, the influence of water molecules and changing Al:Si ratios could also be studied to present a full understanding of all the molecular species' role in the geopolymer network. The methods used to identify the cavities in metakaolin could be used in any future aluminosilicate structures to determine locations for the placement of the defect species for these investigations.

The geopolymerisation reaction occurs in a caustic solution, and the investigations of the surfaces-water interfaces presented in this thesis can be extended to compare the effects of alkali solutions such as sodium hydroxide and potassium hydroxide. Longer time periods or the use of reactive force fields will be beneficial to further characterise interactions responsible for the dissolution mechanisms in geopolymerisation. Through the combination of the atomic level detail gained from computational simulations and experimental studies, a greater understanding of geopolymers will elevate the rates of adoption of this new technology in industry, and ultimately lead to more sustainable and environmentally conscious industrial practices in the future.

Appendix A

Model Parameters and Tests

Chapter 3 investigates three different potential models from the literature for suitability in the simulation of a disordered aluminosilicate network. Model 1, is from Catlow and colleagues *et al.* [182, 216, 224, 255–257] and from Schröder *et al.* [160]. Model 2, is from Kramer *et al.* [230] and model 3 is from Teter [247]. The parameters for these models are given in Tables A.2 to A.3.

Table A.1: Potential parameters for model 1.

Atomic Charges			
Structural Oxygen (O2) shell	-2.86902	Silicon (Si)	4.000
Structural Oxygen (O2) core	0.86902	Potassium (K)	1.000
Hydroxyl Oxygen (O1)	-1.426	Hydrogen (H)	0.426
Aluminium (Al)	3.000	Sodium (Na)	1.000
2-Body Buckingham potential parameters			
Atomic Pair	A (eV)	ρ (Å)	C (eVÅ^6)
Al - O1	1142.687	0.29912	0.00
Al - O2 shell	1460.300	0.29912	0.00
Si - O1	983.557	0.32052	10.66158
Si - O2 shell	1283.907	0.32052	10.66158
Na - O2 shell	1226.840	0.30650	0.00
O1, O2 shell - O1	22764.00	0.14900	27.89700
O1, O2 shell - O2 shell	22764.00	0.14900	27.89700
H - O2 shell	311.97	0.25	0.00
Morse potential parameters			
Atomic Pair	D_e (eV)	α (Å^{-1})	r_o (Å)
O2 shell - H	7.0525	2.1986	0.94850
Angle-Bending parameters			
Dihedral group		A (eV/rad^2)	θ_o (°)
(Si or Al) - O1,O2 - O1,O2		2.09724	109.47
Core-Shell Spring constants			
O2 core - O2 shell		k = 74.92 eV/$\mathring{A}^2$	

Table A.2: Potential parameters for model 2.

Atomic Charges			
Silicon (Si)	2.400	Sodium (Na)	1.000
Aluminium (Al)	1.400	Chlorine (Cl)	-1.000
Oxygen (O)	-1.200	Phosphorous (P)	3.400
2-Body Buckingham potential parameters			
Atomic Pair	A (eV)	ρ (Å)	C (eVÅ^6)
Al - O	16008.5345	0.208478	130.5659
Si - O	18003.7572	0.205205	133.5381
O - O	1388.7730	0.362319	175.0000
P - O	9034.2080	0.192642	19.8793
Na - O	3542.2072	0.241864	0.000
Na - Cl	5783.1124	0.320931	521.3348

Table A.3: Potential parameters for model 3.

Atomic Charges			
Silicon (Si)	2.400	Calcium (Ca)	1.200
Aluminium (Al)	1.800	Sodium (Na)	0.600
Structural Oxygen (O1)	-1.200	Potassium (K)	0.600
Hydroxyl Oxygen (O2)	-0.856	Hydrogen (H)	0.256
2-Body Buckingham potential parameters			
Atomic Pair	A (eV)	ρ (Å)	C (eVÅ^6)
Al - O1	12201.417	0.195628	31.997
Si - O1	13702.905	0.193817	54.681
Na - O1	2755.0323	0.258583	33.831
K - O1	20510.758	0.233726	51.490
Ca - O1	7385.3075	0.255185	100.26
O1,2 - O1,2	1844.7548	0.343645	192.58
O1,2 - H	100.0	0.250	0.0
Al - O2	9701.4170	0.195628	31.997
Si - O2	12433.827	0.193817	54.681
Morse potential parameters			
Atomic Pair	D_e (eV)	α (Å^{-1})	r_o (Å)
O2 - H	7.0525	1.800	0.94850

The SPC/Fw [277] water model was chosen for the interactions of the water molecules in the simulations of the water–mineral interfaces in Chapter 6. These parameters are given in Table A.4.

TABLE A.4: The parameters for the 3–point planar SPC/Fw model, which uses a two–body Lennard–Jones function with partial charges, a harmonic bonded interaction for the O–H bonds and a bond–angle term describing the H–O–H bond angle.

ε (eV)	σ (Å)	d_i (Å)	q_H	q_O	θ (°)
0.674×10^{-2}	3.166	1.012	+0.4100	–0.8200	113.24

The interactions of the water molecules with the aluminosilicate materials needed to be determined, and the potential model by Chanajaree *et al.* [314] was used as a starting point to fit new potential parameters for these interactions. The original potential parameters are given in Table A.5.

TABLE A.5: Initial parameters for the water-aluminosilicate interactions from literature.

Atomic Charges		**2 - Body Lennard-Jones parameters**		
Type	Charge	Atomic Pair	ε (eV)	σ (Å)
Silicon (Si)	2.050	Si - OW	0.80655×10^{-2}	1.6213
Calcium (Ca)	2.000	Al - OW	0.53149×10^{-2}	1.6926
Aluminium (Al)	1.750	OW - OW	0.67457×10^{-2}	3.1690
Water Oxygen (OW)	-0.8476	O - OW	0.24309×10^{-1}	2.4952
Structural Oxygen (O)	-1.200	Si - HW	0.35871×10^{-2}	1.3555
Hydrogen (HW)	0.4238	Al - HW	0.22459×10^{-2}	1.4242

The calculated energies per formula unit after energy optimisation of each of the structures given in Figures 3.1 and 3.3 using each potential model are given in Table A.6.

TABLE A.6: Calculated energies for the SiO_2 and Al_2SiO_5 polymorphs. All values in eV.

Model	Quartz	Coesite	Cristobalite	Stishovite	Andalusite	Kyanite	Sillimanite
1	-25.738	-25.736	-18.465	-25.515	-22.279	-22.282	-22.236
2	- 19.463	-19.455	-19.405	-19.526	- 16.980	-17.127	-17.057
3	-18.570	-18.569	-18.465	-18.293	-15.173	-15.132	-15.024

Appendix B

De-hydroxylation Statistics

The thermal de-hydroxylation of kaolinite to metakaolin described in Chapter 4 was simulated ten times to produce 10 metakaolin structures. The total radial distribution functions and images of the 100 % de-hydroxylated metakaolin structures for each simulation from Chapter 4 are given in Figures B.1 to B.10, showing the changes for all ten structures follow the same trends.

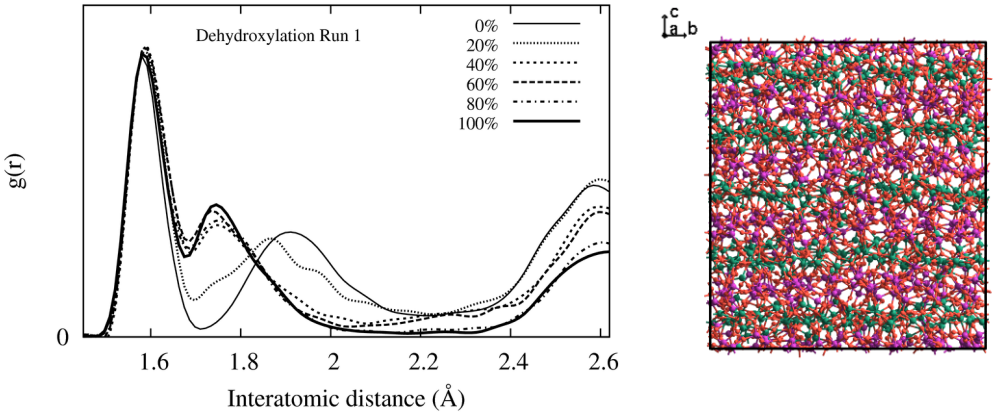

FIGURE B.1: RDF and Final Structure for De-hydroxylation Run 1

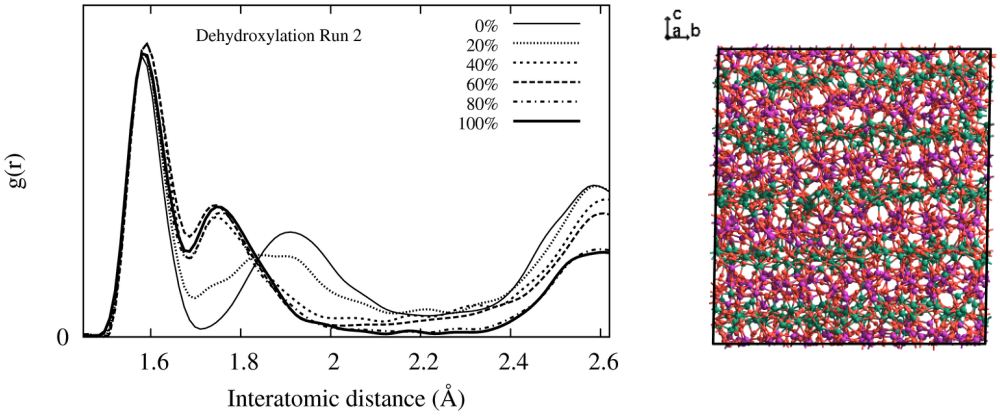

FIGURE B.2: RDF and Final Structure for De-hydroxylation Run 2

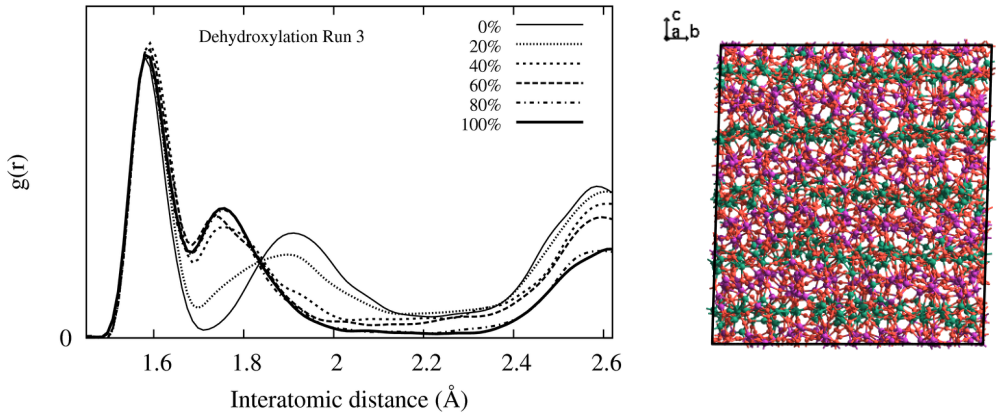

FIGURE B.3: RDF and Final Structure for De-hydroxylation Run 3

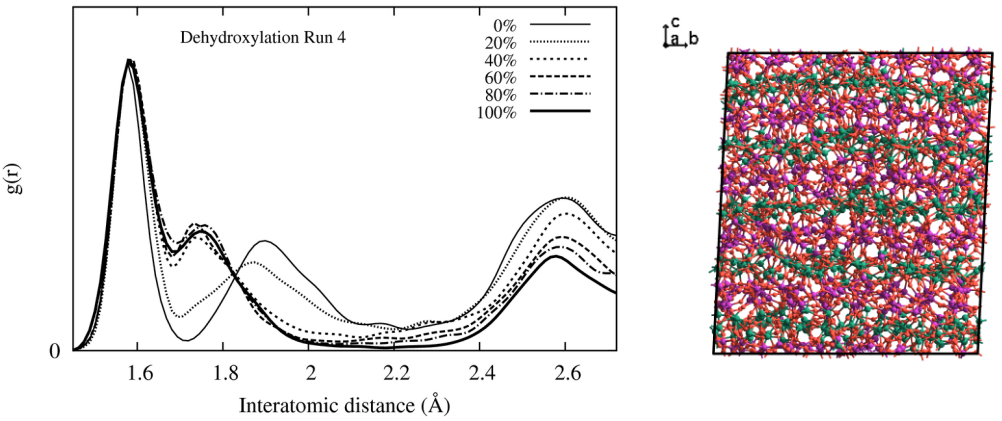

FIGURE B.4: RDF and Final Structure for De-hydroxylation Run 4

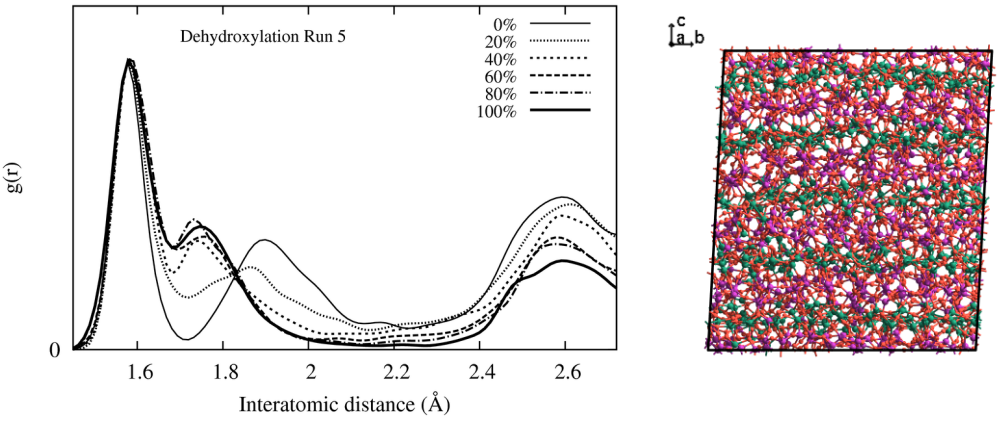

FIGURE B.5: RDF and Final Structure for De-hydroxylation Run 5

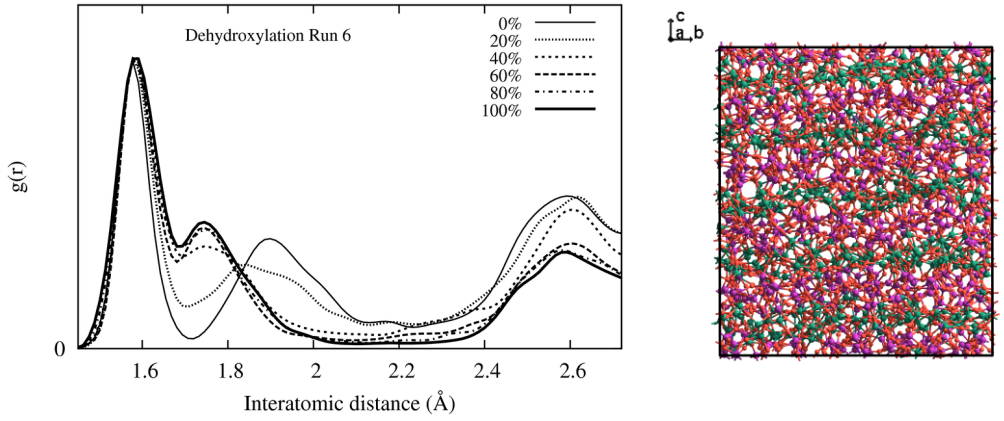

FIGURE B.6: RDF and Final Structure for De-hydroxylation Run 6

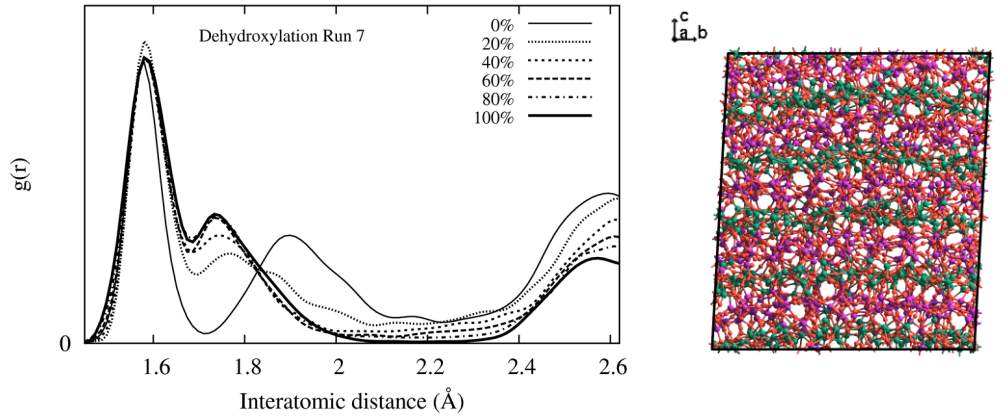

FIGURE B.7: RDF and Final Structure for De-hydroxylation Run 7

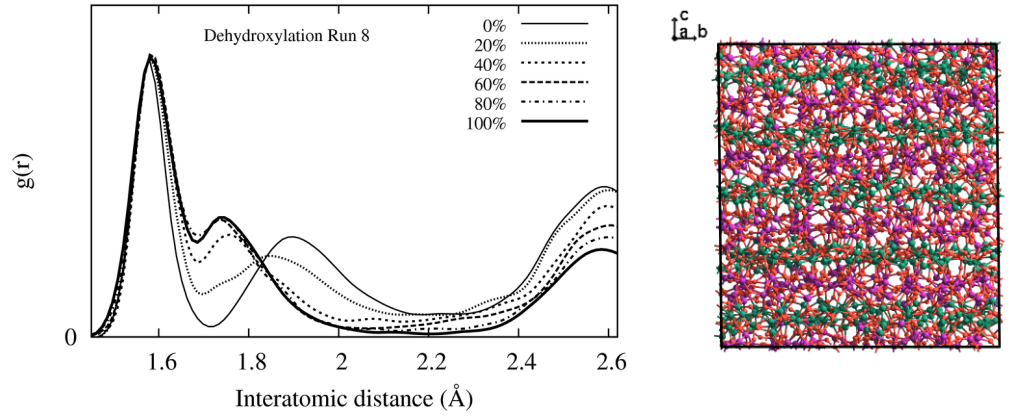

FIGURE B.8: RDF and Final Structure for De-hydroxylation Run 8

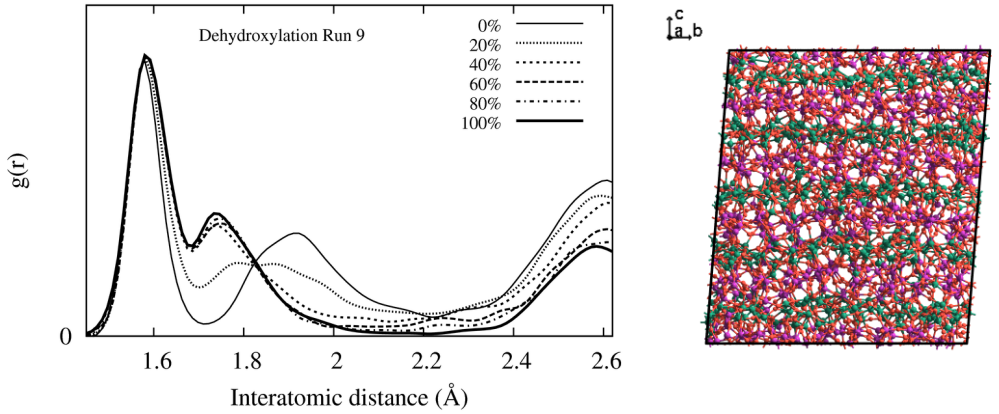

FIGURE B.9: RDF and Final Structure for De-hydroxylation Run 9

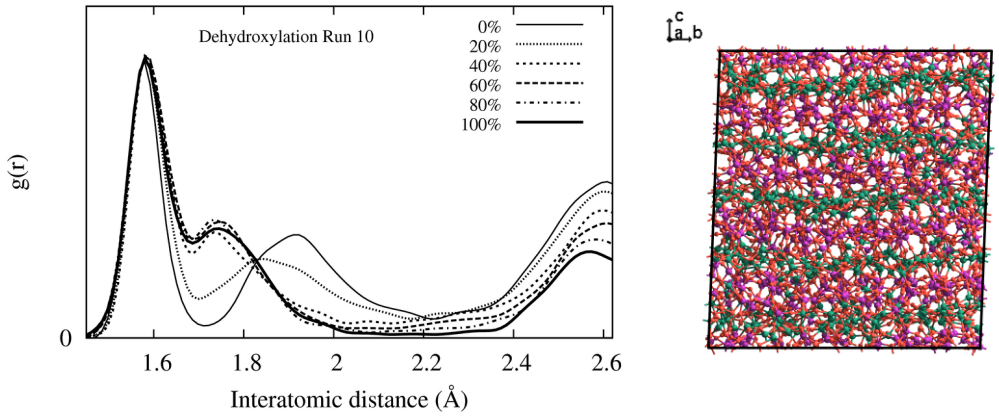

FIGURE B.10: RDF and Final Structure for De-hydroxylation Run 10

The final volumes, densities and calculated porosities for the 10 de-hydroxylated metakaolin structures are given in Table B.1. This information is used in Chapters 4 and 5, with the uncertainties representing the standard deviations on the average values.

TABLE B.1: Average Porosity, Volume and Density data for each De-hydroxylation step.

% DH	Pore Volume V_p (Å^3)	Total Volume V (Å^3)	Porosity ε	Density ρ (g cm^{-3})	Surface Area (Å^2) s (Å^2)	Pore Density ρ_{pore} (cm^{3}g^{-1})
0	23162.92	45075.40	0.514	2.600	4345.03	0.193
10	13625.25 ± 936.24	45459.04 ± 26.06	0.30 ± 0.02	2.60 ± 0.01	2565.20 ± 119.79	0.12 ± 0.01
20	18416.47 ± 890.87	45468.12 ± 224.57	0.41 ± 0.04	2.57 ± 0.01	3473.14 ± 191.60	0.16 ± 0.01
30	23002.38 ± 1720.69	45308.89 ± 268.35	0.51 ± 0.04	2.54 ± 0.02	4278.12 ± 277.05	0.20 ± 0.02
40	27622.06 ± 2265.92	45073.59 ± 301.41	0.61 ± 0.05	2.51 ± 0.02	5209.38 ± 340.37	0.24 ± 0.02
50	31738.95 ± 2652.20	44569.77 ± 329.26	0.71 ± 0.05	2.51 ± 0.02	5804.13 ± 262.32	0.28 ± 0.02
60	31338.17 ± 2592.51	43521.79 ± 343.04	0.72 ± 0.05	2.53 ± 0.02	5928.96 ± 471.22	0.29 ± 0.02
70	30813.50 ± 2565.92	42305.45 ± 331.29	0.73 ± 0.06	2.56 ± 0.02	5898.33 ± 355.65	0.29 ± 0.02
80	26240.28 ± 1007.80	40597.80 ± 230.96	0.65 ± 0.03	2.63 ± 0.02	5103.63 ± 209.34	0.25 ± 0.01
90	23471.00 ± 492.85	39061.01 ± 177.11	0.60 ± 0.03	2.69 ± 0.01	4681.16 ± 134.00	0.22 ± 0.01
100	20601.75 ± 1364.35	37334.10 ± 199.33	0.55 ± 0.03	2.77 ± 0.02	4126.51 ± 317.07	0.20 ± 0.01

Appendix C

Interstitial Cation Statistics

The size of the minimum kaolinite supercell used in Chapter 5 to ensure no periodic image effects were present was determined by relaxing successively larger supercells with a single sodium defect ion present. The resulting energies compared to cell volume are given in Figure C.1.

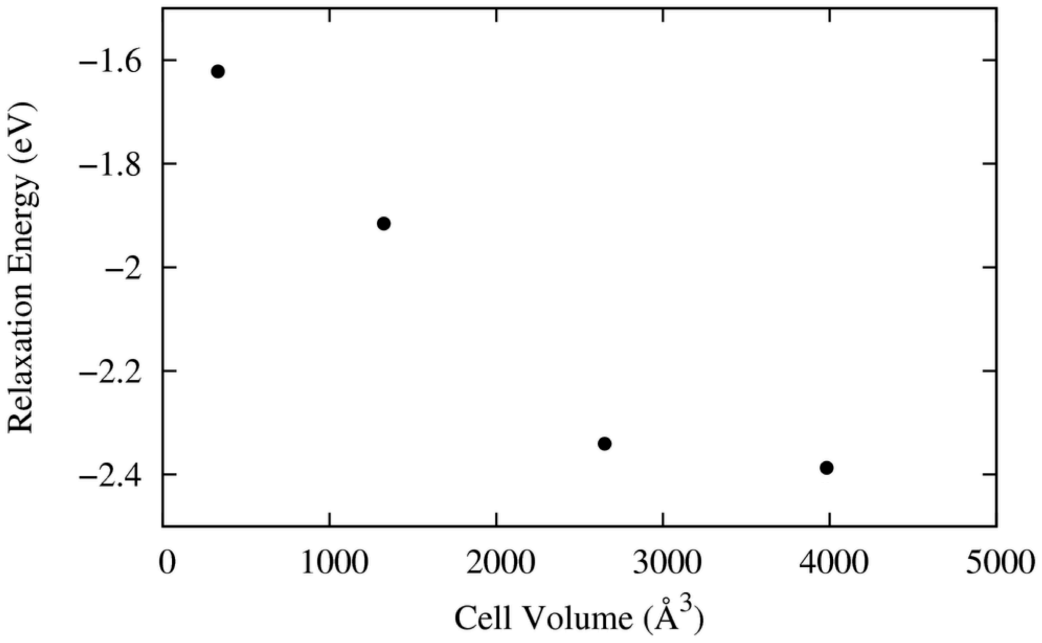

FIGURE C.1: The relaxation energies for the cation inclusion of sodium into kaolinite. The minimum simulation cell required to negate periodic boundary effects is a $2 \times 2 \times 2$ super-cell with a volume of 2650.5Å^3.

The partial radial distribution functions calculated from the centres of the cavities in the 100 % and 80 % de-hydroxylated metakaolin structures determined with AVAS are given in Figure C.2 and Figure C.3 respectively.

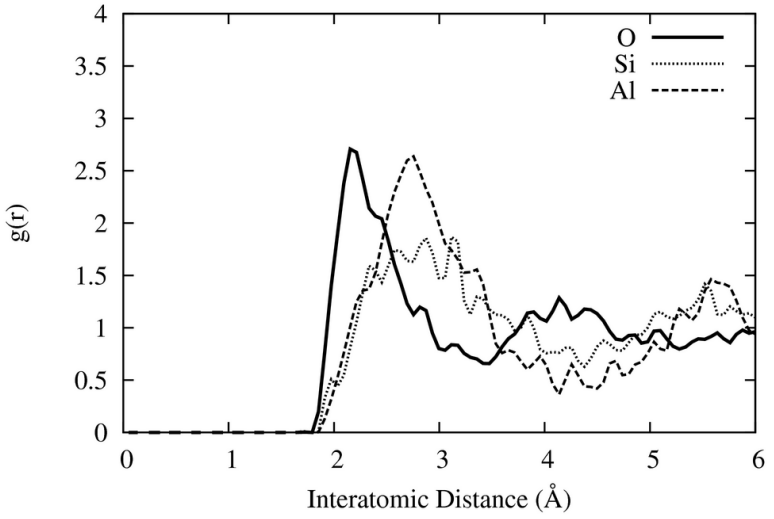

FIGURE C.2: The average partial $g(r)$ calculated for the 100 % de-hydroxylated metakaolin structure.

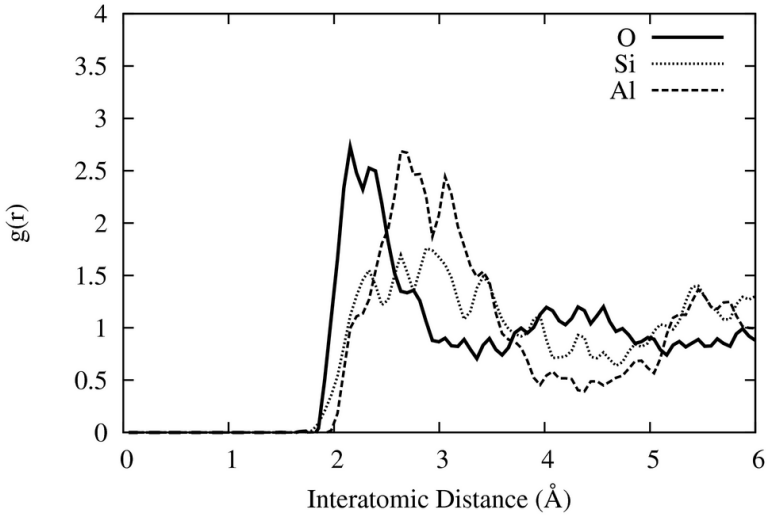

FIGURE C.3: The average partial $g(r)$ calculated for the 80 % de-hydroxylated metakaolin structure.

The partial distribution functions calculated for the cavities in the 80 % dehydroxylated metakaolin structure after optimisation with the calcium interstitial defect ion are given in Figure C.4, with those for the potassium ion given in Figure C.5.

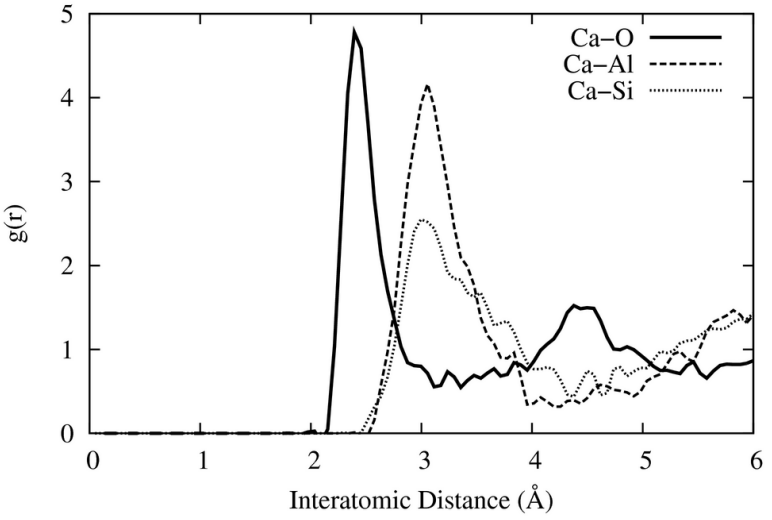

FIGURE C.4: The partial $g(r)$ calculated for each interaction with the defect ion after optimisation with calcium defects.

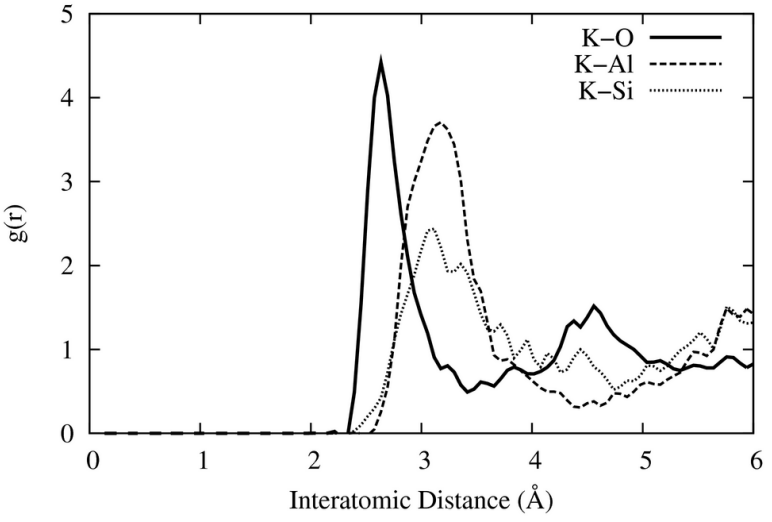

FIGURE C.5: The partial $g(r)$ calculated for each interactions with the defect ion after optimisation with potassium defects.

The partial distribution functions calculated for the cavities in the 80 % de-hydroxylated metakaolin structure after optimisation with the sodium interstitial defect ion are given in Figure C.6.

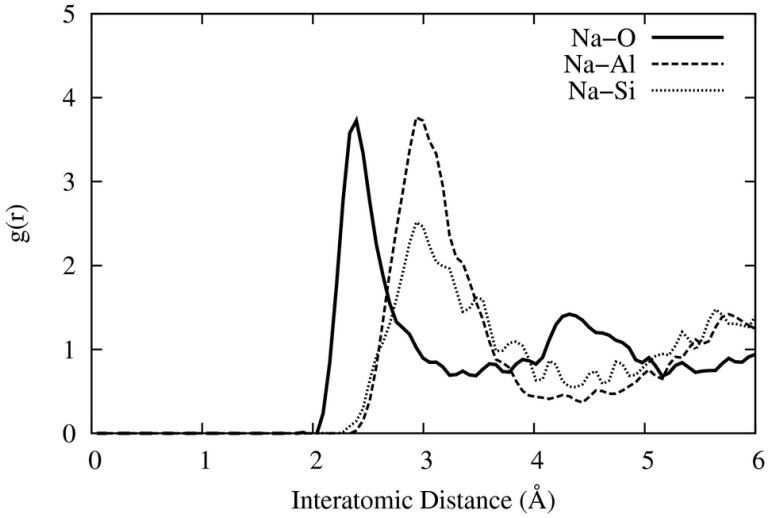

FIGURE C.6: The partial $g(r)$ calculated for each interaction with the defect ion after optimisation with sodium defects.

The initial and final site radii for the 80 % de-hydroxylated metakaolin structure are given in Figure C.7.

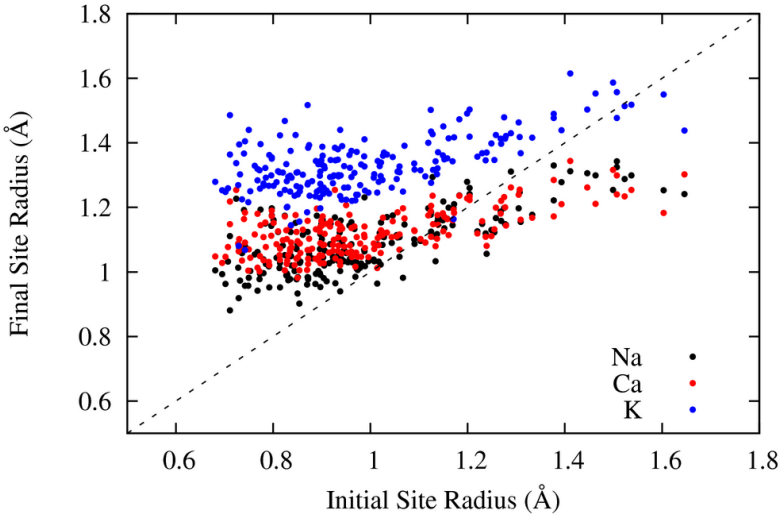

FIGURE C.7: The relationship between the initial and final site radii for the inclusion of the cations into the 80% de-hydroxylated metakaolin structure.

The site separation distances for the 80 % de-hydroxylated metakaolin structure are given in Figure C.8.

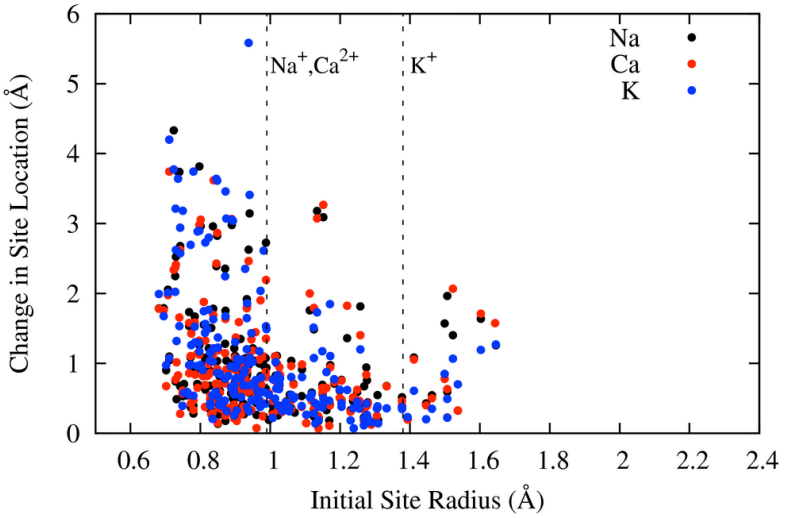

FIGURE C.8: The distance between the initial site and final site for each cation in the 80% de-hydroxylated metakaolin structure.

The site potentials in the final cavities in the 80 % de-hydroxylated metakaolin structure are given in Figure C.9 as a function of final site radius.

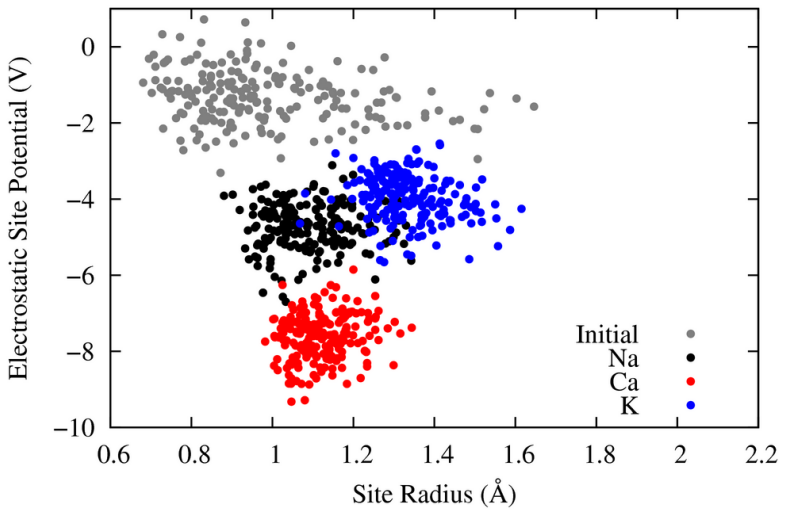

FIGURE C.9: Site potential after optimisation for each interstitial cation site in the 80 % de-hydroxylated metakaolin structure. Each ion is shown as a function of the final site radius, with the initial values (in grey) given as a function of the initial site radius.

Appendix D

Surface - Water Statistics for Secondary Metakaolin Slab

Chapter 6 involved the simulation of two metakaolain slabs in the presence of water. The density profiles in the chapter are from the first slab (slab 1, see Table 6.1) whilst those calculated for the second slab are given in Figures D.1 and D.2, and show similar trends to those reported.

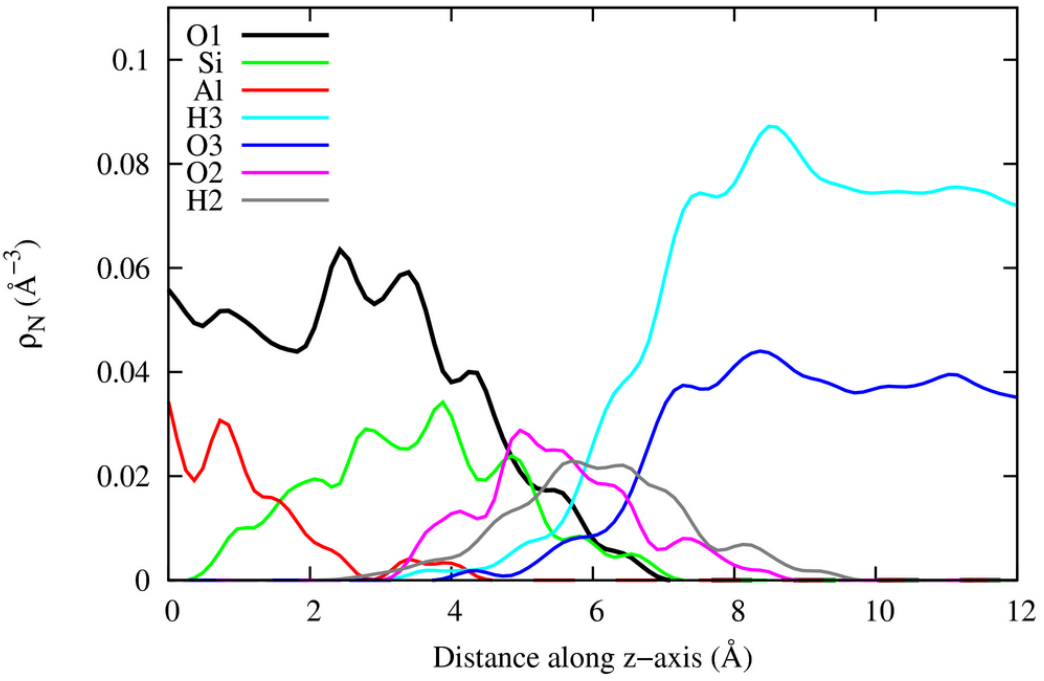

FIGURE D.1: The average distances for the water–Si interactions for the metakaolin slab 2.

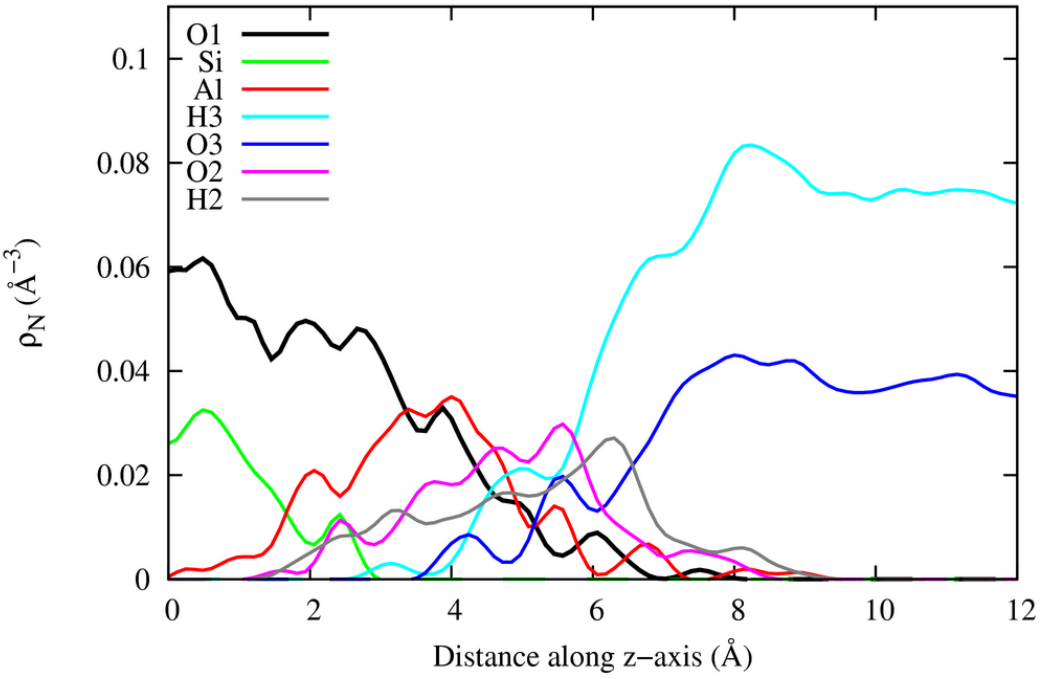

FIGURE D.2: The average distances for the water–Al interactions for the metakaolin slab 2.

Bibliography

[1] Australia's emissions projections 2010. Technical report, DCCEE, Canberra, ACT, 2010.

[2] J. Davidovits. Global Warming Impact on the Cement and Aggregates Industry. *World Resource Review*, 6:263–278, 1994.

[3] T. W. Cheng and J. P. Chui. Fire-resistant geopolymer produced by blast furnace slag. *Minerals Engineering*, 16:205–210, 2003.

[4] K. Komnitsas and D. Zaharaki. Geopolymerisation: A review and prospects for the minerals industry. *Minerals Engineering*, 20:1261–1277, 2007.

[5] W. M. Kriven, M. Gordon, and J. L. Bell. Geopolymers: nanoparticulate nanoporous ceramics make under ambient conditions. *Microscopy and Microanalysis (Proc. 62nd Annual Meeting of the Microscopy Society of America)*, 2004.

[6] J. Davidovits. Geopolymers of the first generation: SILIFACE-Process. *Geopolymer '88, 1st European Conference on Soft Mineralurgy, Compiegne, France*, pages 49–67, 1988.

[7] P. Duxson, J. L. Provis, C. Grant, and J. S. J van Deventer. The role of inorganic polymer technology in the development of 'green concrete'. *Cement and Concrete Research*, 37:1590–1597, 2007.

[8] D. Khale and R. Chaudhary. Mechanism of geopolymerization and factors influencing its development: a review. *Journal of Materials Science*, 42: 729–746, 2007.

[9] P. Duxson, J. L. Provis, G. C. Lukey, S. W. Mallicoat, W. M. Kriven, and J. S. J. van Deventer. Understanding the relationship between geopolymer composition microstructure and mechanical properties. *Colloids and Surfaces A*, 269:47–58, 2005.

[10] D. Hardjito. *Studies on Fly Ash-Based Geopolymer Concrete*. PhD thesis, Curtin University, 2005.

[11] D. Panias, I. P. Giannopoulou, and T. Perraki. Effect of synthesis parameters on the mechanical properties of fly ash-based geopolymers. *Colloids and Surfaces A: Physicochemical and Engineering Aspects*, 301:246–254, 2007.

[12] S. Andini, R. Cioffi, F. Colangelo, T. Grieco, F. Montagnaro, and L. Santoro. Coal fly ash as raw material for the manufacture of geopolymer-based products. *Waste Management (New York, N.Y.)*, 28:416–23, 2008.

[13] M. Izquierdo, X. Querol, J. Davidovits, D. Antenucci, H. Nugteren, and C. Fernández-Pereira. Coal fly ash-slag-based geopolymers: microstructure and metal leaching. *Journal of Hazardous Materials*, 166:561–566, 2009.

[14] R. R. Lloyd, J. L. Provis, K. J. Smeaton, and J. S. J. van Deventer. Spatial distribution of pores in fly ash-based inorganic polymer gels visualised by Wood metal intrusion. *Microporous and Mesoporous Materials*, 126:32–39, 2009.

[15] J. S. J. van Deventer, J. L. Provis, and P. Duxson. Technical and commercial progress in the adoption of geopolymer cement. *Minerals Engineering*, 29: 89–104, 2012.

[16] H. Wang, H. Li, and F. Yan. Synthesis and mechanical properties of metakaolinite-based geopolymer. *Colloids and Surfaces A: Physicochemical and Engineering Aspects*, 268:1–6, 2005.

[17] J. S. J. van Deventer, J. L. Provis, P. Duxson, and G. C. Lukey. Reaction mechanisms in the geopolymeric conversion of inorganic waste to useful products. *Journal of Hazardous Materials*, 139:506–13, 2007.

[18] J. L. Bell, P. Sarin, P. E. Driemeyer, R. P. Haggerty, P. J. Chupas, and W. M. Kriven. X-Ray pair distribution function analysis of a metakaolin-based, $KAlSi_2O_6$–$5.5H_2O$ inorganic polymer (geopolymer). *Journal of Materials Chemistry*, 18:5974, 2008.

[19] M. R. Rowles and B. H. O'Connor. Chemical and Structural Microanalysis of Aluminosilicate Geopolymers Synthesized by Sodium Silicate Activation of Metakaolinite. *Journal of the American Ceramic Society*, 92:2354–2361, 2009.

[20] V. Medri, S. Fabbri, J. Dedecek, Z. Sobalik, Z. Tvaruzkova, and A. Vaccari. Role of the morphology and the dehydroxylation of metakaolins on geopolymerization. *Applied Clay Science*, 50:538–545, 2010.

[21] Y. S. Zhang, W. Sun, and Z. J. Li. Dissolution-Reorientation-Polycondensation Process of Metakaolin in Alkaline Solutions Related to Geopolymerization. *Advances in Science and Technology*, 69:41–50, 2010.

[22] C. F. Maitland, C. E. Buckley, B. H. O'Connor, P. D. Butler, and R. D. Hart. Characterization of the pore structure of metakaolin-derived geopolymers by neutron scattering and electron microscopy. *Journal of Applied Crystallography*, 44:697–707, 2011.

[23] C. E. White, J. L. Provis, A. Llobet, T. Proffen, and J. S. J. van Deventer. Evolution of Local Structure in Geopolymer Gels: An In Situ Neutron Pair Distribution Function Analysis. *Journal of the American Ceramic Society*, 94:3532–3539, 2011.

[24] S. A. Bernal, J. L. Provis, V. Rose, and R. Mejía de Gutierrez. Evolution of binder structure in sodium silicate-activated slag-metakaolin blends. *Cement and Concrete Composites*, 33:46–54, 2011.

[25] R. P. Williams, R. D. Hart, and A. van Riessen. Quantification of the Extent of Reaction of Metakaolin-Based Geopolymers Using X-Ray Diffraction, Scanning Electron Microscopy, and Energy-Dispersive Spectroscopy. *Journal of the American Ceramic Society*, 94:2663–2670, 2011.

[26] C. E. White, J. L. Provis, T. Proffen, and J. S. J. van Deventer. Molecular mechanisms responsible for the structural changes occurring during geopolymerization: Multiscale simulation. *American Institute of Chemical Engineers Journal*, 58:2241–2253, 2012.

[27] J. Davidovits. Solid phase synthesis of mineral blockpolymer by low temperature polycondensation of alumino-silicate polymers. In *Proceedings from the Long-term Properties of Polymers and Polymeric Materials, Stockholm*, 1976.

[28] J. Davidovits. Properties of Geopolymer Cements. *Concrete International*, 9:23–25, 1987.

[29] J. Davidovits. Geopolymer chemistry and properties. *Geopolymer '88, 1st European Conference on Soft Mineralurgy, Compiegne, France*, pages 25–48, 1988.

[30] D. C. Comrie and J. Davidovits. Long term durability of hazardous toxic and nuclear waste disposals. *Geopolymer '88, 1st European Conference on Soft Mineralurgy, Compiegne, France*, pages 125–134, 1988.

[31] J. Davidovits. Geopolymers and geopolymeric materials. *Journal of Thermal Analysis*, 35:429–441, 1989.

[32] M. R. Rowles. *The Structural Nature of Aluminosilicate Inorganic Polymers : A Macro to Nanoscale Study*. PhD thesis, Curtin University, 2004.

[33] J. Giancaspro, P. N. Balaguru, and R. E. Lyon. Use of Inorganic Polymer to Improve the Fire Response of Balsa Sandwich Structures. *Journal of Materials in Civil Engineering*, 18:390, 2006.

[34] S. Bourbigot and S. Duquesne. Fire retardant polymers: recent developments and opportunities. *Journal of Materials Chemistry*, 17:2283, 2007.

[35] W. M. Kriven, M. Gordon, B.L. Ervin, and H Reis. Corrosion Protection Assessment of Concrete Reinforcing Bars with a Geopolymer Coating. In Manuel Brito, Eldon Case, Waltraud M. Kriven, Jonathan Salem, and Dongming Zhu, editors, *Developments in Porous, Biological and Geopolymer Ceramics*, pages 373–381. John Wiley & Sons, Inc., Hoboken, NJ, USA, 2007.

[36] J. Temuujin, W. Rickard, M. Lee, and A. van Riessen. Preparation and thermal properties of fire resistant metakaolin-based geopolymer-type coatings. *Journal of Non-Crystalline Solids*, 357:1399–1404, 2011.

[37] B. A. Latella, D. S. Perera, T. R. Escott, and D. J. Cassidy. Adhesion of glass to steel using a geopolymer. *Journal of Materials Science*, 41:1261–1264, 2005.

[38] J. Temuujin, A. Minjigmaa, W. Rickard, M. Lee, L. Williams, and A. van Riessen. Preparation of metakaolin based geopolymer coatings on metal substrates as thermal barriers. *Applied Clay Science*, 46:265–270, 2009.

[39] S. de Barros, K. C. Gomes, J. R. de Souza, N. P. Barbosa, and S. M. Torres. Geopolymeric Adhesives for Aluminium Joints. *Materials Science Forum*, 643:143–146, 2010.

[40] J. G. S. van Jaarsveld, J. S. J. van Deventer, and L. Lorenzen. The potential use of geopolymeric materials to immobilise toxic metals: Part I. Theory and applications. *Minerals Engineering*, 10:659–669, 1997.

[41] M. G. Blackford, J. V. Hanna, K. J. Pike, E. R. Vance, and D. S. Perera. Transmission Electron Microscopy and Nuclear Magnetic Resonance Studies of Geopolymers for Radioactive Waste Immobilization. *Journal of the American Ceramic Society*, 90:1193–1199, 2007.

[42] J. G. S. van Jaarsveld, J. S. J. van Deventer, and A. Schwartzman. The potential use of geopolymeric materials to immobilise toxic metals: Part II. Material and leaching characteristics. *Minerals Engineering*, 12:75–91, 1999.

[43] D. Kim, M. Quinlan, and T. F. Yen. Encapsulation of lead from hazardous CRT glass wastes using biopolymer cross-linked concrete systems. *Waste Management*, 29:321–328, 2009.

[44] M. L. Granizo, M. T. Blanco-Varela, and A. Palomo. Influence of the starting kaolin on alkali-activated materials based on metakaolin. Study of the reaction parameters by isothermal conduction calorimetry. *Journal of Materials Science*, 35:6309–6315, 2000.

[45] S. Alonso and A. Palomo. Alkaline activation of metakaolin and calcium hydroxide mixtures: influence of temperature, activator concentration and solids ratio. *Materials Letters*, 47:55–62, 2001.

[46] S. Alonso and A. Palomo. Calorimetric study of alkaline activation of calcium hydroxide-metakaolin solid mixtures. *Cement and Concrete Research*, 31:25–30, 2001.

[47] J. L. Provis, P. Duxson, J. S. J. van Deventer, and G. C. Lukey. The role of mathematical modelling and gel chemistry in advancing geopolymer technology. *Chemical Engineering Research and Design*, 83:853–860, 2005.

[48] J. L. Provis and J. S. J. van Deventer. Geopolymerisation kinetics. 2. Reaction kinetic modelling. *Chemical Engineering Science*, 62:2318–2329, 2007.

[49] J. L. Provis, J. S. J. van Deventer, and G. C. Lukey. A conceptual model for solid-gel transformations in partially reacted geopolymeric systems. *Ceramic Transactions*, 165:49–70, 2005.

[50] J. L. Provis, G. C. Lukey, and J. S. J. van Deventer. Do geopolymers actually contain nanocrystalline zeolites? A re-examination of existing results. *Chemical Materials*, 17:3075–3085, 2005.

[51] H. Rahier, J.F. Denayer, and B. van Mele. Low-temperature synthesized aluminosilicate glasses. Part IV. Modulated DSC study on the effect of particle size of metakaolinite on the production of inorganic polymer glasses. *Journal of Materials Science*, 38:3131–3136, 2003.

[52] S. Auerbach, M. Ford, and P. Monson. New insights into zeolite formation from molecular modeling. *Current Opinion in Colloid & Interface Science*, 10:220 – 225, 2005.

[53] C. A. Rees, J. L. Provis, G. C. Lukey, and J. S. J. van Deventer. The mechanism of geopolymer gel formation investigated through seeded nucleation. *Colloids and Surfaces A: Physicochemical and Engineering Aspects*, 318:97–105, 2008.

[54] C. E. White, J. L. Provis, T. Proffen, and J. S. J van Deventer. Quantitative Mechanistic Modeling of Silica Solubility and Precipitation during the Initial Period of Zeolite Synthesis. *The Journal of Physical Chemistry C*, 115:9879–9888, 2011.

[55] P. Rovnaník. Effect of curing temperature on the development of hard structure of metakaolin-based geopolymer. *Construction and Building Materials*, 24:1176–1183, 2010.

[56] J. G. S. van Jaarsveld, J. S. J. van Deventer, and G. C. Lukey. The effect of composition and temperature on the properties of fly ash- and kaolinite-based geopolymers. *Chemical Engineering Journal*, 89:63–73, 2002.

[57] Z. Zuhua, Y. Xiao, Z. Huajun, and C. Yue. Role of water in the synthesis of calcined kaolin-based geopolymer. *Applied Clay Science*, 43:218–223, 2009.

[58] H. M. Khater. Effect of Calcium on Geopolymerization of Aluminosilicate Wastes. *Journal of Materials*, 24:92–101, 2012.

[59] C. K. Yip and J. S. J. van Deventer. Microanalysis of calcium silicate hydrate gel formed within a geopolymer binder. *Journal of Materials Science*, 38:3851–3860, 2003.

[60] I. Lecomte, C. Henrist, M. Liegeois, F. Maseri, A. Rulmont, and R. Cloots. (Micro)-structural comparison between geopolymers, alkali-activated slag cement and Portland cement. *Journal of the European Ceramic Society*, 26:3789–3797, 2006.

[61] S. Bernal, R. Mejía de Gutiérrez, A. L. Pedraza, J. L. Provis, E. D. Rodriguez, and S. Delvasto. Effect of binder content on the performance of alkali-activated slag concretes. *Cement and Concrete Research*, 41:1–8, 2011.

[62] R. Williams and A. van Riessen. Determination of the reactive component of fly ashes for geopolymer production using XRF and XRD. *Fuel*, 89: 3683–3692, 2010.

[63] A. Filippidis and A. Georgakopoulos. Mineralogical and chemical investigation of fly ash from the Main and Northern lignite fields in Ptolemais, Greece. *Fuel*, 71:373 – 376, 1992.

[64] R. Gieré, L. E. Carleton, and G. R. Lumpkin. Micro- and nanochemistry of fly ash from a coal-fired power plant. *American Mineralogist*, 88:1853–1865, 2003.

[65] P. De Silva, K. Sagoe-Crenstil, and V. Sirivivatnanon. Kinetics of geopolymerization: Role of Al_2O_3 and SiO_2. *Cement and Concrete Research*, 37: 512–518, 2007.

[66] R. Fletcher, K. Mackenzie, C. Nicholson, and S. Shimada. The composition range of aluminosilicate geopolymers. *Journal of the European Ceramic Society*, 25:1471–1477, 2005.

[67] V. Petkov, S. J. Billinge, S. D. Shastri, and B Himmel. Polyhedral units and network connectivity in calcium aluminosilicate glasses from high-energy X-Ray diffraction. *Physical Review Letters*, 85:3436–9, 2000.

[68] M. L. Granizo, S. Alonso, M. T. Blanco-Varela, and A. Palomo. Alkalina activation of metakaolin: Effect of calcium hydroxide in the products of reaction. *Journal of the American Ceramic Society*, 85:225–231, 2002.

[69] V. F. F. Barbosa, K. J. D. MacKenzie, and C. Thaumaturgo. Synthesis and characterisation of materials based on inorganic polymers of alumina and silica: sodium polysialate polymers. *International Journal of inorganic Materials*, 2:309–317, 2000.

[70] J. Provis, P. Walls, and J. S. J. van Deventer. Geopolymerisation kinetics. 3. Effects of Cs and Sr salts. *Chemical Engineering Science*, 63:4480–4489, 2008.

[71] E. Najafi Kani, A. Allahverdi, and J. L. Provis. Efflorescence control in geopolymer binders based on natural pozzolan. *Cement and Concrete Composites*, 34:25–33, 2012.

[72] C. Panagiotopoulou, E. Kontori, T. Perraki, and G. Kakali. Dissolution of aluminosilicate minerals and by-products in alkaline media. *Journal of Materials Science*, 42:2967, 2007.

[73] H. Xu and J. S. J. van Deventer. The geopolymerisation of alumino-silicate minerals. *International Journal of Mineral Processing*, 59:247–266, 2000.

[74] J. L. Provis. *Modelling the Formation of Geopolymers*. PhD thesis, The University of Melbourne, 2006.

[75] P. Duxson, G. C. Lukey, F. Separovic, and J. S. J. van Deventer. The effect of alkali cations on aluminium incorporation in geopolymer gels. *Industrial Engineering Chemical Research*, 44:832–839, 2005.

[76] Y. Zhang, W. Sun, and Z. Li. Preparation and microstructure of K-PSDS geopolymeric binder. *Colloids and Surfaces A: Physicochemical and Engineering Aspects*, 302:473–482, 2007.

[77] J. Davidovits. *Geopolymers: Chemistry and Applications*. Institut Geopolymere, Saint-Quentin, France, 2008.

[78] H. Xu and J. S. J. van Deventer. Micro-structural characterisation of geopolymers synthesised from kaolinite/stilbite mixtures using XRD, MAS-NMR, SEM/EDX, TEM/EDX and HREM. *Cement and Concrete Research*, 32:1705–1716, 2002.

[79] P. Duxson, A. Fernández-Jiménez, J. L. Provis, G. C. Lukey, A. Palomo, and J. S. J. Deventer. Geopolymer technology: the current state of the art. *Journal of Materials Science*, 42:2917–2933, 2006.

[80] Z. Zhang, X. Yao, H. Zhu, S. Hua, and Y. Chen. Activating process of geopolymer source material: Kaolinite. *Journal of Wuhan University of Technology-Mater. Sci. Ed.*, 24:132–136, 2009.

[81] E. Prud'homme, P. Michaud, E. Joussein, C. Peyratout, A. Smith, S. Arrii-Clacens, J. M. Clacens, and S. Rossignol. Silica fume as porogent agent in geo-materials at low temperature. *Journal of the European Ceramic Society*, 30:1641 – 1648, 2010.

[82] S. G. Lee, Y. J. Kim, and H. Moon. Energy-Filtering Transmission Electron Microscopy (EF-TEM) Study of a Modulated Structure in Metakaolinite , Represented by a 14 Å Modulation. *Journal of the American Ceramic Society*, 86:174–176, 2003.

[83] V. Stubican and R. Roy. Isomorphous substitution and infrared spectra of lattice layer silicates. *American Mineralogist*, 46:32–51, 1961.

[84] O. Bortnovsky, J. Dedecek, Z. Tvarovzkova, and Z. Sobalik. Metal Ions as Probes for Characterization of Geopolymer Materials. *Journal of the American Ceramic Society*, 91:3052–3057, 2008.

[85] C. Xuemin, H. Yan, L. Leping, and C. Jinyu. Na-A-zeolite synthesis from geopolymer precursor. *MRS Communications*, 1:49–51, 2011.

[86] J. L. Bell, M. Gordon, and W. M. Kriven. Nano- and Microporosity in Geopolymer Gels. In *Microscopy and Microanalysis*, volume 12, pages 552–554, Chicago, Illinois, USA, 2006.

[87] D. Dollimore, P. Spooner, and A. Turner. The bet method of analysis of gas adsorption data and its relevance to the calculation of surface areas. *Surface Technology*, 4:121 – 160, 1976.

[88] K. S. Walton and R. Q. Snurr. Applicability of the BET Method for Determining Surface Areas of Microporous Metal-Organic Frameworks. *Journal of the American Chemical Society*, 129:8552–8556, 2007.

[89] W. M. Kriven, M. Gordon, and J. L. Bell. Geopolymers: Nanoparticulate, nanoporous ceramics under ambient conditions. Technical report, University of Illinois, 2003.

[90] R. R. Lloyd, J. L. Provis, and J. S. J. van Deventer. Pore solution composition and alkali diffusion in inorganic polymer cement. *Cement and Concrete Research*, 40:1386–1392, 2010.

[91] K. Okada, A. Ooyama, T. Isobe, Y. Kameshima, A. Nakajima, and K. J. D. MacKenzie. Water retention properties of porous geopolymers for use in cooling applications. *Journal of the European Ceramic Society*, 29:1917–1923, 2009.

[92] H. Rahier, J. Wastiels, M. Biesemans, R. Willem, G van Assche, and B. van Mele. Reaction mechanisms, kinetics and high temperature transformations of geopolymers. *Journal of Materials Science*, 42:2982–2996, 2007.

[93] L. Zhang and A. Luttge. Aluminosilicate dissolution kinetics: a general stochastic model. *Journal of Physical Chemistry B*, 112:1736–1742, 2008.

[94] H. Xu and J. S. J. van Deventer. Ab-initio calculations on the five-membered alumino-silicate framework rings model: Implication for dissolution in alkaline solutions. *Computers and Chemistry*, 24:391–404, 2000.

[95] Y. Zhang, Y. Jia, W. Sun, and Z. Li. Study of ion cluster reorientation process of geopolymerisation reaction using semi-empirical AM1 calculations. *Cement and Concrete Research*, 39:1174–1179, 2009.

[96] Y. S. Zhang and W. Sun. Semi-empirical AM1 calculations on 6-membered aluminosilicate rings model: Implications for dissolution process of metakaoline in alkaline solutions. *Journal of Material Science*, 42: 3015–3023, 2009.

[97] W. Loewenstein. The distribution of aluminum in the tetrahedra of silicates and aluminates. *American Mineralogist*, 39:92–96, 1954.

[98] J. A. Tossell. A theoretical study of the molecular basis of the Al avoidance rule and of the spectral characteristics of Al-O-Al linkages. *American Mineralogist*, 78:911–920, 1993.

[99] S. K. Lee and J. F. Stebbins. The degree of aluminum avoidance in aluminosilicate glasses. *American Mineralogist*, 84:937–945, 1999.

[100] J. L. Provis, P. Duxson, G. C. Lukey, and J. S. J. van Deventer. Statistical Thermodynamic Model for Si/Al Ordering in Amorphous Aluminosilicates. *Chemistry of Materials*, 17:2976–2986, 2005.

[101] Y. Zhang, W. Sun, and Z. Li. Semi-empirical AM1 calculations on 6-membered aluminosilicate rings model: implications for dissolution process

of metakaoline in alkaline solutions. *Journal of Material Science*, 42:3015–3023, 2007.

[102] J. L. Provis, C. E. White, and J. S. J. van Deventer. Discussion of Y. Zhang et al., Study of ion cluster reorientation process of geopolymerisation reaction using semi-empirical AM1 calculations, Cem Concr Res 39(12): 11741179; 2009. *Cement and Concrete Research*, 40:827–828, 2010.

[103] S. E. Rankin, L. J. Kasehagen, A. V. McCormick, and C. W. Macosko. Dynamic Monte Carlo simulation of gelation with extensive cyclization. *Macromolecules*, 33:7639–7648, 2000.

[104] Y. Chen. Phase transformation and growth of mullite in kaolin ceramics. *Journal of the European Ceramic Society*, 24:2389–2397, 2004.

[105] N. Tezuka, I. Low, I. Davies, M. Prior, and A. Studer. In situ neutron diffraction investigation on the phase transformation sequence of kaolinite and halloysite to mullite. *Physica B: Condensed Matter*, 385–386:555–557, 2006.

[106] G. W. Brindley. The Kaolinite-Mullite Reaction Series: III, The High-Temperature Phases. *Journal of the American Ceramic Society*, 68:503–324, 1959.

[107] G. B. Mitra and S. Bhattacherjee. Layer disorders in kaolinite during dehydration. *Acta Crystallographica Section B: Structural Crystallography and Crystal Chemistry*, 25:1668–1669, 1969.

[108] G. B. Mitra and S. Bhattacherjee. X-ray diffraction studies on the transformation of kaolinite into metakaolin. II. Study of layer shift. *Acta Crystallographica Section B: Structural Crystallography and Crystal Chemistry*, 26:2124–2128, 1970.

[109] T. W. Davies and R. M. Hooper. Structural changes in kaolinite caused by rapid dehydroxylation. *Journal of Materials Science Letters*, 4:39–42, 1985.

[110] K. J. D. MacKenzie, I. W. M. Brown, R. H. Meinhold, and M. E. Bowden. Outstanding problems in the kaolinite-mullite reaction sequence investigated by ^{29}Si and ^{27}Al solid-state nuclear magnetic resonance: I, metakaolinite. *Journal of the American Ceramic Society*, 68:293–297, 1985.

[111] J. Rocha and J. Klinowski. ^{29}Si and ^{27}Al magic-angle-spinning NMR studies of the thermal transformation of kaolinite. *Physics and Chemistry of Minerals*, 17:179–186, 1990.

[112] J. Rocha, J. M. Adams, and J. Klinowski. The Rehydration of Metakaolinite to Kaolinite : Evidence from NMR and Cognate Techniques. *Journal of Solid State Chemistry*, 89:260–274, 1990.

[113] A. Ortega, F. Rouquerol, S. Akhouayi, Y. Lauriero, and J. Rouguerol. Kinetical study of the thermolysis of kaolinite between - 30 °C and 1000 °C by controlled rate evolved gas analysis. *Applied Clay Science*, 8:207–214, 1993.

[114] M. Bellotto, A. Gualtieri, G. Artioli, and S.M. Clark. Kinetic study of the kaolinite-mullite reaction sequence. Part 1: Kaolinite dehydroxylation. *Physics and Chemistry of Minerals*, 22:207–214, 1995.

[115] R. L. Frost. The Dehydroxylation of the Kaolinite Clay Minerals using Infrared Emission Spectroscopy. *Clays and Clay Minerals*, 44:635–651, 1996.

[116] A. Gualtieri and M. Bellotto. Modelling the structure of the metastable phases in the reaction sequence kaolinite-mullite by X-ray scattering experiments. *Physics and Chemistry of Minerals*, 25:442–452, 1998.

[117] P. Ptáček, D. Kubátová, J. Havlica, J. Brandštetr, F. Šoukal, and T. Opravil. Isothermal kinetic analysis of the thermal decomposition of kaolinite: The thermogravimetric study. *Thermochimica Acta*, 501:24–29, 2010.

[118] C. E. White, J. L. Provis, T. Proffen, D. P. Riley, and J. S. J. van Deventer. Combining density functional theory (DFT) and pair distribution function (PDF) analysis to solve the structure of metastable materials: the case of metakaolin. *Physical Chemistry Chemical Physics*, 12:3239–45, 2010.

[119] C. E. White, J. L. Provis, T. Proffen, D. P. Riley, and J. S. J. van Deventer. Density functional modelling of the local structure of kaolinite subjected to thermal dehydroxylation. *The Journal of Physical Chemistry. A*, 114:4988–96, 2010.

[120] R. Millini. Application of modeling in zeolite science. *Catalysis Today*, 41: 41–51, 1998.

[121] D. W. Lewis, C. R. A. Catlow, and J. M. Thomas. Application of computer modelling to the mechanisms of synthesis of microporous catalytic materials. *Faraday Discussions*, 106:451–471, 1997.

[122] C. R. A. Catlow, D. S. Coombes, D. W. Lewis, J. Pereira, and G. Carlos. Computer modeling of nucleation, growth and templating in hydrothermal synthesis. *Chemistry of Materials*, 10:3249–3265, 1998.

[123] L. Jin, S. M. Auerbach, and P. A. Monson. Modeling Nanoparticle Formation during Early Stages of Zeolite Growth: A Low-Coordination Lattice Model of Template Penetration. *The Journal of Physical Chemistry C*, 114: 14393–14401, 2010.

[124] J. N. Watson, L. E. Iton, R. I. Keir, J. C. Thomas, T. L. Dowling, and J. W. White. TPA- silicalite crystallization from homogeneous solution: kinetics and mechanism of nucleation and growth. *Journal of Physical Chemistry B*, 101:10094, 1997.

[125] B. J. Schoeman. Analysis of the nucleation and growth of TPA-silicalite-1 at elevated temperatures with the emphasis on colloidal stability. *Microporous Mesoporous Materials*, 22:922, 1998.

[126] R. Ravishankar, C. E. A. Kirschhock, P. Knops-Gerrits, E. J. P. Feijen, P. J. Grobet, and P. Vanoppen. Characterization of nanosized material extracted from clear suspensions for MFI zeolite synthesis. *Journal of Physical Chemistry B*, 103:4960, 1999.

[127] S. Yang, A. Navrotsky, D. J. Wesolowski, and J. A. Pople. Study on synthesis of TPA-silicalite-1 from initially clear solutions of various base concentrations by in situ calorimetry, potentiometry, and SAXS. *Chemistry of Materials*, 16:210, 2004.

[128] B. P. Feuston and S. H. Garofalini. Oligomerization in silica sols. *Journal of Physical Chemistry*, 94:5351–5356, 1990.

[129] J. C. G. Pereira, C. R. A. Catlow, G. D. Price, and R. M. Almeida. Atomistic modeling of silica based solgel processes. *Journal of Sol-Gel Science and Technology*, 8:55–58, 1997.

[130] T. T. Trinh, A. P. J. Jansen, R. A. van Santen, and E. Jan Meijer. The role of water in silicate oligomerization reaction. *Physical Chemistry Chemical Physics*, 11:5092–5099, 2009.

[131] G. Sposito, S. H. Park, and R. Sutton. Monte Carlo simulation of the total radial distribution function for interlayer water in sodium and potassium montmorillonites. *Clays and Clay Minerals*, 47:192, 1999.

[132] J. A. Greathouse, K. Refson, and G. Sposito. Molecular dynamics simulation of water mobility in magnesium-smectite hydrates. *Journal of the American Chemical Society*, 122:11459–11464, 2000.

[133] R. T. Cygan, J. J. Liang, and A. G. Kalinichev. Molecular models of hydroxide, oxyhydroxide, and clay phases and the development of a general force field. *The Journal of Physical Chemistry B*, 108:1255–1266, 2004.

[134] R. J. Kirkpatrick. Experimental and molecular dynamics modeling studies of interlayer swelling: water incorporation in kanemite and ASR gel. *Materials and Structures*, 38:449–458, 2005.

[135] J. Wang, A. Kalinichev, and R. Kirkpatrick. Effects of substrate structure and composition on the structure, dynamics, and energetics of water at mineral surfaces: A molecular dynamics modelling study. *Geochimica et Cosmochimica Acta*, 70:562–582, 2006.

[136] A. Kalinichev, J. Wang, and R. Kirkpatrick. Molecular dynamics modelling of the structure, dynamics and energetics of mineralwater interfaces: Application to cement materials. *Cement and Concrete Research*, 37:337–347, 2007.

[137] H. Du and J. Miller. A molecular dynamics simulation study of water structure and adsorption states at talc surfaces. *International Journal of Mineral Processing*, 84:172–184, 2007.

[138] S. Kerisit, C. Liu, and E. S. Ilton. Molecular dynamics simulations of the orthoclase (001)- and (010)- water interfaces. *Geochimica et Cosmochimica Acta*, 72:1481–1497, 2008.

[139] R. T. Cygan, J. A. Greathouse, H. Heinz, and A. G. Kalinichev. Molecular models and simulations of layered materials. *Journal of Materials Chemistry*, 19:2470, 2009.

[140] T. Croteau, A. K. Bertram, and G. N. Patey. Water adsorption on kaolinite surfaces containing trenches. *The Journal of Physical Chemistry. A*, 114: 2171–2178, 2010.

[141] D. Argyris, T. Ho, D. R. Cole, and A. Striolo. Molecular Dynamics Studies of Interfacial Water at the Alumina Surface. *Journal of Physical Chemistry C*, 115:2038–2046, 2011.

[142] J. M. Delaye. Modeling of multicomponent glasses: a review. *Current Opinion in Solid State and Materials Science*, 5:451–454, 2001.

[143] S. W. de Leeuw, H. He, and M. F. Thorpe. Vibrational Spectra of Rings in Vitreous Silica. *Solid State Communications*, 56:343–346, 1985.

[144] L. Guttman and S. M. Rahman. Simulation of the structure of amorphous silicon dioxide. *Physical Review B*, 37:2657–2668, 1988.

[145] J. R. Hill, L. Subramanian, and A. Maiti. *Molecular Modeling Techniques in Material Sciences*. CRC Press, Taylor and Francis Group, Boca Raton, FL, 2005.

[146] D. Frenkel and B. Smit. *Understanding molecular simulations*. Academic Press, San Diego, 1996.

[147] J. Šefcík and S. E. Rankin. Monte Carlo Simulations of Size and Structure of Gel Precursors in Silica Polycondensation. *The Journal of Physical Chemistry B*, 107:52–60, 2003.

[148] N. Z. Rao and L. D. Gelb. Molecular Dynamics Simulations of the Polymerization of Aqueous Silicic Acid and Analysis of the Effects of Concentration on Silica Polymorph Distributions, Growth Mechanisms, and Reaction Kinetics. *The Journal of Physical Chemistry B*, 108:12418–12428, 2004.

[149] A. Malani, S. M. Auerbach, and P. A. Monson. Probing the Mechanism of Silica Polymerization at Ambient Temperatures using Monte Carlo Simulations. *The Journal of Physical Chemistry Letters*, 1:3219–3224, 2010.

[150] B. Vessal, A. C. Wright, and A. C. Hannon. Alkali silicate glasses: interpreting neutron diffraction results using the molecular simulation technique. *Journal of Non-Crystalline Solids*, 196:233, 1996.

[151] J. Du and A. N. Cormack. The medium range structure of sodium silicate glasses: a molecular dynamics simulation. *Journal of Non-Crystalline Solids*, 349:66–79, 2004.

[152] D. M. Zirl and S. H. Garofalini. Structure of Aluminosilicate Glasses. *Journal of the American Ceramic Society*, 73:2848, 1990.

[153] S. P. Adiga, P. Zapol, and L. A. Curtiss. Structure and Morphology of Hydroxylated Amorphous Alumina Surfaces. *Journal of Physical Chemistry C*, 111:7422–7429, 2007.

[154] G. Gutierrez and B. Johansson. Molecular dynamics study of structural properties of amorphous Al_2O_3. *Physical Review B*, 65:104202, 2002.

[155] S. P. Adiga, P. Zapol, and L. A. Curtiss. Atomistic simulations of amorphous alumina surfaces. *Physical Review B*, 74:64204, 2006.

[156] K. Smirnov. Including the polarization in simulations of hydrated aluminosilicates. Model and application to water in silicalite. *Chemical Physics*, 292:53–70, 2003.

[157] J. D. Gale and A. L. Rohl. General Utility Lattice Program - GULP. *Molecular Simulation*, 29:291–341, 2003.

[158] T. S. Bush, J. D. Gale, C. R. A. Catlow, and P. D. Battle. Self-consistent interatomic potentials for the simulation of binary and ternary oxides. *Journal of Materials Chemistry*, 4:831–837, 1994.

[159] P. Morse. Diatomic Molecules According to the Wave Mechanics. II. Vibrational Levels. *Physical Review*, 34:57–64, 1929.

[160] K. Schröder, J. Sauer, M. Leslie, C. R. A. Catlow, and J. M. Thomas. Bridging hydroxyl groups in zeolitic catalysts: a computer simulation of their structure, vibrational properties and acidity in protonated faujasites (H_Y zeolites). *Chemical Physics Letters*, 188:320–325, 1992.

[161] F. H. Stillinger and T. A. Weber. Computer Simulation of Local Order in Condensed Phases of Silicon. *Physical Review B*, 31:5262–5271, 1985.

[162] A. B. Rosenthal and S. H. Garofalini. Structural Role of Zinc Oxide in Silica and Soda-Silica Glasse. *Journal of the American Ceramic Society*, 70:821, 1987.

[163] B. P. Feuston and S. H. Garofalini. Empirical three-body potential for vitreous silica. *The Journal of Chemical Physics*, 89:5818, 1988.

[164] B. P. Feuston and S. H. Garofalini. Water–induced relaxation of the vitreous silica surface. *The Journal of Chemical Physics*, 91:564, 1989.

[165] J. K. Gregory and D. C. Clary. Three-body effects on molecular properties in the water trimer. *The Journal of Chemical Physics*, 103:8924–8230, 1995.

[166] J. E. Lennard-Jones. On the determination of molecular fields. *Proceedings of the Royal Society of London. Series A, Containing papers of a mathematical and physical character*, 106:463, 1924.

[167] J. E. Lennard-Jones and A. E. Ingham. On the calculation of certain crystal potential constants, and on the cubic crystal of least potential energy. *Proceedings of the Royal Society of London. Series A, Containing papers of a mathematical and physical character*, 107:636–653, 1925.

[168] J. E. Lennard-Jones and A. F. Devonshire. Critical phenomena in gases. I. *Proceedings of the Royal Society of London. Series A, Mathematical and Physical Sciences*, 163:53–70, 1937.

[169] R. A. Buckingham. The classical equation of state of gaseous helium, neon and argon. *Proceedings of the Royal Society of London. Series A. Mathematical and Physical Sciences*, 168:264–283, 1938.

[170] M. Born and J. E. Mayer. Zur gittertheorie der ionenkristalle. *Zeitschrift für Physik*, 75:1–18, 1932.

[171] P. P. Ewald. Die berechnung optischer und elektrostatisher gitterpotentiale. *Annals of Physics*, 65:253–287, 1921.

[172] D. A. Darden, D. York, and L. Pederson. Particle-mesh Ewald: An N log(N) medthod for Ewald sums in large systems. *Journal of Chemical Physics*, 98:10089–10092, 1993.

[173] T. Darden, L. Perera, L. Li, and L. Pedersen. New tricks for modelers from the crystallography toolkit: the particle mesh Ewald algorithm and its use in nucleic acid simulations. *Structure*, 7:55–60, 1999.

[174] U. Essmann. A smooth particle mesh Ewald method. *The Journal of Chemical Physics*, 103:8577, 1995.

[175] R. W. Hockney, S. P. Goel, and J. W. Eastwood. A 10000 particle molecular dynamics model with long range forces. *Chemical Physics Letters*, 21:589–591, 1973.

[176] J. W. Eastwood, R. W. Hockney, and D. Lawrence. P3M3DP – the three-dimensional periodic particle-particle/particle-mesh program. *Computational Physics Communications*, 19:215–269, 1980.

[177] B. G. Dick and A. W. Overhauser. Theory of the dielectric constants of alkali halide crystals. *Physical Reviews*, 112:90–103, 1958.

[178] J. D. Gale and N. J. Henson. Derivation of interatomic potentials for microporous aluminophosphates from the structure and properties of berlinite. *Journal of the Chemical Society, Faraday Transactions*, 90:3175, 1994.

[179] C. R. A. Catlow, K. M. Diller, and M. J. Norgett. Interionic potentials for alkali halides. *Journal of Physics C: Solid State Physics*, 10:1395–1412, 1977.

[180] M. J. Sangster, R. M. Atwood, and U. Schroder. Interionic potentials for alkali halides. I. Crystal independent shell parameters and fitted Born-Mayer potentials. *Journal of Physics C: Solid State Physics*, 11:1523–1540, 1978.

[181] A. M. Stoneham and M. J. L. Sangster. Diffusion of ions with multiple valence: The oxidation of transition metal alloys. *Philosophical Magazine B*, 52:717–727, 1985.

[182] G. V. Lewis and C. R. A. Catlow. Potential models for ionic oxides. *Journal of Physical Chemistry: Solid State Physics*, 18:1149–1161, 1985.

[183] C. R. A. Catlow, R. G. Bell, and J. D. Gale. Computer modelling as a technique in materials chemistry. *Journal of Materials Chemistry*, 4:781–792, 1994.

[184] D. F. Shanno. Conditioning of quasi-newton methods for function minimization. *Mathematical Computing*, 24:647–656, 1970.

[185] A. Takada, P. Richet, C. Catlow, and G. Price. Molecular dynamics simulation of temperature-induced structural changes in cristobalite, coesite and amorphous silica. *Journal of Non-Crystalline Solids*, 354:181–187, 2008.

[186] J. Habasaki, R. Casalini, and K. L. Ngai. Molecular dynamics study of thermodynamic scaling of the glass-transition dynamics in ionic liquids over wide temperature and pressure ranges. *The Journal of Physical Chemistry. B*, 114:3902–11, 2010.

[187] G. Floudas, M. Paluch, A. Grzybowski, and K. Ngai. *Molecular Dynamics of Glass-Forming Systems: Effects of Pressure*. Springer, 2010.

[188] A. B. Belonoshko, S. Arapan, and A. Rosengren. An ab initio molecular dynamics study of iron phases at high pressure and temperature. *Journal of Physics: Condensed Matter*, 23:485402, 2011.

[189] Y. D. Li, Q. Cao, C. C. Wang, and C.S. Liu. Molecular dynamics study of structural evolution of aluminum during rapid quenching under different pressures. *Physica B: Condensed Matter*, 406:3745–3751, 2011.

[190] F. H. Stillinger. Improved simulation of liquid water by molecular dynamics. *The Journal of Chemical Physics*, 60:1545, 1974.

[191] M. Tuckerman, K. Laasonen, M. Sprik, and M. Parrinello. Ab Initio Molecular Dynamics Simulation of the Solvation and Transport of $H3O^+$ and OH^- Ions in Water. *The Journal of Physical Chemistry*, 99:5749–5752, 1995.

[192] J. Brodholt. Molecular dynamics simulations of aqueous NaCl solutions at high pressures and temperatures. *Chemical Geology*, 151:11–19, 1998.

[193] T. Driesner. Molecular dynamics simulation study of ionic hydration and ion association in dilute and 1 molal aqueous sodium chloride solutions from ambient to supercritical conditions. *Geochimica et Cosmochimica Acta*, 62: 3095–3107, 1998.

[194] S. J. Halstead and A. J. Masters. A classical molecular dynamics study of the anomalous ionic product in near-critical and supercritical water. *Molecular Physics*, 108:193–203, 2010.

[195] K. Stevanovic. Leonhard Euler (1707-1783) and Rigid Body Dynamics. *Scientific Technical Review*, 57(3):3–12, 2007.

[196] D. C. Young. *Computational Chemistry: A Practical Guide for Applying Techniques to real World Problems*. John Wiley and Sons, Inc., 2001.

[197] A. R. Leach. *Molecular Modelling: Principles and Applications. Second Edition*. Pearson Education Limited, 2001.

[198] H. J. C. Berendsen, J. P. M. Postma, W. F. van Gunsteren, A. DiNola, and J. R. Haak. Molecular dynamics with coupling to an external bath. *Journal of Chemical Physics*, 81:3684, 1984.

[199] S. Nosé. A unified formulation of the constant temperature molecular dynamics methods. *The Journal of Chemical Physics*, 81:511, 1984.

[200] W. G. Hoover. Canonical dynamics: Equilibrium phase-space distributions. *Physical Review A*, 31:1695–1697, 1985.

[201] G. Martyna, M. Tuckerman, D. Tobias, , and M. Klein. Explicit reversible integrators for extended systems dynamics. *Molecular Physics*, 87:1117–1157, 1996.

[202] J. D. Gale. GULP: A computer program for the symmetry-adapted simulation of solids. *Journal of the Chemical Society: Faraday Transactions*, 93: 629–637, 1997.

[203] W. Smith and T. R. Forester. DL_POLY_2.0: A general-purpose parallel molecular dynamics simulation package. *Journal of Molecular Graphics*, 14: 136–141, 1996.

[204] W. Smith. Guest editorial: DLPOLY applications to molecular simulation II. *Molecular Simulation*, 32:933–1121, 2006.

[205] W. Smith, T. R. Forester, and I. T. Todorov. *The DL_POLY_2 User Manual*. STFC Daresbury Laboratory, Cheshire, UK, 2010.

[206] S. Plimpton. Fast Parallel Algorithms for Short-Range Molecular Dynamics. *Journal of Computational Physics*, 117:1–19, 1995.

[207] Sandia National Laboratories. Lammps user manual. 2003. URL http://lammps.sandia.gov.

[208] M. E. Tuckerman, B. J. Berne, and G. J. Martyna. Reversible multiple time scale molecular dynamics. *Journal of Chemical Physics*, 97:1990–2001, 1992.

[209] W. Shinoda, M. L. DeVane, and R. Klein. Multi-property fitting and parameterization of a coarse grained model for aqueous surfactants. *Molecular Simulation*, 33:27–36, 2007.

[210] M. Robinson. *Simulating radiation damage in plutonium*. PhD thesis, Loughborough University, 2010.

[211] J. F. Nye. *Physical properties of crystals*. Oxford University Press, 1957.

[212] M. P. Allen and D. J. Tildesley. *Computer Simulation of Liquids*. Oxford University Press, Great Clarendon Street, Oxford, 1987.

[213] A. Einstein. Über die von der molekularkinetischen Theorie der Wärme geforderte Bewegung von in ruhenden Flüssigkeiten suspendierten Teilchen. *Annalen der Physik*, 322:549–560, 1905.

[214] P. Goode and S. Siegel. A Shell Model Approach to the Calculation of Effective Charges. *Physics Letters*, 31B:418–422, 1970.

[215] W. C Mackrod and R. F. Stewart. Defect properties of ionic solids : II. Point defect energies based on modified electron-gas potentials. *Journal of Physics C: Solid State Physics*, 12:431–449, 1979.

[216] M. J. Sanders, M. Leslie, and C. R. A. Catlow. Interatomic potentials for SiO_2. *Journal of the Chemical Society - Chemical Communications*, page 1271, 1984.

[217] C. R. A. Catlow, C. M. Freeman, M. S. Islam, R. A. Jackson, M. Leslie, and S. M. Tomlinson. Interatomic potentials for oxides. *Philosophical Magazine A*, 58:123–141, 1988.

[218] C. R. A. Catlow and G. D. Price. Computer modelling of solid-state inorganic materials. *Nature*, 347:243–248, 1990.

[219] C. R. A. Catlow and W. C. Mackrodt. *Computer Simulation of Solids Lecture Notes in Physics*, volume 166. Springer, Berlin, 1982.

[220] J. D. Kubicki and A. C. Lasaga. Molecular dynamics simulations of SiO_2 melt and glass: Ionic and covalent models. *American Mineralogist*, 73: 941–955, 1988.

[221] S. C. Parker, C. R. A. Catlow, and A. N. Cormack. Structure prediction of silicate minerals using energy-minimization techniques. *Acta Crystallographica Section B: Structural Science*, 40:200–208, 1984.

[222] G. W. Watson, P. M. Oliver, and S. C. Parker. Computer simulation of the structure and stability of forsterite surfaces. *Physics and Chemistry of Minerals*, 25:70–78, 1997.

[223] J. A. Purton and C. R. A. Catlow. Computer Simulation of Feldspar Structures. *American Mineralogist*, 75:1268–1273, 1990.

[224] R. A. Jackson and R. C. A. Catlow. Computer simulation studies of zeolite structures. *Molecular Simulation*, 1:207–224, 1988.

[225] D. W. Lewis, C. R. A. Catlow, G. Sankar, and S. W. Carr. Structure of Iron-Substituted ZSM-5. *The Journal of Physical Chemistry*, 99:2377–2383, 1995.

[226] G. D. Price, S. C. Parker, and M. Leslie. The lattice dynamics and thermodynamics of the Mg_2SiO_4 polymorphs. *Physics and Chemistry of Minerals*, 15:181–190, 1987.

[227] J. A. Purton, N. L. Allan, and J. D. Blundy. Calculated solution energies of heterovalent cations in forsterite and diopside: Implications for trace element partitioning. *Geochimica et Cosmochimica Acta*, 61:3927–3936, 1997.

[228] K. Wright, R. Freer, and C. R. A. Catlow. Water-related defects and oxygen diffusion in albite: a computer simulation study. *Contributions to Mineralogy and Petrology*, 125:161–166, 1996.

[229] W. van Westrenen, N. L. Allan, J. D. Blundy, J. A. Purton, and B. J. Wood. Atomistic simulation of trace element incorporation into garnets a comparison with experimental garnet-melt partitioning data. *Geochimica et Cosmochimica Acta*, 64:1629–1639, 2000.

[230] G. J. Kramer, N. P. Farragher, B. W. van Beest, and R. A. van Santen. Interatomic force fields for silicas, aluminophosphates, and zeolites: Derivation based on ab initio calculations. *Physical Review B Condensed Matter*, 43:5068–5080, 1991.

[231] P. Saul, C. R. A. Catlow, and J. Kendrick. Theoretical studies of protons in sodium hydroxide. *Philosophical Magazine B*, 51:107–117, 1985.

[232] C. I. Sainz-Diaz, A. Hernández-Laguna, and M. T. Dove. Modeling of dioctahedral 2:1 phyllosilicates by means of transferable empirical potentials. *Physics and Chemistry of Minerals*, 28:130–141, 2001.

[233] J. A. Greathouse, J. S. Durkin, J. P. Larentzos, and R. T. Cygan. Implementation of a Morse potential to model hydroxyl behavior in phyllosilicates. *The Journal of Chemical Physics*, 130:134713, 2009.

[234] P. S. Baram and S. C. Parker. Atomistic simulation of hydroxide ions in inorganic solids. *Philosophical Magazine B*, 73:49–58, 1996.

[235] S. Peroos, Z. Du, and N. H. de Leeuw. A computer modelling study of the uptake, structure and distribution of carbonate defects in hydroxy-apatite. *Biomaterials*, 27:2150–61, 2006.

[236] K. Wright. Atomistic Models of OH Defects in Nominally Anhydrous Minerals. *Reviews in Mineralogy and Geochemistry*, 62:67–83, 2006.

[237] J. S. Braithwaite. A theoretical study of the energetics and IR frequencies of hydroxyl defects in forsterite. *Journal of Geophysical Research*, 108:2284, 2003.

[238] A. M. Walker, S. Demouchy, and K. Wright. Computer modelling of the energies and vibrational properties of hydroxyl groups in α- and β-Mg_2SiO_4. *European Journal of Mineralogy*, 18:529–543, 2006.

[239] F. Zhang and K. Wright. Coupled (Li^+, Al^{3+}) substitutions in hydrous forsterite. *American Mineralogist*, 97:425–429, 2012.

[240] M. Blanchard, K. Wright, and J. D. Gale. A computer simulation study of OH defects in Mg_2SiO_4 and Mg_2GeO_4 spinels. *Physics and Chemistry of Minerals*, 32:585–593, 2005.

[241] K. Wright and C. R. A. Catlow. A computer simulation study of (OH) defects in olivine. *Physics and Chemistry of Minerals*, 20, 1994.

[242] V Ermoshin. Ab initio generalized valence force field for zeolite modelling. 1. Siliceous zeolites. *Chemical Physics*, 202:53–61, 1996.

[243] N. Keskar and J. Chelikowsky. Structural properties of nine silica polymorphs. *Physical Review B*, 46:1–13, 1992.

[244] A. B. Belonoshko and L. S. Dubrovinsky. Molecular dynamics of stishovite melting. *Geochimica et Cosmochimica Acta*, 59:1883–1889, 1995.

[245] V. V. Murashov. Thermal conductivity of model zeolites: molecular dynamics simulation study. *Journal of Physics: Condensed Matter*, 11:1261–1271, 1999.

[246] T. J. H. Vlugt and M. Schenk. Influence of Framework Flexibility on the Adsorption Properties of Hydrocarbons in the Zeolite Silicalite. *The Journal of Physical Chemistry B*, 106:12757–12763, 2002.

[247] D. M. Teter. Personal Communication.

[248] B. J. Teppen, K. Rasmussen, P. M. Bertsch, D. M. Miller, and L. Schäfer. Molecular Dynamics Modelling of Clay Minerals. 1. Gibbsite, Kaolinite, Pyrophyllite, and Beidellite. *The Journal of Physical Chemistry B*, 101: 1579–1587, 1997.

[249] A. N. Cormack, J. Du, and T. R. Zeitler. Alkali ion migration mechanisms in silicate glasses probed by molecular dynamics simulations. *Physical Chemistry Chemical Physics*, 4:3193–3197, 2002.

[250] A. Tilocca and N. H. de Leeuw. Structural and electronic properties of modified sodium and soda-lime silicate glasses by Car-Parrinello molecular dynamics. *Journal of Materials Chemistry*, 16:1950, 2006.

[251] A. Tilocca, N. de Leeuw, and A. Cormack. Shell-model molecular dynamics calculations of modified silicate glasses. *Physical Review B*, 73:1–14, 2006.

[252] J. Du, R. Devanathan, L . Corrales, W. J. Weber, and A. N. Cormack. Short- and medium-range structure of amorphous zircon from molecular dynamics simulations. *Physical Review. B, Condensed matter*, 74:1–14, 2006.

[253] N. T. Skipper, K. Refson, and J. D. C. McConnell. Computer simulation of interlayer water in 2:1 clays. *The Journal of Chemical Physics*, 94:7434, 1991.

[254] D. Bougeard, K. S. Smirnov, and E. Geidel. Vibrational Spectra and Structure of Kaolinite: A Computer Simulation Study. *The Journal of Physical Chemistry B*, 104:9210–9217, 2000.

[255] S. C. Parker and G. D. Price. Computer modelling of phase transitions in minerals. *Advanced Solid State Chemistry*, 1:295–327, 1989.

[256] C. Catlow, R. James, W. Mackrodt, and R. Stewart. Defect energetics in α-Al_2O_3 and rutile TiO_2. *Physical Review B*, 25:1006–1026, 1982.

[257] B. Winkler, M. T. Dove, and M. Leslie. Static lattice energy minimization and lattice dynamics calculations on minerals using three-body potentials. *American Mineralogist*, 76:313–331, 1991.

[258] S. M. Antao, I. Hassan, J. Wang, P. L. Lee, and B. H. Toby. State-of-the-art high-resolution powder x-ray diffraction (HRPXRD) illustrated with Rietveld structure refinement of quartz, sodalite, tremolite, and meionite. *The Canadian Mineralogist*, 46:1501–1509, 2008.

[259] T. Yamanaka, T. Fukuda, and J. Mimaki. Bonding character of SiO_2 stishovite under high pressures up to 30 Gpa. *Physics and Chemistry of Minerals*, 29:633–641, 2002.

[260] D. Ikuta, N. Kawame, S. Banno, T. Hirajima, K. Ito, J. F. Rakovan, R. T. Downs, and O. Tamada. First in situ X-ray identification of coesite and retrograde quartz on a glass thin section of an ultrahigh-pressure metamorphic rock and their crystal structure details. *American Mineralogist*, 92: 57–63, 2007.

[261] R. T. Downs and D. C. Palmer. The pressure behavior of c-cristobalite. *American Mineralogist*, 79:9–14, 1994.

[262] E. Balan. First-principles study of the OH-stretching modes of gibbsite. *American Mineralogist*, 91:115–119, 2006.

[263] A. Kirfel and K. Eichhorn. Accurate structure analysis with synchrotron radiation. The electron density in Al_2O_3 and Cu_2O. *Acta Crystallographica Section A: Foundations of Crystallography*, 46:271–284, 1990.

[264] J. B. Burt. Equations of state and structures of andalusite to 9.8 GPa and sillimanite to 8.5 GPa. *American Mineralogist*, 91:319–326, 2006.

[265] P. Comodi, P. F. Zanazzi, S. Poli, and M. W. Schmidt. High-pressure behavior of kyanite : Compressibility and structural deformations. *American Mineralogist*, 82:452–459, 1997.

[266] H. Yang, R. M. Hazen, L. W. Finger, C. T. Prewitt, and R. T. Downs. Compressibility and crystal structure of sillimanite, Al_2SiO_5, at high pressure. *Physics and Chemistry of Minerals*, 25:39–47, 1997.

[267] I. Hassan, S. M. Antao, and J. B. Parise. Sodalite: High-temperature structures obtained from synchrotron radiation and Rietveld refinements. *American Mineralogist*, 89:359–364, 2004.

[268] J. V. Smith, G. Artioli, and A. Kvick. Low albite, $NaAlSi_3O_8$; neutron diffraction study of crystal structure at 13 K. *American Mineralogist*, 71: 727–733, 1986.

[269] F. F. Foit and D. R. Peacor. The Anorthite Crystal Structure at 410 and 830 °C. *American Mineralogist*, pages 665–675, 1973.

[270] T. J. Ahrens. *Mineral Physics and Crystallography: A Handbook of Physical Constants*. American Geophysical Union: Washington DC, 1995.

[271] F. Franks, editor. *Water - A Comprehensive Treatise*, volume 1. Plenum Press, New York, 1975.

[272] A. Brodsky. Is there predictive value in water computer simulations? *Chemical Physics Letters*, 261:563–568, 1996.

[273] F. Tabbutt. Water: A Matrix of Life, 2nd Edition (Franks, Felix). *Journal of Chemical Education*, 78:593, 2001.

[274] P. Ball. Water, an enduring mystery. *Nature*, 452:291–292, 2008.

[275] M. S. Jhon and J. D. Andrade. Water and hydrogels. *Journal of Biomedical Materials Research*, 7:509–22, 1973.

[276] B. Guillot. A reappraisal of what we have learnt during three decades of computer simulations on water. *Journal of Molecular Liquids*, 101:219–260, 2002.

[277] Y. Wu, H. L. Tepper, and G. A. Voth. Flexible simple point-charge water model with improved liquid-state properties. *The Journal of Chemical Physics*, 124:024503, 2006.

[278] H. J. C. Berendsen, J. R. Grigera, and T. P. Straatsma. The missing term in effective pair potentials. *The Journal of Physical Chemistry*, 91:6269–6271, 1987.

[279] J. R. Grigera. An effective pair potential for heavy water. *The Journal of Chemical Physics*, 114:8064, 2001.

[280] W. L. Jorgensen, J. Chandrasekhar, J. D. Madura, R. W. Impey, and M. L. Klein. Comparison of simple potential functions for simulating liquid water. *The Journal of Chemical Physics*, 79:926, 1983.

[281] M. Chaplin. Water Structure and Science – Water Models, June 2012. URL http://www.lsbu.ac.uk/water/models.html.

[282] W. L. Jorgensen and J. D. Madura. Temperature and size dependence for Monte Carlo simulations of TIP4P water. *Molecular Physics*, 56:1381–1392, 1985.

[283] H. W. Horn, W. C. Swope, J. W. Pitera, J. D. Madura, T. J. Dick, G. L. Hura, and T. Head-Gordon. Development of an improved four-site water model for biomolecular simulations: TIP4P-Ew. *The Journal of Chemical Physics*, 120:9665–78, 2004.

[284] S. W. Rick. Simulations of ice and liquid water over a range of temperatures using the fluctuating charge model. *The Journal of Chemical Physics*, 114: 2276, 2001.

[285] J. L. F. Abascal, E. Sanz, R. García Fernández, and C. Vega. A potential model for the study of ices and amorphous water: TIP4P/Ice. *The Journal of Chemical Physics*, 122:234511, 2005.

[286] H. Yu and W. F. van Gunsteren. Charge-on-spring polarizable water models revisited: from water clusters to liquid water to ice. *The Journal of Chemical Physics*, 121:9549–64, 2004.

[287] A. E. Kunz and W. F. van Gunsteren. Development of a nonlinear classical polarization model for liquid water and aqueous solutions: COS/D. *The Journal of Physical Chemistry. A*, 113:11570–9, 2009.

[288] P. Paricaud, M. Predota, A. A. Chialvo, and P. T. Cummings. From dimer to condensed phases at extreme conditions: accurate predictions of the properties of water by a Gaussian charge polarizable model. *The Journal of Chemical Physics*, 122:244511, 2005.

[289] P. G. Kusalik and I. M. Svishchev. The spatial structure in liquid water. *Science*, 265:1219–21, 1994.

[290] M. W. Mahoney and W. L. Jorgensen. A five-site model for liquid water and the reproduction of the density anomaly by rigid, nonpolarizable potential functions. *The Journal of Chemical Physics*, 112:8910, 2000.

[291] A. Wallqvist and R. D. Mountain. *Reviews in Computational Chemistry*, volume 13, pages 183–247. John Wiley and Sons, Inc., 1999.

[292] W. L. Jorgensen and J. Tirado-Rives. Potential energy functions for atomic-level simulations of water and organic and biomolecular systems. *Proceedings of the National Academy of Sciences of the United States of America*, 102:6665–70, 2005.

[293] P. Jedlovszky and J. Richardi. Comparison of different water models from ambient to supercritical conditions: A Monte Carlo simulation and molecular Ornstein-Zernike. *Journal of Chemical Physics*, 110:8019–8031, 1999.

[294] A. K. Soper and M. G. Phillips. A New Determination of the Structure of Water at 25 degrees Celcius. *Chemical Physics*, 107:47–60, 1986.

[295] K. Kiyohara, K. E. Gubbins, and A. Z. Panagiotopoulos. Phase coexistence properties of polarizable water models. *Molecular Physics*, 94:803–808, 1998.

[296] D. van der Spoel, P.J. van Maaren, and H. J. C. Berendsen. A systematic study of water models for molecular simulation: Derivation of water models optimized for use with a reaction field. *The Journal of Chemical Physics*, 108:10220, 1998.

[297] M. W. Mahoney and W. L. Jorgensen. Diffusion constant of the TIP5P model of liquid water. *The Journal of Chemical Physics*, 114:363–366, 2001.

[298] C. Vega, J. L. F. Abascal, M. M. Conde, and J. L. Aragones. What ice can teach us about water interactions: a critical comparison of the performance of different water models. *Faraday Discussions*, 141:251–276, 2009.

[299] O. Matsuoka, E. Clementi, and M. Yoshimine. CI study of the water dimer potential surface. *The Journal of Chemical Physics*, 64:1351–1361, 1976.

[300] A. Delville. Structure and properties of confined liquids: a molecular model of the clay-water interface. *The Journal of Physical Chemistry*, 97:9703–9712, 1993.

[301] N. T. Skipper, G. Sposito, and F. C. Chang. Monte Carlo Simulation of Interlayer Molecular Structure in Swelling Clay Minerals. 2. Monolayer Hydrates. *Clays and Clay Minerals*, 43:294–303, 1995.

[302] J. R. Hill and J. Sauer. Molecular mechanics potential for silica and zeolite catalysts based on ab initio calculations. 1. Dense and microporous silica. *The Journal of Physical Chemistry*, 98:1238–1244, 1994.

[303] J. R. Maple, M. J. Hwang, K. J. Jalkanen, T. P. Stockfisch, and A. T. Hagler. Derivation of class II force fields: V. Quantum force field for amides, peptides, and related compounds. *Journal of Computational Chemistry*, 19: 430–458, 1998.

[304] M. Arab, D. Bougeard, and Konstantin S. Smirnov. Experimental and computer simulation study of the vibrational spectra of vermiculite. *Physical Chemistry Chemical Physics*, 4:1957–1963, 2002.

[305] H. Heinz, H. J. Castelijns, and U. W. Suter. Structure and phase transitions of alkyl chains on mica. *Journal of the American Chemical Society*, 125: 9500–10, 2003.

[306] H. Sato, A. Yamagishi, and K. Kawamura. Molecular Simulation for Flexibility of a Single Clay Layer. *The Journal of Physical Chemistry B*, 105: 7990–7997, 2001.

[307] B. Rotenberg, V. Marry, N. Malikova, and P. Turq. Molecular simulation of aqueous solutions at clay surfaces. *Journal of Physics: Condensed matter*, 22:284114, 2010.

[308] P. Demontis, J. Gulín-González, H. Jobic, M. Masia, R. Sale, and G. B. Suffritti. Dynamical properties of confined water nanoclusters: Simulation study of hydrated zeolite-Na-A: structural and vibrational properties. *ACS nano*, 2:1603–14, 2008.

[309] V. Crupi, D. Majolino, P. Migliardo, and V. Venuti. Dynamical Properties of Liquids in Restricted Geometries. *Journal of Molecular Liquids*, 117: 165–171, 2005.

[310] C. A. Angell. Insights into Phases of Liquid Water from Study of Its Unusual Glass-Forming Properties. *Science*, 319:582–587, 2008.

[311] K. S. Smirnov and D. Bougeard. Water behaviour in nanoporous aluminosilicates. *Journal of Physics: Condensed matter*, 22:284115, 2010.

[312] D. E. Smith. Molecular computer simulations of the swelling properties and interlayer structure of cesium montmorillonite. *Langmuir*, 14:5959–5967, 1998.

[313] N. T. Skipper, K. Refson, and J. D. C. McConnell. Computer calculations of water-clay interactions using atomic pair potentials. *Clay Minerals*, 24: 411–425, 1989.

[314] R. Chanajaree, Ph.A. Bopp, S. Fritzsche, and J. Kärger. Water dynamics in chabazite. *Microporous and Mesoporous Materials*, pages 1–13, 2011.

[315] P. Demontis, G. B. Suffritti, S. Quartieri, E. S. Fois, and A. Gamba. Molecular Dynamics Studies on Zeolites. 3. Dehydrated Zeolite A. *Journal of Physical Chemistry*, 92:867–871, 1988.

[316] W. H. Baur, D. Kassner, C. H. Kim, and N. H. W. Sieber. Flexibility and distortion of the framework of natrolite; crystal structures of ion-exchanged natrolites. *European Journal of Mineralogy*, 2:761–769, 1990.

[317] S. V. Sinogeikin, F. R. Schilling, and J. D. Bass. Single crystal elasticity of lawsonite. *American Mineralogist*, 85:1834–1837, 2000.

[318] M. C. Mayoral, M. C. Izquierdo, J. M. Andres, and B. Rubio. Aluminosilicates transformations in combustion followed by dsc. *Thermochimica Acta*, 373:173 – 180, 2001.

[319] O. Castelein, B. Soulestin, J. P. Bonnet, and P. Blanchart. The influence of heating rate on the thermal behaviour and mullite formation from a kaolin raw material. *Ceramics International*, 27:517–522, 2001.

[320] C. Y. Chen, G. S. Lan, and W. H. Tuan. Microstructural evolution of mullite during the sintering of kaolin powder compacts. *Ceramics International*, 26: 715–720, 2000.

[321] K. Okada, N. Tsuka, and J. Ossaka. Characterization of spinel phase formed in the kaolin-mullite thermal sequence. *Journal of the American Ceramic Society*, 69:251–253, 1986.

[322] C. E. White, J. L. Provis, D. P. Riley, G. J. Kearley, and J. S. J. van Deventer. What is the structure of kaolinite? Reconciling theory and experiment. *The Journal of Physical Chemistry. B*, 113:6756–65, 2009.

[323] D. L. Bish. Rietveld Refinement of the Kaolinite Structure at 1.5K. *Clays and Clay Minerals*, 41:738–744, 1993.

[324] K. W. Katahara. Clay Mineral Elastic Properties. In *SEG Expanded Abstracts*, Denver, Colorado, 1996.

[325] N. H. Mondol, J. Jahren, K. Bjorlykke, and I. Brevik. Elastic properties of clay minerals. *The Leading Edge*, 27:758, 2008.

[326] G. W. Brindley and M. Nakahira. The Kaolinite-Mullite Reaction Series: Il, Metakaolin. *Journal of the American Ceramic Society*, 42:319–324, 1959.

[327] L. Stoch. Significance of structural factors in dehydroxylation of kaolinite polytypes. *Journal of Thermal Analysis*, 29:919–931, 1984.

[328] J. Alexandre, F. Saboya, B. C. Marques, M. L. P. Ribeiro, C. Salles, M. G. da Silva, M. S. Sthel, L. T. Auler, and H. Vargas. Photoacoustic thermal characterization of kaolinite clays. *Analyst*, 124:1209–1214, 1999.

[329] S. Stackhouse, P. V. Coveney, and D. M. Benoit. Density-Functional-Theory-Based Study of the Dehydroxylation Behavior of Aluminous Dioctahedral 2:1 Layer-Type Clay Minerals. *The Journal of Physical Chemistry B*, 108:9685–9694, 2004.

[330] A. Mikowski, P. Soares, F. Wypych, J. E. F. C. Gardolinski, and C M. Lepienski. Mechanical properties of kaolinite 'macro-crystals'. *Philosophical Magazine*, 87:4445–4459, 2007.

[331] B. T. Poe, P. F. McMillan, C. A. Angell, and R. K. Sato. Al and Si coordination in SiO_2-Al_2O_3 glasses and liquids : a study by NMR and IR spectroscopy and MD simulations. *Chemical Geology*, 96:333–349, 1992.

[332] J. Sanz, A. Madani, J. M. Serratosa, J. S. Moya, and S. Aza. ^{27}Aluminum and ^{29}Silicon Magic-Angle Spinning Nuclear Magnetic Resonance Study of the Kaolinite-Mullite Transformation. *Journal of the American Ceramic Society*, 71:C418–C421, 1988.

[333] J. F. Lambert, W. S. Millman, and J. J. Fripiat. Revisiting kaolinite dehydroxylation: a ^{29}silicon and ^{27}aluminum MAS NMR study. *Journal of the American Chemical Society*, 111:3517–3522, 1989.

[334] R. Meinhold, R. Slade, and T. Davies. High-field ^{27}Al MAS NMR studies of the formation of metakaolinite by flash calcination of kaolinite. *Applied Magnetic Resonance*, 4:141–155, 1993.

[335] S. Fleming and A. Rohl. GDIS: a visualization program for molecular and periodic systems. *Zeitschrift für Kristallographie*, 220:580–584, 2005.

[336] M. H. Zhang and V. M. Malhotra. Characteristics of Thermally Activated Alumino-Silicate Pozzolanic Material and its use in Concrete. *Cement and Concrete Research*, 25:1713–1725, 1995.

[337] L. Hellerkallai and I. Lapides. Reactions of kaolinites and metakaolinites with NaOH comparison of different samples (Part 1). *Applied Clay Science*, 35:99–107, 2007.

[338] J. Feldman, D. Papaconstantopoulos, N. Bernstein, and M. Mehl. Structural and Elastic Properties of Amorphous Silicon. *APS Meeting Abstracts*, page 27010, 2003.

[339] S. Davis and G. Gutiérrez. Structural, elastic, vibrational and electronic properties of amorphous Al_2O_3 from ab initio calculations. *Journal of Physics: Condensed matter*, 23:495401, 2011.

[340] D R. Vollet, J. C. D. Macedo, and Y. P. Mascarenhas. Pore structure characterisation of kaolin, metakaolin and their acid-treated products using small-angle X-ray scattering. *Applied Clay Science*, 8:394–404, 1994.

[341] J. G. S. van Jaarsveld and J. S. J. van Deventer. Effect of the alkali metal activator on the properties of fly-ash based geopolymers. *Industrial and Engineering Chemistry*, 38:3932–3941, 2001.

[342] P. Bankowski, L. Zou, and R. Hodges. Reduction of metal leaching in brown coal fly ash using geopolymers. *Journal of Hazardous Materials*, 114:59–67, 2004.

[343] J. W. Phair and J. S. J. van Deventer. Effect of silicate activator pH on the microstructural characteristics of waste-based geopolymers. *Journal of Mineral Processing*, 66:121–142, 2002.

[344] J. W. Phair and J. S. J. van Deventer. Effect of silicate activator pH on the leaching and material characteristics of waste based inorganic polymers. *Minerals Engineering*, 13:289–304, 2001.

[345] C. K. Yip. *The Role of Calcium in Geopolymerisation.* PhD thesis, University of Melbourne, 2004.

[346] M. A. Caldarone, K. A. Gruber, and R. G.. Burg. High-reactivity Metakaolin: A New Generation Mineral Admixture. *Concrete International*, pages 37–40, 1994.

[347] J. Rouguerol, D. Avnir, C. W. Fairbridge, D. H. Everett, J. H. Haynes, N. Pernicone, J. D. F. Ramsay, K. S. W. Sing, and K. K. Unger. Recommendations for the characterization of porous solids. *Pure Applied Chemistry*, 66:1739–1758, 1994.

[348] P. Kowalczyk, H. Tanaka, K. Kaneko, A. P. Terzyk, and D. D. Do. Grand canonical monte carlo simulation study of methane adsorption at an open graphite surface and in slit-like carbon pores at 273 K. *Langmuir*, 21:5639–46, 2005.

[349] S. K. Jain, R. J. M. Pellenq, J. P. Pikunic, and K. E. Gubbins. Molecular modeling of porous carbons using the hybrid reverse Monte Carlo method. *Langmuir*, 22:9942–8, 2006.

[350] P. Kowalczyk, S. Furmaniak, P. A. Gauden, and A. P. Terzyk. Carbon Dioxide Adsorption-Induced Deformation of Microporous Carbons. *The Journal of Physical Chemistry C*, 114:5126–5133, 2010.

[351] D. D. Do, L. F. Herrera, and H. D. Do. A new method to determine pore size and its volume distribution of porous solids having known atomistic configuration. *Journal of Colloid and Interface Science*, 328:110–9, 2008.

[352] B. Lee and F. M. Richards. The Interpretation of Protein Structures: Estimation of Static Accessibility. *Journal of Molecular Biology*, 55:379–400, 1971.

[353] E. W. Washburn and F. F. Fooyitt. Porosity III: Water as an Absorption Liquid. *Journal of the American Ceramic Society*, 4:961–982, 1921.

[354] R. D. Shannon. Revised Effective Ionic Radii and Systematic Studies of Interatomic Distances in Halides and Chalcogenides. *Acta Crystallographica*, 32:751–767, 1976.

[355] M. Leslie and M. J. Gillan. The energy and elastic dipole tensor of defects in ionic-crystals calculated by the supercell method. *Journal of Physics C: Solid State Physics*, 18:973–982, 1985.

[356] M. R. Wang, D. C. Jia, P. G. He, and Y. Zhou. Influence of calcination temperature of kaolin on the structure and properties of final geopolymer. *Materials Letters*, 64:2551–2554, 2010.

[357] A. Elimbi, H.K. Tchakoute, and D. Njopwouo. Effects of calcination temperature of kaolinite clays on the properties of geopolymer cements. *Construction and Building Materials*, 25:2805–2812, 2011.

[358] J. Ninov. Hygroscopic Sorption Properties of Metakaolin. *Chemical Technology*, pages 47–52, 2010.

[359] R. E. Grim and W. F. Bradley. Rehydration and Dehydration of the Clay Minerals. *American Mineralogist*, 33:50–59, 1948.

[360] H. M. Steele, K. Wright, M. A. Nygren, and I. H. Hillier. Interactions of the (001) surface of muscovite with Cu(II), Zn(II), and Cd(II): a computer simulation study. *Geochimica et Cosmochimica Acta*, 64:257–262, 2000.

[361] A. G. Kalinichev and R. J. Kirkpatrick. Molecular Dynamics Modelling of Chloride Binding to the Surfaces of Calcium Hydroxide, Hydrated Calcium Aluminate, and Calcium Silicate Phases. *Chemistry of Materials*, 14:3539–3549, 2002.

[362] D. Tunega, G. Haberhauer, M. H. Gerzabek, and H. Lischka. Theoretical Study of Adsorption Sites on the (001) Surfaces of 1:1 Clay Minerals. *Langmuir*, 18:139–147, 2002.

[363] X. L. Hu and A. Michaelides. Water on the hydroxylated (001) surface of kaolinite: From monomer adsorption to a flat 2D wetting layer. *Surface Science*, 602:960–974, 2008.

[364] E. S. Boek, P. V. Coveney, and N. T. Skipper. Monte Carlo Molecular Modeling Studies of Hydrated Li-, Na-, and K-Smectites: Understanding the Role of Potassium as a Clay Swelling Inhibitor. *Journal of the American Chemical Society*, 117:12608–12617, 1995.

[365] D. A. Young and D. E. Smith. Simulations of Clay Mineral Swelling and Hydration: Dependence upon Interlayer Ion Size and Charge. *The Journal of Physical Chemistry B*, 104:9163–9170, 2000.

[366] T. J. Tambach, E. J. M. Hensen, and B. Smit. Molecular Simulations of Swelling Clay Minerals. *The Journal of Physical Chemistry B*, 108:7586–7596, 2004.

[367] D. E. Smith, Y. Wang, A. Chaturvedi, and H. D. Whitley. Molecular simulations of the pressure, temperature, and chemical potential dependencies of clay swelling. *The Journal of Physical Chemistry. B*, 110:20046–54, 2006.

[368] H. He, J. Galy, and J. F. Gerard. Molecular simulation of the interlayer structure and the mobility of alkyl chains in HDTMA+/montmorillonite hybrids. *The Journal of Physical Chemistry. B*, 109:13301–13306, 2005.

[369] H. Heinz, R. A. Vaia, R. Krishnamoorti, and B. L. Farmer. Self-Assembly of Alkylammonium Chains on Montmorillonite: Effect of Chain Length, Head Group Structure, and Cation Exchange Capacity. *Chemistry of Materials*, 19:59–68, 2007.

[370] P. W. Tasker. The stability of ionic crystal surfaces. *Journal of Physics C: Solid State Physics*, 12:4977–4984, 1979.

[371] M. Zbik and R. S. C. Smart. Dispersion of kaolinite and talc in aqueous solution: nano-morphology and nano-bubble entrapment. *Minerals Engineering*, 15:277–286, 2002.

[372] J. Kameda, A. Yamagishi, and T. Kogure. Morphological characteristics of ordered kaolinite: Investigation using electron back-scattered diffraction. *American Mineralogist*, 90:1462–1465, 2005.

[373] K. L. Konan, C. Peyratout, A. Smith, J. P. Bonnet, S. Rossignol, and S. Oyetola. Comparison of surface properties between kaolin and metakaolin in concentrated lime solutions. *Journal of Colloid and Interface Science*, 339:103–9, 2009.

[374] D. Tunega, M. H. Gerzabek, and H. Lischka. Ab Initio Molecular Dynamics Study of a Monomolecular Water Layer on Octahedral and Tetrahedral Kaolinite Surfaces. *The Journal of Physical Chemistry B*, 108:5930–5936, 2004.

[375] M. R. Warne, N. L. Allan, and T. Cosgrove. Computer simulation of water molecules at kaolinite and silica surfaces. *Physical Chemistry Chemical Physics*, 2:3663–3668, 2000.

[376] J. Du and A. N. Cormack. Molecular Dynamics Simulation of the Structure and Hydroxylation of Silica Glass Surfaces. *Journal of the American Ceramic Society*, 88:2532–2539, 2005.

[377] S. H. Garofalini. Molecular Dynamics Computer Simulations of Silica Surface Structure and Adsorption of Water Molecules. *Journal of Non-Crystalline Solids*, 120:1–12, 1990.

[378] H. Knozinger and P. Ratnasamy. Catalytic Aluminas: Surface Models and Characterization of Surface Sites. *Catalysis Reviews - Science and Engineering*, 17:31–70, 1978.

[379] P. Fenter and N. C. Sturchio. Mineral–water interfacial structures revealed by synchrotron X-ray scattering. *Progress in Surface Science*, 77:171–258, 2004.

[380] K. S. Smirnov and D. Bougeard. A Molecular Dynamics Study of Structure and Short-time Dynamics of Water in Kaolinite. *The Journal of Physical Chemistry B*, 103:5266–5273, 1999.

[381] L. Cheng, P. Fenter, K. Nagy, M. Schlegel, and N. Sturchio. Molecular-Scale Density Oscillations in Water Adjacent to a Mica Surface. *Physical Review Letters*, 87:1–4, 2001.

[382] P. Fenter, L. Cheng, C. Park, Z. Zhang, and N. C. Sturchio. Structure of the orthoclase (001)- and (010)-water interfaces by high-resolution X-ray reflectivity. *Geochimica et Cosmochimica Acta*, 67:4267–4275, 2003.